DEPARTMENT OF ELECTRONIC & ELECTRICAL ENGINEERING

University of Strathclyde Engineering

CHARACTERISATION AND ANALYSIS OF A CORONA-STABILISED SWITCH FILLED WITH ENVIRONMENTALLY-FRIENDLY GAS MIXTURES

A thesis presented in the fulfilment of the requirement of

The degree of

Master of Philosophy

Ruairidh Worthy Macpherson, B.Eng (Honours)

2019

Department of Electronic and Electrical Engineering

University of Strathclyde

Glasgow, UK

DECLARATION OF AUTHENTICITY AND AUTHORS RIGHTS

‘This thesis is the result of the author’s original research. It has been composed by the author and has not been previously submitted for examination which has led to the award of a degree.’

Signed:

Date:

ACKNOWLEDGEMENTS

I would firstly like to thank Dr Mark Wilson and Professor Scott MacGregor for offering me the chance to complete my Master of Philosophy as well as continually offering advice throughout the duration of the project/degree. As well as Dr Igor Timoshkin who also offered me advice throughout the duration of the project.

I would also like to thank all at the HVT/ROLEST research group for their support as well as being very welcoming.

I would finally like to thank my girlfriend and family, for all their support throughout my degree. Especially my gran, Susan Currie Maxwell, for always encouraging me.

ABSTRACT

Tests have been completed with the intention of finding an alternative switching medium to SF_6 due to environmental concerns. For this purpose, a testing procedure was designed in order to test a novel gas in pulsed power, HFO-1234ze, in mixtures with N_2, used as a buffer gas. Thus, decreasing the global warming potential (GWP) of the switching medium from 23900 in SF_6 to 6 in HFO-1234ze. The performance of the gas was measured in a specific corona-stabilised switch geometry, characterising triggering range and delay time experimentally, and calculating jitter.

Over the testing phase it was shown that N_2/HFO-1234ze mixtures were very promising in terms of breakdown strength, with self-breakdown voltages for a 80% N_2 / 20% HFO-1234ze mixture at 3 bar gauge reaching up to 32.2 kV and 36 kV for positive and negative polarity, respectively, giving an increase of 191% and 306% breakdown increase from using 100% N_2. Furthermore, the triggering ranges recorded reached a maximum of 13.4 kV for positive polarity and 13.6 kV for negative polarity, giving increases of 837% and 174% compared to 100% N_2. The delay time and jitter increased accordingly as the total pressure of each individual mix increased.

Von Laue statistical analysis was conducted on the delay time data, in order to estimate the relative contributions of the statistical and formative times to the overall delay time. Statistical times were found to increase slightly with pressure, with no clear polarity effect. The formative times were found to form the majority of the overall delay times, increasing with increasing pressure for both polarities.

In terms of being a viable replacement for SF_6, the gas HFO-1234ze showed positive characteristics in terms of self-breakdown voltage, triggering range and delay time/jitter, in the tested geometry. Although, after testing completion, the electrodes were found to have a layer of carbon which had formed during the testing process; this requires further investigation.

TABLE OF CONTENTS

1. CHAPTER I

INTRODUCTION

In high voltage, pulsed power switching, the most common switch in operation is the plasma closing switch (PCS). This type of switch consists of 2 electrodes separated by a gas, liquid, or solid, such that upon application of a high enough voltage, electron avalanche processes lead to dielectric breakdown, ultimately closing the switch [1]. Switch closure can also be triggered by an external impulse voltage, applied to a third electrode within the switching system. Such switches have many advantages including robustness, low cost and relatively simple operation, which makes them an appropriate choice for many applications [2]. For repetitive operation, however, problems arise with traditional PCS when trying to extend the pulse repetition frequency (PRF) into the kHz regime. At such high PRFs, voltage recovery between switching events becomes problematic, which can result in premature breakdown. To combat this problem within high PRF applications, the technique of corona-stabilisation can be used [3].

Corona-stabilised switches have purposefully pointed electrodes, which result in the formation of corona discharges at these electrode 'points', upon application of a DC voltage across the switch. The corona discharges aid the voltage recovery process, holding off breakdown until the charging voltage has recovered to close to its initial level, enabling the switch to be operated well into the kHz regime [4]. Although, many factors will influence the capability and behaviour of a corona-stabilised switch, for example, inter-electrode distance, electrode radius, gaseous medium, gas pressure, electrode material, applied DC voltage level and polarity, and trigger pulse characteristics. The gaseous switching medium is the main topic of interest for the present study.

Generally, within corona-stabilised switch technology, SF_6 is the gas of choice for use as a dielectric medium within the switch chamber. The reason for this is that SF_6 has desirable switching properties - for example, it is highly insulating, highly electronegative and non-flammable [4]. SF_6 is also widely used within the high voltage, electrical engineering sector, providing external insulation in power transformers and gas-insulated switchgear (GIS) [5].

From an environmental perspective, however, SF_6 also suffers from severe disadvantages. SF_6 is known to be damaging to the environment as it has a global warming potential (GWP) of 23900 over a 100-year time horizon compared to the CO_2 level of 1[6]. In [7], it is documented that not only is the GWP a problem, but the toxic by-products which are associated with the use of SF_6 also drive research into finding a replacement. When SF_6 breaks down, SF_4 is generated, and when this reacts with oxygen within electrical equipment, SOF, SOF_2, SO_2F_2, along with other toxic substances, are generated. Throughout the world, legislations have come into effect restricting the use of SF_6. The Kyoto protocol, issued in 1996, named SF_6 as one of the six greenhouse gases that is restricted for use. California and the European Union have taken action recently, where they have set targets to reduce the amount of SF_6 in the electrical field by 2020 and 2030, respectively [7]. For these reasons, finding an alternative gas or gas mixture to replace SF_6 is highly desirable.

A potential source of a suitable replacement gas are the hydrofluoroolefins (HFO), which have much lower GWP than SF_6. The gas 1,3,3,3 tetrafluoropropene (known as HFO-1234ze), for example, is electronegative, and has a global warming potential of only 6 over a 100-year time horizon [8]. The potential environmental impact is obviously significantly lower than that of SF_6.

Within this thesis, an array of tests has been undertaken on a corona-stabilised switch filled with compressed ambient air, nitrogen, and different mixtures of HFO-1234ze and nitrogen, when operated in the single-shot regime. This characterisation allowed for the switching performance of gas mixtures containing HFO-1234ze to be directly compared with that of both air and nitrogen, and to be discussed in relation to operation in SF_6.

An overview of the present thesis by chapter is detailed below:

Chapter II (Background and literature review) presents background information on pulsed power, gas discharge and corona discharge theory, as well as discussion on different switch topologies. Von Laue analysis is also introduced and explained in the context of separating measured delay times to breakdown into their component statistical and formative parts.

Chapter III (Modelling corona-stabilised switches) includes work completed when simulating switches using finite element electrostatic modelling software, which

provides a static representation of the field distributions within the corona-stabilised switch under different parameters. Space charge is also introduced into the simulations, in order to show the effect on the electrical field distribution.

Chapter IV (Practical CSS data and testing parameters) presents the switch and circuit parameters used in the practical switching system, including switch design and dimensions. A schematic diagram of the overall experimental arrangement is provided, including circuit schematic, gas handling schematic and an overhead view of the laboratory layout. All equipment utilised is detailed in terms of capabilities and operation. The gas mixing procedure developed and utilised in the study, and the effect of the mixing procedure on the measured breakdown voltages, is discussed.

Chapter V (Testing CSS in ambient air) presents the results obtained when the switch was filled with compressed ambient air. The self-breakdown voltage, trigger threshold voltage and delay time were measured, and jitter in the delay time calculated, in order to provide baseline data for comparison with gas mixtures in subsequent chapters. The switch was tested from 0-3 bar gauge for both negative and positive polarity, to find a suitable switch configuration. The data gathered was also used to facilitate selection of a switch topology to be used for the further gas mixture tests. Von Laue analysis was completed on the delay time data, to further understand the relative contributions of the formative and statistical delays to the overall delay time, and how this varies with the experimental conditions.

Chapter VI (Testing of CSS in alternative gas mixtures) introduces the results obtained for the characterisation of mixtures of N_2 and HFO-1234ze. Again, the measured self-breakdown voltages, trigger threshold voltages and delay times, and calculated values of jitter, are presented over the range 0-3 bar gauge for 100% N_2; 95% N_2 / 5% HFO-1234ze; 90% N_2 / 10% HFO-1234ze; and 80% N_2 / 20% HFO-1234ze, for both negative and positive polarity DC energisation. These tests were completed on the optimal switch configuration found in Chapter V.

Chapter VII (Trend and Von Laue statistical analysis of delay time data) informs on the formative and statistical times extracted from the delay time measurements throughout the testing of the N_2 and HFO-1234ze mixtures, using the von Laue approach.

Chapter VIII (Discussion, Conclusions and further work) summarises the testing of the HFO-1234ze/N_2 mixtures in terms of self-breakdown and trigger threshold voltages, delay times (and their statistical and formative components) and calculated jitter. Also, the contributions and major findings of the work completed throughout the project. The switching performance of the novel gas mixtures is discussed and compared to existing literature data on the performance of SF_6 under similar conditions, to enable conclusions regarding the potential for gas mixtures containing HFO-1234ze to be utilised in pulsed power switching applications to be drawn. Further work to assess the relative merits of HFO-1234ze is suggested, with a view to characterising and optimising PRF capabilities, including working with faster trigger pulses to decrease timing jitter.

2. CHAPTER II

BACKGROUND AND LITERATURE REVIEW

2.1. GENERAL

The following chapter focuses on the pertinent background information, latest developments and ongoing research into corona-stabilised switching. This includes the basic concepts of pulsed power, corona discharge, and corona stabilisation theory. Firstly, an overview of pulsed power concepts is covered in terms of switching mechanisms. This is followed by an in-depth review of corona stability and breakdown theory related to plasma closing switches (PCS), with emphasis on corona-stabilised switches (CSS), with the use of a triggering mechanism to initiate controlled switch closure.

2.2. PULSED POWER THEORY

The meaning of pulsed power originates from the method of charging energy-storage components over relatively long times (ms - s), then releasing the energy in a fraction of the charging time (ps - μs) [8]. Therefore, the resulting peak power seen by the load is far greater than the input source average power, increasing from kW to GW in some circumstances [9].

The energy is stored by either inductive or capacitive elements in the system. Within the tests completed in this thesis, only capacitive storage applies. The way in which a capacitive element is added to the circuit will determine the polarity of the impulse that the load will ultimately see [9].

Figure 1 and 2 shows the two ways in which a capacitive pulsed power system can be configured in order to generate impulses of each polarity, when V_{DC} is a positive applied voltage. If a negative voltage were applied, these culminating waveforms would be reversed in polarity.

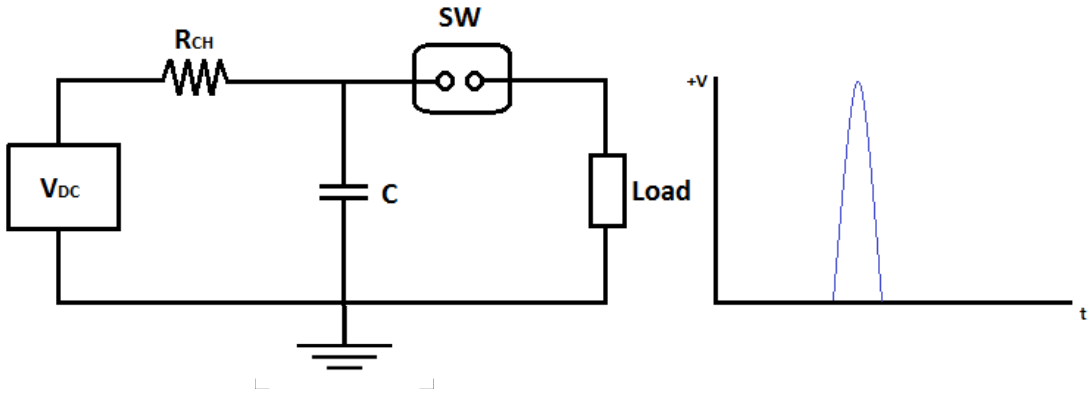

Figure 1 - Non-inverting impulse capacitive circuit with DC voltage supply (V_{DC}), charging resistor (R_{CH}), capacitor (C), spark gap switch (SW) and load; also, an example of a pulse waveform at the load

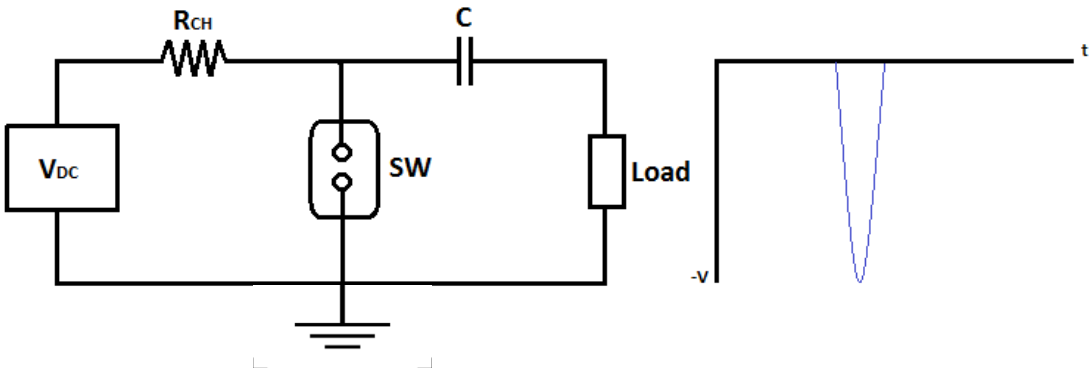

Figure 2 - Inverting impulse capacitive circuit with DC voltage supply (V_{DC}), charging resistor (R_{CH}), capacitor (C), spark gap switch (SW) and load; also, an example of a pulse waveform at the load

Within Figure 1 and 2, it is clear to see that the impulse voltage waveform produced by each individual circuit is dependent on the placement of the capacitive energy-storage element. Therefore, the output voltage polarity can be easily changed to match the requirements of the application, with the same DC supply. The switching element, SW, is traditionally either a self-breaking PCS, or a triggered PCS, incorporating the use of a trigger pulse to initiate breakdown and, ultimately, switch closure.

2.2.1. Plasma

Plasma consists of an abundance of neutral particles, electrons and ionised particles, also known as ions. Plasma is known to be mostly found in a quasi-neutral state, meaning that the amount of negative and positive charge is very close to being equal. The degree of ionisation is given by 2.0

$$X = \frac{n_e}{n_e + n_n} \qquad 2.0$$

where:

- n_e = Density of ions
- n_n = Density of neutral atoms

From equation 2.0, a strongly ionised plasma can be considered as satisfying the condition:

$$X \approx 1$$

If a plasma is weakly ionised, then:

$$X \ll 1$$

The way in which plasma is characterised is defined by the electrostatic interactions, which are governed by Coulomb's law. There are 2 different states that can define a plasma:

- Ideal plasma
- Non-ideal plasma

The charge density within the plasma is relative to each of these types. Ideal plasma has a high charge density contained within the Debye length. Within ideal plasma, the electrostatic energy is lower than the thermal energy associated with the plasma. If the Debye length of the plasma is much greater than the mean distance between the charged particles, then the plasma can be considered as ideal [10].

In non-ideal plasma, the charge density is low, meaning that the electrostatic energy is relatively close to the thermal energy [10].

2.2.2. Ionisation

The process of ionisation is started when energy of sufficient magnitude is introduced into a system occupied with neutral particles. Ionisation takes place where this energy results in interactions with neutral particles and, in terms of positive ionisation, displaces an electron [11]. The minimum magnitude of the energy required for the process is known as the ionisation potential. The gain in energy must be greater than or equal to the ionisation potential of the gas, given by equation 2.1:

$$\lambda_e \geq \frac{V_i}{E} \qquad 2.1$$

where λ_e is the average distance that an electron travels, termed the mean free path, E is the magnitude of the applied electrical field and V_i is the ionisation potential.

The ionisation potential varies by gas type. Table 1 shows the ionisation potential of some gases relevant to this study [12].

Table 1 - Ionisation potential of relevant gases

Material	**Ionisation potential (eV)**
N_2	15.5
O_2	12
SF_6	19.3
CO_2	13.8
Ar	15.7

2.2.2.1. Photoelectric ionisation

The way in which photoelectric ionisation takes place is when a photon of sufficient energy manages to extricate an electron from a neutral atom. This is shown in Figure 3, where a photon is seen to collide with an atom which consequently frees an electron, leaving behind a positive ion [13]. The energy, E, seen is given by equation 2.2:

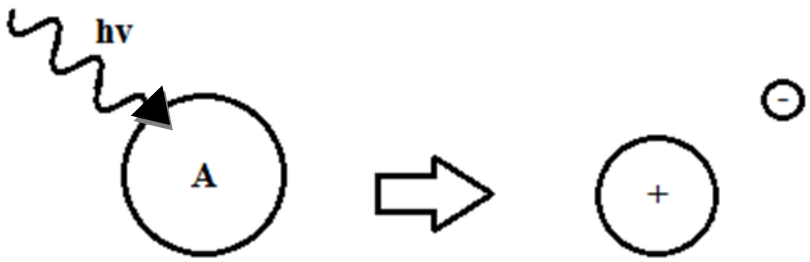

Figure 3 - Photoionization process

$$E = hv \qquad 2.2$$

where Planck's constant, h, $\approx 6.626 \times 10^{-34}$, and v is the frequency.

Equation 2.3 characterises this process [11], [13].

$$A + hv \rightarrow A^{+} + e^{-} \qquad 2.3$$

2.2.2.2. Small particle collisional ionisation

This process occurs when a fast-moving electron, *e*, which has been accelerated by an electrical field, comes into contact with a neutral particle, *A*. Thus, the kinetic energy can free another electron. The energy transfer that takes place has sufficient magnitude that the electron can escape the particle. This results in a situation where the positive ion A^{+} will be left with two free electrons, $2e$ [13], as shown in equation 2.4:

$$A + e \rightarrow A^{+} + 2e \qquad 2.4$$

2.2.2.3. Large particle collisional ionisation

A large particle collision takes place when a large particle collides with a neutral particle. Thus, again, the kinetic energy frees an electron. Again, the electron is able to gain a sufficient amount of energy such that it is able to dislodge itself from the neutral particle:

$$A^{+} + B \rightarrow A^{+} + B^{+} + e \qquad 2.5$$

So, as shown in equation 2.5, the neutral particle *B* collides with the ion A^{+}, which in turn creates A^{+} and B^{+} ions, with a free electron [13].

2.2.2.4. Recombination

Referring to equation 2.3, recombination is the reverse process of the photoelectric ionisation process. This process results when a free electron recombines with a positive

ion, resulting in a neutral particle being formed, as well as a photon given off. This process can be seen in equation 2.6 [13].

$$A^+ + e \rightarrow A + hv \qquad 2.6$$

2.2.2.5. Attachment

This process occurs when a neutral molecule accepts a free electron, which in turn creates a negative ion by attachment. This process occurs mainly in electronegative gases such as SF_6 and HFO-1234ze, where the gas is missing electrons from the outer shell of its atom. This can be illustrated by equation 2.7:

$$A + e \leftrightarrow A^- + hv \qquad 2.7$$

When an electron attaches to a neutral particle, a negative ion is formed, and a photon of light is given off. The free electron being absorbed by the atom results in a much heavier negative ion, which is a much larger and slower particle. From this change, the probability for the negative ion to go on to cause further ionisations is reduced. This results in higher applied voltages being required in order for the negative ions to go on to cause further ionisations. Electron attachment is more prevalent in electronegative gases [14].

In the reverse process, the collision of a photon and a negatively charged ion can release the attached electron, leaving a neutral particle and a free electron. This process is known as photoelectric detachment [13].

2.2.2.6. Electron affinity

For a negative ion to exist and remain stable, its total energy has to be lower than that of the atom in the ground state. After a free electron attaches itself to a neutral particle, the change in energy is known as electron affinity. Dependent upon the attraction between the electron and the neutral particle, this will alter the amount of energy released; the larger the attractive force, the higher the energy. The reason for the halogens' strong electronegativity is dependent on the higher positive charge in the

nucleus and how close the bonding pair of electrons is to the nucleus of the halogen. The larger pull from the nucleus to the bonded pair is how the electronegativity is determined [13].

2.2.3. Townsend Discharge

When a voltage is applied between two electrodes insulated by a gas such that a uniform electrical field is established, the current in the gas is affected. The relationship between current, *I*, and voltage, *V*, can be seen in Figure 4.

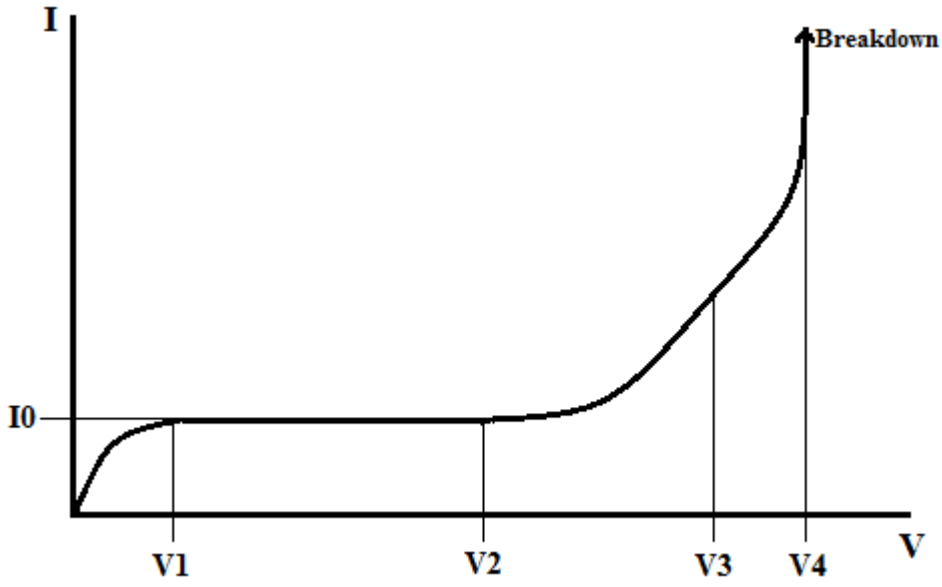

Figure 4 – I-V characteristics of two electrode spark gap [12], [15]

At first, *dI/dV* is proportionate where the current increases linearly with voltage up until point *I0* has been reached. Between *V1* and *V2*, the current remains constant at *I0*, known as the saturation current. Once the applied voltage reaches *V2*, the current then increases at an exponential rate. The exponential relationship between the current and voltage after *V2* is such that the current then rises above *I0* rapidly until a spark is established across the inter-electrode gap. In this phase, the increasing electric field then accelerates electrons leaving the cathode, which in turn creates more collisions, leading to further ionisation of the gas.

The number of electrons produced by an electron per unit length of path in the direction of the field is referred to as Townsend's first ionisation coefficient, α [13]. The number of electrons that reach the anode can be found using equation 2.8:

$$n = n_0 e^{\alpha d} \qquad 2.8$$

where,

- n = number of electrons produced by collisions
- n_0 = number of electrons generated at cathode
- α = Townsend's first ionization coefficient
- d = inter-electrode gap spacing

This is related to the currents in the gas by equation 2.9:

$$I = I_0 e^{\alpha d} \qquad 2.9$$

where,

- I_0 = cathode current
- I = discharge current

An illustration of an electron avalanche is shown in Figure 5. The first electron emitted from the cathode collides with a neutral particle within the inter-electrode gap spacing and transfers its kinetic energy into the creation of two free electrons and a positive ion (see section 2.2.2.2). Further collisions then take place as the electrons accelerate away from the formed positive ion at an exponential rate. Thus, an electron avalanche is formed.

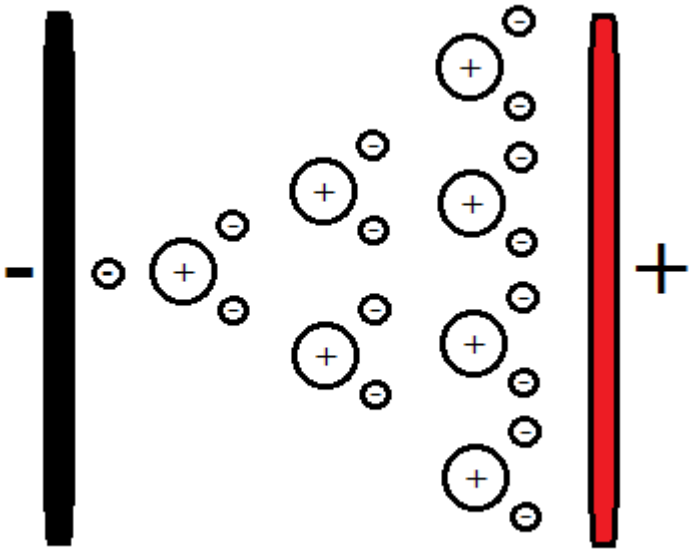

Figure 5 - Electron avalanche illustration [13]

2.2.3.1. Secondary ionisation

Also occurring within the gas is a process known as secondary ionisation, where the positive ions formed by the collisions in the electron avalanche then accelerate towards the cathode. This mass collision with the cathode then creates further injection of electrons from the cathode. This process is accounted for by the addition of the secondary ionisation coefficient, γ, to the governing equations [12], [15].

In addition to equation 2.8 therefore, the number of electrons ultimately formed from the ion collisions with the cathode results in equations 2.10 and 2.11:

$$n = (n_0 + n_+)e^{\alpha d} \qquad 2.10$$

$$n = \gamma[n - (n_0 + n_+)] \qquad 2.11$$

Eliminating n_+, equation 2.12 is found:

$$n = \frac{n_0 e^{\alpha d}}{1 - \gamma(e^{\alpha d} - 1)} \qquad 2.12$$

In the steady-state, the circuit current will be given by equation 2.13:

$$I = \frac{I_0 e^{\alpha d}}{1 - \gamma(e^{\alpha d} - 1)} \qquad 2.13$$

From equation 2.13, the process can be seen as self-sustaining when:

$$\gamma(e^{\alpha d} - 1) = 1 \qquad 2.14$$

As a result of the ion attraction and mass collision with the cathode releasing electrons, the process repeats. Thus, electron avalanches will continue to materialise without the need for external systems having to deliver energy for the continuation of the avalanche process [13], [14]. Equation 2.14 is referred to as the Townsend criterion for breakdown.

2.2.3.2. Townsend's criterion for spark breakdown

Equation 2.13 describes the development of the current that is seen between the electrodes prior to the occurrence of spark breakdown. From Figure 4, at low field strengths (low voltages) $e^{\alpha d}$ is closer to 1, and the current is then equal to $I_0 e^{\alpha d}$ in the region between *V2* and *V3*. As the voltage continues to increase, $e^{\alpha d}$ and $\gamma e^{\alpha d}$ both continue to increase until $\gamma e^{\alpha d}$ is unity, when $e^{\alpha d}$ approaches infinity. The current is capped by the resistance of the power supply.

For a gap spacing of distance, *d*, breakdown will occur when α and γ reach their critical values [15], [16].

Accounting for electron attachment, η, equation 2.14 becomes equation 2.15:

$$\gamma\left(e^{(\alpha-\eta)d} - 1\right) = 1 \qquad 2.15$$

Therefore, if the electron attachment coefficient (η) is greater than the first ionisation coefficient, then breakdown will not occur due to no electron multiplication [17].

2.2.4. Paschen's Law

In a plane-plane electrode geometry under DC stress, the field strength within the inter-electrode gap will be uniform. Under these conditions, equation 2.16 applies:

$$E = \frac{V}{d} \qquad 2.16$$

where

- E = Electrical field strength (V/m)
- V = Applied voltage (V)
- d = Inter-electrode gap distance (m)

The coefficients γ *and* α, are defined by equations 2.17 and 2.18, respectively:

$$\gamma = F_1\left(\frac{E}{p}\right) \qquad 2.17$$

$$\alpha = pF_2\left(\frac{E}{p}\right) \qquad 2.18$$

Combining equations 2.16-2.18 with equation 2.14 yields equation 2.19:

$$\left(F_1\left(\frac{V_b}{pd}\right)\right)\left[e^{\left(pF_2\left(\frac{V_b}{pd}\right)\right)d} - 1\right] = 1 \qquad 2.19$$

Where:

- E = Electrical field strength
- p = Gas pressure
- d = Inter-electrode spacing
- α = Townsend's first ionisation coefficient
- γ = Townsend's second ionisation coefficient
- V_b = Breakdown voltage

Analysing equation 2.19, the value of the breakdown voltage, V_b, is only related to the pressure (p) of the gas and the inter-electrode spacing (d) within the system [16], [18].

The breakdown voltage is the same for a given value of the product *pd*:

$$V_b = F(pd) \qquad 2.20$$

Equation 2.20 is known as Paschen's law.

The typical relationship between the breakdown voltage of a gas and the pressure-distance (*pd*) product is illustrated in Figure 6 [16], [18].

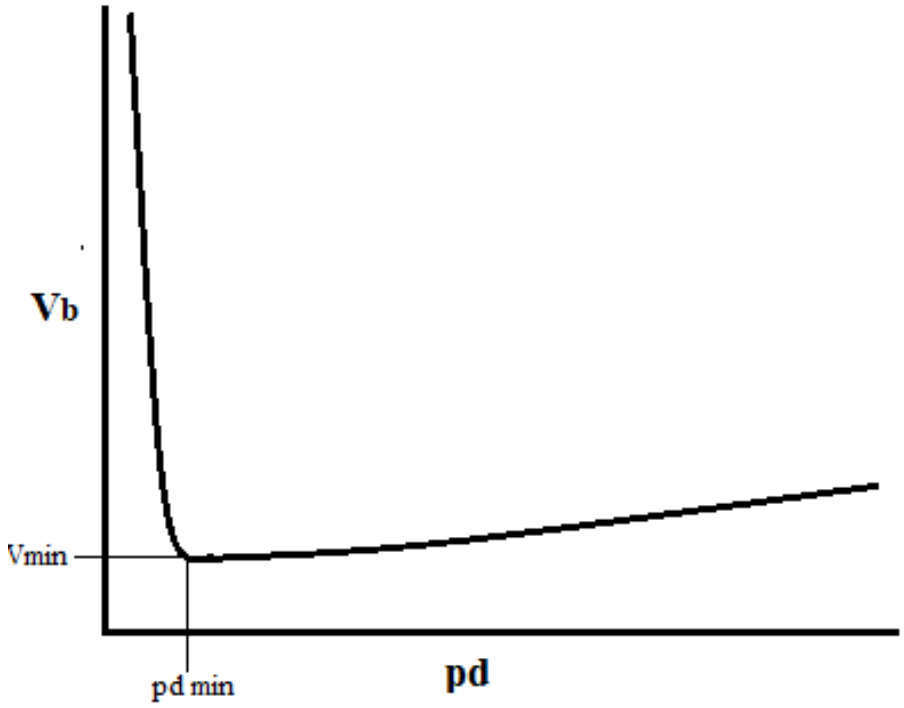

Figure 6 – Paschen Curve - Breakdown voltage / pd relationship [16], [18]

Referring to Figure 6, V_{min} is the minimum voltage required to break down the gas, which occurs at the Paschen minimum, shown as pd_{min}. All gases have different V_{min} and pd_{min} values, and Table 2 shows the minimum breakdown voltages for various gases.

Table 2 - Minimum breakdown voltage for various gases [18]

Gas	**V_b (min) (V)**	***pd* at V_b (min) (Pa.m)**
Air	327	0.754
CO_2	420	0.678
N_2	251	0.891

What can also be seen from Figure 6 is that is the relationship is not linear: at $pd > pd_{min}$, the breakdown voltage is higher than that at pd_{min}. The reason for this occurrence is due to the shorter electron mean free path, whereby electrons traversing the gap are colliding with more gas molecules compared to the electrons travelling at pd_{min}, reducing their kinetic energy. Therefore, for the breakdown process to commence, a higher potential has to be applied. When $pd < pd_{min}$, the breakdown voltage also increases, as free electrons have the possibility to cross the gap making very few or no ionising collisions in the process.

2.2.5. Streamers

Townsend breakdown only takes into account the ionisation process during the current growth leading to breakdown. Townsend theory does not take into account the other parameters associated with breakdown, like gas pressure and electrode geometry. This is where streamer mechanism theory comes into effect. Within Townsend breakdown theory, it is known that the electric field under an electron avalanche can be characterised as an exponential function, shown in equation 2.9 as $e^{\alpha d}$. However, this does not take into account the effect of space charge, where the electric field is distorted across the gap, dependent upon the polarity of the streamer.

The following discussion will focus on streamers in gaseous discharges. The polarity of the streamers created is dependent upon the applied voltage within the system. Therefore, the location of the formation of a streamer determines the polarity of said streamer [16]. Streamers propagating from the cathode are known as ‘negative streamers’; also, as such streamers will be travelling towards the anode, they can also be called ‘anode-directed streamers’. Positive polarity streamers propagate from the anode of the system and can also be called ‘cathode-directed streamers’ [19].

Streamers form in the shape of long, thin, ionised channels. The space charge that is produced has an effect on the growth of the electron avalanche. The minimum breakdown strength of gases has been shown to correspond to a critical charge density of 10^8 per cm^3; when the charge density was measured as between 10^6 and 10^8, the growth of an impending avalanche was weakened due to the lower probability of breakdown occurring [15], [16], [19].

2.2.5.1. Streamer structure

The way in which a streamer is structured is illustrated in Figure 7. Shown is the structure of both a negative and a positive streamer.

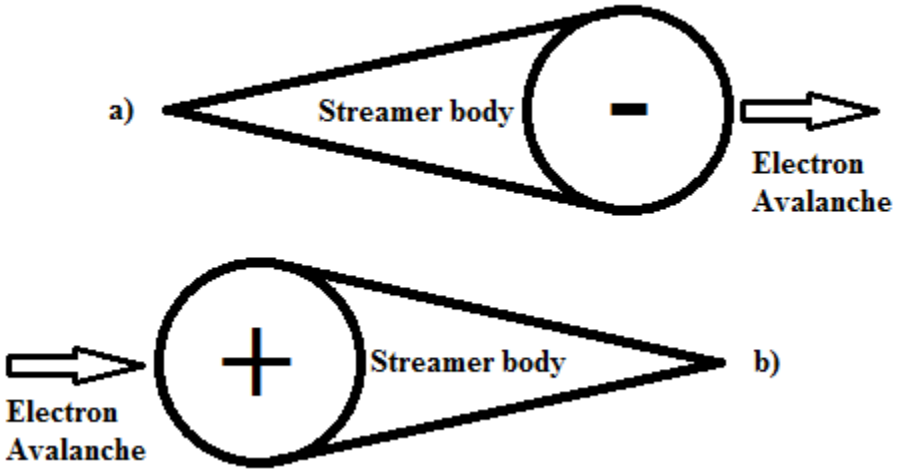

Figure 7 - Structure of a) negative (anode-directed) streamer and b) positive (cathode-directed) streamer,

As seen from Figure 7, both negative and positive streamers have been illustrated. In Figure 7a, the head of the negative streamer has a strong electric field towards the anode because of space charge. Ionisation takes place as the electrons are dislodged, leaving behind positive ions. The electrons move at a far greater speed than the heavier positive ions [15], [16].

The electrical field distribution associated with both negative and positive streamers is illustrated in Figure 8 and 9, respectively.

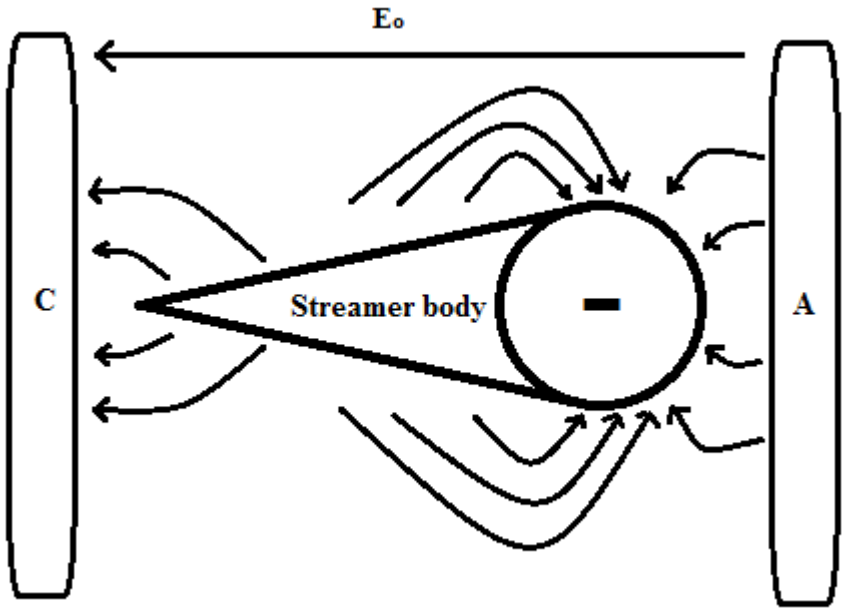

Figure 8 - Negative streamer electrical field line distribution

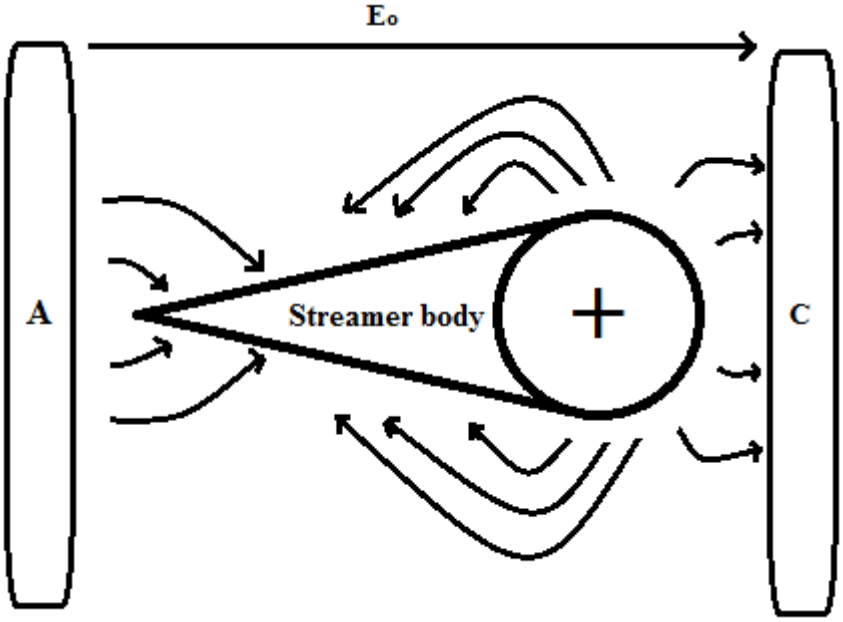

Figure 9 - Positive streamer electrical field line distribution

In Figure 8, a local electrical field is formed between the negative streamer head and the positive streamer body, which is in the opposite direction to the applied electrical field, reducing the overall electrical field strength, as seen in the graph associated with Figure 10. In Figure 9, for the positive streamer, the electrical field distribution creates a local field between the positive head of the streamer and negative streamer body, just like in the case of the negative streamer [16].

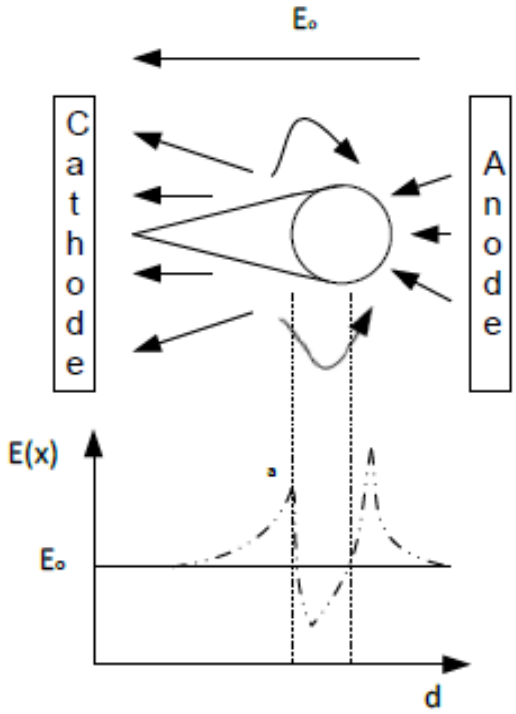

Figure 10 - Electrical field distribution graph [16]

Figure 10 shows the change in electrical field strength over the length of the streamer within the electrode gap. It shows a negative streamer where the local field creates this weak region of electrical field strength between the space charge head and the positive streamer body due to the opposing electric fields. It is seen as the streamer crosses the gap and the electron avalanche within the gap reaches a sufficient size. Due to the external applied field and the space charged formed, the avalanche head can experience intense ionisation, which can result in the field strength at this point being the strongest point across the gap. This will then result in more electrons being formed and secondary ionisation occurring, which will end with an ionised spark channel becoming formed and cause full breakdown.

2.3. Corona Discharge Theory

Corona discharge refers to the phenomena of discharges at irregular edges or points where the radius is very small. At these points a non-uniform electric field is established. Where corona takes place, it can be seen by a blue/purple glow and audible discharges are also present. This occurs prior to breakdown occurring and can be in the form of transient or steady-state discharges [1], [12], [20].

Visibly, corona is shown in Figure 11a and 11b, where positive and negative discharge phenomena can be seen, respectively.

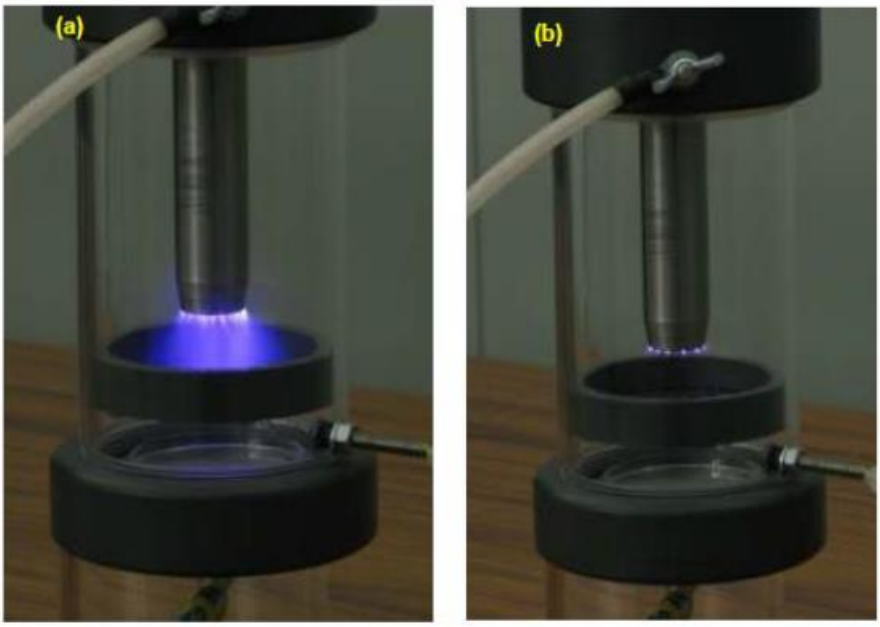

Figure 11 - Practical representation of a) positive corona b) negative corona [17]

What can be seen in Figure 11, is two different visual coronas which are established at the high-voltage electrode, dependent upon polarity. As shown, the positive polarity corona is much greater in terms of extending further into the electrode gap than the negative - this is due to negative ions forming near the anode surface, resulting in the formation of onset streamers. These streamers are short in length and are numerous. They form a glow which takes up a significant area of the electrode which can be seen in Figure 11a [12]. The negative corona is much smaller in size and produces cone-like spots. The electrons are repelled away from the electrode towards the anode until the point where the field becomes too weak for ionisation by collision to take place. Beyond this point the electrons are attached to atoms, creating negative ions which continue to drift slowly towards the anode. As the avalanche continues, some photons radiate from the electrode in all directions, as seen in Figure 11b [12].

2.3.1. Negative corona

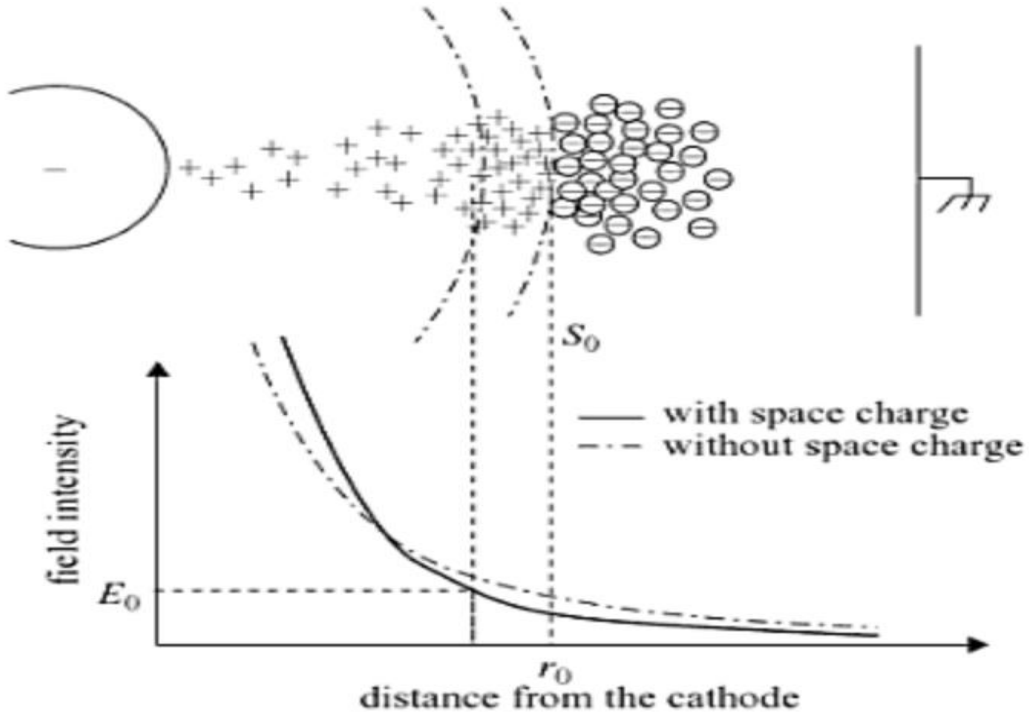

Figure 12 - Negative polarity corona with electrical field strength distribution in the gap [74]

Figure 12 shows the process when a negative polarity is applied to the point electrode. As seen, electrons are repelled away from the highly-stressed, negative-polarity electrode. These electrons travel and develop towards the anode in a decreasing field. The electron avalanche stops at the boundary surface S_0, where the net ionisation coefficient is 0 due to the non-uniformity of the field distribution. Due to electron attachment, these free electrons go on to form negative ions in the area after S_0 [22], [23]. This has an effect on the overall local field distribution seen in Figure 12, which shows the comparison of with and without space charge. It is this space charge which determines this increase in field near the cathode but reduces at the anode. If the gaseous dielectric is strongly electronegative, for example SF_6 or HFO-1234ze, these free electrons will be absorbed. Within this geometry, a space charge 'cathode sheath' is formed a distance away from the pointed electrode, which ultimately weakens the field at this point due to the high velocity of electrons being repelled from the anode - this weakened field then stops an avalanche taking place. As time progresses, positive space charge moves towards the cathode, which in turn increases the local electrical field strength [20]. Over time and with increasing applied potential, the negative space charge starts to disperse, making electron avalanches possible and leading to electrical breakdown. As a result, negative polarity breakdown voltages are higher than those for positive polarity in highly electronegative gases. Figure 12 shows the relationship

of the electric field strength with and without space charge throughout the length of the gap. The dashed line represents the Laplacian [24] electric field, and the solid line is when space charge has been added [20].

2.3.2. Positive corona

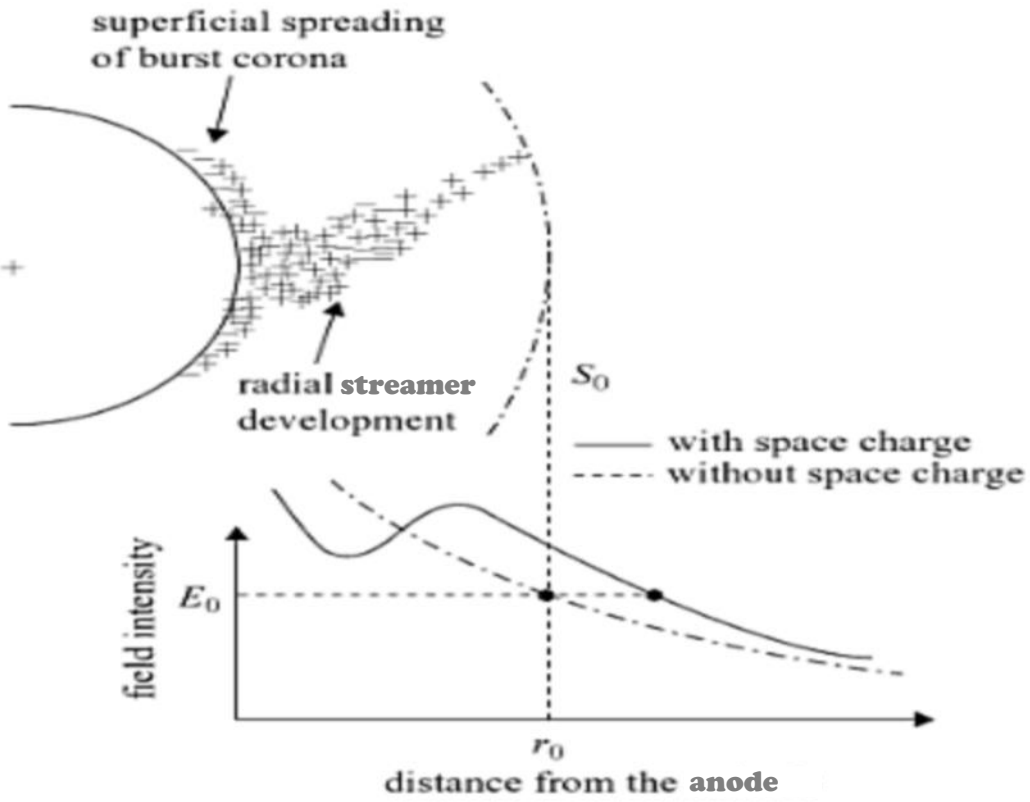

Figure 13 - Positive polarity corona with electrical field strength distribution in the gap [74]

When a positive polarity voltage is applied to the pointed electrode, a non-uniform electrical field is established in the gap at the pointed electrode. The radius of the point determines how non-uniform the electrical field will be [20]. Shown in Figure 13 is the electrical field strength in the inter-electrode gap. There are two different distributions shown - the dashed line is the electrical field distribution when there is no space charge, where the electrical field strength decreases as the distance increases; whereas the solid line shows the space-charge-modified electrical field distribution. The reason for this increase in electrical field strength at the anode is due to high electron mobility in a continuously increasing field. The positive electrode attracts electrons towards its surface, which, in turn, leaves behind positive space charge. The region between the positive electrode and the positive space charge has reduced local

electrical field strength up to S_0. Afterwards the field decreases towards the cathode. The space charge causes the field to strengthen until a point where the field starts to decrease due to the distance from the HV electrode, and the fact that the positive ions start to travel towards the cathode [20].

2.4. CORONA STABILISATION

Corona stabilisation is a phenomenon that occurs in the region between corona onset and breakdown. The relationship between voltage and pressure, as relevant for corona stabilisation, is shown in Figure 14.

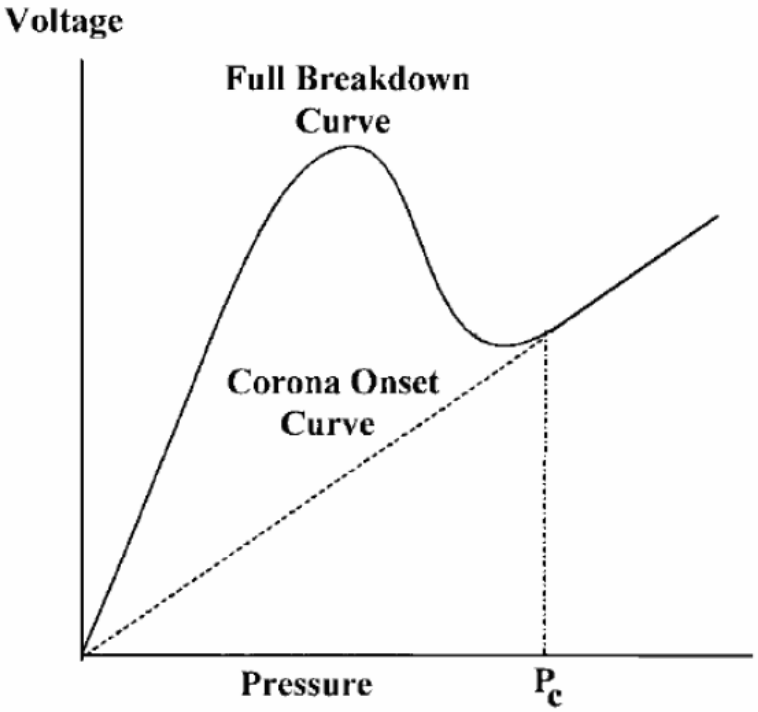

Figure 14 - V-p characteristic in an electronegative gas [2], [25], [26], [27], [28]

In Figure 14, the two key parameters of corona stabilisation in order to enable high pulse-repetition frequency (PRF) operation can be established, with an electronegative gas. The corona onset level is the voltage at which corona is established at the pointed electrode at a specific pressure; as the applied voltage is increased, the point of breakdown is reached, portrayed by the solid, non-linear, curve [29]. Corona-stabilisation is most efficient when the distance between these two curves is great. Within the corona stabilisation region there are different types of corona which can be established. At a critical pressure, P_c, however, there is no pre-corona discharge appears before full breakdown. Therefore, when testing the suitability of a gas to be used in high-repetition rate switching, the area between the corona onset curve and the

breakdown curve must be established to be wide enough so that the stabilisation region is sufficient [30].

Once corona has been established at the pointed electrode, space charge increases. This will continue until a critical value has been reached and at this point corona will reduce. At this point the corona is local to the pointed electrode, which prevents full breakdown from occurring. The pressure of the gaseous medium used within the system will determine what type of corona will be seen for the duration of operation [20], [21].

2.5. TYPES OF CORONA

Corona type is dependent upon the specific electrode geometry as well as polarity. The radius of the HV electrode is linked to the non-uniformity of the electric field which is produced under applied voltage. The smaller the radius of the electrode the stronger the electric field strength will be at the point of the electrode compared to an electrode of greater radius. This is explained in greater detail with reference to the electrode geometry simulated in section 2.8.

Types of corona extend from a glow at corona onset voltage to streamers propagating before breakdown occurs. This is dependent on the polarity, distance, electrode topology, pressure [31] and applied voltage. Figure 11 provides an example of polarity differences in corona. What can be seen is that the positive corona is much greater than that of the negative polarity in terms of size and extension into the gap. This has been explained extensively in 2.3. If the applied voltage was higher, this would lead to more corona and possibly leading to breakdown if the electrical breakdown strength of the gas is reached [34].

As discussed in 2.4, the pressure of the system also has an effect on the corona type. This alters the effect of the corona: as the pressure is greater, there are more atoms which electrons can collide with during the ionization process, so the region between the corona onset voltage curve and the full breakdown voltage curve will narrow, caused by the development of filamentary leader discharges, these leader discharges curve around the stabilised region to the opposing electrode, inhibiting pre-breakdown glow corona and streamers [2], [5], [25], [26]. This can be seen in Figure 14, as the pressure increases beyond the point of the widest corona stabilisation region, it then

narrows towards the critical pressure, where breakdown will occur with no initial corona [25].

Figure 15 shows the relationship between voltage and current within an electrical breakdown. This starts off with a dark discharge, characterised by low current and low voltage, where nothing can be seen at the electrode as the field strength is not high enough to provide sufficient ionisation. At D, the current has increased sufficiently for a glow discharge to be evident; this point corresponds to the corona inception voltage. As the current is increased, a drop-in voltage is seen as the potential is lost to the initiation of the corona within the gap. The voltage continues to fall until point G, where the current rises towards point I, the transition to an arc, where a spark channel has been formed and the current will then increase exponentially if not regulated.

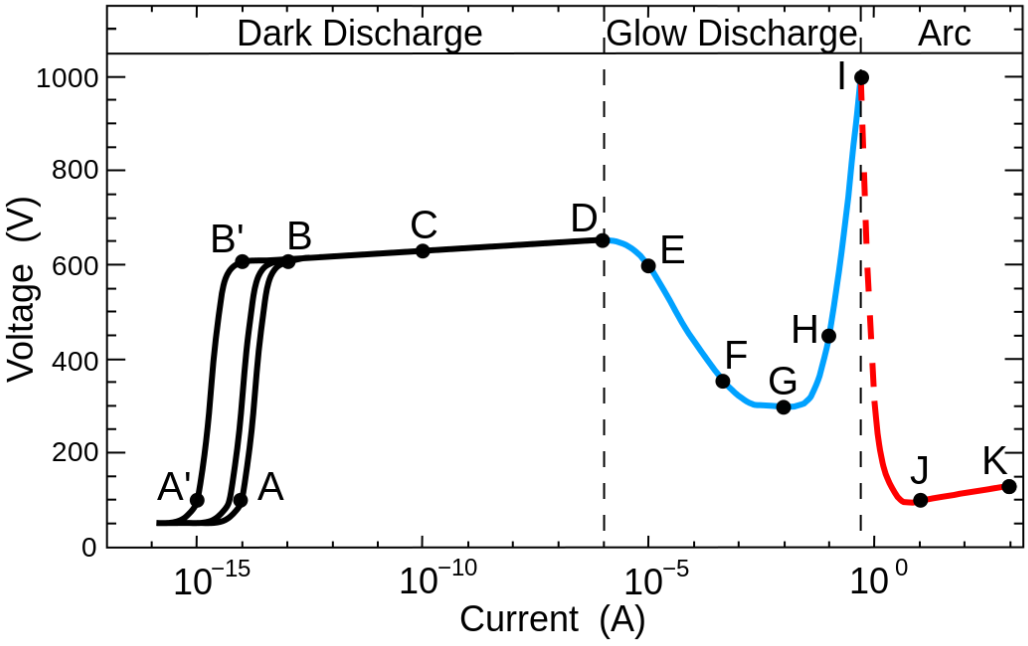

Figure 15- Voltage and current representation of breakdown [32]

2.6. CSS vs PCS

The main reason that a system requiring high PRF operation would be fitted with a corona stabilised switch (CSS) rather than a plasma closing switch (PCS) is to do with voltage recovery [26], [33]. As the HV electrode of the CSS is stressed to high DC

voltage, the non-uniformity of the HV electrode establishes a corona. The electrical field strength at this point is low enough that breakdown will not occur until triggered by another potential applied to the system [34], [35]. In a conventional PCS, the neutral gas density does not have time to recover to its previous state before the commencement of the next trigger pulse [26] - this results in the switch closing at a lower voltage and affects the performance of the switch [33]. In a CSS however, the corona that has been established creates an ionisation region, preventing premature breakdown. According to the Kapstov hypothesis, the corona at the HV electrode will clamp the electrical field strength at a level corresponding to the corona onset voltage soon after a previous breakdown has occurred [75]. During this process, space charge is accumulated within the gap. This space charge then decouples the electrode from the gap itself. This then allows the neutral gas density time to recover before the next trigger pulse has arrived. Therefore, the breakdown voltage of the switch is not compromised for subsequent switch closures. Referring to Figure 14, it is up until the pressure P_c where a CSS can perform reliably due to the phenomena discussed. With the correct design and characterisation, a CSS can work well into the kHz regime [25].

2.7. COMPOSITION OF GAS THEORY

This section will contain all relevant information on the gaseous dielectrics used in the testing process, including data on air, SF_6 and a gas novel to pulsed power applications, 1,3,3,3 Tetrafluoropropene, also known as HFO-1234ze. These gases will be discussed in terms of chemistry in section 2.7.2, as well as the performance when used in switching applications in Chapter VI of this thesis.

2.7.1. SF_6

Within high-voltage engineering and testing the use of SF_6 has become threatened as new policies have come into effect where the use of greenhouse gases is to be phased out of applications presently requiring them [37]. SF_6 is known to have a global warming potential (GWP) of 23900 (measured within a 100-year time horizon) [6], [38], [39]. To put this into perspective, GWP is calculated as the potential for the gas trapping heat within the atmosphere in relation to CO_2 therefore, SF_6 has a GWP 23900 times worse than CO_2 [40]. Because of this, new gases are being tested in order to replace SF_6, without compromising on the performance of the switch, in the context of

the present study. The use of SF_6 within switching applications is made so advantageous as the gas is well known to be highly electronegative, has high dielectric strength, and is non-flammable [41].

The structure of SF_6 is shown in Figure 16. There are 6 Fluorine atoms attached to a single sulphur atom. As Fluorine is the most electronegative element within the periodic table this then creates a strongly electronegative compound.

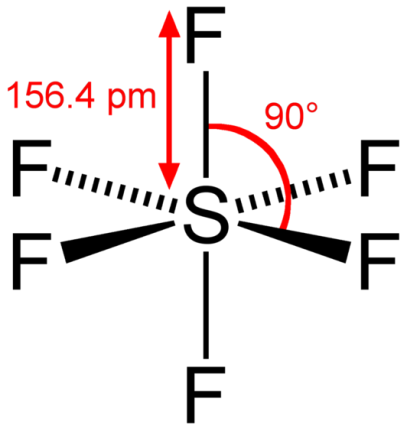

Figure 16 - Skeletal structure of SF6

The electronegativity of SF_6 makes it ideal for switching applications as the breakdown strength is ~3 times higher than that of air, at 89 kV/bar.cm where air has a breakdown strength of 30 kV/bar.cm [18], [41]. The use of SF_6 will therefore create a switch with a higher operation voltage or the switch can be ~3 times smaller and be as effective as an air-filled switch. In terms of switching characteristics, the triggering range is seen to be broader in SF_6 than air, meaning that the switch can be operational at a smaller fraction of the self-breakdown voltage [42].

2.7.2. HFO-1234ze

1,3,3,3 Tetrafluoropropene - more commonly known as HFO-1234ze - is a novel gas within pulsed power and other high voltage technologies. This gas is a Hydrofluoroolefin with the chemical formula in equation 2.21

$$C_3H_2F_4 \qquad 2.21$$

It has the following skeletal structure, shown in Figure 17.

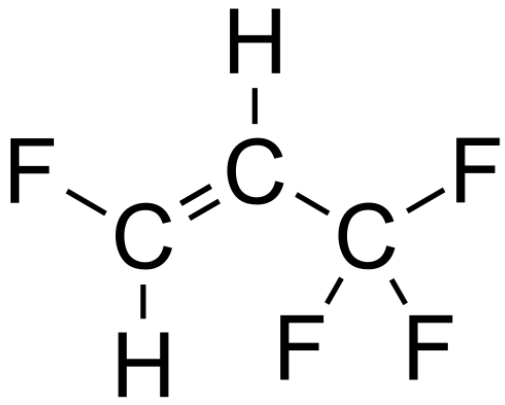

Figure 17 - Skeletal structure of HFO-1234ze

Given that it is a fluorinated gas, HFO-1234ze is known to be electronegative, giving the possibility of using this gas to replace SF_6 within switching applications. The double carbon bond is responsible for the low GWP of this gas [43], [44]. HFO-1234ze has a GWP of 6 (in a 100-year time horizon), giving a significant advantage over SF_6. HFO-1234ze also has an ozone depletion potential of 0 [45], [46], [47].

2.7.2.1. Problems with Air/HFO-1234ze mixtures

A problem that arises when HFO-1234ze is mixed with air is that, under certain conditions, the resulting gas is considered 'mildly flammable'[47]. Factors that alter the flammability region are ambient temperature, pressure and humidity [8], [48,] [50]. HFO-1234ze is considered non-flammable when humidity of <10% is controlled at a temperature of 23 ^{o}C [50], as seen in Figure 18. The upper and lower flammability limits are found using equations 2.22 and 2.23 [51]:

$$L = L_{25}\left\{1 - \frac{100C_{P,L}}{L_{25}.Q}(t-25)\right\} \qquad 2.22$$

$$U = U_{25}\left\{1 + \frac{100C_{P,L}}{L_{25}.Q}(t-25)\right\} \qquad 2.23$$

where –

L_{25} = Lower flammability limit (vol%) at 25 ^{o}C

U_{25} = Upper flammability limit (vol%) at 25 ^{o}C

$C_{P,L}$ = Heat capacity of unburnt gas at lower flammability limit at 25 °C

Q = Molar heat of the fuel gas

$C_{P,L}$ and Q can be assumed to be constant at temperatures in the range of 5 °C – 100 °C [50].

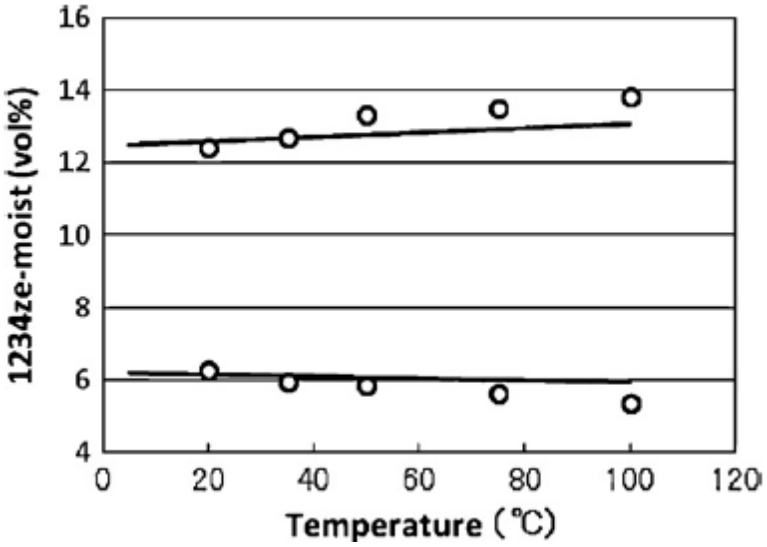

Figure 18 - Flammability limits with respect to ambient temperature [50]

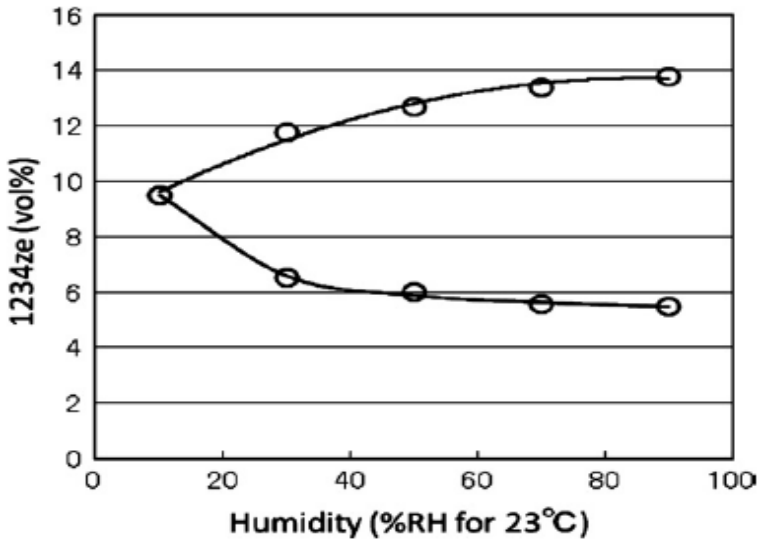

Figure 19 - Flammability limits with respect to humidity [50]

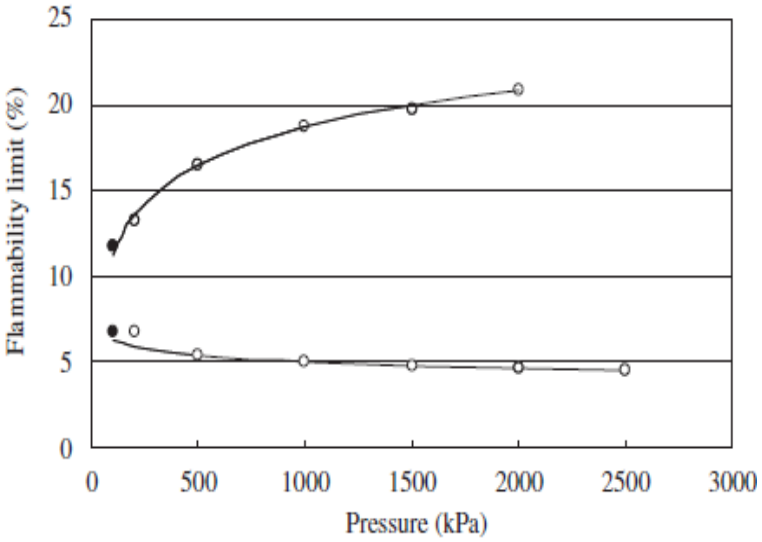

Figure 20 - Flammability limits of HFO-1234yf with respect to pressure [52]

From Figure 18, 19 and 20, it is possible to see the upper and lower flammability limits of the gas mixtures. The *y*-axis on each of these graphs indicates the percentage of HFO-1234ze (or HFO-1234yf in Figure 20) in terms of flammability characteristic by pressure. Therefore, the upper and lower flammability limits can be seen at each increment of pressure, temperature or humidity. The solid line on each of the graphs represents the theoretical value obtained using equations 2.23 and 2.24 and the data-points represent measured data within these specific increments. In Figure 20, the graph shows the relationship of pressure to lower explosive limit and upper explosive limit (LEL and UEL) for HFO-1234yf. Data on HFO-1234ze is not available for varying pressure, but HFO-1234yf is considered more flammable than HFO-1234ze, therefore this data can also be used as reference information for the ratios of HFO-1234ze and air mixtures to be avoided. Additionally, as the gas mixtures for testing in this thesis will include high percentages (≥80%) of high-purity N_2, this then eradicates the oxidising element O_2, making the mixture non-flammable [50], [52].

2.7.3. SF_6 vs HFO-1234ze

In terms of comparing HFO-1234ze to SF_6, it has been found that the dielectric strength of HFO-1234ze is 0.8 – 0.95 times that of SF_6 (used in AC for GIS conditions)

[53]. Therefore, in theory, HFO-1234ze should not have as high a breakdown strength as SF_6. Also, for the safety reasons described in 2.6.2.1, HFO-1234ze will only be used in small percentages and mixed with the electropositive gas nitrogen, reducing electron attachment and leading to a lower breakdown strength in comparison to using 100% HFO-1234ze.

2.8. TRIGGERING METHODOLOGY

Within high voltage technologies, spark gap switches are used as they are capable of operating within the highly stressed environments encountered. This includes very high voltages, >100 kV, as well as very high currents, in the range of kA [56]. Due to high rates of change of voltage and current with respect to time, these switches are capable of switching in very short times of the order of nanoseconds, with low jitter [57]. As discussed in section 2.8.1, these switches consist of two electrodes separated by an insulating medium; it is how these elements work together that determines the overall switch capability. This section will discuss two methods in order for a switch closure to be affected:

- Self-closing
- Field distortion triggering

A short overview of each method is given, followed by discussion of the advantages and disadvantages of each.

2.8.1. Self-closing switches

Self-closing switches are the simplest of the switch types. The electrode geometries in section 2.8.1 could all form the basis of a self-closing switch, since they consist of two electrodes, separated by an insulating medium, without any extra triggering mechanism added. Simply, a self-closing switch will operate when the field exceeds the critical value which ultimately leads to breakdown across the gap. The advantages of such arrangements are as follows [9], [25]:

- Robust switch design
- Reliable
- Relatively cheap

The operation of the self-closing switch is completed by applying a high enough voltage such that the breakdown voltage of the particular gaseous medium is reached with respect to pressure. The way in which this switch can be altered in order to have different switching parameters is to change the gap length or alter the pressure within the switching chamber. Although, moving electrodes can add to the complexity of the switch design, resulting in loss of the simplicity of a self-closing switch design. Therefore, in order for the breakdown level to be changed without having to manipulate any moving parts, it is necessary to alter the gas pressure within the vessel. This type of switch is used throughout the high voltage industry, for example in Marx generators [9].

2.8.2. Overvoltage triggering

Overvoltage triggering switches are used when the application needs high-performance and a more consistent switching time. The topology of these switches are in their simplest form three electrodes. The first electrode is the high voltage electrode, which is paired with a ground electrode like a self-closing switch. The difference however, is the addition of a third electrode, situated between the two main electrodes, which does not have any effect on the field distribution until a triggering voltage is applied to this additional electrode [1], [9], [18].

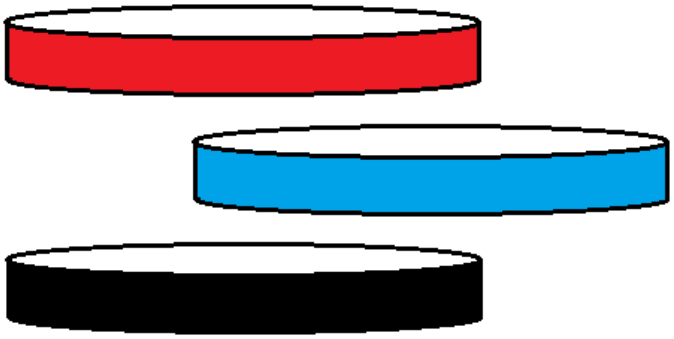

Figure 21 – Basic electrode setup within the switch vessel with field distortion triggering being utilised. Red electrode = HV, Black electrode = Ground, Blue electrode = Trigger impulse

When the switch is operated, a DC voltage is applied to the HV electrode, such that the voltage does not exceed that of the breakdown level, with respect to pressure and inter-electrode distance. A pulse, usually of opposite polarity to the main DC voltage, is then applied to the trigger electrode, forcing the switch to close as the electrical field strength is distorted throughout the gas gap. As well as the applied DC voltage not having a sufficient amplitude for breakdown without the trigger pulse voltage, the

trigger pulse also does not have sufficient amplitude to close the switch without the applied DC voltage.

Shown in Figure 21 is a very basic electrode setup which utilises the overvoltage triggering regime, shown by the blue electrode added halfway between the main switch electrodes. The effect of the addition of this middle electrode in terms of switch operation is illustrated in Figure 22 [9].

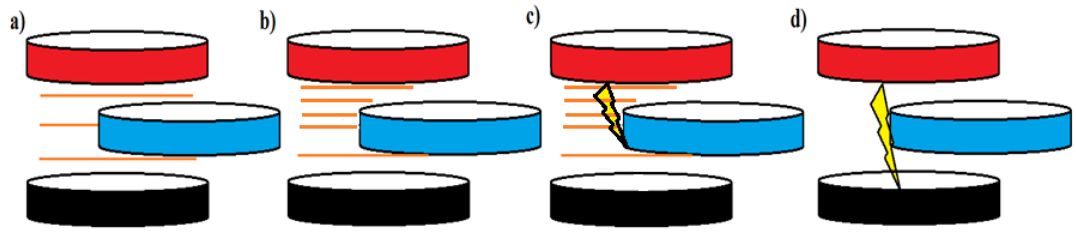

Figure 22 - method of switch operation when overvoltage triggering has been utilised. a) represents the uniform field between the plane-plane electrodes before the trigger electrode has been enrergised. b) represents the field enhancement due to the energisation of the trigger electrode. c) represents the discharge which forms in the high field region d) represents the complete breakdown of the gap between the main electrodes and, therefore, closure of the switch.

This type of switch is capable of operation to >100 kV, with the capability of a low jitter, dependent upon the trigger pulse characteristics. This setup is used within systems where the application requires a high pulse repetition rate. This type of switching is dependent upon the voltage applied to the HV electrode, and the trigger pulse rise time and magnitude. This switch will be capable of operating between the self-breakdown voltage level and trigger threshold voltage level of the switch, with respect to the pressure in the vessel and the inter-electrode spacing [9]. Therefore, the time to breakdown for the switch will be reduced as the applied DC voltage is increased towards the self-breakdown voltage level; operating at high percentages of the self-breakdown voltage can cause premature closure of the switch, however. A modified version of overvoltage triggering is employed in the experimental part of this thesis.

2.9. MULTIPLE-STAGE CLOSING SWITCHES

In order to achieve higher breakdown voltages at relatively low pressures, a multi-stage closing switch can be designed and implemented, as shown in [49]. The design will incorporate two or more stacked electrode stages, operating on the same principles

as the overvoltage triggering regime discussed in section 2.9.2. Such switches can remain relatively compact in size and can meet the higher breakdown voltage specifications of pulsed power applications, such as stage switches of Marx generators.

2.10. STATISTICAL ANALYSIS METHODS

The method that will be used to analyse the time delay to breakdown data will be the Laue method, introduced by von Laue in 1925 [9], [58], [76]. This method is commonly used within the analysis of gaseous breakdown data. Liquid breakdown is more complex, although attempts have been made in order for von Laue analysis to be used on liquid breakdown data too [11], [58].

The basic von Laue probability of an electron appearing within a gap and causing breakdown is uniform with time. Therefore, this leads to an exponential distribution in a plot of time to breakdown data.

The time for breakdown to occur is made up of statistical time (t_s) and formative time (t_f). The statistical time reflects the time for an electron to appear to initiate breakdown and is inversely proportional to the probability of such an electron appearing in the gap P_{eB} equation 2.24 [1], [59]

$$t_s = \frac{1}{P_{eB}} \qquad 2.24$$

t_f, is the time after the initiation has started, up to breakdown completing [1], [59]. This leads to the expression in equation 2.25 –

$$\frac{N_t}{N_0} = exp\left(-\frac{t - t_f}{t_s}\right) \qquad 2.25$$

Therefore, a plot of $-\ln\left(\frac{N_t}{N_0}\right)$ versus time will produce a straight line with gradient $1/t_s$ that crosses the time axis at t_f. This will then assume a constant value of t_f. The von Laue analysis is known by equation 2.26.

$$-\ln\left(\frac{N_t}{N_0}\right) = \frac{t - t_f}{t_s} \qquad 2.26$$

where

- t = Total breakdown time
- t_f = Formative time
- t_s = Average statistical time

In practical cases however, the value of t_f will have a distribution of values. Some researchers [77] have suggested that the distribution of t_f is normal. This leads to lower values of $-\ln\left(\frac{N_t}{N_0}\right)$ deviating from the straight line predicted by von Laue. These two statistical processes can be seen from Figure 23. Where the straight line crossing the *x*-axis at t_f is evident, as well as the shorter normal distribution deviating from this predicted straight line. Within this work there are also graphs which resemble only one statistical process, for example, Figure a.24 in appendix.

The way in which this helps to analyse the delay time data is to determine whether the delay time is reduced with DC energization in terms of applied voltage to the system or a reduction in terms of statistical or formative time which will have an overall effect on the delay time to breakdown.

The formative and statistical times with respect to the overall delay time can be estimated by isolating the linear section of the graph. This can then give information on the formative time, identified where the straight line crosses the *x*-axis. The statistical time can be found as the inverse of the gradient of the linear distribution of the graph. It is convenient to use a constant 1 on the *y*-axis as shown in Figure 23. Also, the statistical time can then be found by simply subtracting the formative time from the average delay time [9], [60], [61].

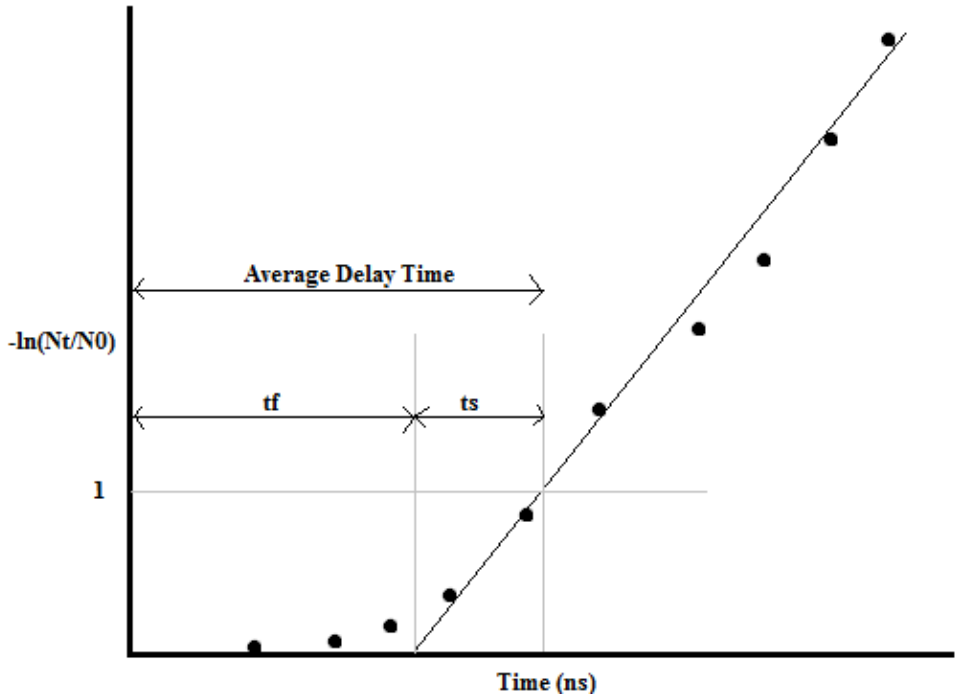

Figure 23 - Example Laue plot with Formative time and Statistical time shown in the ns regime

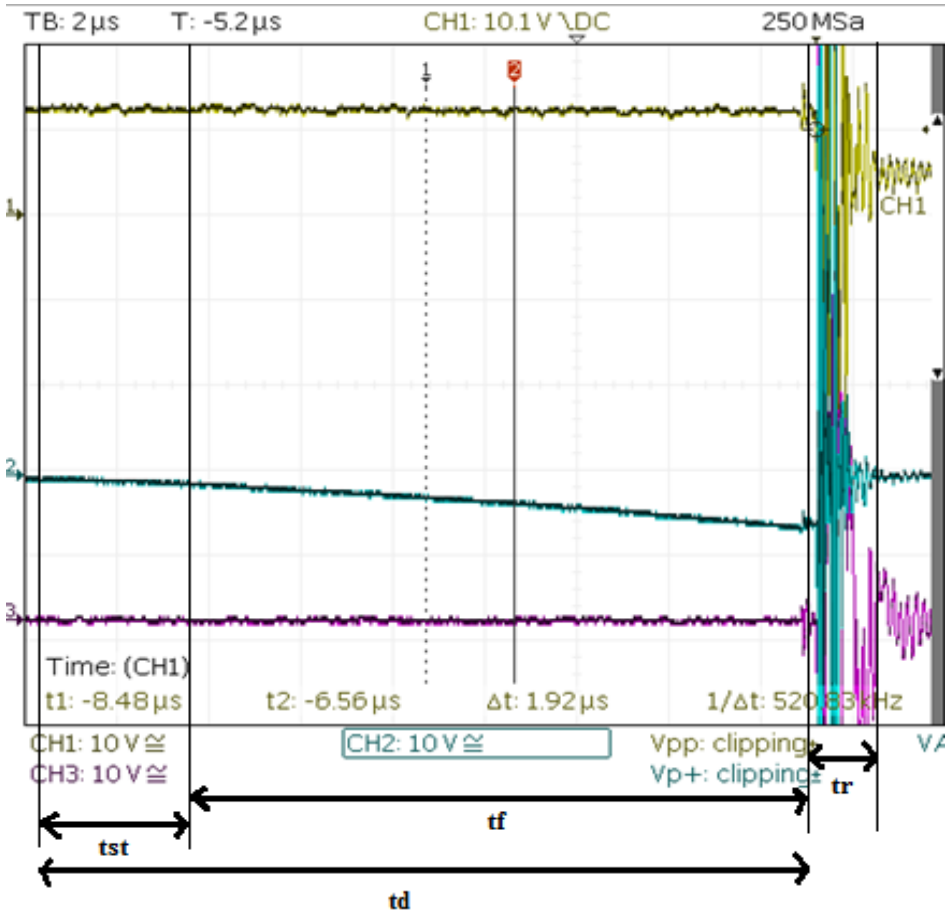

Figure 24 - Showing an example of statistical time and formative time within an actual waveform collected during the testing process. td = delay time of switch, tst = Statistical time, tf = Formative time and tr = Rise time of the spark gap

Figure 24 shows an example of the delay time, t_d, which has been split into statistical time, t_{st}, and formative time, t_f. On Figure 24, the delay time has a value of ~17 μs, composed of a statistical time of ~3 μs, and a formative time of ~14 μs. As well as these times, Figure 24 also shows t_r, the 'rise time' of the spark gap. This is the time during which the switch transitions from a high resistance (open circuit) at the end of t_d, to a low resistance (short circuit) after t_r. However, the nominal bandwidth of the voltage probes used was 80 MHz, and therefore, this value may not be exact. Figure 24 also shows the need for von Laue analysis to be conducted, as the individual contributions of the statistical time and formative time cannot be determined from the measurements, only the overall delay time to breakdown.

2.11. CONCLUSIONS

From the findings within the literature review, this information can now be taken into practise using simulations and practical work. Simulation work has been completed to conform to the work completed in 2.3, in terms of negative polarity. This to see the effect of angle change within the simulation and non-trigger and trigger operation of the switch. This prompted practical work electrode angle to be held constant at 30^o as to continue work with use of this angle [4].

In terms of gases, work has been completed using air [42] which would be an ideal gas in terms of GWP. Although, what can be seen is the narrow triggering range which is associated with air as well as the breakdown strength being ~3 times weaker (taken from atmospheric pressure). Therefore, in attempt to increase these parameters preliminary tests were completed with N_2 using high concentrations with low concentrations of HFO-1234ze (more electronegative than air and lower GWP than SF_6) in small quantities in order to determine safety from work completed in 2.7.2 and avoiding mixing with air altogether. Therefore, 5%, 10% and 20% mixtures were chosen.

3. CHAPTER III

MODELLING CORONA STABILISED-SWITCHES

3.1. GENERAL

In order to gain some electrical field strength data on specific electrode geometries and topologies relevant to the study, work was completed with simulation/modelling software package, FEMM.

The modelling and simulation of a practical corona-stabilised switch (CSS) geometry, was completed on Finite Element Model Magnetics (FEMM). The model was built to the same specifications, with each individual material used within the switch being input to the system to make the model as accurate as possible.

FEMM was utilised in order to analyse the effect of the angle of the pointed electrodes on the electrostatic field distribution within the switch. The values at Dh and Dg are the gap distances between each disc electrode respectively and the body of the switch.

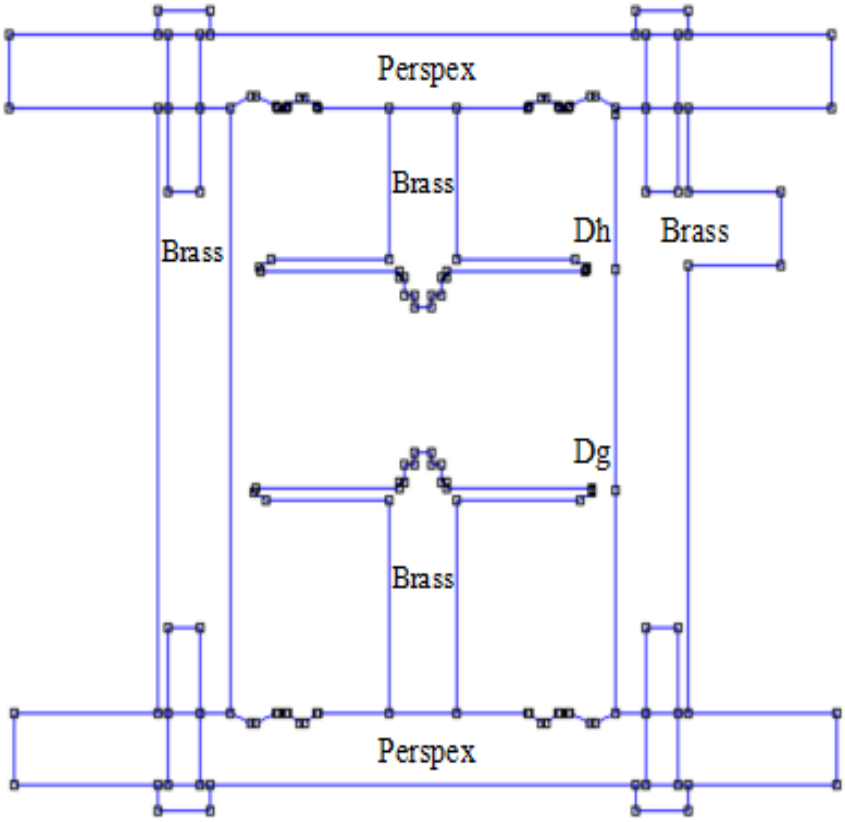

Figure 25 - FEMM model of CSS to enable simulation of electrostatic field distribution under different conditions

Shown in Figure 25 is the model of the switch geometry built in FEMM to enable simulation of the electrostatic field distribution under different conditions. The top gap (*Dh*) was set to 5 mm and the bottom gap (*Dg*) was set to 3 mm for all simulations. These values were chosen to match an important configuration used in the experimental phase of the study, and there is further extensive explanation of each of these parameters in Chapter IV. Also, what is shown in Figure 25 is the solid insulating parts of the switch geometry, which are made of Perspex. The reason for this addition is to insulate the HV electrode and the trigger electrode (main body) of the switch. Grooves machined into the Perspex lids to increase the flashover path length are included in the model. As this is an important part of the switch design the simulations will also show the field strength along this part of the switch, giving an insight into the probability of flashover occurring.

3.2. FEMM CHANGE OF ELECTRODE ANGLE SIMULATION

Firstly, simulations were run to see how the electrical field strength changed with relation to electrode angle, as illustrated in Figure 26. The electrodes were measured and then rounded off by the rounding tool on FEMM, in order to further emulate the machined electrodes and avoiding a perfect point. The applied voltage was kept at a constant 10kV for all tests.

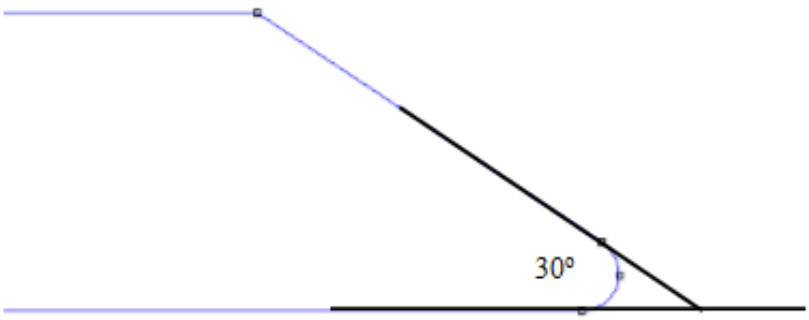

Figure 26 - Angle of electrode measurement

In Figure 26, the way in which the electrode angle was determined is illustrated. The electrode angle was varied in order to determine the effect on the electrical field strength at the point of the electrode.

The angles tested were approximately –

1. 27 Degrees
2. 30 Degrees
3. 34 Degrees
4. 36 Degrees
5. 39 Degrees
6. 45 Degrees
7. 53 Degrees

The reason for these angles was to see within literature [21], [27], [29], [30], [57], why a value of 30 degrees was chosen in the design of this switch. Larger angles were chosen in order to increase the radius of the point, reducing the effects of erosion of the electrodes during extensive operation of the switch.

The results of the change in electrical field strength with relation to the angle of the electrode are shown in Figure 27 and 28, where Figure 27 shows the difference in electric field strength in relation to the angle at the electrode tip and Figure 28 shows the electrical field strength for all angles across the whole of the gap.

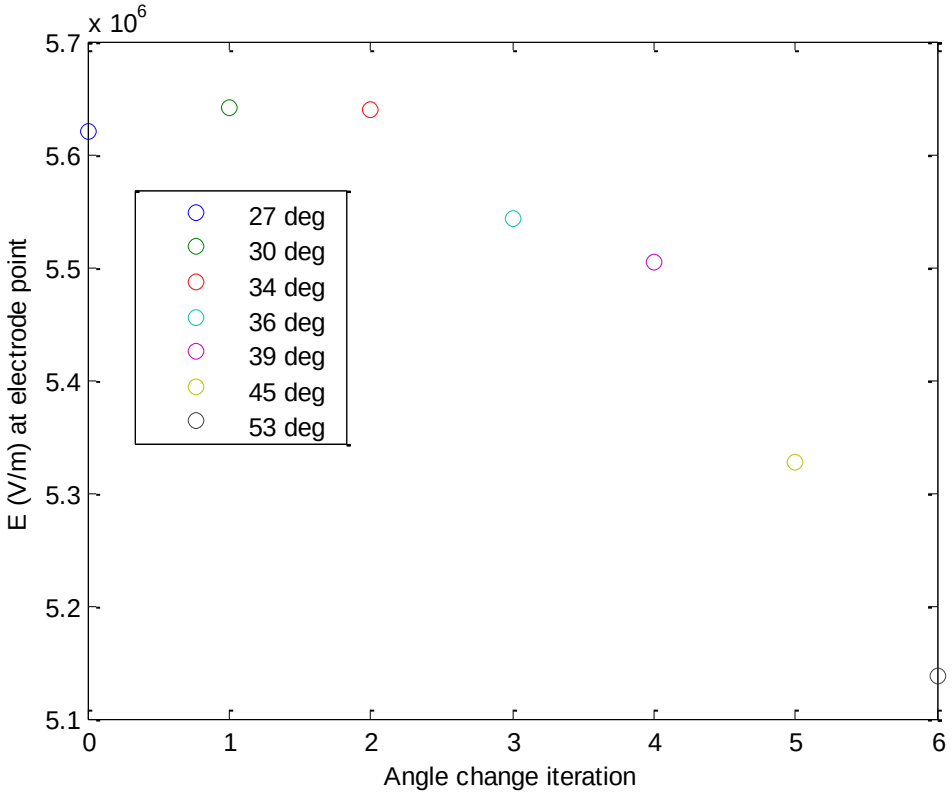

Figure 27 - Electrical field strength at electrode point for electrode angles between 27 and 53 degrees

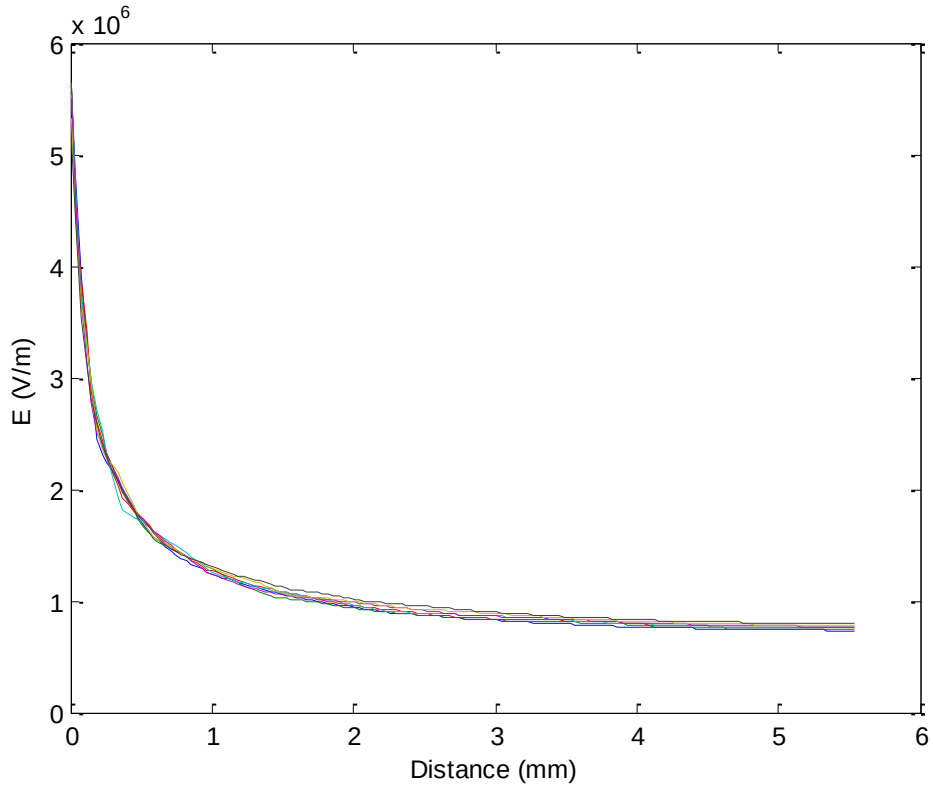

Figure 28 - Electrical field strength across the gap spacing for electrode points between 27 and 53 degrees

Looking at the overall electrical field distribution across the gap in Figure 28, it can be seen that the electrical field strength does not differ greatly as the electrode angle is changed. In Figure 27, however, where the *y*-axis scale is restricted to the high field levels seen at the electrode tip, it can be seen that at the point electrode there is a range of different electrical field strengths as the electrode angle is changed. The highest electrical field strength is situated at 30 degrees with a strength of 5.64×10^6 V/m, compared to the lowest at 53 degrees at a value of 5.13×10^6 V/m. The electrical field strength is seen to peak at 30 degrees, therefore the angle which the electrodes have been machined to in the practical phase of this work is ~30 degrees, to coincide with this peak in electrical field strength.

3.3. FEMM SIMULATION OF BRASS SWITCH

Within the FEMM simulations, the switch model described in section 3.1 was simulated to see the electrostatic field distribution under various applied DC and trigger voltage conditions. Table 3 shows the materials used in the simulation profile, along with the conductivity settings for these particular materials, which were all catalogued in FEMM as well as [72].

Table 3 - Conductivity of materials used in FEMM within CSS

Material	Conductivity (S/m)
Brass	15.9^{6}
Perspex	10^{-11}
Nylon	10^{-12}
Air	8^{-15}

3.3.1. Switch characteristics

In this section, a practical switch will be simulated in order to understand the electrical field distributions in the electrode gaps within the switch. The switch characteristics are described in 3.1 and 3.2. The switch electrode gap spacings were kept at 5 mm for the HV to trigger electrode gap (*Dh*), and 3 mm for the trigger to ground electrode gap (*Dg*). Within these simulations a fixed value of -6kV was used as the DC energisation level, which will be within the operating conditions of the switch in practical use. The trigger electrode voltage was fixed at 32.2 kV, as this was the measured peak value of the trigger generator output voltage pulse. This will be discussed in detail in section 4.4.

3.3.1.1. Under DC applied voltage only

In Figure 29, the cross-section of the switch schematic is shown, with -6 kV applied to the HV electrode and 0 V was applied to the lower disc electrode and the switch body, and the electrical field distribution within the switch under these certain conditions. As expected, the electrical field strength is seen to be stronger around thepoint electrode situated at the disc edge; a closer image of this can be seen in Figure 30.

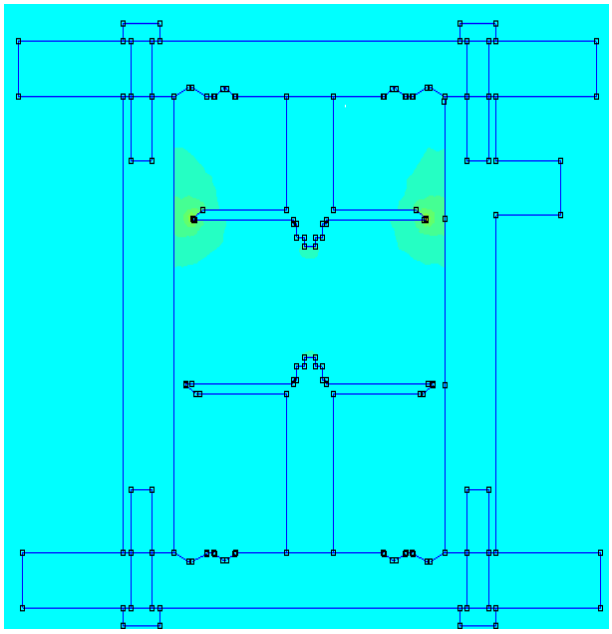

Figure 29 - Simulation of enclosed brass switch with applied HV

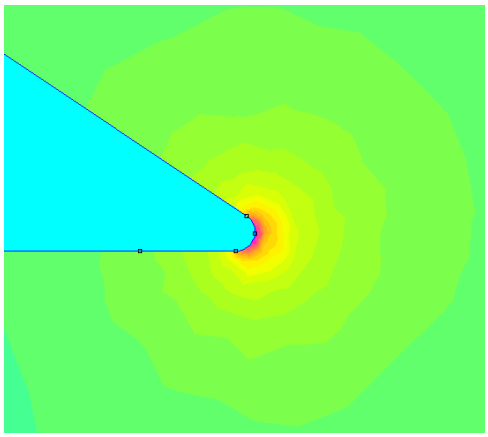

Figure 30 - Non-uniform electrical field at the point electrode

Shown in Figure 30 is the non-uniform electrical field around the disc electrode circumference, which takes on the same form as the point-plane electrical field distribution seen in 2.8.1.5. Due to this high electric field strength within this region, this will ultimately produce corona when a high enough voltage is applied so ionisation can take place, as discussed in 2.2.2.

3.3.1.2. Triggered impulse operation added

Figure 31 shows the electrical fields within the switch when an external triggering voltage has been added to the system, to enable full closure of the switch to be established.

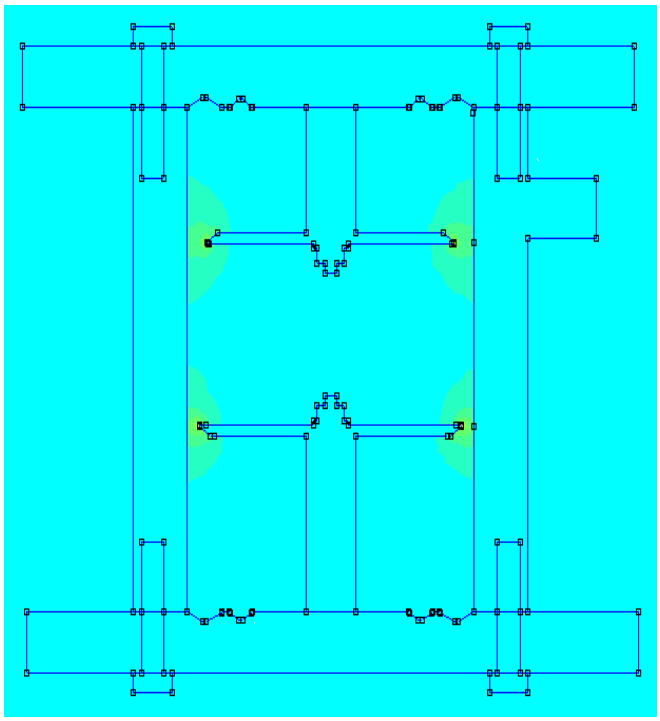

Figure 31- Simulation of CSS with applied HV and triggering voltage

As seen, there is an electrical field strength at both disc electrodes shown. This is caused by the addition of a voltage of 32.2 kV to the trigger electrode as well as -6 kV on the HV electrode, corresponding to the peak voltage of the triggering impulse used in the practical phase of the work. The lower (earthed) disc is at 0 V potential. This will therefore create an electrical field distribution at each of the electrode gaps respectively. Figure 32 shows the relationship between the electrical field strength and the position along the gap between the electrodes. The blue curve shows the electrical field strength between the HV and trigger electrodes when a voltage is applied to the HV electrode only, with no external triggering voltage added. The green curve shows the electrical field strength between the HV and trigger electrodes when a peak voltage of 32.2 kV has been applied to the trigger electrode by the trigger generator. Finally, the red curve shows the electrical field strength between the trigger and ground electrodes, with the 32.2 kV voltage applied to the trigger electrode.

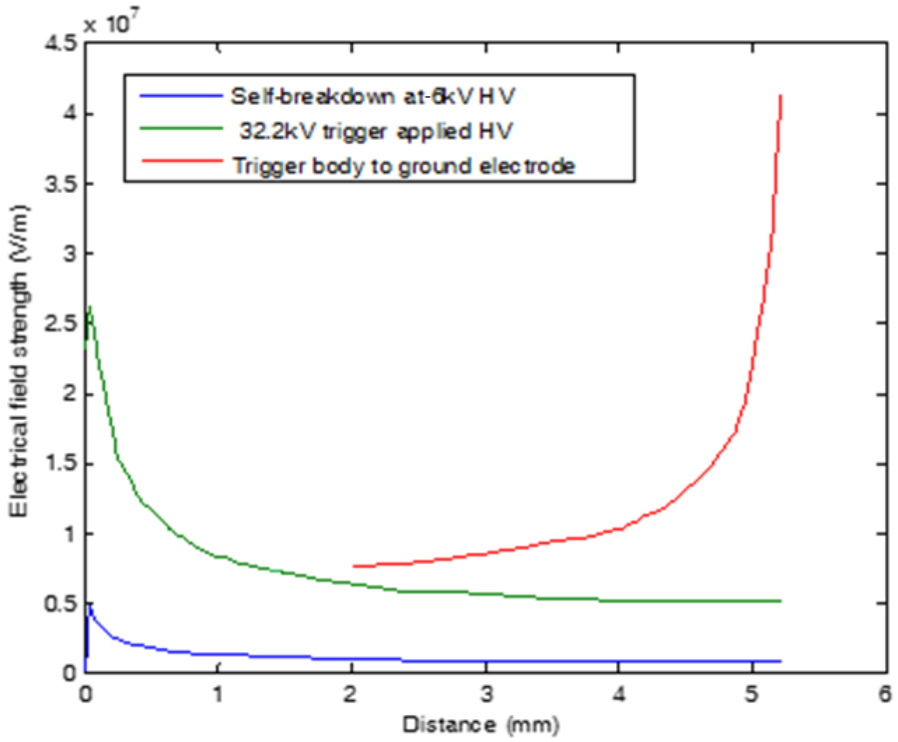

Figure 32 - Graphical representation of electrical field strengths within the switch with HV only applied (blue curve), and with both HV and trigger pulse applied (green and red curves). At 0mm is the disc electrode and 5mm is the body of the switch. The red distribution at 5mm lower electrode disc tip and 2mm is the body of the switch. Thus, showing Dh distance of 5mm and Dg distance of 3mm

Looking at the three field distributions at the key points within the switch geometry, it is clear to be seen that the highest electrical field strength occurs at the trigger to ground electrode, when the trigger voltage is added. This can be explained as the trigger to ground electrode gap (*Dg*) is 3 mm, compared to the HV to trigger electrode gap (*Dh*) of 5 mm. Although, the difference between the applied voltage only and trigger applied is 5 times greater electrical field strength at the point electrode at *Dh* when the trigger impulse is present as the application of the trigger generator pulsing 32.2 kV in the opposite polarity to the applied. The red distribution is reversed to differentiate between the electrode which was being tested. The maximum field strength was still found at the point electrode.

3.3.2. Space charge addition

The actual electrical field distribution will also depend on the space charge which develops due to the corona. Initial attempts were made to model this, but the capability of the software did not allow a solution to be developed within the time constraints of the project.

3.4. CONCLUSIONS

From the simulations conducted, there was enough information in order to hypothesise the results which will be generated by the practical work. The next chapter will show the technical details of the switch that has been simulated within this chapter in terms of dimensions, circuit design and the testing involved.

4. CHAPTER IV

PRACTICAL CSS DATA AND TESTING PARAMETERS

4.1. GENERAL

This section will inform on the experimental part of the project. The switch characteristics will be described, as well as the circuit theory used when testing, the laboratory setup, gases used, and the gas mixing setup.

4.2. BRASS SWITCH TOPOLOGY

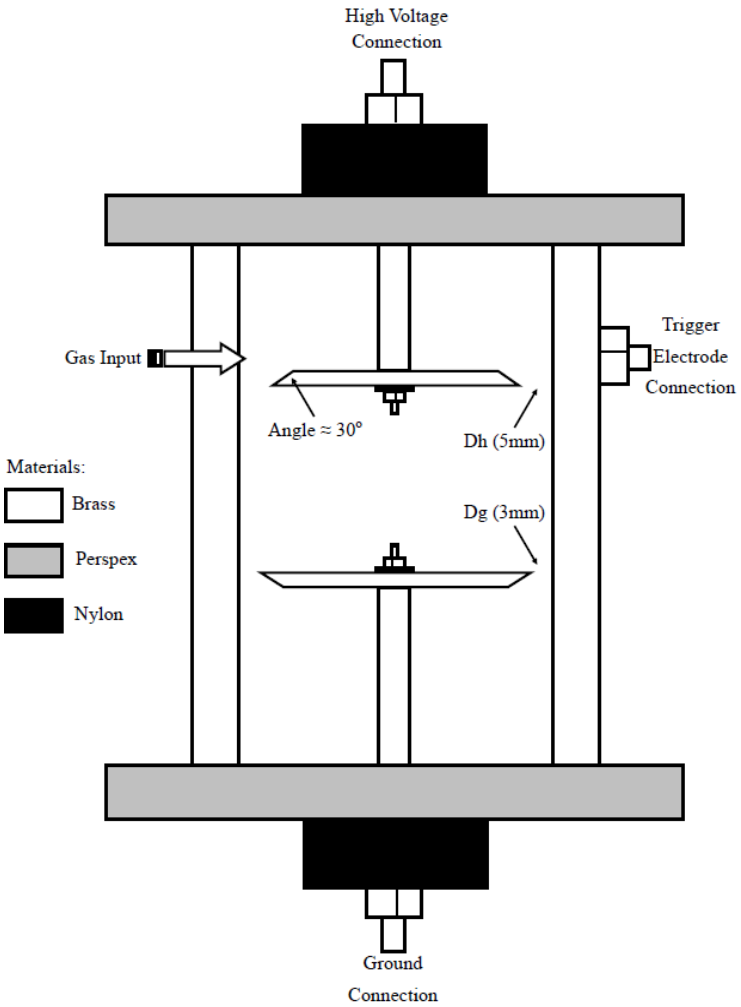

Figure 33 – Cross-section of switch showing different materials, gap spacings and inputs/connections

Figure 33 is a cross-sectional illustration of the brass CSS. The two disc electrodes can be seen with their gaps to the trigger electrode, which is the brass body of the switch. The gaps have been labelled as *Dh* for the HV to trigger electrode gap, which was

fixed at 5 mm. The trigger to ground gap (*Dg*) is shown also, with the gap being fixed at 3 mm for the duration of the tests. The tip of the disc electrodes had a radius measured at ~0.5 mm. These fixed gap spacings were chosen after preliminary testing with air, reported in Chapter V, where these distances were shown to give the best performance in both negative and positive polarity.

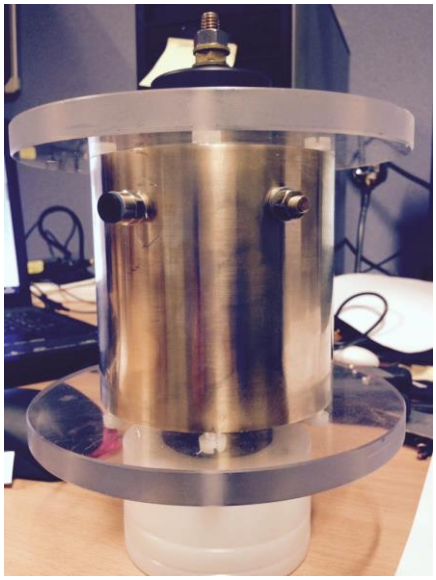

Figure 34 – Closed brass CSS used in testing.

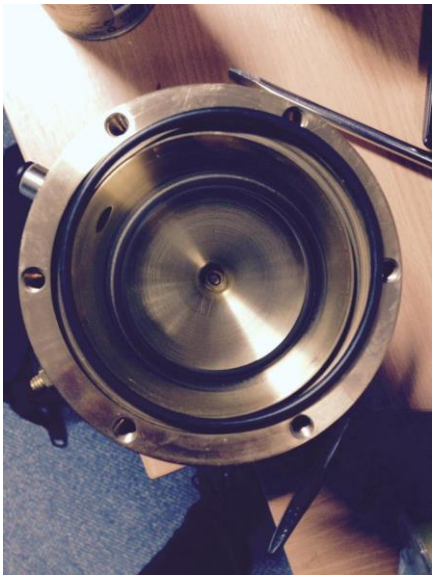

Figure 35 - Top view of switch with Perspex lid removed showing the disc electrode and gap to brass body trigger electrode

Figure 34 and 35 show photos of the switch used within the laboratory testing phase. In Figure 34, the connections are shown for the gas inlet, trigger connection point, and the HV electrode connection. The ground connection is covered by the nylon spacers, seen at the bottom of Figure 35, which were used as a base, allowing the switch to be operated standing upright. Figure 35 shows a top view of the CSS. The threaded holes

around the circumference accommodate six nylon screws, which hold down the Perspex lid and ultimately the disc electrode. The gas inlet valve is also seen on the left of the figure. The disc seen within the switch body is the ground disc electrode.

The dimensions of the brass switch are illustrated in Figure 36, including the spacings between the HV and ground electrodes and the distance between the HV/Ground electrode and the body of the switch. The 40 mm distance between the disc electrodes is large enough that breakdown will not occur under the range of voltages (<40 kV) used throughout testing. The distance between the HV/Ground electrode at the central rod point and the body of the switch was also large enough so that flashover did not occur. This was further ensured by an addition of a nylon cap covering the triple junction point of the HV/Ground electrode, the Perspex and the gaseous medium. Also, the Perspex was machined with indentations machined with a 6 threads per inch chaser to increase the flashover path length between the HV/Ground electrode and the body of the switch. These design features can be seen in Figure 37.

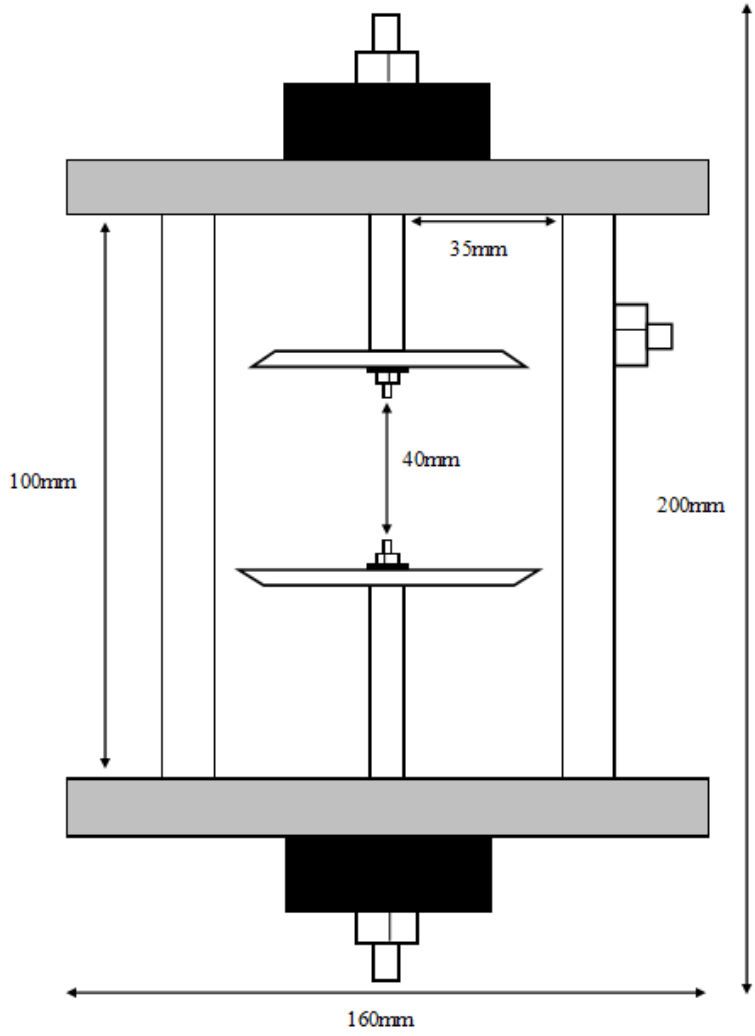

Figure 36 - Switch dimensions

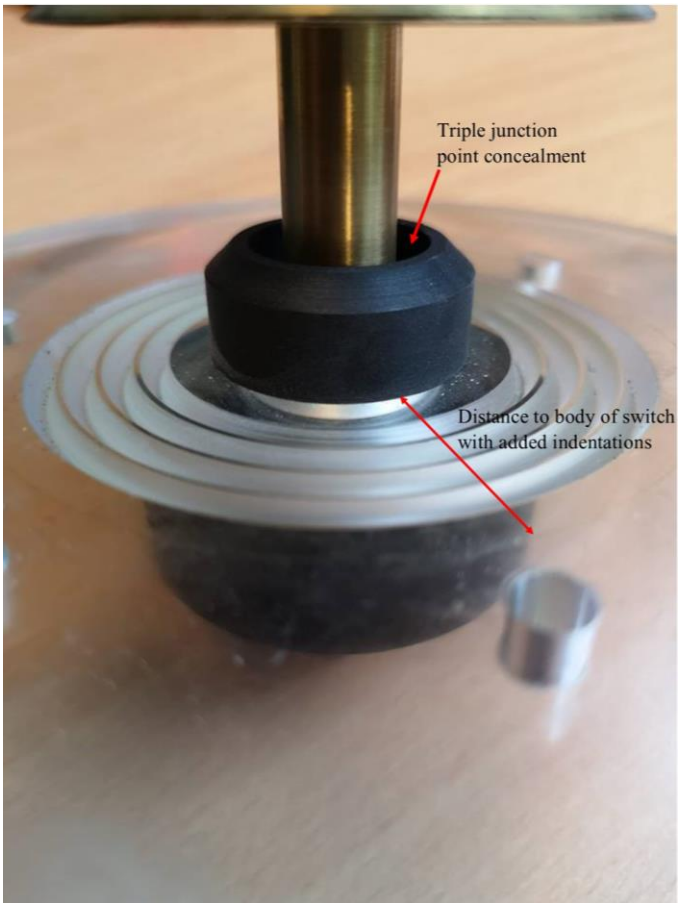

Figure 37 - Triple junction point and indentations on CSS

4.3. GAS SETUP AND MIXING PROCEDURE

This section is to inform on the gas handling procedures employed for the duration of the laboratory work. During the project, the gases utilised were:

- Air (compressor)
- Nitrogen (N_2)
- Tetrafluoropropene (HFO-1234ze)

Preliminary tests were conducted using air to provide baseline data on switch operation, and to determine the effect of changing the inter-electrode gap spacings and operating pressure, as discussed in Chapter V. The results of these tests informed the electrode arrangements used for the novel gas mixture tests in Chapter VI.

Testing with HFO-1234ze required safety precautions to be taken. As the gas is considered mildly flammable (see section 2.7.2), isolation valves were placed throughout the gas handling system, which can be seen in Figure 38.

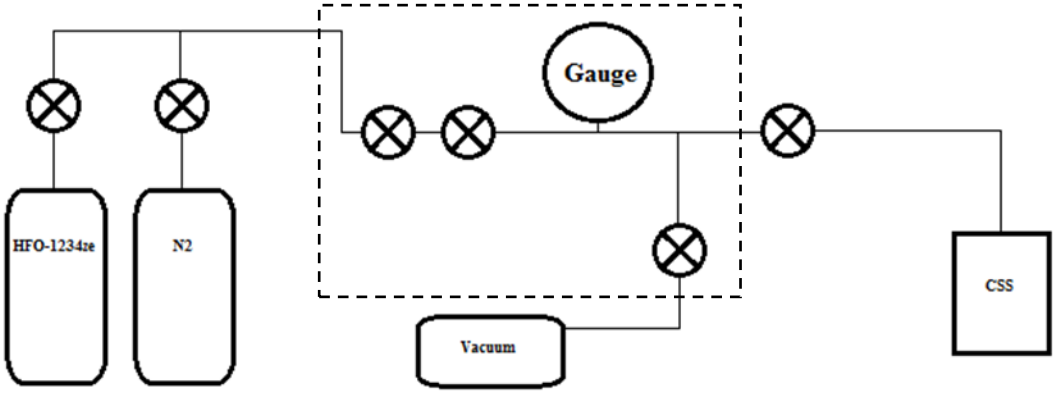

Figure 38 - Gas connection schematic

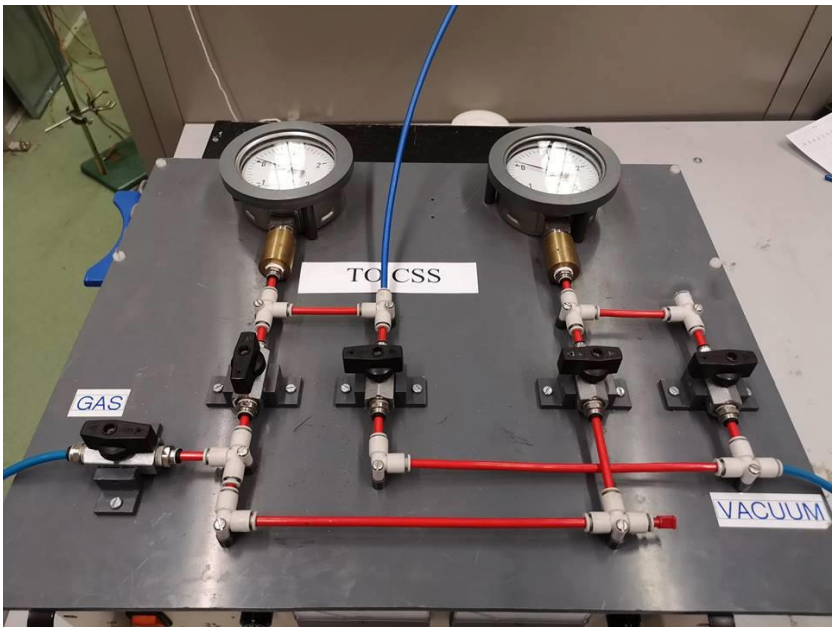

Figure 39 - Gas board used within testing procedure

The two gas bottles can be seen to the left of the schematic, both being followed by an isolation valve. Two additional isolation valves were then incorporated from the gas distribution board that can be seen within the dotted section of Figure 38 and Figure 39. The gas pressure is then read from the gauge which can also be seen on the left in Figure 39. Connected to this is the vacuum with its own isolation valve and the output to the CSS with another isolation valve between. The reason for the isolation valve between the gas board and the switch is extra added safety. Once the gas has been added to the specific pressure needed this connection means that the switch could be completely disconnected from the rest of the gas system in case of ignition. As well as

this precaution, the HFO-1234ze gas bottle was kept in a yellow safety cabinet which can be seen in Figure 48.

When mixing the gases, a specific mixing procedure was established during the testing phase. The molecular weight of HFO-1234ze is 114 kg/mol [46], while that of N_2 is 28 kg/mol. As HFO-1234ze is a heavier gas than N_2, it was decided to add N_2 to the mixture first. Although, based on initial results, a binary mix was assumed to be apparent within the switch, and a second method was implemented to aid the mixing process. This involved firstly filling the switch with N_2 to half of the total desired N_2 fractional pressure. After this, the required fractional pressure of HFO-1234ze was added in its entirety. For example, for a 1 bar gauge (2 bar absolute) mixture of 20/80% HFO-1234ze/N_2, the switch was initially filled from -1.0 to -0.2 bar gauge, the HFO-1234ze mixture was added from -0.2 to 0.2 bar gauge, and then the rest of the N_2 was added until 1 bar gauge. This procedure was seen to be a much more efficient way of mixing the gases compared to adding all the N_2 and topping up with the desired amount of HFO-1234ze. After the gases were added to their desired pressures, the switch was isolated from the gas system and a settlement period of five minutes was observed in order for the gases to fully mix before testing was carried out.

Figure 40 shows the difference found when adopting the two mixing procedures discussed above. What can be seen is that the self-breakdown voltages were found to be greater for both positive and negative polarity DC voltages for the amended mixing procedure, at every point over the range 0-3 bar gauge. Thus, throughout the testing of the N_2/HFO-1234ze mixtures in Chapter V, this procedure was implemented over the course of testing.

Paired *t*-test statistical analyses were conducted, comparing the measured self-breakdown voltages for mixing procedure 1 and mixing procedure 2, for each polarity. A *p*-value of <0.01 was computed between the data for mixing procedure 1 and mixing procedure 2, for both polarities. Therefore, the self-breakdown voltages for the two different mixing procedures are statistically different.

It is hypothesised that the difference in performance of the gas mixtures is that for mixing procedure 1, the binary mix created by adding each individual element sequentially creates the largest split for the blending process to complete. Whereas, following mixing procedure 2, the addition of the heavier element between fractional

pressures of the other gas in the mixture creates a greater turbulence within the switch during the mixing process. This turbulence speeds up the mixing process, resulting in a settled blend of the gases being formed more quickly [62], [63]. As the blend is formed more quickly, the electronegative element that has been added (HFO-1234ze) distributes itself evenly throughout the switch faster, leading to a higher breakdown strength.

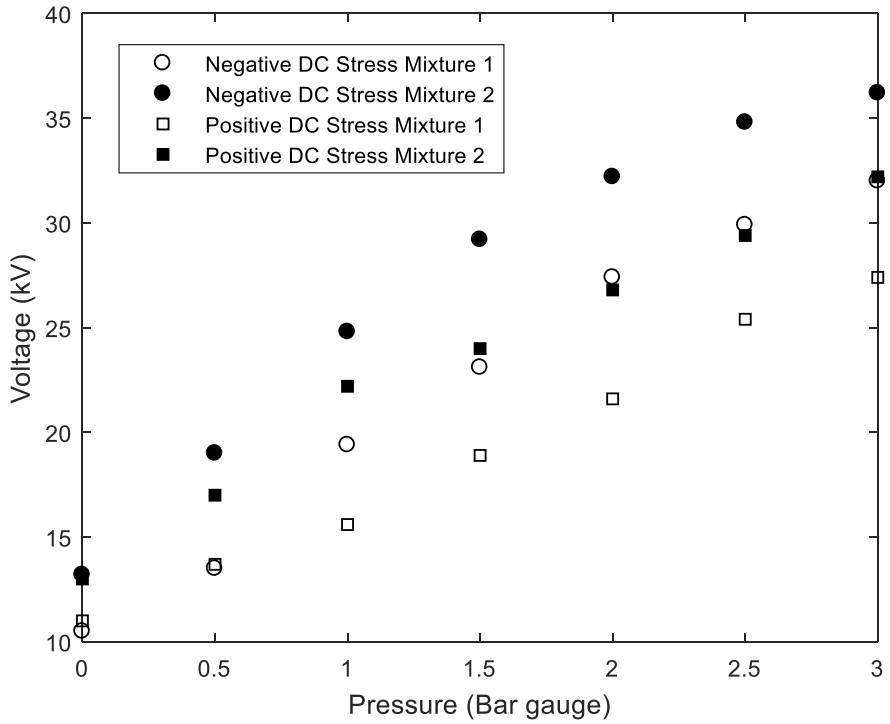

Figure 40 - Difference between mixing procedures for 80% N_2 / 20% HFO-1234ze self-breakdown voltages

4.4. CIRCUIT SET-UP AND OPERATION

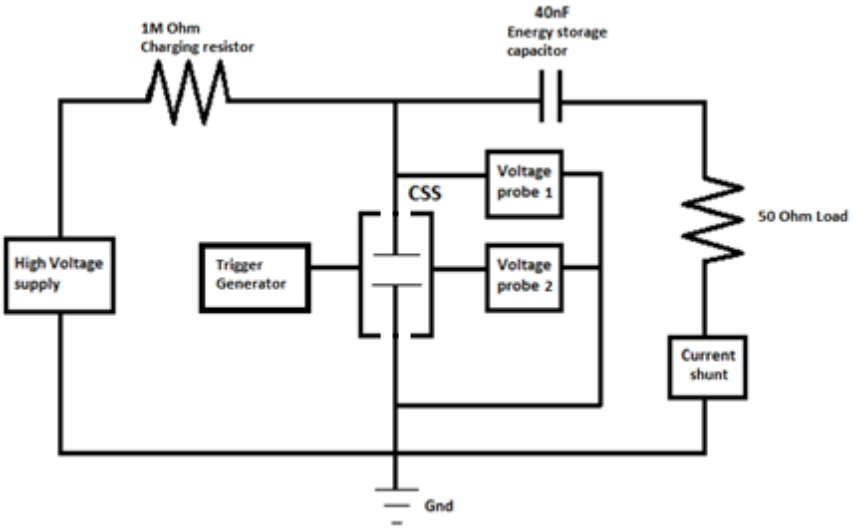

Figure 41 - Test circuit schematic, showing individual components and positions of probes [42], [64]

The following section discusses the connection of the CSS system in order for the operation to be analysed. The circuit schematic can be seen in Figure 41, with each individual component labelled with its specific value if applicable. The setup includes a 100 kV, 2.5 mA Glassman DC supply, set to produce either a positive or negative polarity output. This is connected to a 1 MΩ charging resistor [42], [64]. This then led on to the CSS and capacitor. The capacitor is 40 nF, connected to a 50 Ω load. The trigger pulse used was a positive- or negative-polarity voltage pulse from a Samtech Ltd. TG-01 trigger generator, applied directly to the brass body of the CSS. The TG-01 was activated by a remote-control unit, connected to the trigger impulse generator by a 3 m long fibre-optic cable [42], [64]. A typical positive-polarity trigger pulse voltage waveform is shown in Figure 42.

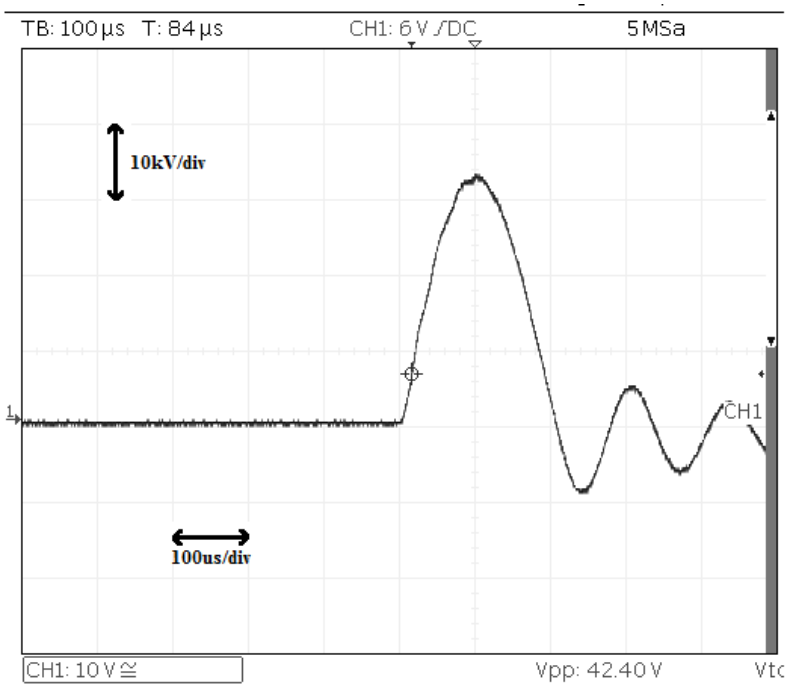

Figure 42 - Positive polarity impulse from Samtech TG-01 trigger generator

Shown in Figure 42 is a positive impulse voltage from the output of the Samtech TG-01 trigger generator. The oscilloscope was set to 10 kV/div, and the time base was set to 100 µs/div. The trigger generator output a ~32.2 kV pulse with 80 µs rise time and 128 µs FWHM. Within the trigger generator itself was an integrated selector switch, which enabled the polarity to be switched from positive to negative dependent upon the desired system operation.

Also, connected to the CSS were two 1000:1 North Star PVM-5 HV probes (80 MHz nominal bandwidth). Each was connected to their own specific measurement point. The first voltage probe was connected across the main (disc) electrodes, used to identify the switch closure within the system. The second voltage probe was connected between the trigger electrode (brass body) of the switch and ground, which ultimately gave confirmation of the overall delay time associated with a switching operation, defined as the period between the trigger pulse being applied until complete closure of the switch being established. Monitoring of the current with a Samtech Ltd. DE(CP)-01 current shunt, with a sensitivity of 14 V/kA, allowed for conformation of switch

closure. An example of switch operation with the three probes included is detailed in Figure 43.

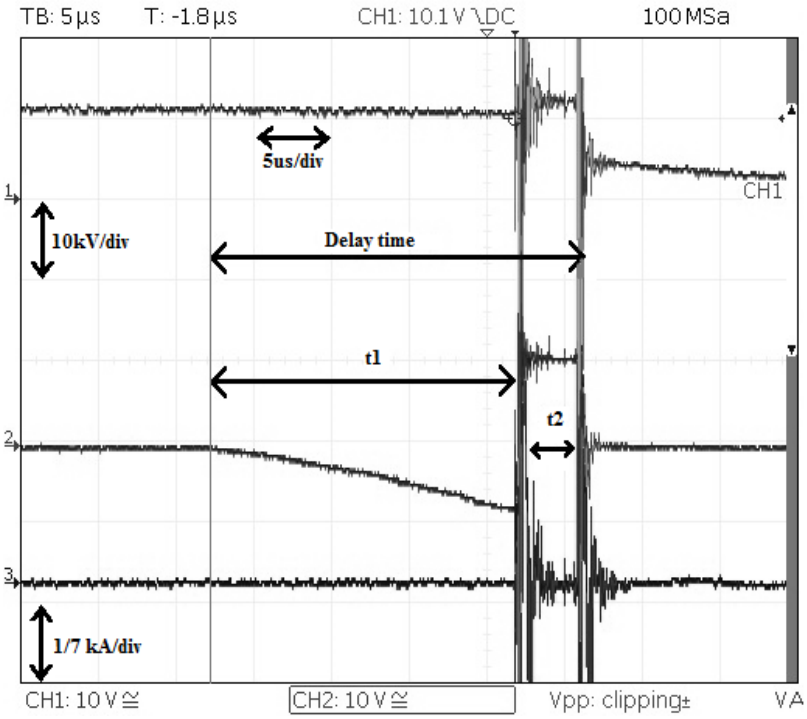

Figure 43 - CSS characteristics with trigger voltage waveform and current to earth waveform. Delay time = 24 µs, t1 = 20 µs, t2 = 4 µs. Upper (1): voltage collapse across switch (voltage probe 1); middle (2): trigger pulse voltage waveform (voltage probe 2); and bottom (3): current waveform.

As seen in Figure 43, the top waveform (1) was measured by the voltage probe across the whole of the switch, with confirmation of switch closure at the voltage collapse at the end of the delay time. The middle waveform (2) shows the trigger pulse voltage, with the time between the impulse commencing and breakdown of the trigger to HV electrode gap (*Dh*) shown by *t*1. The subsequent time period from this *Dh* breakdown until full breakdown of the switch is represented by *t*2. Hence, the full delay time can be found by summing *t*1 and *t*2. The bottom waveform (3) represents the current flowing to earth. This then confirms that the switch has in fact broken down, as current flows to the load side of the circuit. As shown however, at this HV electrode break there is a current spike shown followed by another at actual full breakdown of the switch. This will be a product of noise within the system as the voltage polarities changing will effect displacement current flow at the ground electrode. Therefore, the second voltage at waveform 1 probe connection is important as to see when the exact time of switch breakdown occurs.

Alternatively, there are two other operation modes that become apparent within the closure of the switch. These are illustrated in Figure 44 and 62. What is shown in Figure 44 is the ideal closure of the switch after the trigger pulse has been applied. What is different about these waveforms and those in Figure 43 is that *t*2 can be seen to be negligible. This waveform is evident when operating the switch with applied voltage >> trigger threshold level. In Figure 45, these are the resulting waveforms of a non-closure of the switch. As the trigger pulse voltage waveform increases, the HV gap is closed as the potential of the trigger electrode is seen to be equal to the dc voltage applied to the HV electrode after *t*1. The difference is that the *t*2 is seen as infinite as the fields were not high enough in order to break the ground gap, *Dg*, so the switching operation is incomplete.

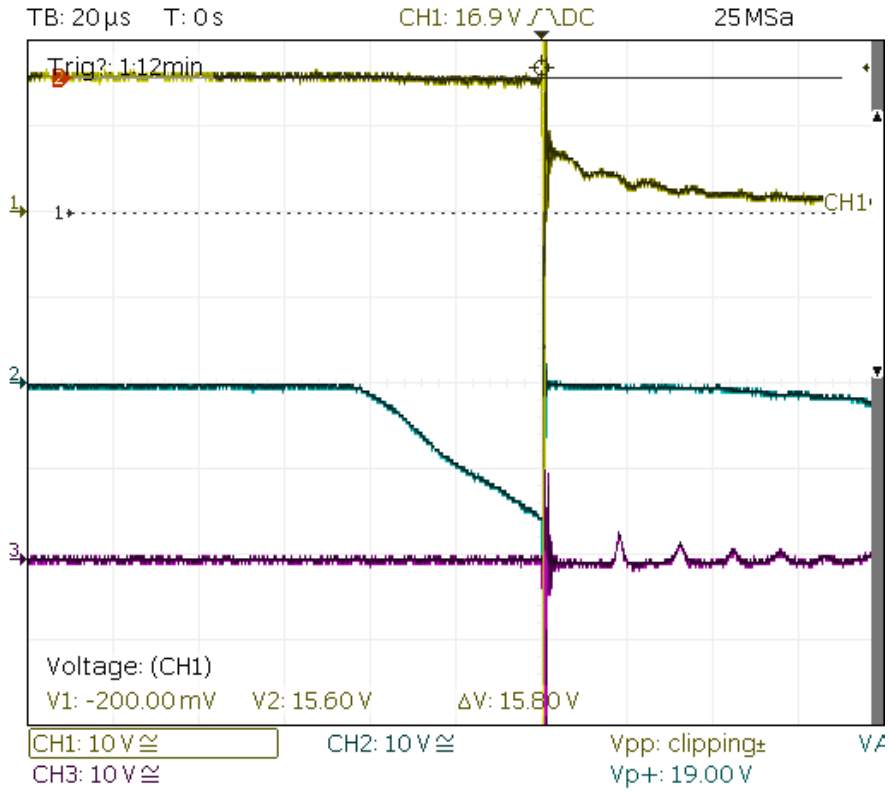

Figure 44 - Negligible t2 switch operation Upper (1): voltage collapse across switch (voltage probe 1); middle (2): trigger pulse voltage waveform (voltage probe 2); and bottom (3): current waveform.

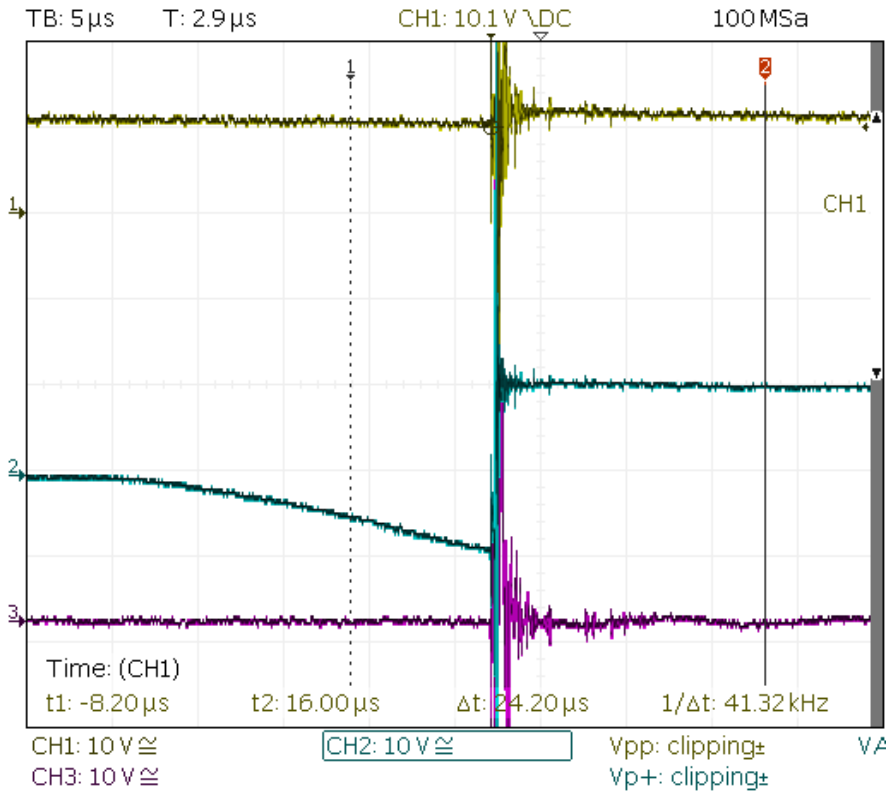

Figure 45 - Non-switch closure. Upper (1): voltage across switch (voltage probe 1); middle (2): trigger pulse voltage waveform (voltage probe 2); and bottom (3): current waveform.

The way in which the system operates is that, firstly, the capacitor is charged up through the 1 MΩ resistor by the Glassman supply to the specific applied voltage of either negative or positive polarity. The trigger generator then provides a pulse to the body of the switch of the opposite polarity to that of the applied DC voltage, therefore increasing the potential difference between the HV and trigger electrodes, leading to closure of the gap *Dh*. There is then, generally, a short time delay, *t*2, before the gap *Dg* closes. Since the application of the trigger pulse leads to switch closure, this is, therefore, a controlled breakdown, similar to the mechanism discussed in section 2.8.

A photograph of the system used in the testing procedure is shown in Figure 46.

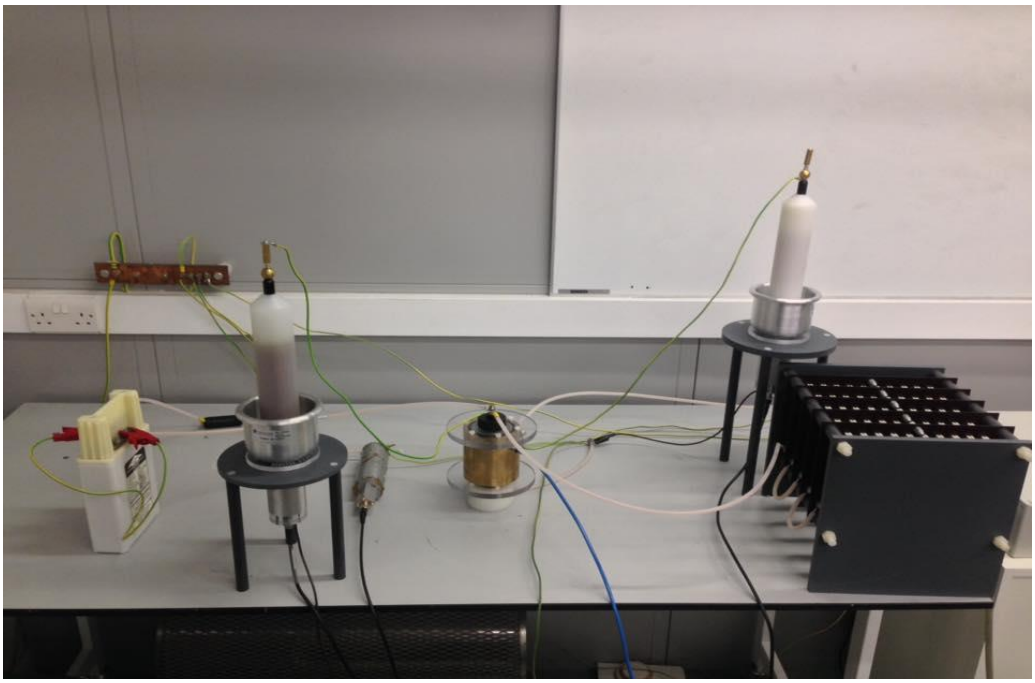

Figure 46 - Photo of CSS HV test circuit

4.5. LABORATORY OVERVIEW SET-UP

The laboratory setup is discussed in this section, with a birds-eye view of the laboratory layout, along with a photograph of the actual setup used. Figure 47 is a birds-eye view of the entirety of the lab - the system setup is situated at the bottom of the lab at opposite ends to the door. The equipment used for applying voltage, triggering and for analysis is situated at a safe distance from the live equipment. The earth connections are shown in green. With a full lab set-up shown in Figure 48, showing all equipment as well as the HFO-1234ze bottle housed inside the yellow safety cabinet.

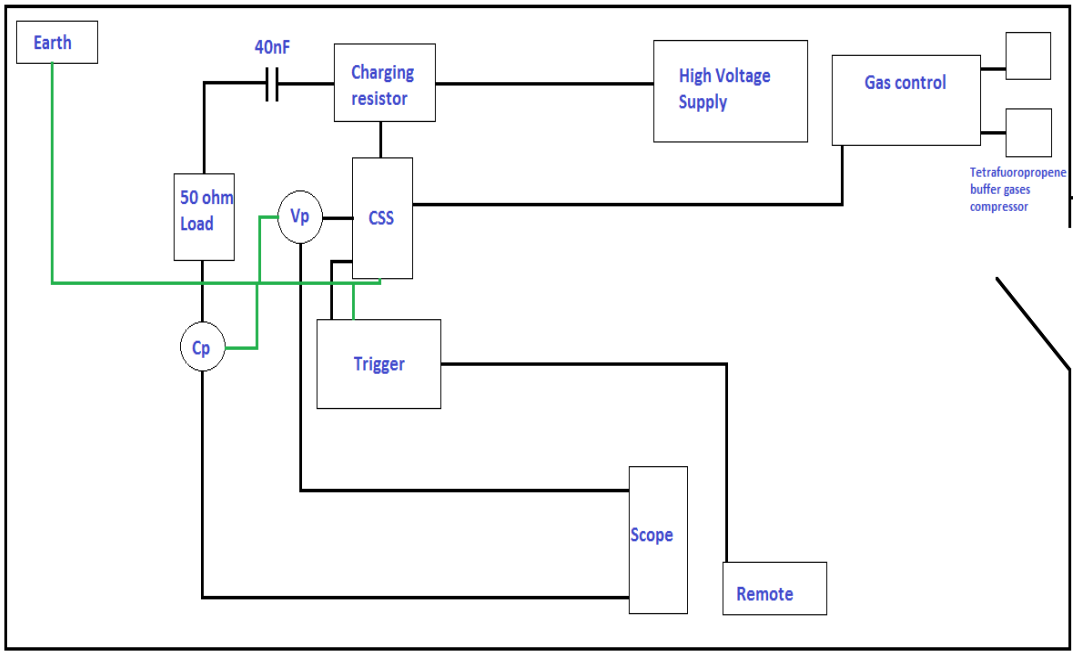

Figure 47 - Lab overview showing individual components and connections in lab

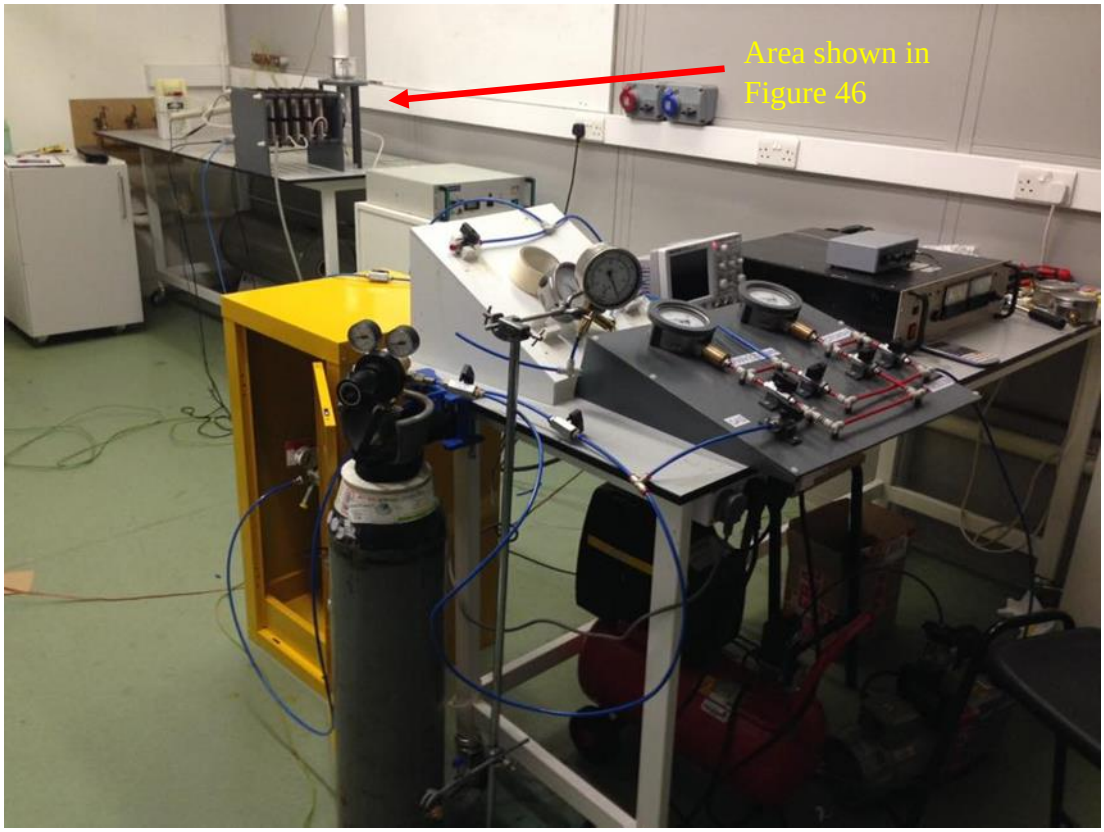

Figure 48 - Photo of overall laboratory

4.6. Self-Breakdown and Triggering threshold measurements

The self-breakdown and triggering threshold results have been separated by polarity. Self-breakdown voltages were determined by monitoring the voltage across the switch, increasing the applied DC stress until the voltage collapsed. The trigger threshold voltage was determined by lowering the applied DC voltage in 1-kV increments from the self-breakdown voltage and applying a trigger pulse five times. If the switch closed upon application of all five trigger pulses, the applied DC voltage was again lowered by 1 kV, until the switch failed to close for any one of the five triggering events. The DC voltage was then increased by 0.2 kV increments until the switch again closed for all five applied trigger pulses, and this voltage was recorded as the trigger threshold voltage.

Once these values were found for each of the gases or gas mixtures being tested then a graph was plotted as in Figure 49.

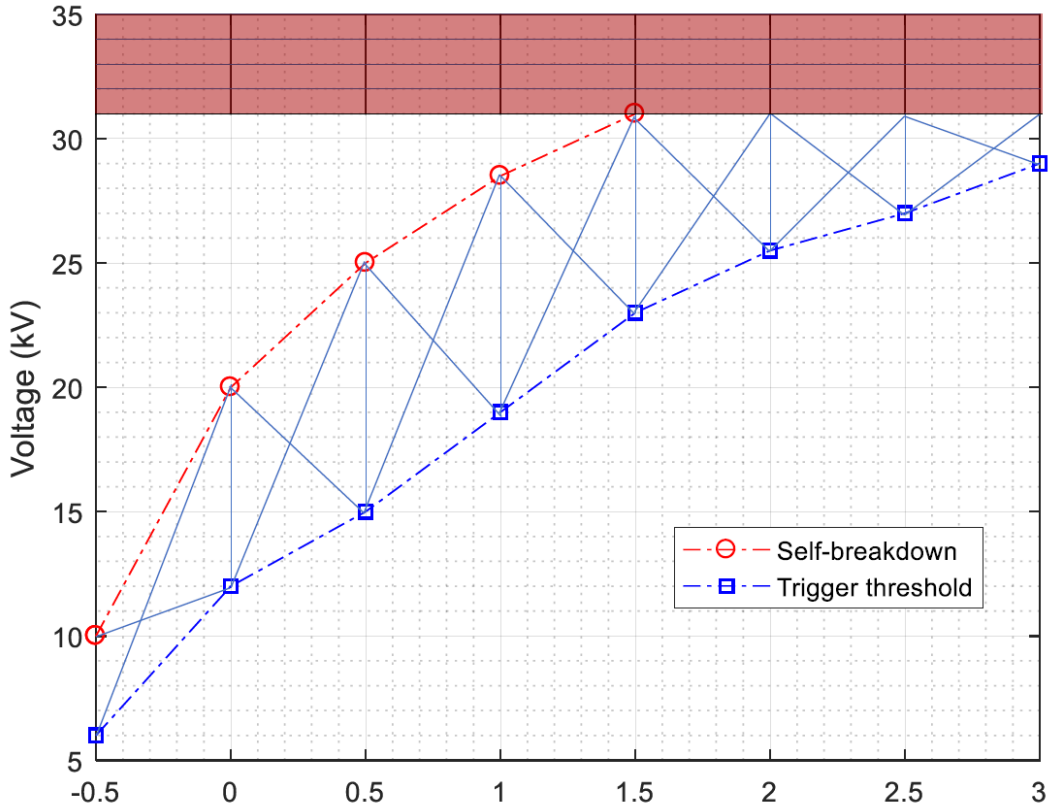

Figure 49 - Example of triggering range (hatched region) over a range of pressures from switch characterisation

What can be seen from Figure 49 is an example of the self-breakdown and trigger threshold levels of a CSS. Also, an additional area in red at the top of the figure has been added, corresponding to the maximum DC voltage achieved from the supply

within the study. The area that has been hatched in between the self-breakdown and the trigger threshold voltages is the operational range of the switch. Dependent upon the application, a particular pressure can be chosen for the required operating voltage. For example, at 1 bar gauge, the voltage can be set to anywhere between 19 kV and 28.5 kV. Below 19 kV, the probability of the switch closing will be 0, and above 28.5 kV the switch will be liable to self-close. Therefore, a suggested operational voltage for 1 bar would be around 24 kV, as this is far enough from these two points to ensure reliable operation.

4.7. Delay Time Measurement and Jitter Calculation

The delay time was measured between 0 and 3 bar gauge, in increments of 0.5 bar. This was conducted by measuring the time from the initiation of the trigger pulse to the breakdown of the switch, as shown in Figure 43 and 44. Each of the delay time data points is an average of 25 individual measurements at each pressure throughout. The jitter at each pressure was then calculated as the standard deviation of each set of 25 delay time measurements. Jitter data has been shown in the form of error bars, corresponding to the calculated standard deviation in both directions, found at each pressure iteration.

5. CHAPTER V

TESTING OF CSS WITH AMBIENT AIR

5.1. GENERAL

This section details the preliminary tests, undertaken to characterise the switch using compressed ambient air. This characterisation was performed by measuring the self-breakdown voltages, triggering threshold voltages, and the delay times to breakdown, to determine the electrode geometry which will be kept constant throughout subsequent testing with the novel gas mixtures, incorporating percentages of HFO-1234ze.

5.2. CHARACTERISATION OF SWITCH PERFORMANCE

5.2.1. Self-breakdown of different gap spacings

5.2.1.1. Positive applied polarity

Firstly, the self-breakdown voltages for a single gap spacing (*Dh*) were measured, for gap spacings of 3 mm to 8 mm, over the pressure range 0-3 bar gauge, in increments of 0.5 bar. The measured breakdown voltages are shown in Figure 50. In order to do this, the body of the switch was grounded so that it was just a single gap switch in operation. As seen from the graph in Figure 50, as the gap spacing increases, the self-breakdown voltage is greater. This is the case for all gap spacings apart from 5 mm, which is seen to have a higher breakdown strength for the given pressure than 6 mm. The reason for this is that upon inspection after testing the electrode angle point radius differed between the 5 mm and 6 mm disc electrodes. Upon completion of the tests, it was found that the radius of the electrode yielding a 6 mm gap was slightly smaller than that yielding a 5 mm gap, meaning that the peak field strength would be stronger than for the 5 mm gap, and explaining the observed occurrence of breakdown at lower

applied voltages. Noteworthy from Figure 50 is the large relative increase in the self-breakdown voltages between 4 mm and 5 mm.

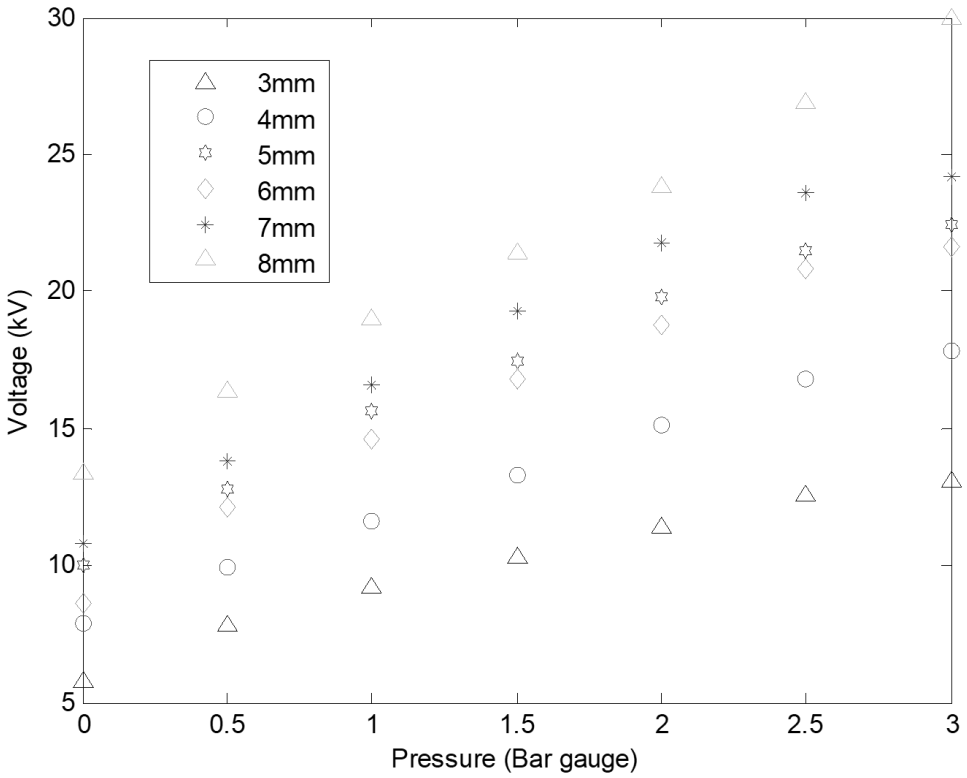

Figure 50 - Positive polarity self-breakdown voltages for 3 mm to 8 mm gap (Dh) spacings w.r.t pressure

5.2.1.2. Negative applied polarity

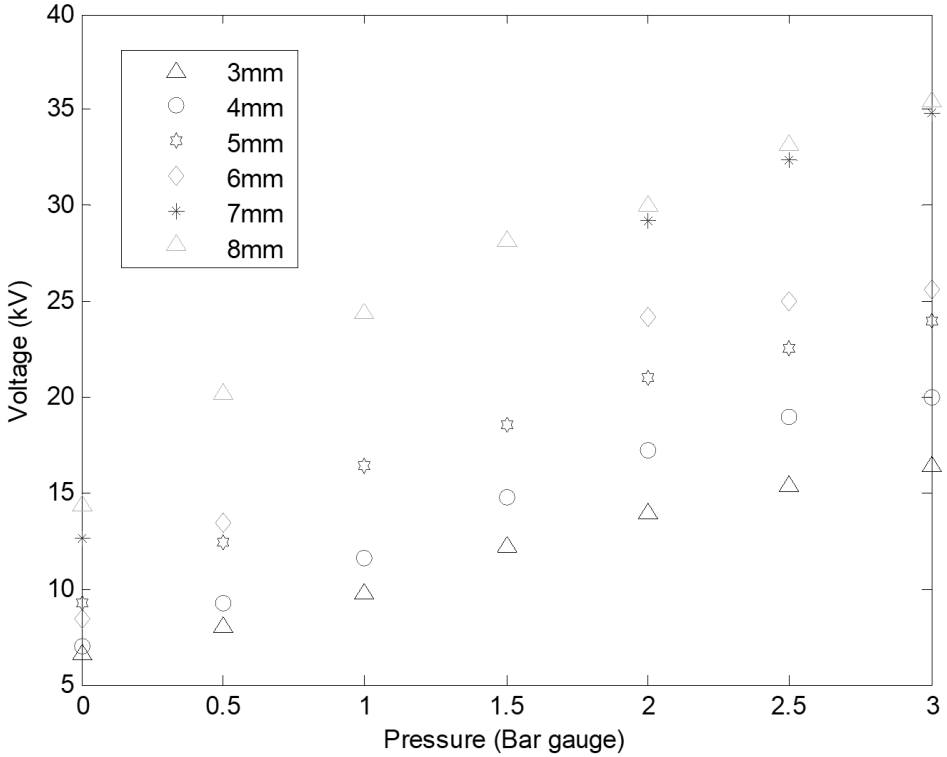

Figure 51 Negative polarity self-breakdown voltages for 3 mm to 8 mm gap (Dh) spacings w.r.t pressure

Figure 51 shows the breakdown strengths of 3 mm to 8 mm air gaps, characterised from 0-3 bar gauge in 0.5 bar increments, for negative DC voltages. What can be seen is a clear increase in self-breakdown voltage as the distance (gap spacing) increases. Although, at some of the longer gap distances at specific pressures, no breakdown was achieved. This was due to the high corona current, leading to the current from the Glassman supply to reach its maximum output current level of 2.5 mA. This problem arose at distances of 6 mm and 7 mm.

So, from self-breakdown voltage trends alone, a HV-trigger electrode gap (*Dh*) of 5 mm was chosen, since it provided good performance for both positive and negative polarities.

5.2.2. Triggering ranges

Triggering ranges were measured by determining the trigger threshold voltages for different trigger-earth (*Dg*) gap spacings. Following from the results in section 5.2.1, the HV-trigger (*Dh*) gap was fixed at 5 mm. The triggering range is the operating range

of the switch and is the area between the triggering threshold level and the self-breakdown level. This is discussed in section 4.6. In Figure 52, the voltage range between the self-breakdown and trigger threshold curves are able to be used, to be sure that switch closure can be affected in a controlled manner, i.e. only when a trigger pulse is applied. For each of the iterations tested, the polarity of the trigger pulse was always the opposite to the polarity of the applied HV.

5.2.2.1. Positive applied polarity

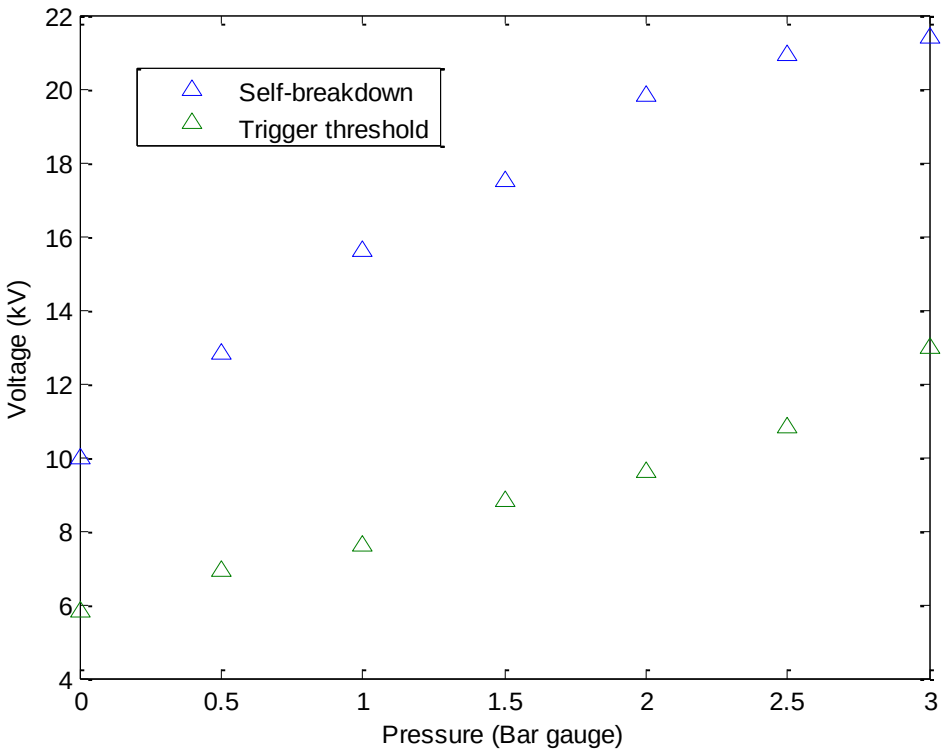

Figure 52 – Positive polarity trigger range for 5 mm HV gap (Dh) and 3 mm Ground gap (Dg) electrode geometry

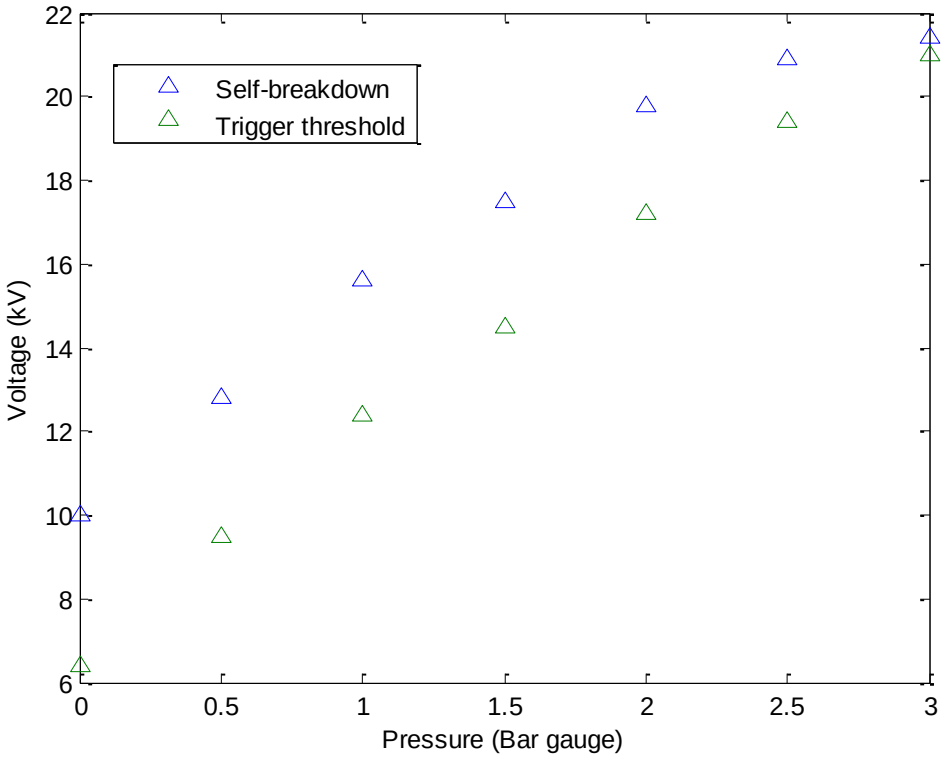

Figure 53 - Positive polarity trigger range for 5 mm HV gap (Dh) and 4 mm Ground gap (Dg) electrode geometry

Shown in Figure 52 and 53 are the self-breakdown and the triggering threshold voltages for air, in 0.5 bar iterations, between 0 and 3 bar gauge, for two different electrode geometries –

- 5 mm HV – Trigger electrode gap (*Dh*), 3 mm Trigger – Ground gap (*Dg*)
- 5 mm HV – Trigger electrode gap (*Dh*), 4 mm Trigger – Ground gap (*Dg*)

As seen from Figure 52, the triggering range is wide throughout all of the pressure iterations from 0-3 bar gauge. The maximum triggering range which was measured for this geometry was 10.2 kV at 2.5 bar gauge, and the minimum triggering range was measured as 4.2 kV at 0 bar gauge. Comparing this data to the corresponding self-breakdown voltage levels, it was found that the highest percentage of self-breakdown was measured at 58% and the lowest at 42%. This means that throughout the testing, using a value of 75% of the self-breakdown voltage was far enough from both the self-breakdown and trigger threshold voltages (i.e. in the region between these two curves) for stable operation over the full pressure range. Moreover, testing was also undertaken with applied DC voltages corresponding to a value of 60% of the self-breakdown voltages, as reported in section 5.2.3. Although, operating so close to the triggering

threshold voltages (58% of the self-breakdown voltages at some pressures), then the switch has a higher probability of non-closure when the triggering impulse is applied.

In Figure 53, the triggering range is illustrated for again 0.5 bar iterations between 0 and 3 bar gauge, but with a *Dg* of 4 mm. The switch performance under these conditions is seen to be poorer in terms of triggering range through the pressure iterations. The maximum triggering range is 3.6 kV at 0 bar gauge, falling to only 0.5 kV at 3 bar gauge. It can be seen that the relationship between trigger threshold voltage and pressure is relatively linear for this specific electrode geometry. In terms of percentage of self-breakdown voltages, the values were at a much higher value compared to the 5/3 mm arrangement, between 64% and 89%, meaning that reliable switch operation in this geometry will need an applied voltage of at least 90% of the self-breakdown voltage. The narrow triggering range means that this point of operation is close to both the triggering threshold level and the self-breakdown level. Therefore, the switch has higher probability of non-closure or self-closure, compared to the geometry where *Dg* is 3 mm.

5.2.2.2. Negative applied polarity

Shown in Figure 54 and 55 are the self-breakdown and trigger threshold level voltages for air, with *Dg* of 3 mm and 4 mm, respectively. As previously, *Dh* was fixed at 5 mm. It is apparent that there are very different switching characteristics between the two *Dg* values. In Figure 54 (*Dg* is 3 mm), the maximum triggering range was measured at 3 bar gauge, with a value of 6.8 kV, and the minimum triggering range of 4 kV was found at 0 bar gauge. In Figure 55 (*Dg* is 4 mm), the maximum triggering range was measured at 3 bar gauge with a value of 12.8 kV, and the minimum was 3.2 kV at 0 bar gauge. So, from this analysis, *Dg* of 4mm is shown to have the better performance in terms of triggering range, and switch operation could be affected at lower percentages of the self-breakdown voltages than for *Dg* of 3 mm.

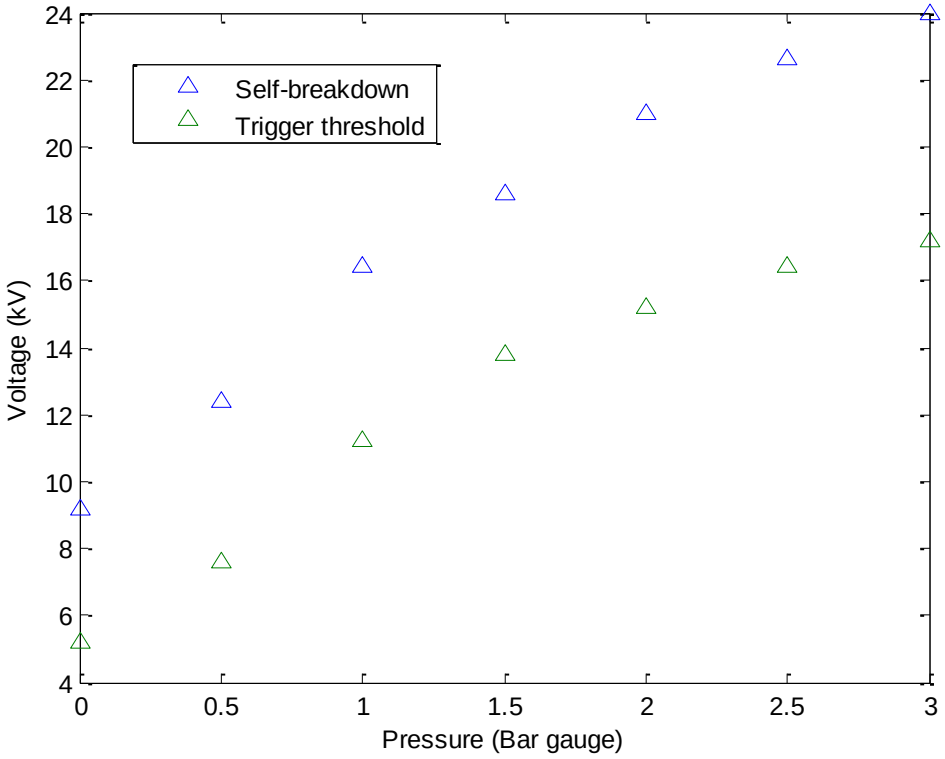

Figure 54 - Negative polarity triggering range for 5 mm HV gap (Dh) and 3 mm Ground gap (Dg)

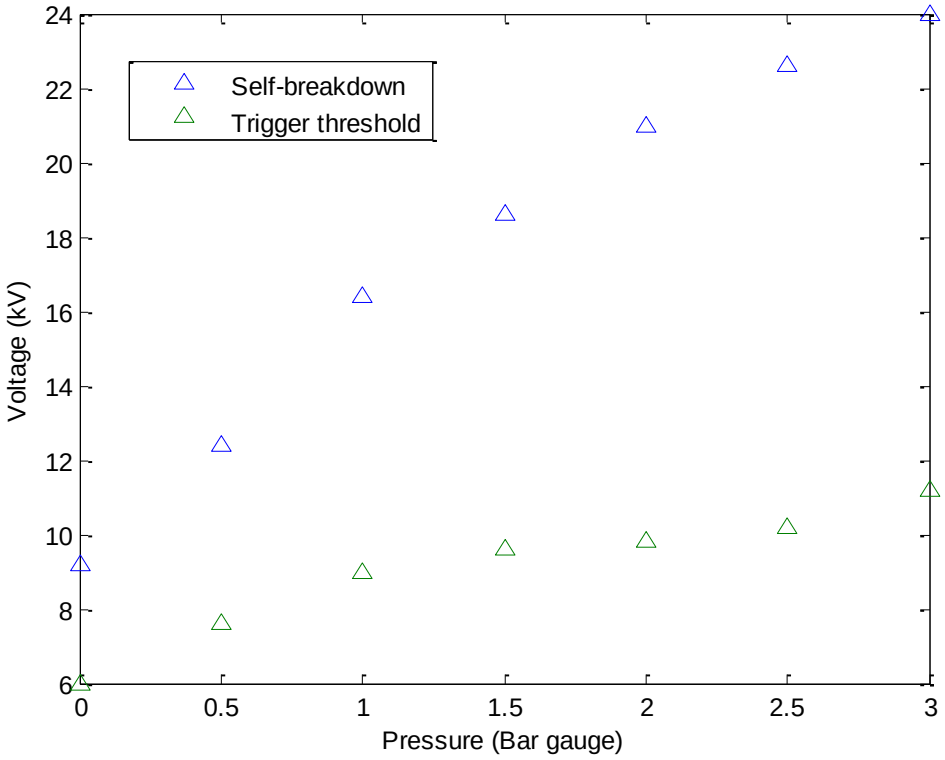

Figure 55 - Negative polarity triggering range for 5 mm HV gap (Dh) and 4 mm Ground gap (Dg)

However, as with the positive-polarity characterisation, 75% of the self-breakdown voltages could be used as an operational point for each of these geometries for negative polarity, so both *Dg* values are sufficient. As the switch intended for use with the novel gas HFO-1234ze is to be used in both polarities, then gaps of *Dh* = 5 mm and *Dg* = 3 mm were selected for further testing, given the much better switching performance for positive polarity (compared to when *Dg* = 4 mm); and the overall capability to operate reliably, for both negative and positive polarity, at 75% of the self-breakdown voltages, over a wide range of pressures (0-3 bar gauge).

5.2.3. Delay time

5.2.3.1. Positive applied polarity

The delay times are shown for the geometries characterised in section 5.2.2 at their respective self-breakdown voltage levels, dependent upon the specific triggering range. This was tested under positive applied voltage and a negative trigger pulse. Figure 56 and 57 show the average measured delay times measurements and calculated jitters for the 25 iterations collected when testing. As shown, the 5/3 mm geometry shows an increase in delay time as the pressure increases. The jitter remains relatively consistent throughout each iteration. The maximum delay time measured was 19 μs at 0 bar gauge, with a maximum of 36.5 μs at 3 bar gauge. The maximum and minimum jitters were 1.3 μs and 3 μs, respectively, which were not directly related to pressure, as seen in Figure 56. Figure 57 shows the delay times and jitters for the 5/4 mm geometry for positive polarity, and this reflected a much different characteristic. The testing was very erratic, and no clear trend in terms of delay time with pressure was discernible; the jitter remained fairly consistent through the minimum and maximum delay times, which were measured as 15.7 μs and 22.1 μs, respectively, with corresponding jitters between 1.5 μs and 2.8 μs. Although, in this geometry, the delay times are seen to be shorter than for the 5/3 mm geometry. This data was taken at 90% of the self-breakdown voltage. As there is a clear increase in delay time with respect to pressure, and operation could be reliably triggered at 75% of the self-breakdown voltage, the 5/3 mm geometry was considered to be more useful to merit further characterisation.

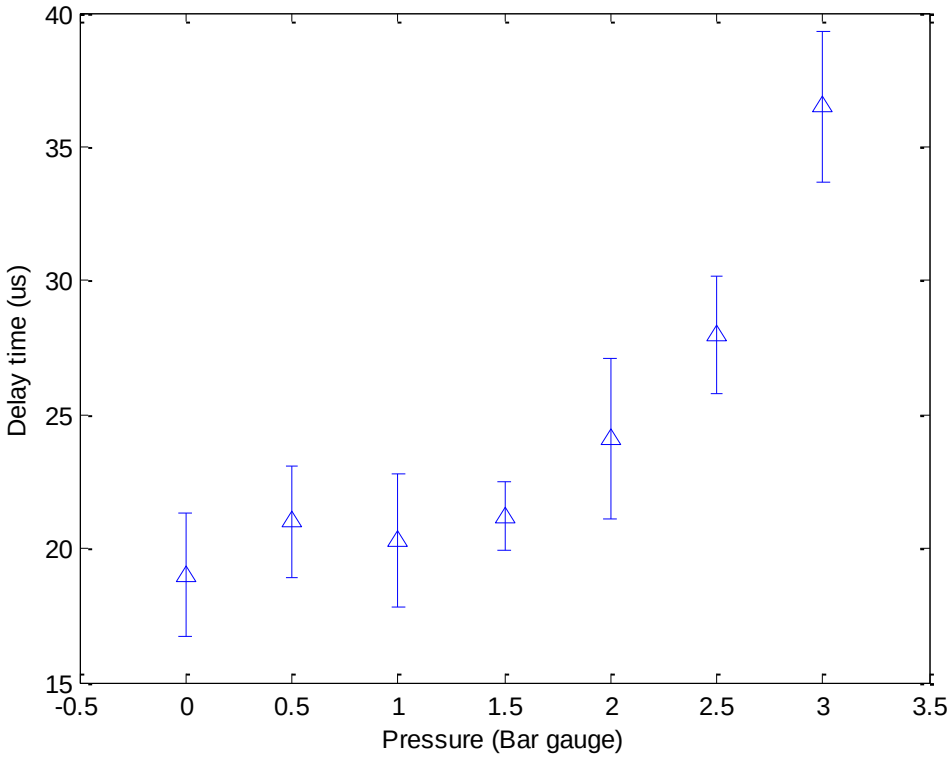

Figure 56 – Positive polarity average (mean) delay times calculated from 25 delay times measurement and jitter calculation for 5/3 mm geometry at 75% of the self-breakdown voltage level

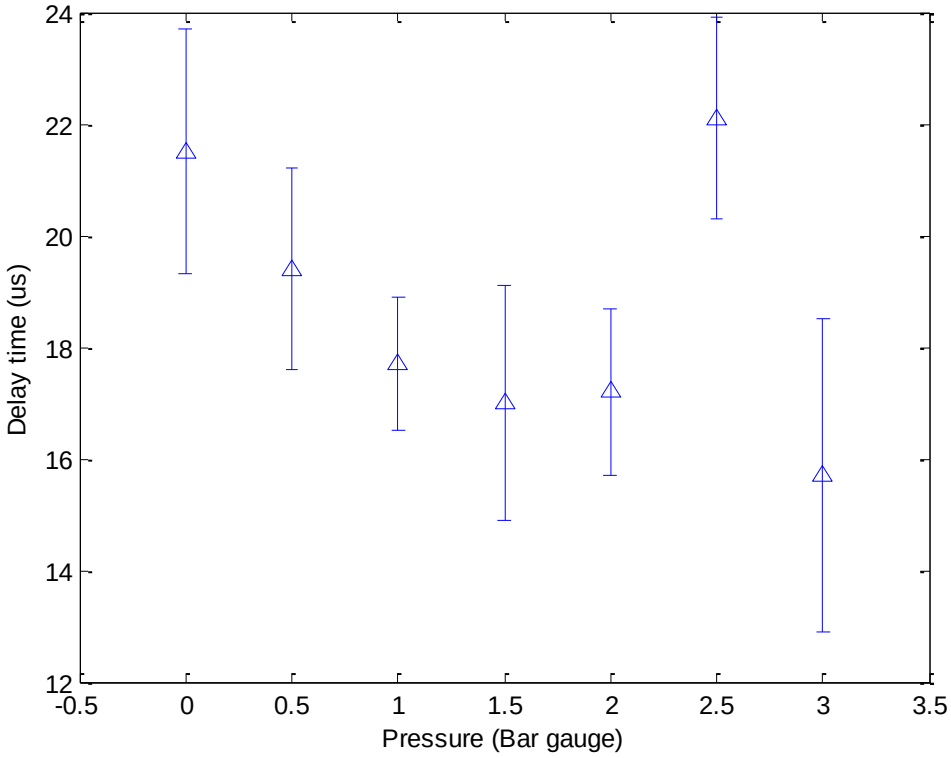

Figure 57 - Positive polarity, average (mean) delay times calculated from 25 delay time measurements and jitter calculation for 5/4 mm electrode geometry at 90% of the self-breakdown voltage level

5.2.3.2. Negative applied polarity

The section details the negative applied polarity and positive trigger impulse delay time and jitter data for the two electrode geometries tested.

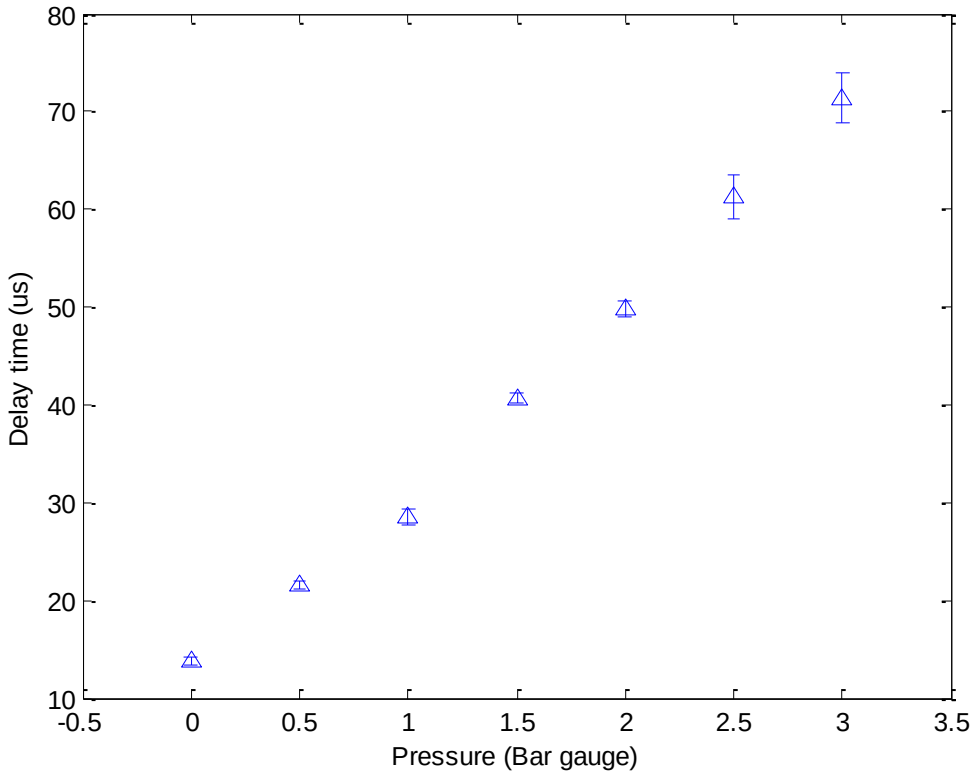

Figure 58 - Negative polarity average (mean) delay times calculated from 25 delay times and jitter for 5 mm HV gap and 3mm Ground gap at 75% of the self-breakdown voltage level

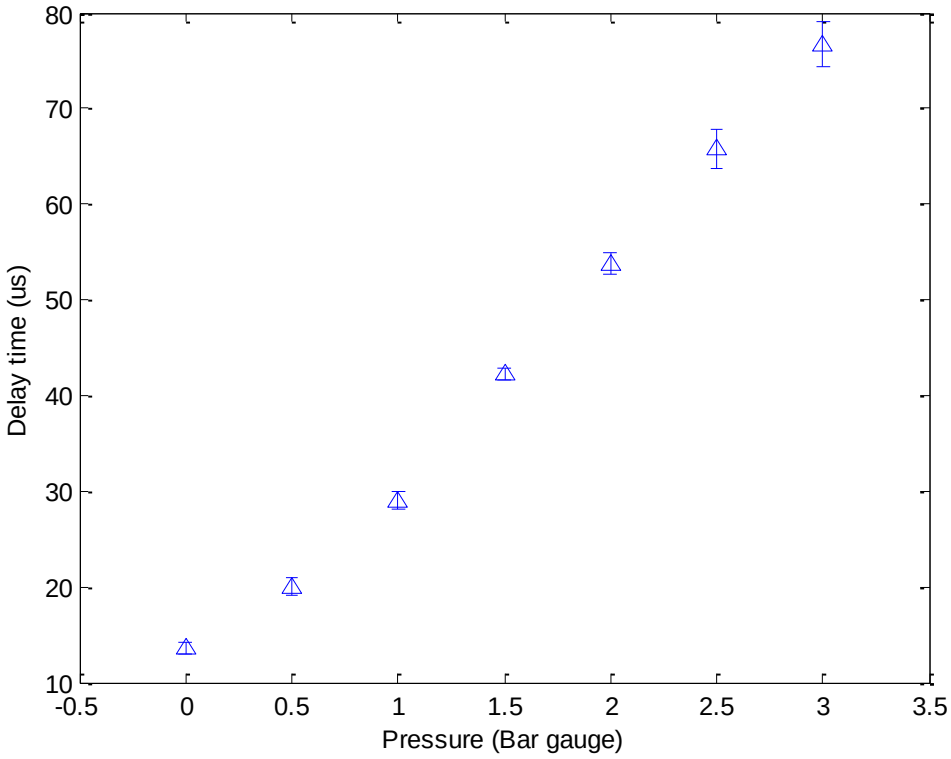

Figure 59 - Negative polarity average (mean) delay times calculated from 25 delay times and jitter for 5 mm HV gap and 4 mm Ground gap at 75% of the self-breakdown voltage level

In Figure 56 and 58, the delay time and jitter are shown for the same parameters with respect to the percentage of self-breakdown used. Although, for Figure 57 and 59, the parameters changed for the applied DC voltage with respect to the triggering threshold as shown from Figure 53 as this resulted from a narrow trigger range at higher pressures, therefore, two different percentages of the self-breakdown level were used. This data were measured for negative polarity DC voltage/ positive polarity trigger pulse (Figure 58 and 59) and positive polarity DC voltage and negative polarity trigger pulse (Figure 56 and 57). In Figure 58, an increase in both delay time and jitter is apparent as the pressure increases. The trend is the same in Figure 59. The ranges of the measured delay times and calculated jitters for 5/3 mm were 13.7 µs – 71.4 µs, and 0.4 µs – 2.6 µs, respectively. For the 5/4 mm electrode geometry, the corresponding ranges were 13.6 µs – 76.7 µs and 0.6 µs – 2.2 µs. Although there is a slight increase in delay time for 5/4 mm, the operation for both topologies is similar.

If this switch was to be used for negative polarity only, each geometry would be acceptable. However, as the intent is for the switch to be operational for both polarities,

the 5/3 mm geometry is better, as it shows a predictable performance for both polarities in terms of self-breakdown voltages, trigger threshold voltages, delay times and jitter.

5.3. VON LAUE STATISTICAL ANALYSIS OF DELAY TIME DATA

5.3.1. Applied voltage in accordance with percentage of self-breakdown level

Shown in Table 4 are the applied voltage values used when performing delay time analysis for both electrode geometries. Throughout the analysis, the applied voltage would be set to these values, dependent upon pressure, electrode geometry and polarity, thus giving a consistent analysis for each section. For positive applied DC voltage and the 5/4 mm geometry, it was necessity to use 90% of the self-breakdown voltage, as discussed in 5.2.2.1 and shown in Figure 53; the applied DC voltages corresponded to 75% of the self-breakdown voltage level for all other conditions.

Table 4 - Applied voltages for delay time analysis

Pressure (bar gauge)	**5/3 mm**		**5/4 mm**	
All 25 shots	**Positive 75% (kV)**	**Negative 75% (kV)**	**Positive 90% (kV)**	**Negative 75% (kV)**
0	8	7	9	7
1	12	12	14	12
2	15	16	21	16
3	16	18	22	18

5.3.2. Delay time in accordance with breakdown number

The following section outlines the delay time data with respect to breakdown number, where breakdowns 1 to 25 are plotted in order for trend analysis to be conducted.

5.3.2.1. 5/3 mm breakdown analysis

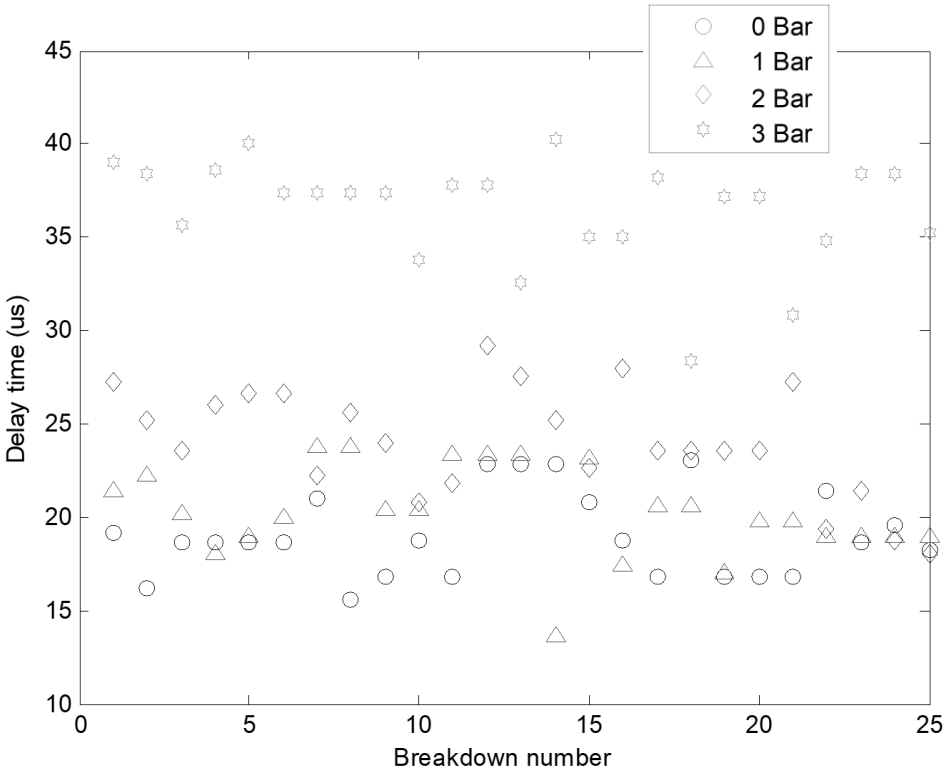

Figure 60 Positive polarity delay time/breakdown number for ambient air at 0, 1, 2 and 3 bar gauge.

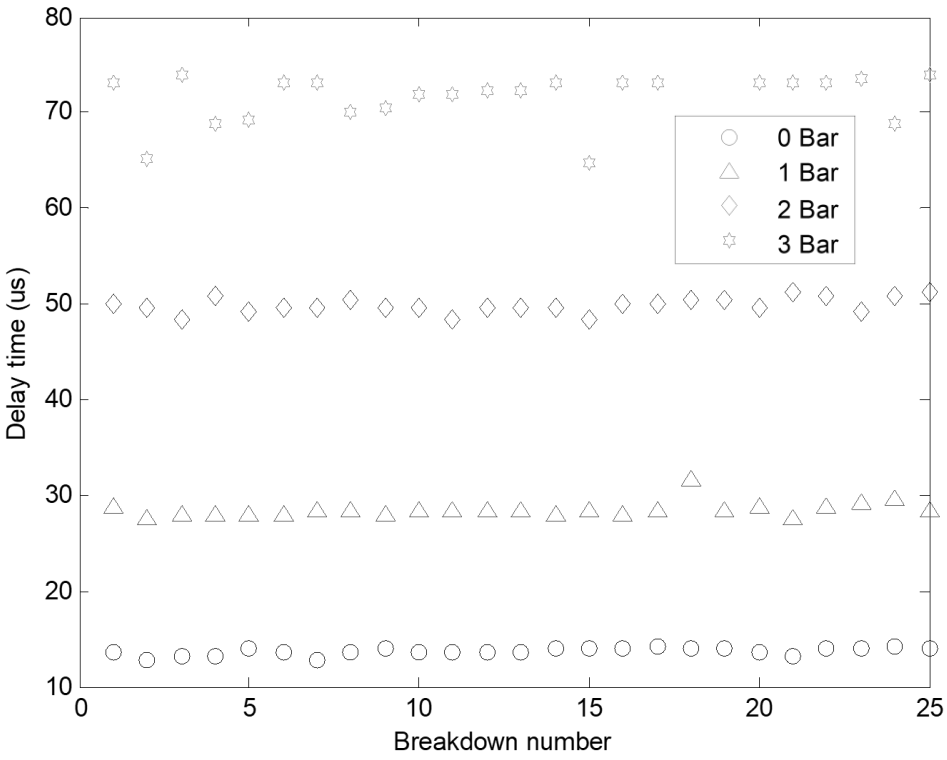

Figure 61 Negative polarity delay time vs. breakdown number for ambient air at 0, 1, 2 and 3 bar gauge.

Figure 60 and 61 illustrate the positive and negative polarity delay times for self-breakdown in the 5/3 mm electrode geometry. The data was plotted in this way to see if there was a clear increase or decrease in delay time with an increasing number of breakdowns. What is evident from Figure 60 is an erratic distribution of delay time values over the 25 breakdowns; there is no clear increase or decrease in the delay time as the number of breakdowns increases. Figure 61 shows the negative polarity delay times, which can be seen to be a lot more consistent over the 25 breakdown events than for positive polarity. As the higher gas pressures are reached, the delay time begins to show more of a fluctuation, but the delay time is relatively consistent for the full test.

5.3.2.2. 5/4 mm breakdown analysis

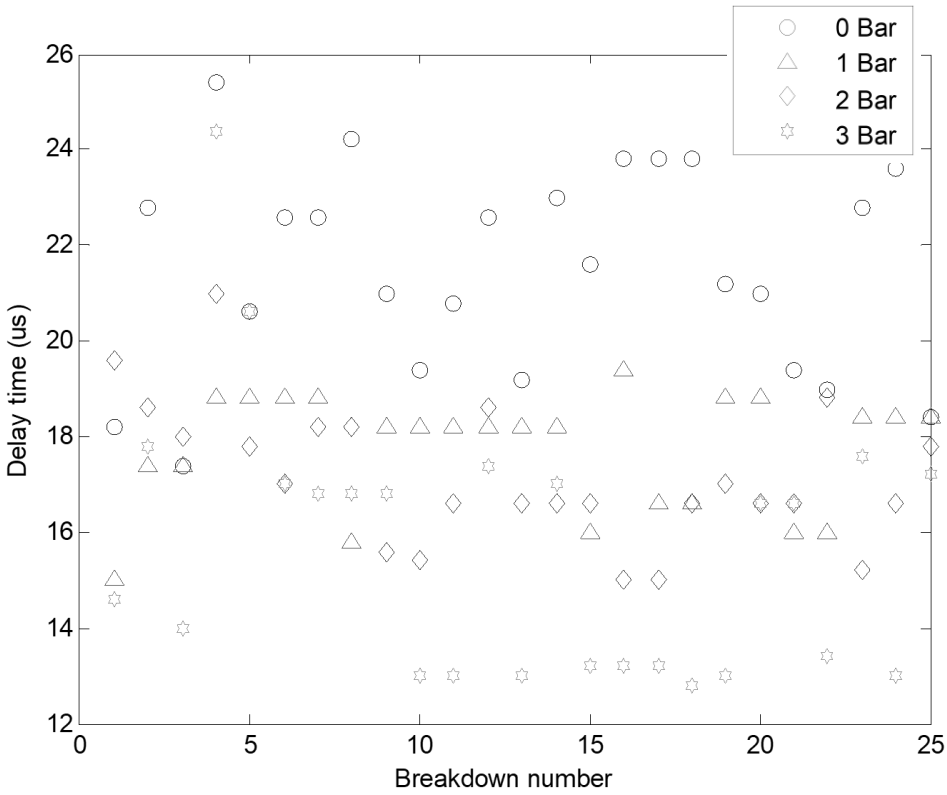

Figure 62 Positive polarity delay time vs. breakdown number for ambient air at 0, 1, 2 and 3 bar gauge.

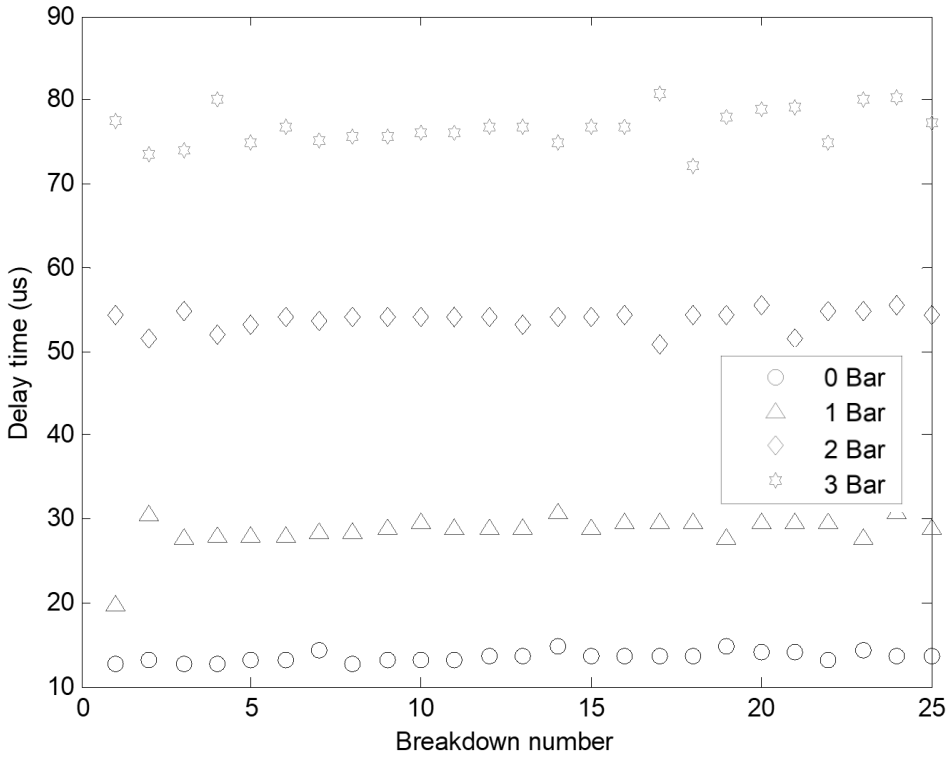

Figure 63 - Negative polarity delay time vs. breakdown number for ambient air at 0, 1, 2 and 3 bar gauge.

Figure 62 and 63 show the delay times over the 25 shots required for the von Laue analysis. Figure 62 shows the type of distribution which was also apparent in Figure 60, where the distribution of the delay times was very erratic over the course of the breakdowns. In Figure 63, the plots are much more consistent compared to those in Figure 61; again, as the pressure increases, the delay time is shown to become slightly more erratic. From inspection of Figure 60-63, there is no clear evidence that there is any overall increasing or decreasing trend over the course of the breakdowns. Therefore, due to previous trigger threshold information gathered, a 5/3 mm geometry was considered as optimum overall.

5.3.3. Analysis of time delay to breakdown

Von Laue analysis graphs (‘Laue plots’) are presented in Figure 64 and 65, showing the difference between positive and negative polarity for the 5/3 mm geometry. From time zero to the first red line is measured as the formative time, and the time between the two red lines is the statistical time, which is explained in detail in section 2.11. Table 5 shows the statistical and formative times for positive and negative polarity for

0 – 3 bar gauge, in increments of 1 bar. Laue plots for the other experimental conditions are included in Appendix A for reference.

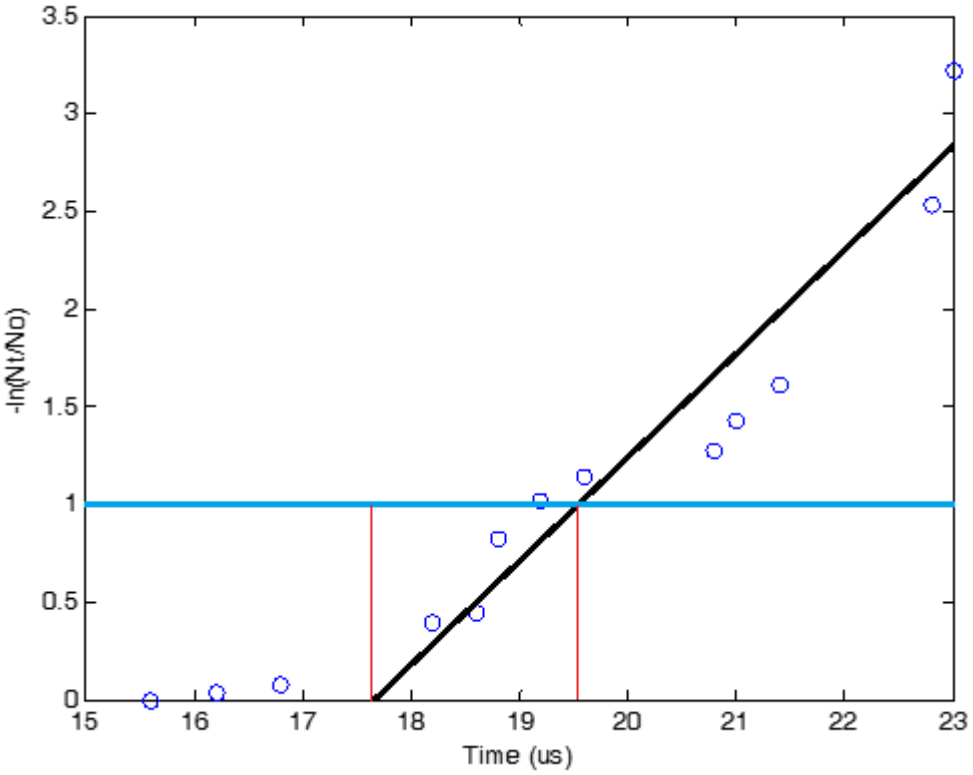

Figure 64 - Example of von Laue analysis for 5/3 mm positive polarity with a measured t_f of 17.6 µs and a t_{st} of 1.9 µs.

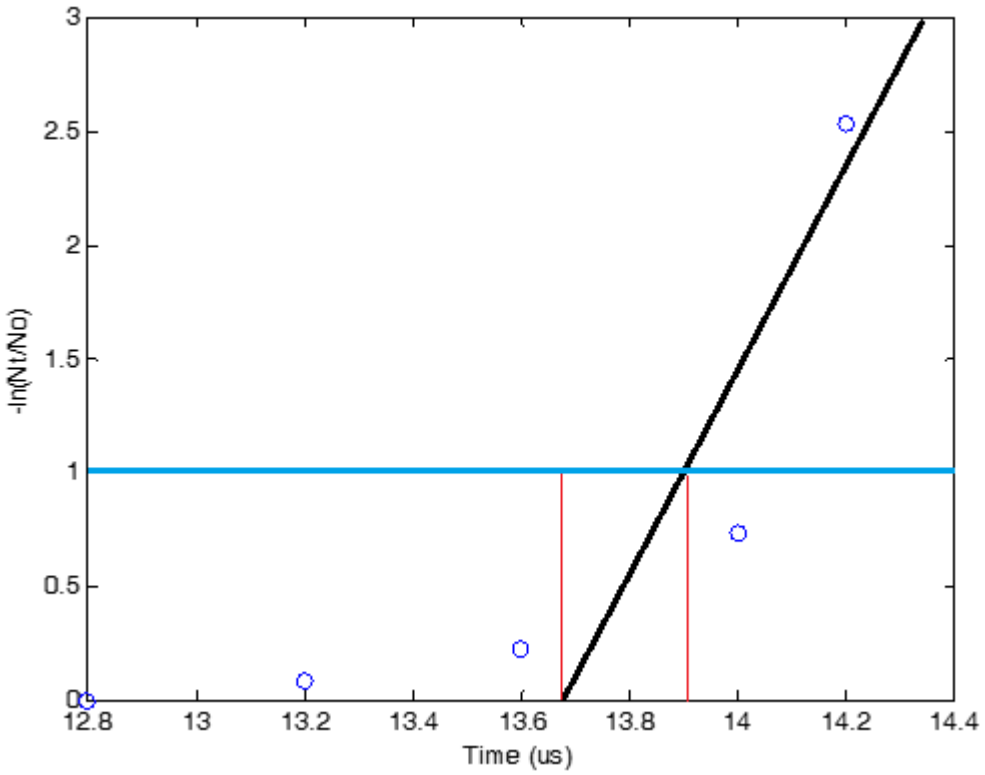

Figure 65 - Example of von Laue analysis for 5/3 mm negative polarity with a measured t_f of 13.7µs and a t_{st} of 0.3µs.

Table 5 - Statistical and Formative delay times in ambient air

Pressure	**Polarity**	**5mm/3mm**		**5mm/4mm**	
		t_f **(µs)**	t_s **(µs)**	t_f **(µs)**	t_s **(µs)**
0	Positive	17.7	1.8	21	1.4
	Negative	13.7	1.1	13.2	0.6
1	Positive	19	2.2	18	0.4
	Negative	27.1	1.4	18.6	0.9
2	Positive	23	2	15.7	1.7
	Negative	49.5	0.75	53.5	0.8
3	Positive	35.5	1.7	12	4
	Negative	71	1.1	76	1.5

In order to view trends, the data in Table 5 has been plotted in Figure 66 (formative times) and 67 (statistical times), where at each pressure iteration both geometries

(5/3mm and 5/4mm) of the 2 electrode geometries tested at both negative and positive polarity are shown.

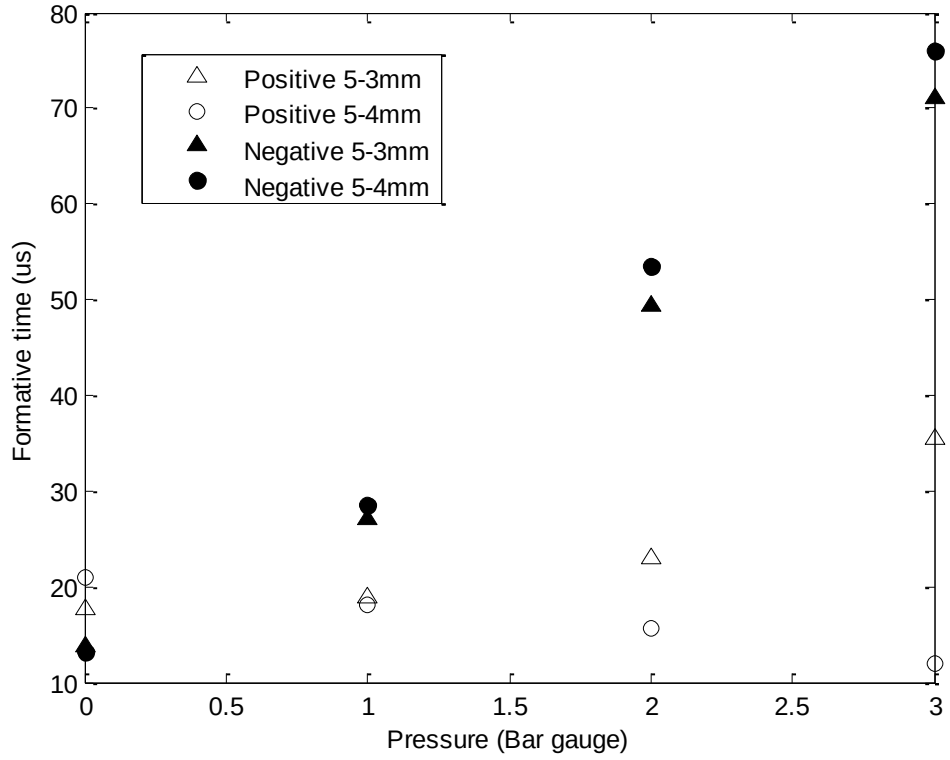

Figure 66 Formative times extracted from Laue plots

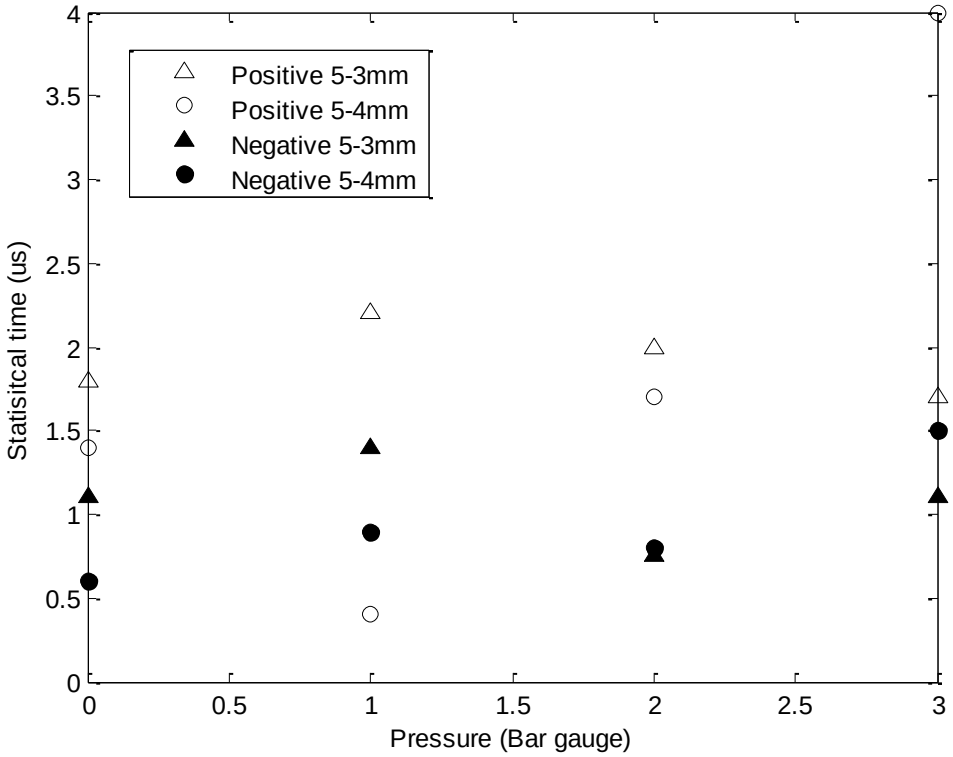

Figure 67 Statistical times extracted from Laue plots

The formative times in Figure 66 show the ultimate difference between negative and positive polarity results. It can be seen that the formative time for the negative polarity regime is much longer than that for positive polarity. This can be taken from the general propagation of positive and negative streamers where positive streamers are said to far exceed the velocity of negative streamers [79], implying that formative times are longer for negative polarity. Also, the triggering characteristics related to the negative polarity in terms of the distance from the triggering threshold are much closer compared to positive polarity. The formative times generally increase with pressure, the exception being for 5/4 mm with positive polarity, reflecting the erratic overall delay times (Figure 57) for these tests. In Figure 67, the statistical data is shown and compared to the formative time, but there is no clear trend for any of the polarity/geometry regimes.

6. CHAPTER VI

TESTING OF CSS IN ALTERNATIVE GAS MIXTURES

6.1. GENERAL

This chapter explains the characterisation of a CSS when filled with 4 different gases/gas mixtures, 3 of which involve novel gas HFO-1234ze. First of all, a characterisation with 100% N_2 was conducted for reference against the 3 mixtures involving HFO-1234ze. As discussed in section 2.7.2, as this gas is classified as 'mildly flammable' [47], the buffer gas N_2 was used as the predominant gas within the spark chamber. The 3 gas mixtures used in this chapter are shown below–

- 95% N_2/5% HFO-1234ze
- 90% N_2/10% HFO-1234ze
- 80% N_2/20% HFO-1234ze

The results of these tests made clear the differences in the switch characteristics, dependent upon the percentage of HFO-1234ze in the mixture. The switch was characterised by measuring 3 different parameters: self-breakdown voltage, trigger threshold voltage, and delay time. The tests were conducted at 0.5 bar intervals from 0 to 3 bar gauge.

6.2. CHARACTERISATION OF SWITCH PERFORMANCE IN 100% N_2 FOR 5/3 MM SWITCH GEOMETRY

6.2.1. Self-breakdown and triggering thresholds

The switch was set up for the preliminary tests to be completed on 100% N_2 in order to provide reference data to be compared against when tests on the different N_2/HFO-1234ze/ mixtures were conducted (section 6.3).

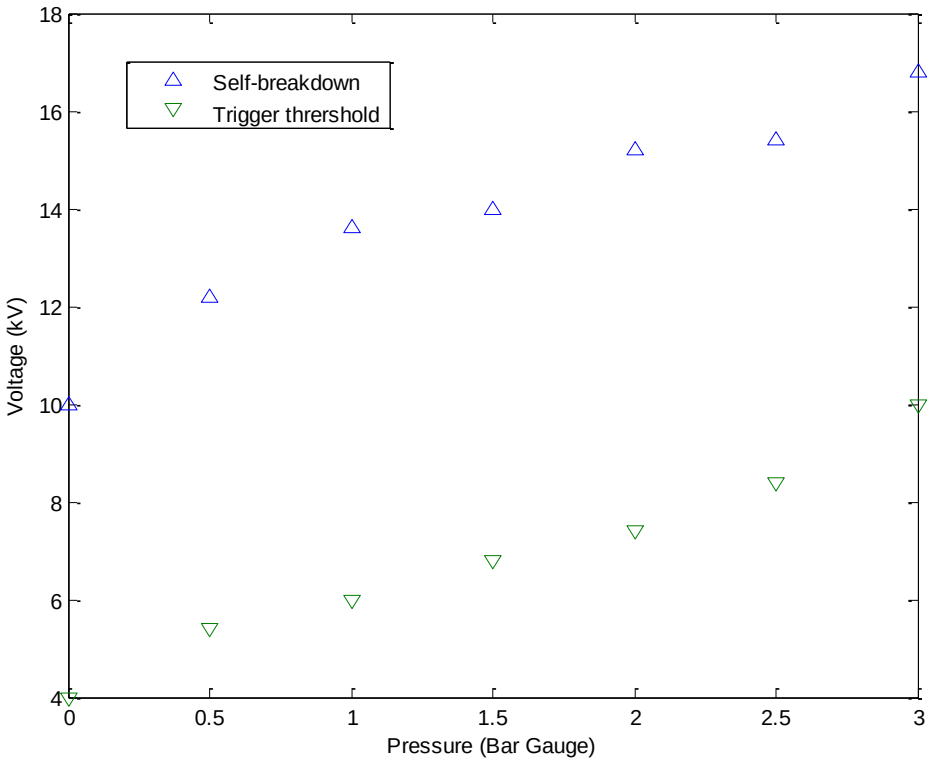

Figure 68 - Positive polarity self-breakdown and trigger threshold voltages from 0 to 3 bar gauge for 100% N_2

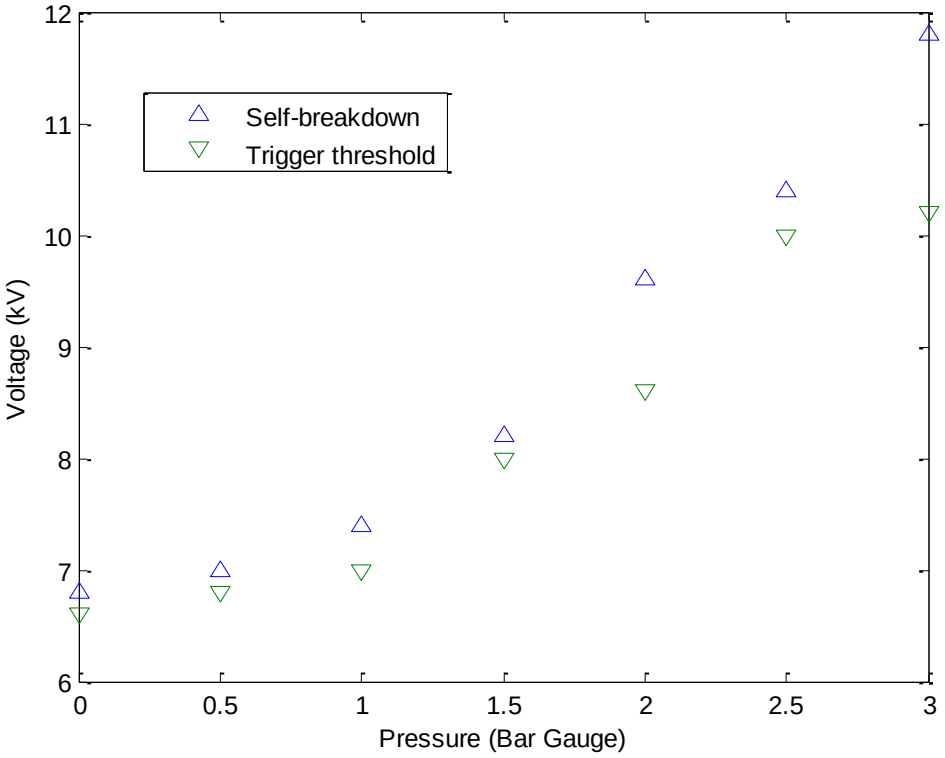

Figure 69 - Negative polarity self-breakdown and trigger threshold voltages from 0 to 3 bar gauge for 100% N_2

Shown in Figure 68 and 69 are the relationships between the self-breakdown voltages and the trigger threshold voltages for positive and negative polarity, respectively. The area between these 2 values is known as the 'triggering range', the range of voltages at each particular gas pressure where the switch is able to be operated reliably. In triggered switch design, a certain percentage of the switch self-breakdown voltage will be selected as the operating point. A wide triggering range is optimal, since the operating point needs to be far enough away from the self-breakdown level, preventing unwanted breakdown from occurring. Also, the operating point needs to be far enough away from the trigger threshold voltage that the switch closes reliably when triggered by the external impulse. In this case, the trigger impulse had peak magnitude of ±32 kV, depending upon the polarity of the applied HV; under positive applied DC voltage the applied trigger pulse would be negative, and vice-versa.

The widest triggering range for positive polarity (Figure 68) was 7.8 kV at 2 bar gauge, and the narrowest triggering range was measured at 6 kV at 0 bar gauge. For negative polarity, the triggering range was very narrow due to the electropositive nature of N_2; as can be seen in Figure 69, the maximum triggering range over the pressures tested was only 1.6 kV at 3 bar gauge. This is due to the electropositive characteristic of being able to donate electrons in the process. In terms of triggering range, the formative time makes up a much larger percentage of the overall delay time than the other gas mixtures.

6.2.2. Delay time

The delay times were measured at a suitable level of applied DC voltage, dependent upon the switch triggering range characteristics. The positive polarity regime was tested at 75% of the self-breakdown voltage, as this was a good mid-point between the self-breakdown and trigger threshold curves, therefore ensuring breakdown when the trigger pulse is applied as well as preventing unwanted closures. For the negative switching regime, however, as the triggering range was so narrow, it was necessary to apply 98% of the self-breakdown voltage. This value is extremely close to the self-breakdown and the trigger threshold voltage at most of the pressure intervals, so good switching performance was not expected; the testing was undertaken for completeness,

to facilitate comparison with the three gas mixtures containing the electronegative HFO-1234ze.

In Figure 70 and 71, the delay time and jitter characteristics can be seen for a particular self-breakdown percentage. Within the delay time graphs, blue diamonds show the

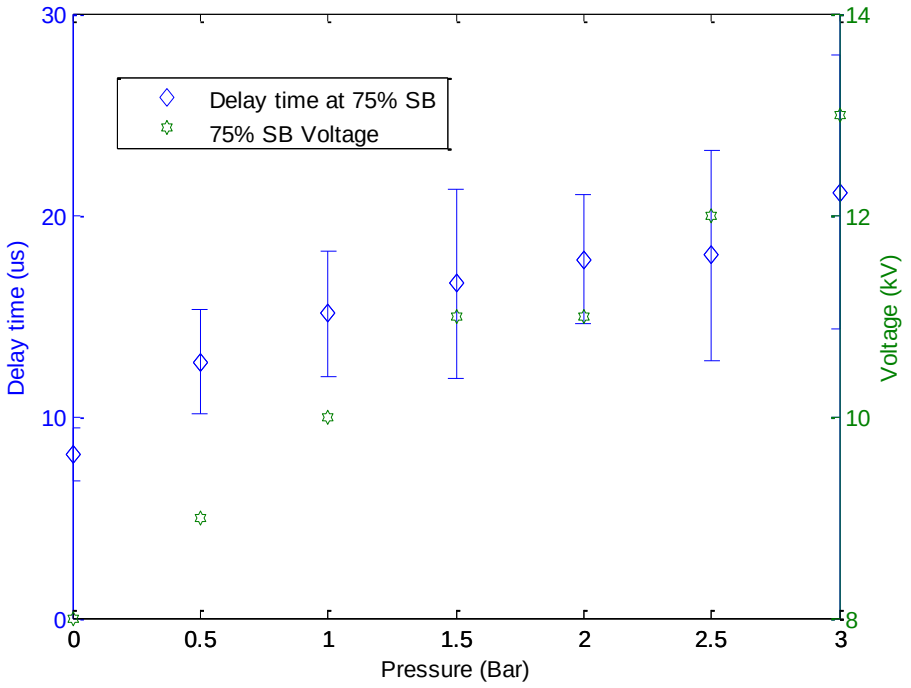

Figure 70 - Positive polarity delay times and jitter (error bars) at 75% of the self-breakdown voltage for 100% N_2

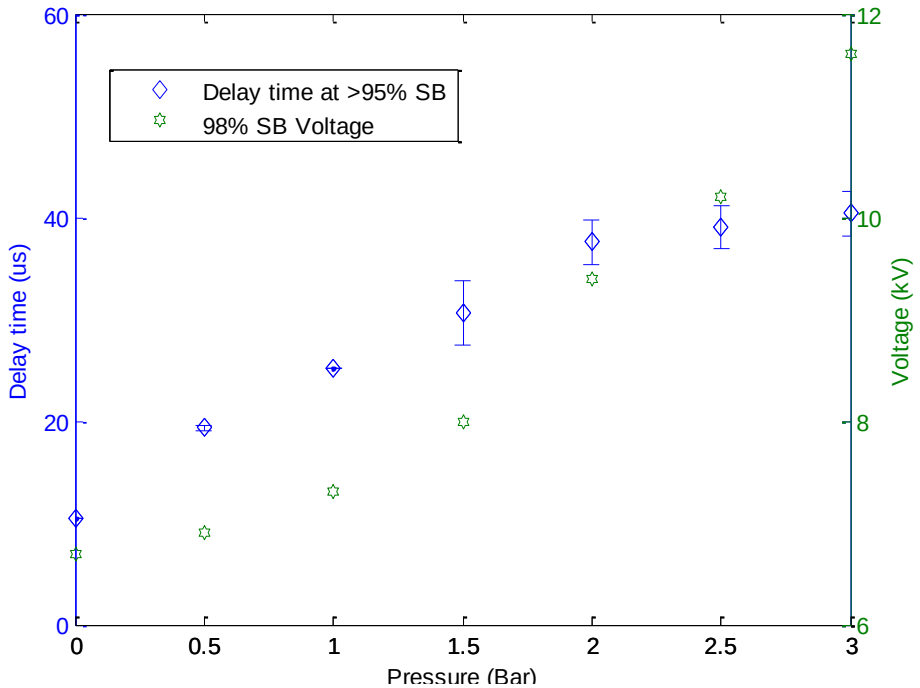

Figure 71 - Negative polarity delay times and jitter (error bars) at 98% of the self-breakdown voltage for 100% N_2

average (mean) delay time, and the green stars show the applied voltage level at each pressure iteration.

From Figure 70 and 71, the delay time characteristics can be seen for the percentage of self-breakdown value, with calculated jitter shown in the form of error bars. There were 25 delay time measurements conducted for each pressure iteration, used to calculate the average delay time and the jitter. The information on these figures shows that the applied voltage level increases with respect to pressure in both cases, corresponding to the increasing self-breakdown voltages in Figure 68 and 88. The average delay time for each polarity is shown to increase with pressure also. The maximum delay time for the positive polarity arrangement was 21.1±6.8 μs at 3 bar gauge, with a minimum delay time of 8.1±1.3 μs at 0 bar gauge. The maximum and minimum jitter (written as ± values) were found to occur at these two points also.

For the negative polarity arrangement, the maximum delay time was measured at 3 bar gauge, with a value of 40.4±2.2 μs, and the minimum delay time was at 0 bar gauge, with a value of 10.4±0 μs (i.e. for the time-base required to view the full waveforms, the delay time was the same for all 25 measurements). The jitter measurement varied throughout the negative testing, with effectively no jitter measured at 0 bar gauge, and a maximum jitter of 3.1 μs at 1 bar gauge. Although the delay time was consistent at 0 bar gauge, this is only due to the applied voltage position being so close to the self-breakdown voltage, meaning that this switching arrangement is not acceptable.

6.3. CHARACTERISATION OF SWITCH PERFORMANCE IN NOVEL HFO-1234ZE/N_2 MIXTURES FOR 5/3 MM SWITCH GEOMETRY

A comparison between 100% N_2 and the 3 gas mixtures containing HFO-1234ze is conducted in this section. Firstly, the self-breakdown and triggering threshold voltages were measured, in order to determine the triggering range at each individual pressure interval. The 100% N_2 data in Figure 68 and 69 are included in the following graphs for ease of comparison.

6.3.1. Self-breakdown and triggering threshold voltages

The same process used in section 6.2 was repeated for the self-breakdown and triggering threshold values to be measured in the gas mixtures. This data can be seen for both positive and negative polarity in Figure 72 and 73, respectively, for 100% N_2; 95% N_2 / 5% HFO-1234ze; 90% N_2 / 10% HFO-1234ze; and 80% N_2 / 20% HFO-1234ze.

Figure 72 shows the self-breakdown and trigger threshold voltage levels for 100% N_2, and for the 3 HFO-1234ze/N_2 gas mixtures from 0-3 bar gauge, for positive applied DC stress.

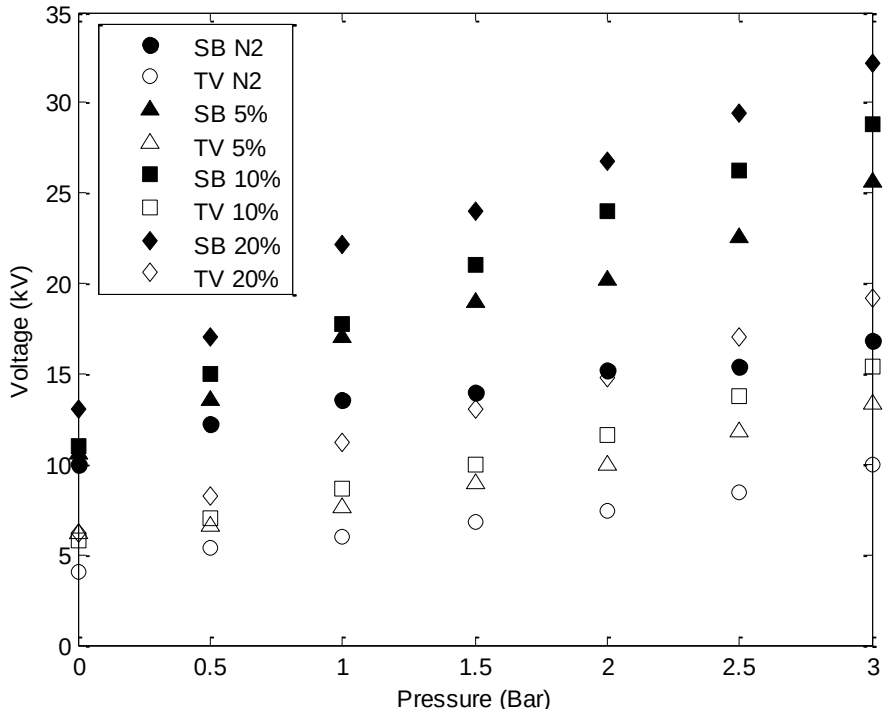

Figure 72 - Positive polarity self-breakdown and trigger threshold voltages for 0-3 bar gauge for 100% N_2; 95% N_2 / 5% HFO-1234ze; 90% N_2 / 10% HFO-1234ze; and 80% N_2 / 20% HFO-1234ze

Figure 73 shows the self-breakdown and trigger threshold voltage levels for N_2 and the 3 HFO-1234ze/N_2 gas mixtures from 0-3 bar gauge, for negative applied DC stress.

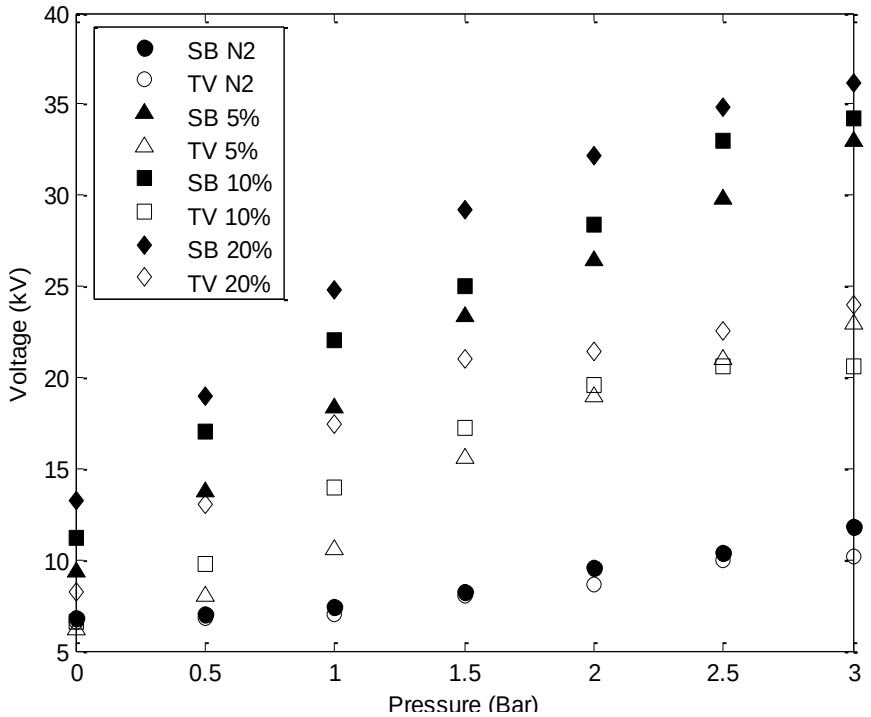

Figure 73 - Negative polarity self-breakdown and trigger threshold voltages for 0-3 bar gauge for 100% N_2; 95% N_2 / 5% HFO-1234ze; 90% N_2 / 10% HFO-1234ze; and 80% N_2 / 20% HFO-1234ze

In Figure 72, the distribution of the self-breakdown and trigger threshold voltages is shown over the pressure range 0-3 bar gauge. The circles represent the self-breakdown and trigger threshold voltages shown in Figure 68. The other plots are the 3 different mixtures tested, which can be deciphered by the legend on the plot. Firstly, the increase in self-breakdown voltage is clear where, as the percentage of HFO-1234ze increases, the self-breakdown voltage increases also.

For 95% N_2 / 5% HFO-1234ze, the maximum increase in self-breakdown voltage was found at 3 bar gauge, with an increase of ~152% compared to 100% N_2; the minimum increase in self-breakdown voltage was measured at 0 bar gauge, with an increase of ~106%. The maximum triggering range that was measured over the pressures was at 3 bar gauge with a value of 12.2 kV, and the minimum triggering range was at 0 bar with a value of 4.4 kV. For 90% N_2 / 10% HFO-1234ze, the maximum increase in self-breakdown voltage was measured at 3 bar gauge, at a value of~171% of the self-breakdown voltage of N_2; the minimum increase was measured at 0 bar gauge at a value of~110%. The triggering ranges of this mixture were measured with the maximum found at 13.4 kV at 3 bar gauge, and a minimum of 5.2 kV at 0 bar gauge.

Lastly, the 80% N_2 / 20% HFO-1234ze mixture showed a maximum self-breakdown voltage increase of ~ 191% of that of N_2; the minimum increase was found at 0 bar gauge with an increase of ~ 130%. The triggering range peaked at 3 bar gauge with a value of 13 kV, and the minimum triggering range was 6.8 kV at 0 bar gauge.

Viewing the positive polarity data as a whole, it is clear to see a trend of increasing breakdown voltages is forming as the pressure is increased, and as the percentage of HFO-1234ze in the gas mixture increases. At lower pressures, however, the triggering range of N_2 is still wider than that of the 5% and 10% HFO-1234ze mixtures, which shows that the switch has to be pressurised to a certain level before the real operational advantages become apparent.

Table 6 – Positive polarity trigger range in relation to percentage of self-breakdown (SB) voltage applied

Gas mixture	Minimum trig. range (% of SB)	Maximum trig. range (% of SB)
95% N_2 / 5% HFO-1234ze	58.4	44.7
90% N_2 / 10% HFO-1234ze	53.4	46.6
80% N_2 / 20% HFO-1234ze	59.6	47.7

In the case for negative polarity in Figure 68, for 95% N_2 / 5% HFO-1234ze, the maximum increase in self-breakdown voltage is shown at 3 bar gauge with an increase of ~ 279% compared to that for 100% N_2; the minimum increase in self-breakdown voltage was measured at 0 bar gauge, with an increase of ~ 138%. The maximum triggering range that was measured over the tested pressures was at 3 bar gauge with a value of 10 kV, and the minimum triggering range was at 0 bar with a value of 3.2 kV. For 90% N_2 / 10% HFO-1234ze, the maximum increase in self-breakdown voltage was measured at 3 bar gauge, at a value of ~ 289% of the self-breakdown voltage of N_2; the minimum increase was measured at 0 bar gauge, at a value of ~ 164%. The triggering ranges for this mixture were measured with the maximum found at 13.6 kV at 3 bar gauge, and a minimum of 4.6 kV at 0 bar gauge. Lastly, the 80% N_2 / 20% HFO-1234ze mixture showed a maximum self-breakdown voltage increase of ~ 306% relative to that of N_2 at 3 bar gauge; the minimum increase was found at 0 bar gauge, with an increase of ~ 194%. The triggering range peaked at 3 bar gauge with a value of 12.2 kV, and a minimum triggering range of 5 kV at 0 bar gauge.

Viewing the negative polarity data as a whole, a trend of increasing breakdown voltages is clear to see as the pressure is increased, and as the percentage of HFO-1234ze in the gas mixture increases. It is clear that the breakdown strengths for all gas mixtures containing HFO-1234ze are much greater than the corresponding breakdown strengths of 100% N_2.

The triggering range is increased greatly over the course of the HFO-1234ze tests. The addition of this electronegative gas counteracts the poor performance of the electropositive 100% N_2. Although the triggering ranges compared to those for positive polarity are not as wide, they are wide enough that a suitable operating point can be selected for stable and reliable triggered operation.

Table 7 - Negative polarity trigger range in relation to percentage of self-breakdown (SB) voltage applied

Gas mixture	Minimum trig. range (% of SB)	Maximum trig. range (% of SB)
95% N_2 / 5% HFO-1234ze	71.9	57.6
90% N_2 10% / HFO-1234ze	69	57.6
80% N_2 20% / HFO-1234ze	71.9	62.1

Tables 6 and 7 show the triggering ranges in terms of percentage of the self-breakdown voltage level; these values correspond to the lowest and highest voltage where the switch can be considered as operational. Anything above the minimum triggering range can be seen as a viable voltage level to be in operation. Although, a clear distance from the triggering threshold is desirable as the switch will have a lower probability of closing closer to the triggering threshold. The highest value is 71.9% of the self-breakdown voltage; hence the chosen value of 75% of self-breakdown voltage for all tests, for direct comparison.

6.3.2. Delay time

As measured in section 6.2.2, the delay time measurements are illustrated here, again with intervals of 0.5 bar from 0-3 bar gauge. Each delay time data point consists of the average of 25 delay time measurements. For the three HFO-1234ze gas mixtures overall, the minimum triggering range was 59.4% of the self-breakdown voltage for

positive polarity, and the minimum triggering range was 71.9% of the self-breakdown voltage for negative polarity, as can be seen in Tables 6 and 7, respectively. The delay time measurements and the corresponding jitter calculations were, therefore, all taken at an applied voltage of 75% of the self-breakdown voltage at each individual pressure interval from 0-3 bar gauge. Thus, all tests will result in switch closure when the triggering impulse is delivered, and unwanted breakdown (due to the operating point being too close to the self-breakdown voltage) can be avoided.

6.3.2.1. Positive applied polarity

This section includes the average delay time and jitter values as well as the value of positive polarity DC stress level used for each pressure interval from 0-3 bar gauge.

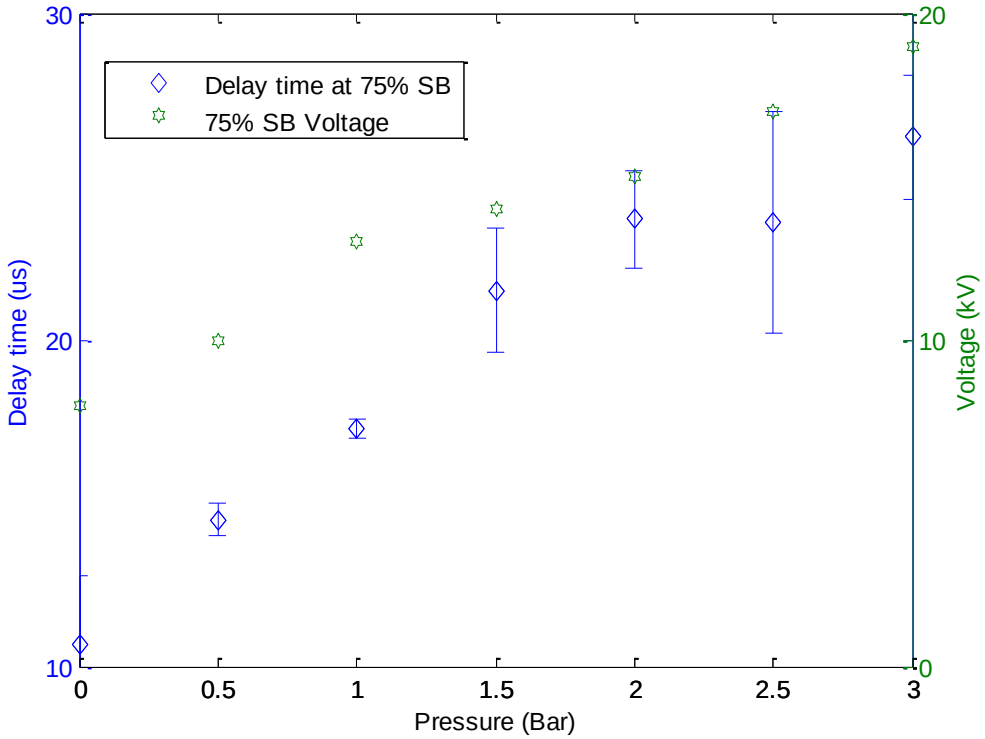

Figure 74 - Positive polarity average (mean) delay times calculated from 25 delay times and jitter at 75% of the self-breakdown voltage for 95% N_2 / 5% HFO-1234ze

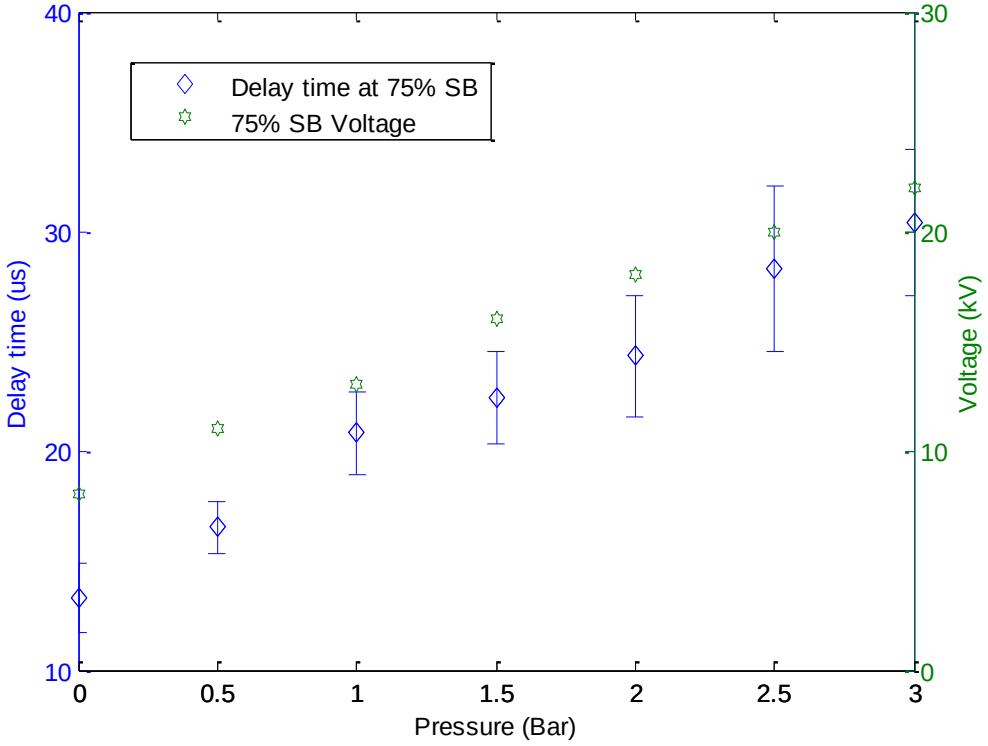

Figure 75 - Positive polarity average (mean) delay times calculated from 25 delay times and jitter at 75% of the self-breakdown voltage for 90% N_2 / 10% HFO-1234ze

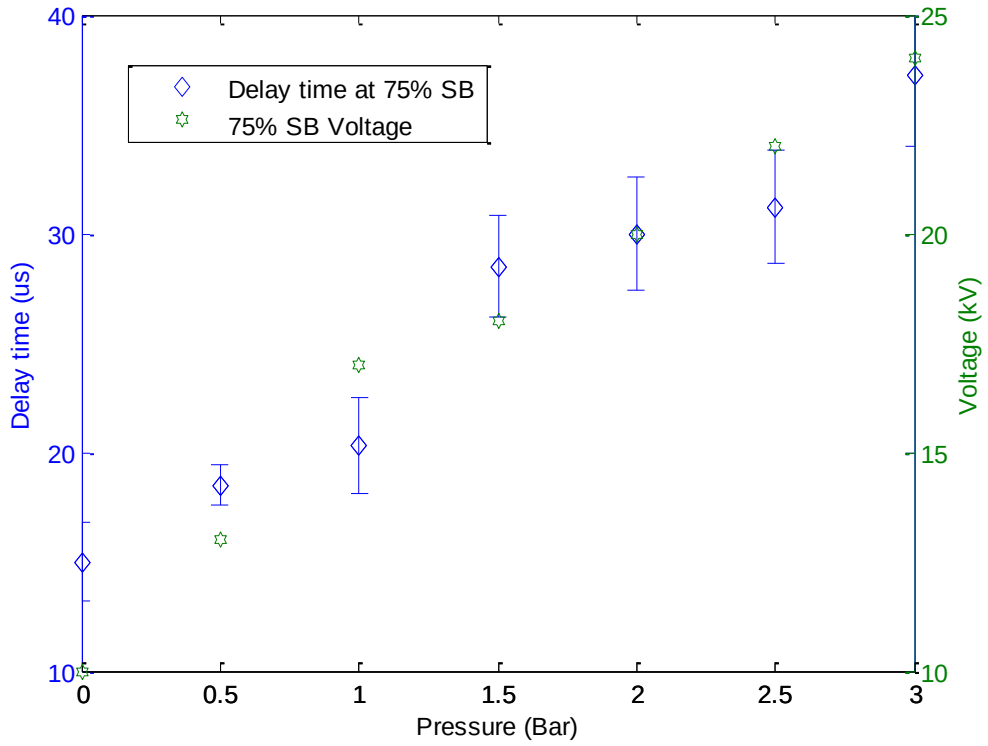

Figure 76 - Positive polarity average (mean) delay times calculated from 25 delay times and jitter at 75% of the self-breakdown voltage for 80% N_2 / 20% HFO-1234ze

Figure 69, 70 and 71 show the average delay times from 25 measurements and the calculated jitter, as well as the applied voltage, at each tested pressure. What can be seen from Figure 74 is an increase in average delay time with increasing pressure. As well as this, the calculated jitter increases with respect to pressure also. The same trend is apparent in Figure 75 and 76. As the percentage of HFO-1234ze in the gas mixture increases, so too does the overall delay time to breakdown of the switch. The maximum and minimum delay times and calculated jitters are shown in Table 8.

Table 8 – Positive polarity maximum and minimum delay time (DT) and jitter data for the three HFO-1234ze mixtures

Gas mixture	**Max. DT (µs)**	**Min. DT (µs)**	**Max. Jitter (µs)**	**Min. Jitter (µs)**
95% N_2 5% / HFO-1234ze	26.2	10.7	3.4	0.3
90% N_2 10% / HFO-1234ze	30.4	13.3	3.8	1.2
80% N_2 20% / HFO-1234ze	37.2	15	3.2	0.9

From Table 8, there is a direct correlation between the percentage of HFO-1234ze in the gas mixture and the average delay time. As an electronegative gas is being mixed to the electropositive N_2, this is having an effect on delay time to breakdown as the addition of a higher percentage of electronegative gas results in a shorter mean electron travel distance due to electron attachment increasing the amount of collisions needed before a breakdown occurs. Thus, a larger delay time is experienced.

When compared to the 100% N_2 delay time and jitter data in Figure 70, there is an increase in both average delay time and the calculated jitter. Therefore, for positive polarity, the addition of HFO-1234ze creates a much higher breakdown strength - with value of up to ~ 191% of the self-breakdown voltage in 100% N_2 - but the time to breakdown is compromised, in that the maximum achievable pulse repetition rate will be reduced as the delay time to switch closure increases.

6.3.2.2. Negative applied polarity

This section includes the delay time and jitter values as well as the value of negative polarity DC stress level used for each pressure interval from 0-3 bar gauge.

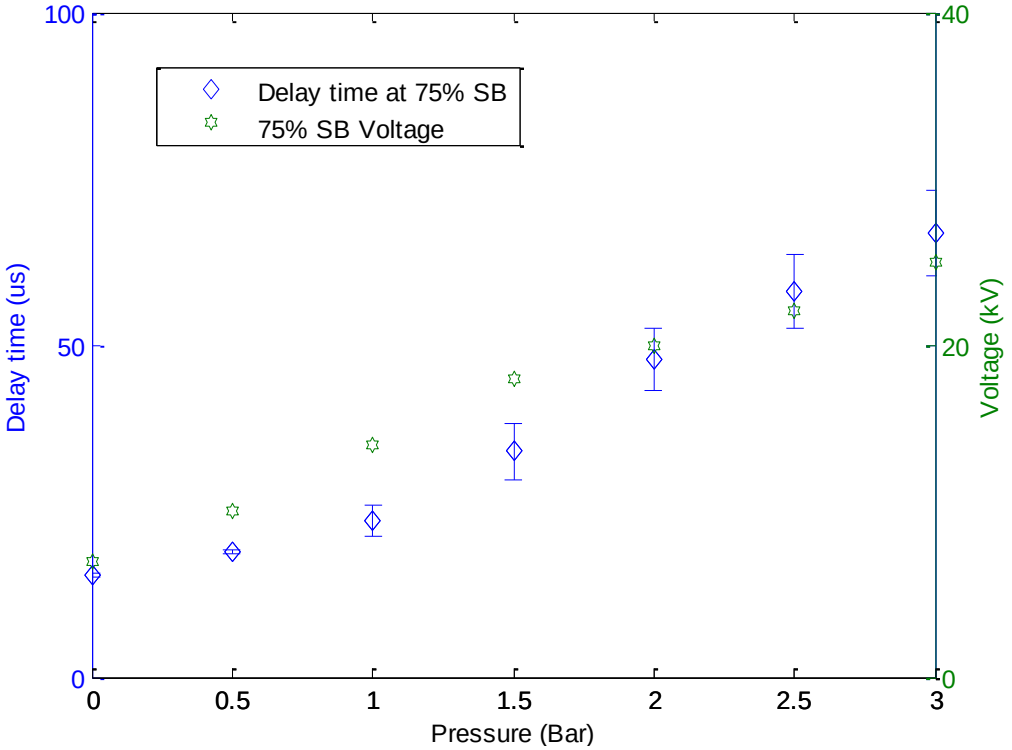

Figure 77 - Negative polarity average (mean) delay times calculated from 25 delay times and jitter at 75% of the self-breakdown voltage for 95% N_2 / 5% HFO-1234ze

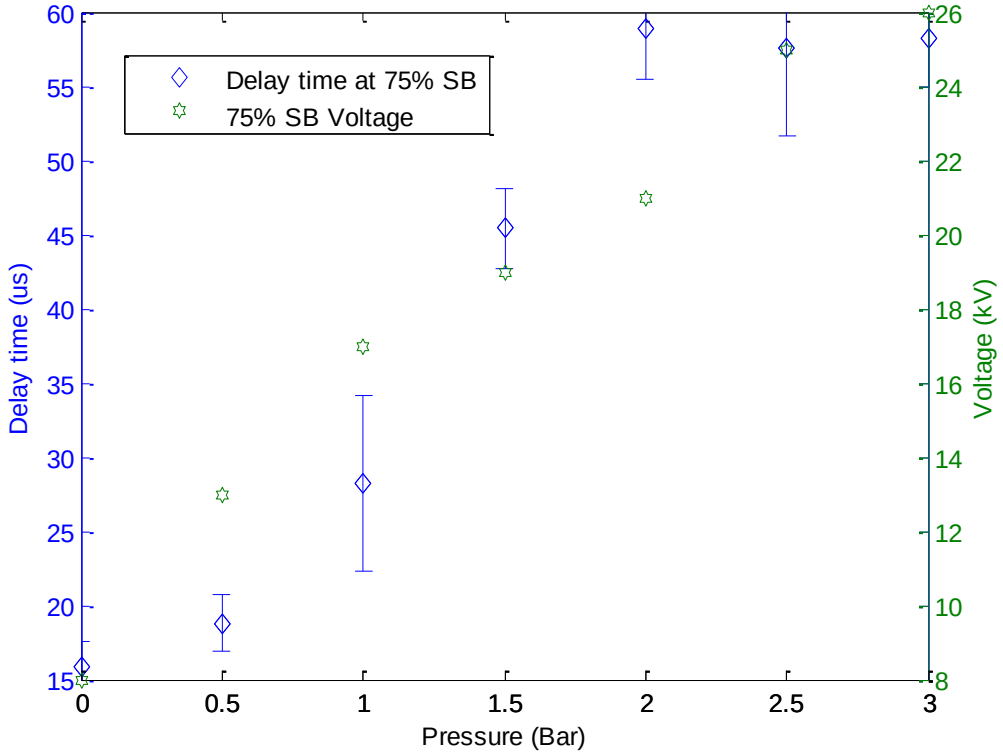

Figure 78 - Negative polarity average (mean) delay times calculated from 25 delay times and jitter at 75% of the self-breakdown voltage for 90% N_2 / 10% HFO-1234ze

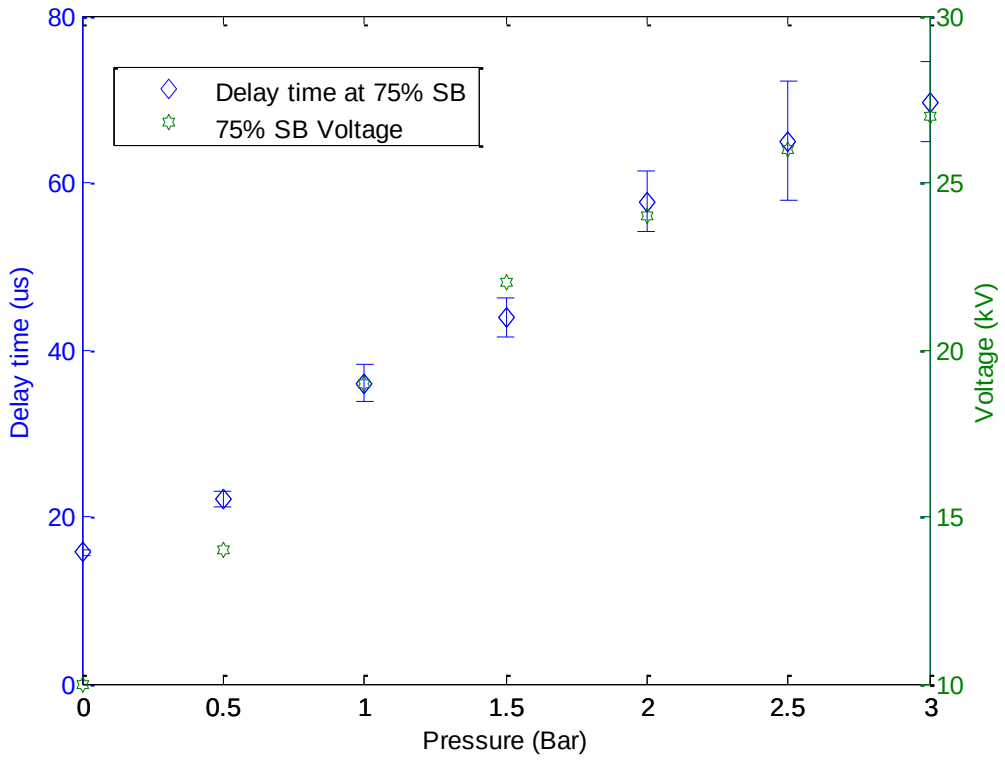

Figure 79 - Negative polarity average (mean) delay times calculated from 25 delay times and jitter at 75% of the self-breakdown voltage for 80% N_2 / 20% HFO-1234ze

What can be seen from Figure 77, 78 and 79 is the delay time and jitter characteristics for the negative polarity tests for the three gas mixtures. Each point within the 0-3 bar gauge scale was taken at 75% of the self-breakdown voltage at that particular point, as shown by the green data points in each of the figure. The delay time at this particular voltage is shown in blue with the standard deviation calculated to show jitter using error bars. What can be seen from these three figures is again a correlation between delay time and pressure for each gas mixture: as the pressure increases, the average delay time also increases. In terms of jitter, it is fairly conclusive that the jitter follows the same pattern (increasing with pressure), especially in Figure 77 and 78. Although there are changes in the delay time statistics for the three different gas mixtures, there is no clear correlation between delay time and percentage of HFO-1234ze for negative polarity. This can be seen in more detail in Table 9, where the maximum and minimum delay times and jitters have been stated.

Table 9 - Negative polarity maximum and minimum delay time (DT) and jitter data for the three HFO-1234ze mixtures

Gas mixture	Max. DT (µs)	Min. DT (µs)	Max. Jitter (µs)	Min. Jitter (µs)
95% N_2 / 5% HFO-1234ze	66.8	15.3	6.4	0.2
90% N_2 / 10% HFO-1234ze	58.2	15.9	5.9	1.7
80% N_2 / 20% HFO-1234ze	69.7	15.7	7.2	0.4

In comparison to Table 8, there is no clear trend in Table 9, for example, the average delay time does not show an obvious increasing trend with percentage of HFO-1234ze. Comparison with Figure 71 (100% N_2) shows a great increase in average delay time when HFO-1234ze is included. Although, it must be noted that the results in Table 9 were gathered at 75% of the self-breakdown voltage at each pressure, where the 100% N_2 values had to be measured at 98% of the self-breakdown voltage, due to the narrow triggering range, so the switch would not close at 75% of the self-breakdown voltage level for 100% N_2. Therefore, the switch characteristics for negative polarity can be seen as a great improvement upon those for 100% N_2.

6.4. CONCLUSIONS

The high dielectric strength of SF_6 and HFO-1234ze is governed by the electronegativity of each of these gases, that is, their ability to attach free electrons. It has been found previously that the dielectric strength of HFO-1234ze is (0.8-0.95) times that of SF_6 [53]. Being fluorinated, HFO-1234ze is known to be a highly electronegative gas [8]; when free electrons attach to neutral gas molecules, they are converted to heavy, low-mobility negative ions. These negative ions do not have the same capability as free electrons to cause further ionization [65], [66]. Therefore, higher voltages must be applied to provide more free electrons before breakdown can occur. The buffer gas used here, N_2, is an electropositive gas. With the addition of relatively low proportions (5%-20% here) of the electronegative HFO-1234ze, however, the breakdown voltage can be significantly increased, for both polarities. The effective ionisation coefficient of HFO-1234ze decreases with increasing pressure [36], reducing the probability of a free electron becoming available to initiate

breakdown [66]. Therefore, increased breakdown strength is observed as the pressure increases.

The overall probability of a breakdown-initiating event is related to $1/t_{st}$, and is dependent upon two probabilities: the probability of an initiatory electron appearing in the gap; and the probability of this electron successfully initiating a breakdown [66]. This second probability is proportional to the ionisation coefficient, leading to an increase in statistical time with pressure.

Overall, considering the switching performance exhibited by HFO-1234ze in this work, particularly the breakdown strength, it can be seen that there is a possibility of this gas becoming an alternative to SF_6. Although, due to the practical observations detailed in section 6.5, the problem of carbon build-up needs to be further investigated and resolved before this gas can be considered an alternative to SF_6 for switching applications, especially when operating into the kHz regime. Further work to be conducted is characterisation of the switch under repetitive conditions, with shorter (ns) trigger pulses, and detailed comparison with previous data for operation in SF_6 [25], [27], [35], [64], [67], [68].

6.5. POST-TESTING OBSERVATIONS

After testing was completed, the switch was opened for inspection, and some potential issues were found, as shown in Figure 80 and 81. The HV, trigger and ground electrodes were all covered in carbon residue. This is a potential problem, as this residue could adversely affect the operation of the switch after a sufficient amount has formed. The chance of surface flashover and ultimate failure of the switch is also very high because of this carbon coating. This discovery then limits the possibility for HFO-1234ze to be used as a switching medium, especially when used at PRFs extending into the kHz regime [55]. This was also seen to have been a problem when testing in [53] within GIS also.

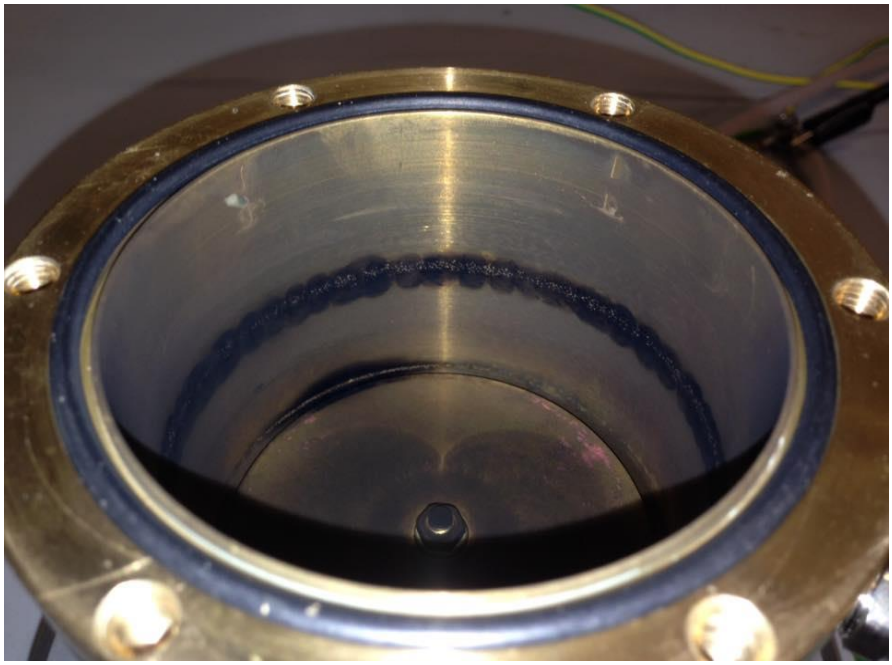

Figure 80 - Carbon residue build-up on trigger electrode (main body)

Figure 81 - carbon residue build-up on HV electrode

7. CHAPTER VII

TREND AND VON LAUE STATISTICAL ANALYSIS OF DELAY TIME DATA

Detailed in this chapter are the results of von Laue statistical analyses which are linked with the testing of the HFO-1234ze/N_2 novel gas mixtures to further understand the breakdown process in terms of formative and statistical time, which have been defined in section 2.11. Firstly, the delay time will be analysed in terms of breakdown number to monitor if any visual differences are appearing over the duration of a test (clear increase or decrease in delay time measurement with increasing breakdown number). This could indicate a problem with the switch or the gas properties changing over the testing regime. This will then be followed by the von Laue analysis.

7.1. DELAY TIME IN CONJUNCTION WITH BREAKDOWN NUMBER

This section presents the delay time to breakdown versus breakdown number at four different pressures for the gas/gas mixture specified within the sub heading.

During this part of the analysis, some of the data taken for specific polarities and gases/gas mixtures show a flat response, this meaning that the delay time did not change significantly over the course of the 25 measurements. The accuracy of the delay time was down to 200 ns throughout the testing of each mixture. If the accuracy was increased, there would be fluctuations within these flat responses, although the statistical variation in the delay times for some of the test conditions meant that the accuracy had to be restricted to 200 ns, since longer time-bases were required to ensure that the pertinent parts of the waveforms were always captured for all breakdown events. For consistency, the accuracy was therefore kept at 200 ns for all tests. The effect of this can be seen in Figure 83 and 85, where the delay time is consistent at lower pressures. As the pressure increases, then variations in the delay time are apparent.

These graphs have been included to show that, during the experimental process, the conditions have remained constant, and there is no increasing or decreasing trend in the delay times over the course of testing.

7.1.1. 100% N_2 Analysis

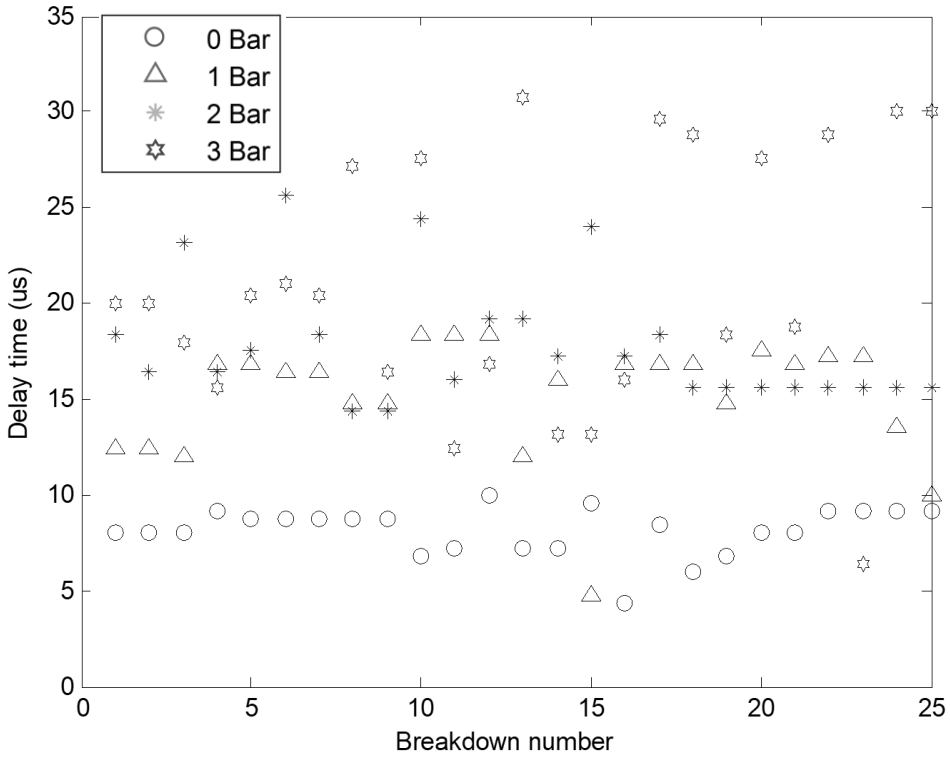

Figure 82 - Positive polarity delay time measurements in relation to breakdown number for 100% N_2

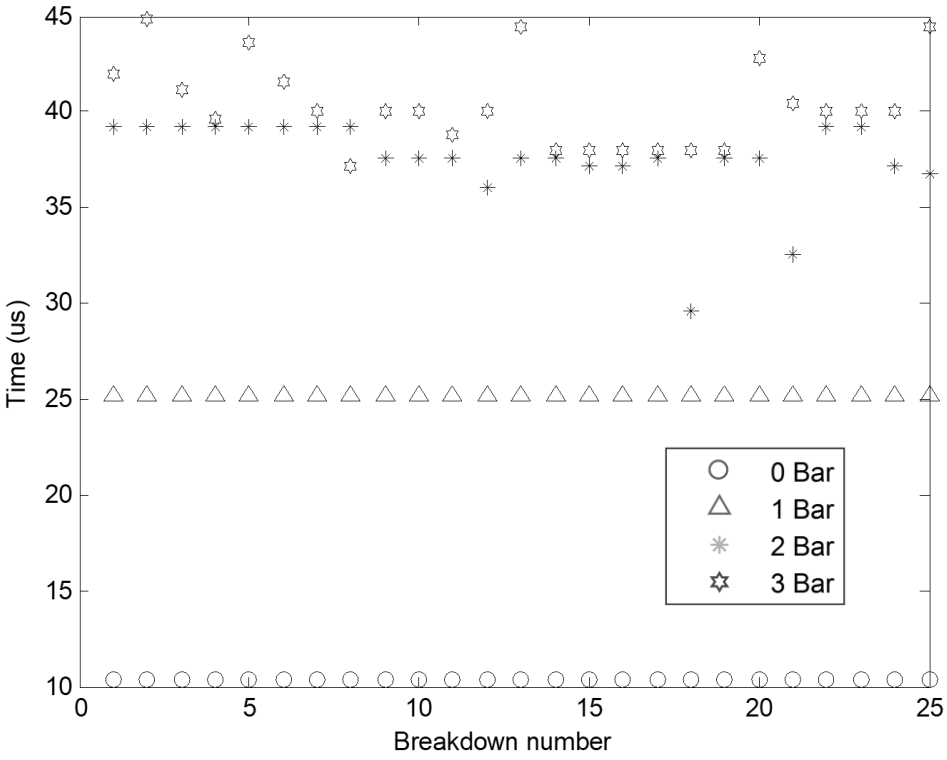

Figure 83 - Negative polarity delay time measurements in relation to breakdown number for 100% N_2

It can be seen that for tests with 100% N_2, there is a clear difference between the positive (Figure 82) and negative (Figure 83) plots. As the gas pressure increases, the delay times are generally seen to increase. Also, the negative polarity delay times are seen to be of longer duration compared to those for positive polarity. This can also be seen in section 6.3.2. As seen at 0 and 1 bar for negative polarity, the delay time was constant throughout the 25 breakdowns, with the aforementioned accuracy of 200 ns. Therefore, in the subsequent von Laue analysis, this results in a negligible statistical time; the effect of this can be seen in Appendix A, Figure a.29, where only one data point is visible. It is seen that there is no clear increasing or decreasing trend in delay times for each of the pressures.

7.1.2. 95% N_2 / 5% HFO-1234ze Analysis

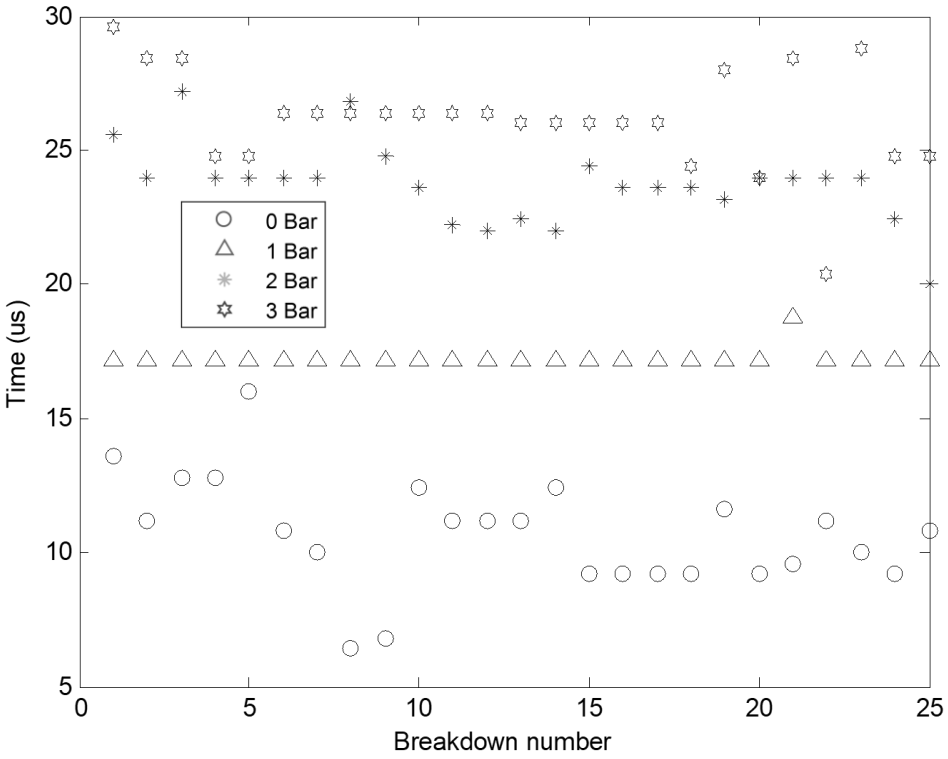

Figure 84 - Positive polarity delay time measurements in relation to breakdown number for 95% N_2 / 5% HFO-1234ze

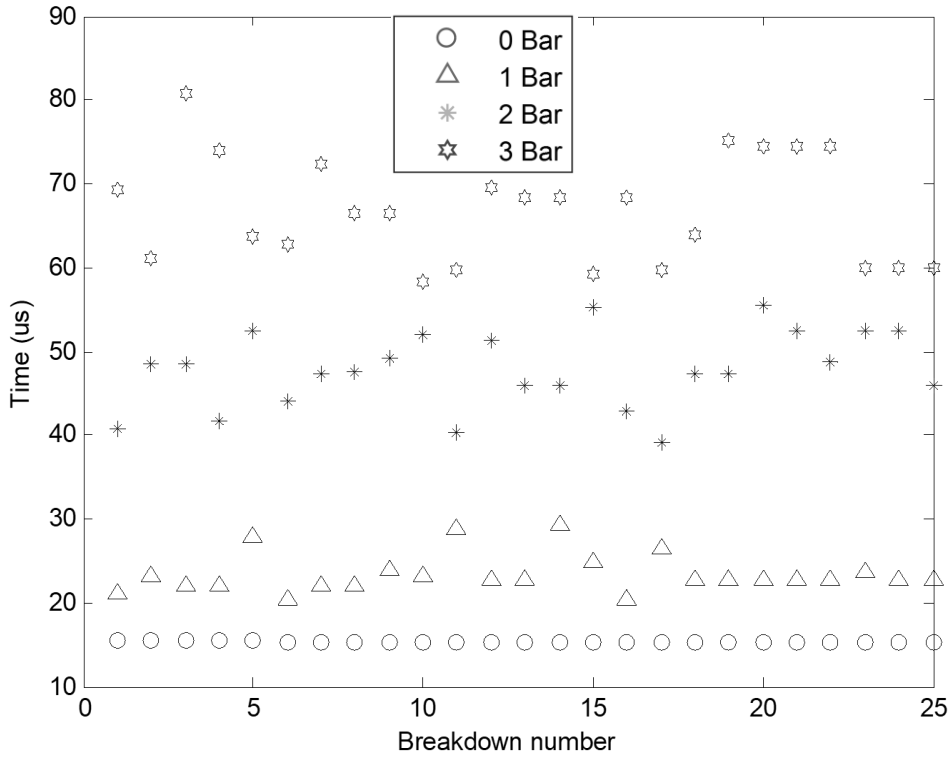

Figure 85 - Negative polarity delay time measurements in relation to breakdown number for 95% N_2 / 5% HFO-1234ze

Plotted in Figure 84 and 85 are the variations in delay time with breakdown number for 95% N_2 / 5% HFO-1234ze for positive and negative polarity, respectively. A clear increase in delay time with increasing pressure can be seen, as reflected in the average delay times discussed in section 6.3.2. Again, it can be seen that, at each of the pressures for both negative and positive polarity, there is no clear increasing or decreasing trend in the delay time.

7.1.3. 90% N_2 / 10% HFO-1234ze Analysis

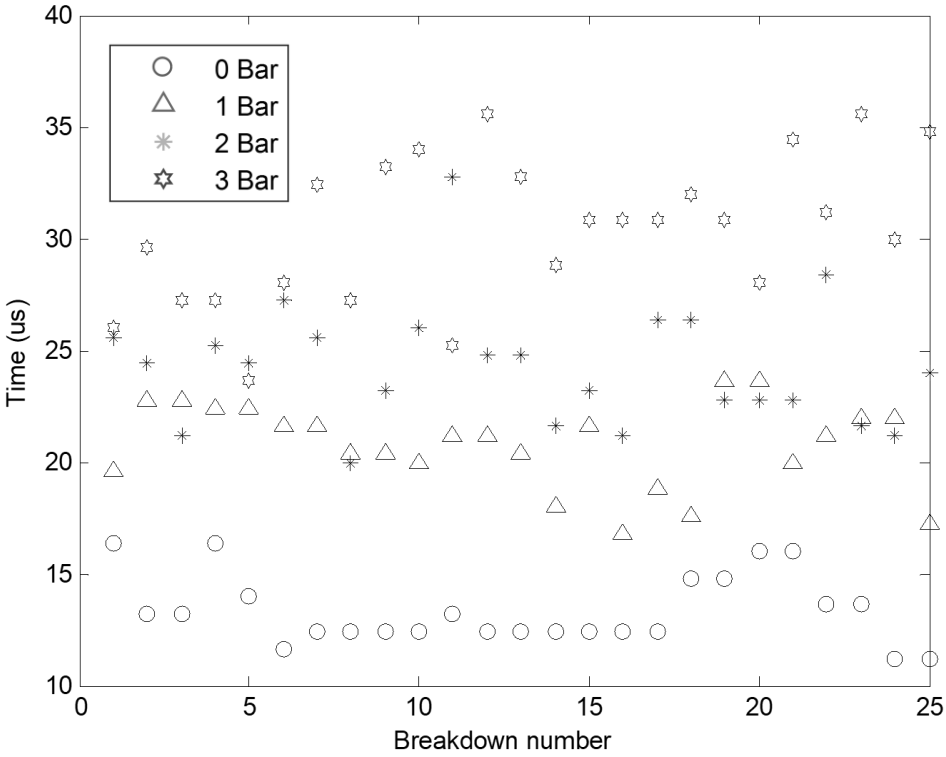

Figure 86 - Positive polarity delay time measurements in relation to breakdown number for 90% N_2 / 10% HFO-1234ze

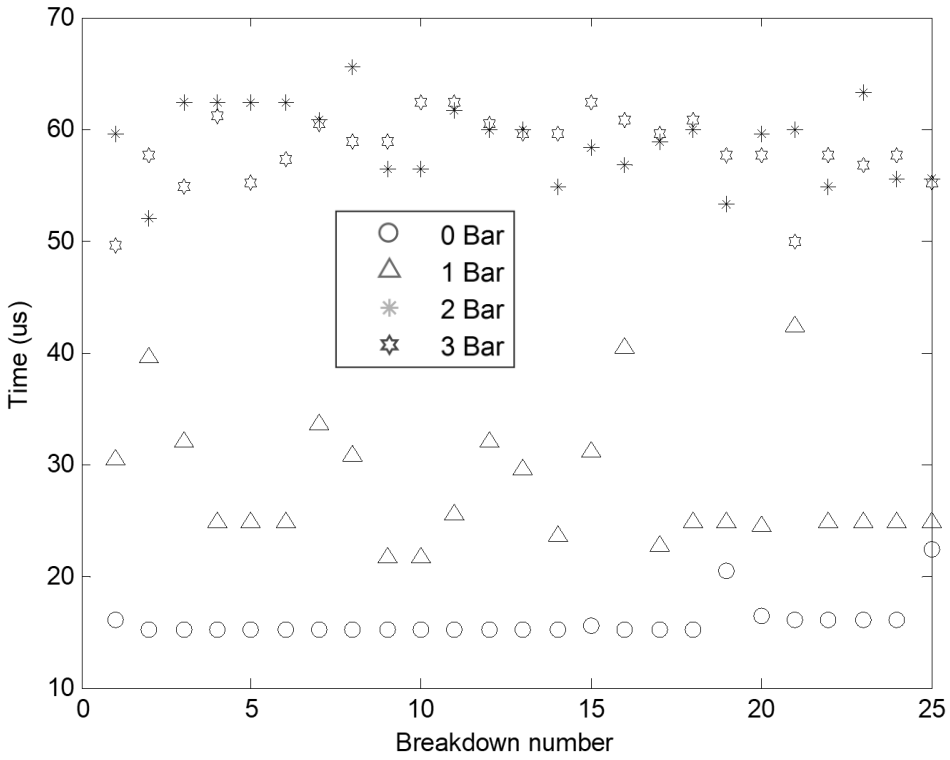

Figure 87 - Negative polarity delay time measurements in relation to breakdown number for 90% N_2 / 10% HFO-1234ze

In Figure 86 and 87, the delay time with respect to breakdown number analysis is shown for both positive and negative polarity, respectively, for 90% N_2 / 10% HFO-1234ze. Through the delay time analysis, it can be seen that as the pressure increases, the delay times also increase. Again, there is no clear increasing or decreasing trend during the testing operation.

7.1.4. 80% N_2 / 20% HFO-1234ze Analysis

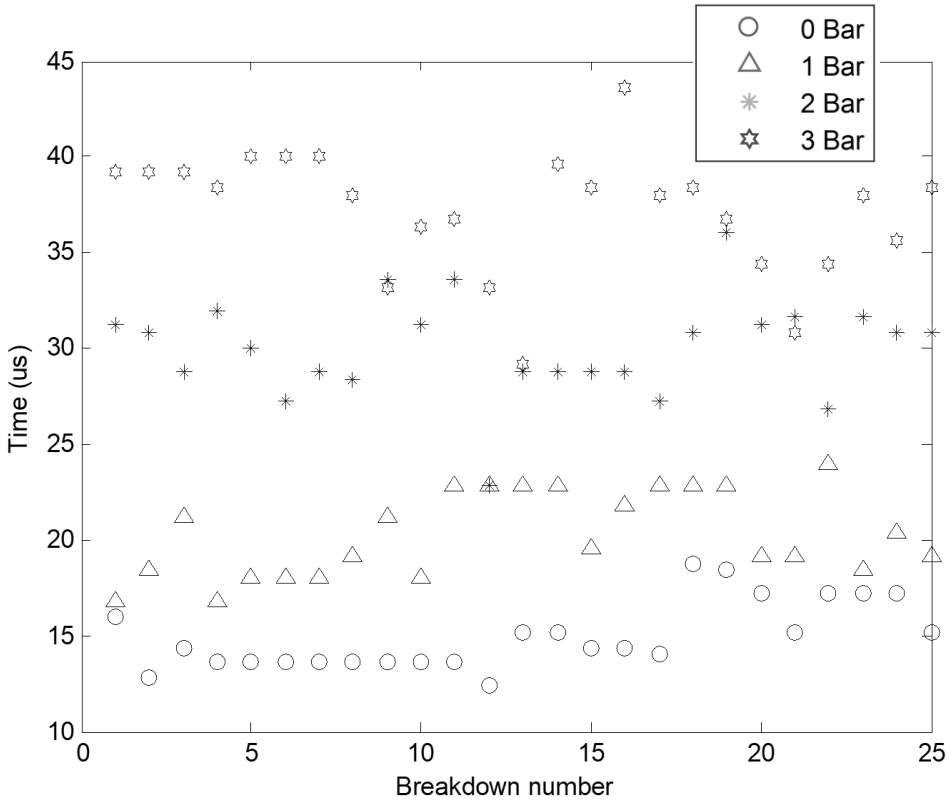

Figure 88 - Positive polarity delay time measurements in relation to breakdown number for 80% N_2 / 20% HFO-1234ze

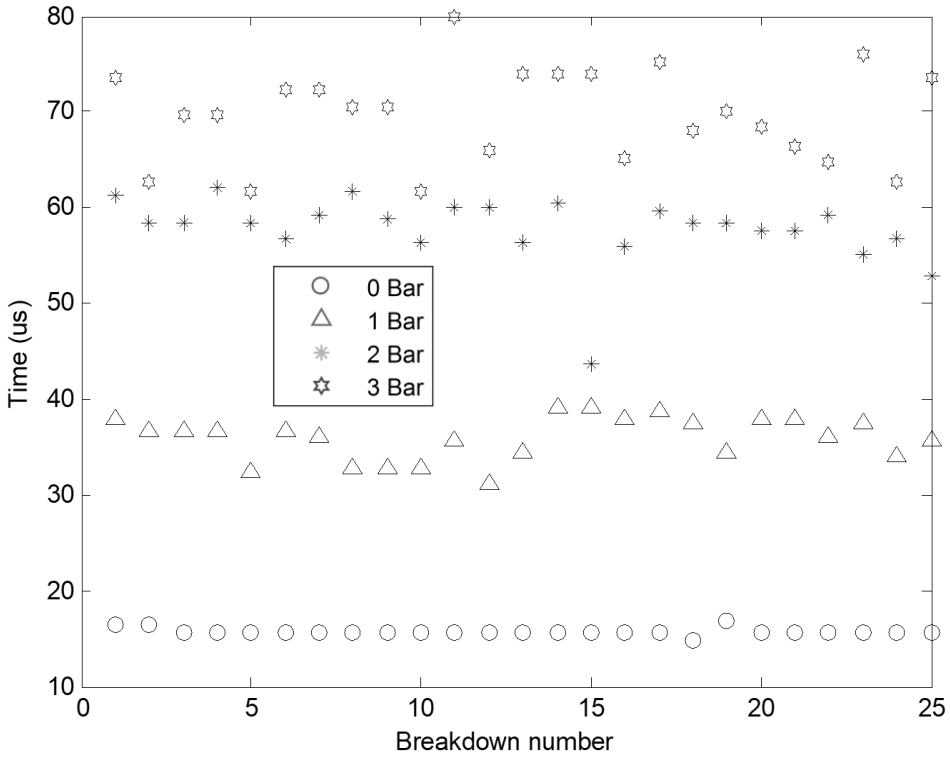

Figure 89 - Negative polarity delay time measurements in relation to breakdown number for 80% N_2 / 20% HFO-1234ze

In Figure 88 and 89, the delay time analysis in terms of breakdown number is shown for 80% N_2 / 20% HFO-1234ze. There is an increase in delay time with respect to pressure for both polarities. Again, there is no clear indication of increasing or decreasing trend in the delay times throughout the tests.

7.1.5. Conclusions

It is important that this analysis is recorded to make sure that the delay time is not increasing or decreasing with an increasing number of breakdowns. If this occurs, then the gas is seen to be getting more or less insulating, or the electrode has eroded over the course of the tests, causing the delay time to increase or decrease. This was not found for any of the test conditions. After this was determined, the von Laue statistical analysis could then proceed for each of the test conditions analysed.

7.2. STATISTICAL ANALYSIS OF TIME DELAY TO BREAKDOWN

Von Laue statistical analysis was undertaken for each of the data sets. Two example Laue plots are shown in Figure 90 and 91, for 90% N_2 / 10% HFO-1234ze at 1 bar gauge for negative and positive polarity, respectively.

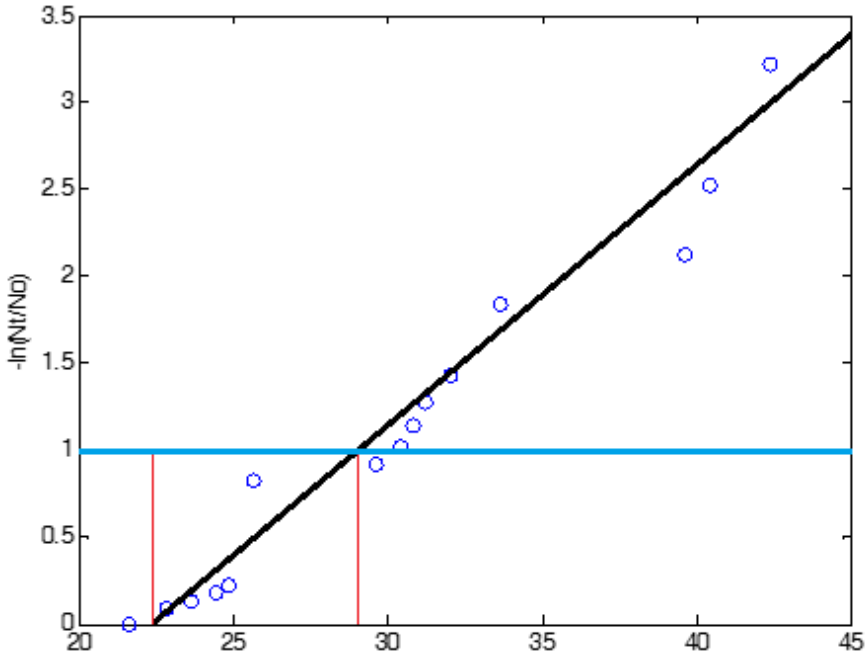

Figure 90 - Example of tf and tst extraction from Laue plot with shallow gradient and therefore a longer statistical time taken for negative polarity 90% N_2 / 10% HFO-1234ze at 1 bar gauge

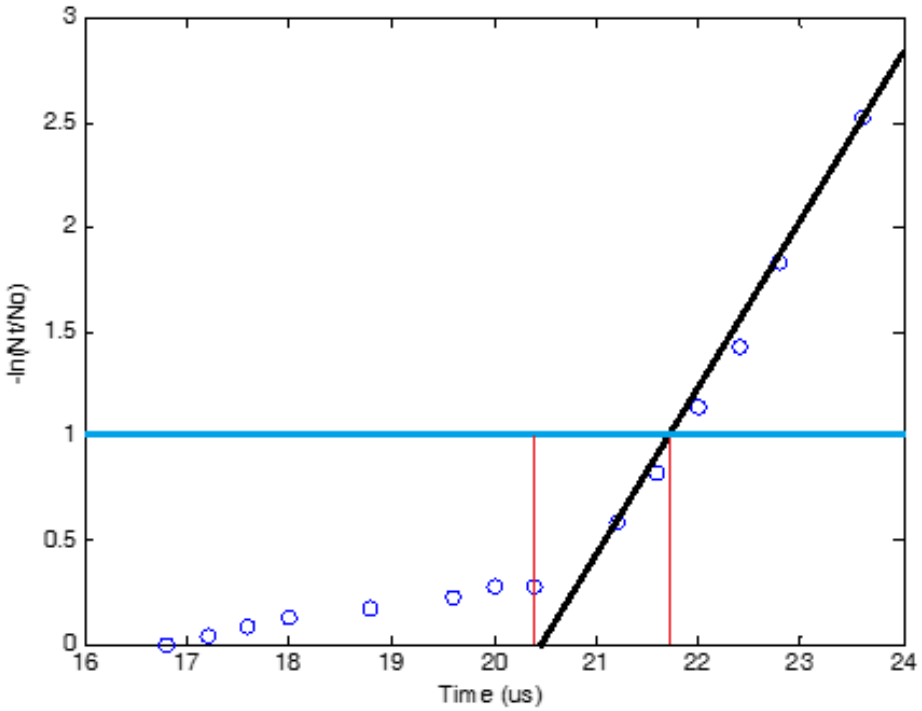

Figure 91 - Example of tf and tst extraction from Laue plot with steep gradient and therefore a shorter statistical time taken for positive polarity 90% N2 / 10% HFO-1234ze at 1 bar gauge

In this section the statistical and formative times have been extracted using the method outlined in section 2.11. The time before the first red line is taken as the formative time. For these two example plots here, it can be seen that the negative polarity formative time is ~22.5 µs (Figure 9), and for positive polarity ~20.2 µs (Figure 91). The statistical time is measured as the time between the two red lines, which can be seen to be ~7µs for negative polarity (Figure 90) and ~1.5µs for positive polarity (Figure 91). The other Laue plots have been included in Appendix A for reference, and the formative and statistical time data extracted from each of the plots is summarised in Table 10.

Table 10 - Statistical and formative times for the N_2/HFO-1234ze mixtures from 0-3 bar gauge, positive and negative polarity, all in µs.

Pressure	**Polarity**	**100% N_2**		**95% N_2 / 5% HFO-1234ze**		**90% N_2 / 10% HFO-1234ze**		**80% N_2 / 20% HFO-1234ze**	
		t_f (µs)	t_s (µs)	t_f (µs)	t_s (µs)	t_f (µs)	t_s (µs)	t_f (µs)	t_s (µs)
0	Positive	8	0.7	9.2	2	12	1.9	13.3	1.9
	Negative	10.4	0*	15.2	0.18	13.5	2.7	15.6	0.35
1	Positive	13.5	2.5	17.2	0.5	20.2	1.43	19.2	2
	Negative	25.2	0*	21.5	2.5	22.5	7	35.8	1.7
2	Positive	16	2.6	22.5	1.5	21.8	3.2	28.6	2.5
	Negative	37.4	1.2	47	2.8	56.5	2.5	57.5	1.5
3	Positive	18.5	4.5	25.3	1.5	29	2.5	36.4	2.5
	Negative	38.5	2.3	61.5	7	56.5	3	67	4.2

*0 results have been discussed and justified in section 7.1.1

Table 10 summarises the information taken from each of the von Laue graphs. The information that has been extracted is the negative and positive formative and statistical delay times for pressures of 0, 1, 2 and 3 bar gauge. This information has also been plotted into formative and statistical time graphs, shown in Figure 92 and 93, respectively.

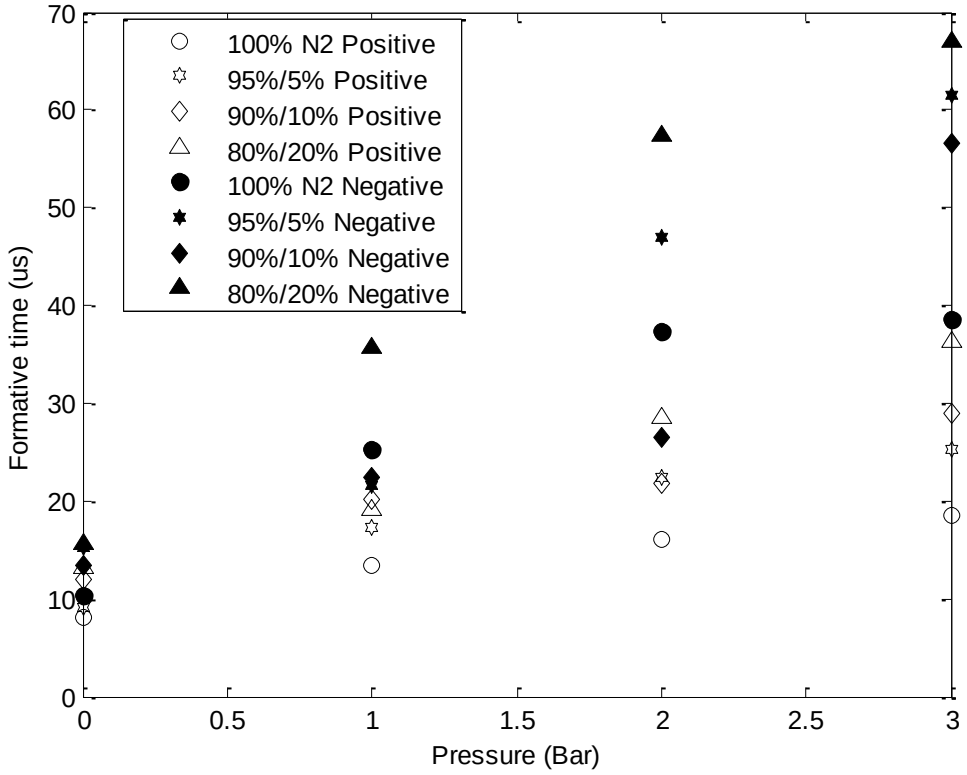

Figure 92 - Formative times for 100% N_2; 95% N_2/5% HFO-1234ze; 90% N_2/10% HFO-1234ze; and 80% N_2/20% HFO-1234ze, for positive and negative polarity

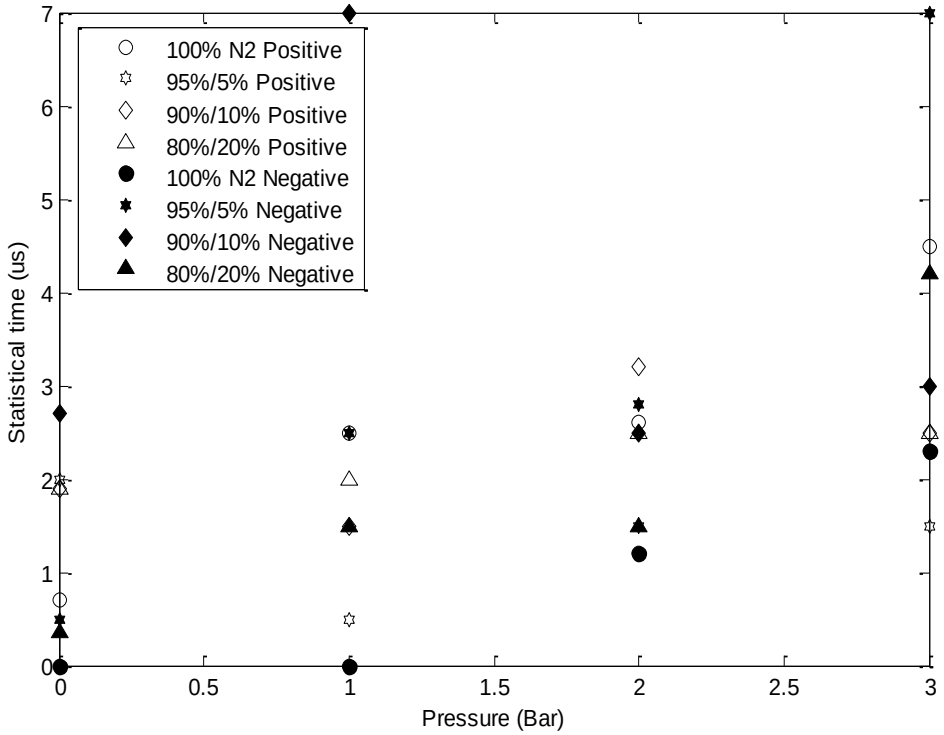

Figure 93 - Statistical times for 100% N_2; 95% N_2/5% HFO-1234ze; 90% N_2/10% HFO-1234ze; and 80% N_2/20% HFO-1234ze, for positive and negative polarity

In Figure 92, the formative time is seen to increase as the pressure increases for each of the gases/gas mixtures, for both negative and positive polarity. Therefore, from this graph it is clear to see there is a direct correlation between the pressure and the formative time. What is also clear is that the negative formative times are seen to be longer than the positive polarity results. This can be seen looking back to section 6.3.2, where the overall delay times were significantly longer for negative polarity. Compared to 100% N_2, the addition of concentrations of HFO-1234ze ≥10% (by pressure) also results in an increase in formative time. Therefore, dependent upon the pressure, gas mixture and polarity, the formative time can be relatively easy to predict, as there is a clear correlation for each of these parameters.

In Figure 93, the statistical times are shown. In terms of pressure, again there is correlation between this and the statistical time, with a few exceptions. Polarity does not have much effect on the statistical time, as the data is mostly clustered together with both positive and negative data points. Although, both erratic points which were collected were of negative polarity, with statistical times of ~7 μs. The statistical time is not greatly affected by the different gases/gas mixtures that were tested throughout, with the data-points being largely clustered between 0 - 4 μs.

A method to alter the times recorded would be to introduce a nanosecond regime trigger pulse, which would decrease these times by a factor dependent upon the rise-time of the trigger pulse.

8. CHAPTER VIII

DISCUSSION, CONCLUSIONS AND FURTHER WORK

8.1. DISCUSSION OF HFO-1234ZE/N_2 MIXTURES

This section will outline the discussion points for the results of the self-breakdown, trigger threshold, delay time and jitter results from the 3 gas mixtures at their respective pressures.

8.1.1. Self-Breakdown and Triggering threshold

The increases in self-breakdown voltages are down to the phenomena which occur as free electrons are absorbed by gas molecules. This process changes fast moving electrons with a high probability of ionisation to heavier, slow moving negative ions with a much lower potential for further ionisation to take place. Therefore, in order for breakdown to occur, the applied voltage must be increased in order for sufficient ionisation to occur. As HFO-1234ze is an electronegative gas, this gives the gas an ability to absorb these free electrons. This means that the gas has a high electron attachment, resulting in a higher breakdown strength as the fractional pressure increases. The ionisation coefficient of HFO-1234ze decreases with respect to increasing pressure. This is a product of electron attachment, with electrons attaching to gas molecules as discussed above. From the decrease in ionisation coefficient with respect to pressure, this will decrease the probability of a free electron becoming available to initiate breakdown [36]. From this phenomenon, an increase in breakdown strength as pressure increases is apparent for each of the gas mixtures tested. Therefore, these phenomena were the results of the maximum increase of breakdown voltage to a value of ~306% and ~191% for negative and positive polarity compared to 100% N_2.

The triggering characteristics of the CSS are affected by the degree of electronegativity of the fill gas, and by the stabilising effect of the space charge produced by the corona discharges. It is known that the use of SF_6 leads to long formative delay times at low pressures [68]. From Figure 92 and 93, it is clear that the overall delay time to

breakdown for the gas mixtures tested here is mostly determined by the formative delay time at lower pressures [68], [69], [70], [71]. This phenomenon can account for the narrow triggering range seen at lower pressures in Figure 72 and 73.

In order to increase the triggering range at lower pressures, the length of the gap *Dg* (see Figure 33) within the switch can be increased, and a higher voltage trigger pulse applied. This can be seen from the preliminary air tests in Figure 55, where the triggering threshold is seen to increase to a value of 13 kV compared to Figure 54, which has the shorter triggering gap (*Dg*) and lower (7 kV) triggering threshold. However, using this method can cause delayed triggered breakdown when operating at DC charging voltages close to the triggering threshold voltage [68]. This operation can be seen in Figure 43, where there is an increase in *t*2 within the overall delay time.

In terms of polarity effect on switching performance between the pos–neg (HV-trigger) and neg–pos configurations, this cannot be explained by the changes that occur in the electric field during triggering, as the field enhancement will be the same for both configurations. For further explanation, the source of initiatory electrons available for discharge inception must be considered in each case as in [80]. In the pos–neg configuration, the most likely source of initiatory electrons in an HFO-1234ze/N_2 mixture is via collisional detachment from negative ions in the enhanced field regions around the HV and ground electrodes. These free electrons will produce positive streamers which are cathode directed. It has been reported that the velocity of a positive streamer can far exceed that of a negative streamer [79], and this rapid propagation across the electrode gap may mean that the streamer will arrive at the cathode or be well established before the trigger gap breaks down (trigger to earth). The streamer will leave behind an ionized plasma channel with relatively high resistance [80], which will then absorb energy from the applied electric field and develop into a highly ionized plasma channel with very low resistance. In the neg–pos configuration, the main source of initiatory electrons is most likely to be via field emission from the negative HV and ground electrodes [78]. It is likely that this will result in early breakdown of the trigger to ground electrode because of the multiple avalanche emissions from the ground electrode. Breakdown of the main electrode gap may then follow the same mechanism. Breakdown of the main gap is initiated by a relatively slow negative streamer, which is propagating in a reduced electric field.

There is therefore no field intensification for streamer propagation as the trigger voltage will have collapsed relatively quickly following inception.

The difference in switching performance found for the two configurations is believed to be attributed to the different mechanisms of inception and the subsequent discharge development. For the neg–pos configuration, inception of the negative discharge occurs through field emission. For the pos–neg configuration, inception of the discharge is believed to occur through negative ion detachment giving rise to a positive streamer. The positive streamer propagates up to 20 times faster than a negative streamer and it also has been shown that the positive streamer leaves behind a plasma column of higher ionization density than that left by the negative streamer. These latter points are thought to be important in enhancing the development of the high-temperature plasma column into a conducting arc. In conclusion, the combination of these factors is believed to account for the superior switching characteristics displayed by the pos–neg configuration compared with the neg–pos configuration [78].

The triggering range of the switch can also be increased via the application of a faster trigger pulse, within the nanosecond regime [64].

As the trigger pulses deployed for the single-shot characterisation in this study can be considered as slow (dV/dt ~0.4 kV/µs), and a short (3 mm) *Dg* gap was used, this limits the achievable triggering range. These characteristics could be altered in future work by using a different *Dg* spacing, as well as a faster, higher-amplitude trigger pulse. This will result in a wider operating range for the switch as part of an overall pulsed power system. The length of the gap *Dg* was set at 3 mm here as a compromise, sacrificing a slightly wider trigger range with negative-polarity DC voltages, for a better performance with positive-polarity DC voltages. This can be seen from Figure 69 – 72. Although, these different parameters account for the achievable triggering range, a value of 837% and 174% compared to 100% N_2 was still achieved for positive and negative polarity compared to 100% N_2.

8.1.2. Delay time discussion

From the delay time measurements that have been conducted, a trend of longer average delay times has become apparent for the negative polarity switch closures. This is due to the phenomena of positive streamers exceeding the speed of negative streamers [79],

also the electron attachment associated with the added electronegative gas, absorbing electrons and producing slower moving negative ions. This therefore has slowed the breakdown process for the negative polarity breakdowns. Also, as the pressure increases, the mean free path of electrons is reduced and they will collide with more neutral particles until breakdown has been established. This then culminates in longer delay times as the pressure is increased for all tests. Overall, in terms of applications that require repetitive switching, longer delay times to breakdown limit the maximum achievable pulse repetition frequency.

8.2. COMPARISON WITH SF_6

A major objective of this work was to determine the suitability of a gas, novel to pulsed power, to replace SF_6 in switching applications. The operational characteristics of SF_6 in switching applications are investigated in [42], [64], [68]. These papers have been used to provide information on the switching characteristics of SF_6, given the legislative barriers to using SF_6 in the present study. In [68], a similar corona-stabilised switch with HV electrode tip radius of 0.5 mm and the same distance *Dh* of 5 mm (*Dg* was 1.5 mm – 3.5 mm) was used, with a gas mixture of 25% SF_6 to 75% air. Although ultimately the design of the switch was different, these similarities were used for comparison of operation. Therefore, the gas mixtures containing HFO-1234ze tested here were compared to the 25% SF_6/75% air mixture tested in [68].

Within [42], [64], the same general switch design as used in this thesis was characterised for 100% SF_6 and 100% dry air. The SF_6 tests were completed between 0-1 bar absolute and the dry air tests were completed between 0-3 bar gauge. Therefore, a comparison can be made between these results and the N_2/HFO-1234ze gas mixture results found here. The positive self-breakdown voltage at 0 bar gauge for SF_6 was found to be 40 kV [42], where the 3 mixtures were determined to have self-breakdown voltages between 10-13 kV here, significantly lower compared to SF_6; however, the geometry characterised in [42] had *Dh* = 8 mm and *Dg* = 5mm, accounting for the significant differences in self-breakdown voltage level. What can be taken from the SF_6 data is the triggering range at 0 bar gauge, where a triggering range of around 16 kV was found [42]. Whereas, with the 3 HFO-1234ze gas mixtures tested here, the maximum triggering range at 0 bar was 6.6 kV for 80% N_2 / 20% HFO-

1234ze. What can be seen from the SF_6 results is that the maximum triggering range of 19 kV is achieved at 0 bar gauge. For air, however, the triggering range is between 4-5 kV over the full pressure range, from 0-3 bar gauge. Comparing this to the three N_2/HFO-1234ze mixtures tested here, with positive polarity, the triggering ranges were: 4.4 kV to 12.2 kV for a mixture of 95% N_2 / 5% HFO-1234ze; 5.2 kV to 13.4 kV for 90% N_2 / 10% HFO-1234ze mixture; and 6.8 kV to 13 kV for 80% N_2 / 20% HFO-1234ze mixture. Therefore, the triggering range at 0 bar of SF_6 is still 6 kV wider than those of the 3 mixtures tested, at 3 bar gauge. In order to widen the triggering ranges achieved here, the total pressure of the gas mixtures could be increased, or the volume (by pressure) of HFO-1234ze could be increased, to match the triggering range seen at 0 bar gauge for 100% SF_6. Also, a change in switch geometry to match the specific inter-electrode gaps used in [42], [64] could also be completed.

For negative polarity, the HFO-1234ze mixtures have self-breakdown voltages at 0 bar gauge of around 10-13 kV, which are much lower compared to the 40 kV self-breakdown voltage of the 100% SF_6 mixture [42]. This however, can be accounted for as the gap Dh was much smaller in size compared to [42]. Higher breakdown strengths were found at higher pressures of HFO-1234ze, which can be used to compensate for this. The breakdown strengths found here are very similar for both negative and positive polarity, meaning that this switch configuration is of flexible design, widening opportunities for use in different applications. The triggering ranges for the HFO-1234ze mixtures for negative polarity were: 3.2 kV to 10 kV for 95% N_2 / 5% HFO-1234ze; 4.6 kV to 13.6 kV for 90% N_2 / 10% HFO-1234ze; and 5 kV to 12.2 kV for 80% N_2 / 20% HFO-1234ze. So again, the triggering ranges are of similar magnitude to those found for positive polarity. This means that this switch geometry has an advantage as the two different polarities work similarly, meaning the switch design is more flexible to change of polarity, culminating in potential use in a broader range of applications.

The delay time and jitter characteristics of the HFO-1234ze mixtures followed the trend of, generally speaking, as the pressure increased, the delay time and jitter increased accordingly. For positive polarity, as the percentage of HFO-1234ze in the gas mixture increased, the delay time and jitter also increased. While in the negative regime, the delay time and jitter did not show any clear trend, although the delay time measurements were of considerably longer duration compared to those of the positive

regime. Each gas or gas mixture was tested here at 75% of the self-breakdown voltage level. In [42], at 0 bar gauge, SF_6 showed a delay time of ~40 μs at 60%-70% of the self-breakdown voltage, and ~ 25 μs at 80%-90% of the self-breakdown voltage. Whereas, for the HFO-1234ze mixtures tested here, when measured at 0 bar gauge, the average delay times were 10.7, 13.3 and 15 μs for positive polarity, with 5%, 10% and 20% of HFO-1234ze, respectively; these shorter delay times in HFO-1234ze compared to SF_6 would enable higher pulse repetition frequencies, noting however that the test conditions were not identical. The jitter in each case is dependent upon the percentage of self-breakdown voltage applied, where there is an increase in jitter with SF_6 [42] as well as with HFO-1234ze as the applied voltage is reduced to a lower percentage of the self-breakdown voltage. Average delay times of 15.9, 15.3 and 15.7 μs were found here for negative polarity with 5%, 10% and 20% HFO-1234ze, respectively, again, shorter than those measured in SF_6 [42], [64]. Although, in the positive polarity regime, there is a wider range of delay times compared to negative polarity; the average delay times were 26.4, 30.4 and 37.2 μs for positive polarity, and 66.8, 59.2 and 66.7 μs for negative polarity, for 5%, 10% and 20% HFO-1234ze, respectively.

For the chosen electrode geometry of 5/3 mm, the von Laue statistical analysis conducted for ambient air, 100% N_2 and the 3 mixtures of N_2/HFO-1234ze, revealed that increasing pressure increases both formative and statistical time. For the 5/4 mm electrode geometry in ambient air, however, the delay time measured showed no real trend compared to the other electrode arrangements. This was reflected in the formative and statistical times for air, with no real trend becoming apparent. The formative time in SF_6 has been described in [73], where the jitter of the breakdown has been discussed in terms of increasing formative time due to a pressure increase. The authors show that there is no significant jitter change as the formative time increases with increasing pressure. Looking at the HFO-1234ze mixtures tested here, there is also no real conclusive increase or decrease in jitter with increasing formative delay time. Further work can be carried out on this at higher percentages of HFO-1234ze to see if this trend changes. Work with SF_6 would also be an advantage if this was possible with the required reclamation facility, then testing and subsequent analysis could be conducted under the same arrangement as the HFO-1234ze mixtures for direct comparison.

Overall, the gas mixtures incorporating the novel switching gas HFO-1234ze have shown many positive characteristics, which can, under certain circumstances, be compared to switching operation in SF_6. Where the performance is lacking, more work can be completed for different inter-electrode gap length combinations, for example the 8/5 mm gaps used in [42], [64], to enable direct comparison. The percentage volume of the electronegative HFO-1234ze could also be increased, taking appropriate safety precautions. As discussed in 2.7.2.1, the upper and lower explosive limits show the areas where HFO-1234ze is considered flammable when mixing with air. From this data, having >20% HFO-1234ze, at this parameter change (temperature, humidity and pressure) is too concentrated to ignite and therefore is possible for use. However, a low energy system should be constructed to test with low volumes before larger systems are tested, especially under repetitive conditions where the energy will be increased. Also, however, the build-up of a carbon-like substance on the electrodes themselves can be seen as a real problem, which could result in change of the geometry of the switch being altered to a point where the switching characteristics could be compromised. Also, if under repetitive operation carbon continued to coat the inside of the switch, this could compromise the insulating properties of the Perspex flanges, leading to a coating of carbon and a higher probability of flashover between the main electrodes and the trigger body of the switch. Therefore, in order for HFO-1234ze to be seen as a suitable replacement for SF_6, more research will have to be undertaken to characterise and ultimately eradicate this problem.

8.3. FURTHER WORK

Further work that could be completed on the switch is to characterise the PRF performance of the CSS. Although, the carbon build-up on the electrodes is not ideal, to solve this, different gas mixtures should be tested in order to try and eradicate this problem. If this problem is solved, then different electrode geometries and electrode types could be tested, in order for the switch to be used well into the kHz regime. The use of a faster trigger impulse generator, with rise time in the nanosecond regime, could also be tested in order to reduce delay time and jitter and, thus, create a sufficient voltage recovery period in order for the fill gas/gas mixture to ‘recover’ in time to

enable operation at these high frequencies. Changing electrode geometry, with the aim of generating corona on certain parts of electrodes could be completed to further improve this PRF characteristic. For example, using equipotential spacing arrangements, as in [21], where using this improves the PRF ability of the switch under repetitive conditions. Also, further work could be conducted into cascaded corona-stabilised switches, where the addition of an extra electrode could increase the hold-off voltage of the switch, as in [49], where the voltage has been increased up to 100 kV.

If sufficient work were to be completed on the safety aspects of the gas HFO-1234ze, then increasing the fractional pressure in a gas mixture would further the understanding of how this gas behaves under more extreme conditions in terms of high volumes of HFO-1234ze under PRF operation. Since the breakdown strength of gas mixtures including concentrations of HFO-1234ze up to 20% (by pressure) was found to be up to three times the breakdown strength of N_2 alone, it would be interesting to increase the volume of HFO-1234ze towards 100%, in order that the switching performance could be directly compared to that of 100% SF_6. This testing could reveal some key information as the percentage by volume of HFO-1234ze is increased towards 100%, facilitated by appropriate testing and safety precautions.

REFERENCES

[1] J Lehr P Ron ‘Foundations of pulsed power technology’ [Book]. - New Jersey : John Wiley and Sons, 2017. - Vols. 147-235.

[2] J. R. Beveridge, S. J. Macgregor, M. J. Given, I. V. Timoshkin and J. M. Lehr, "A corona-stabilised plasma closing switch," in *IEEE Transactions on Dielectrics and Electrical Insulation*, vol. 16, no. 4, pp. 948-955, August 2009.

[3] J. R. Beveridge, S. J. Macgregor, I. V. Timoshkin, J. Lehr, “A corona-stabilised plama closing switch” *2008 IEEE International Power Modulators and High-Voltage Conference*, Las Vegas, NE, 2008, pp. 487-490.

[4] J A Harrower S J Macgregor, F A Tuema 'Design considerations for corona-stabilised repetitive switches' : *J Phys, D:Appl phys, 1998. - Vol. 32 pp. 790-797.*

[5] Koch D 'SF6 properties and use in MV and HV switchgear' - 6 9 2017. - www2.schneider-electric.com/documents/technical-publications/en/shared/electrical-engineering/breaking-techniques-switchgear/general-knowledge/ect188.pdf.

[6] C. T. Dervos & Vassiliou, Panayota. (2000). Sulfur Hexafluoride (SF 6): Global Environmental Effects and Toxic By-product Formation. Journal of the Air & Waste Management Association (1995). 50. 137-41. 10.1080/10473289.2000.10463996.

[7] Song Xiao, Xiaoxing Zhang, Ju Tang, Siqi Liu, A review on SF6 substitute gases and research status of CF3I gases, Energy Reports, Volume 4, 2018, Pages 486-496, ISSN 2352-4847

[8] M. Koch and C. M. Franck, "High voltage insulation properties of HFO1234ze," in *IEEE Transactions on Dielectrics and Electrical Insulation*, vol. 22, no. 6, pp. 3260-3268, December 2015.

[9] Hogg M G 'High-performance compact gas filled spark switches' PhD thesis. - Glasgow: University of Strathclyde, 2015.

[10] I.H.Hutchinson Introduction to Plasma Physics [Online] // Introduction to Plasma Physics. - I.H.Hutchinson, 2001. - 5 09 2017. - http://silas.psfc.mit.edu/introplasma/chap1.html#tth_sEc1.1..

[11] Hogg M G 'Liquid water as a dielectric insulator' MRes thesis. - Glasgow: University of Strathclyde, 2012.

[12] M Abdel-Salam H Anis, A El-Morshedy, R Radwan 'High Voltage Engineering' [Book Section] // High Voltage Engineering. - NY: Marcel Dekker, 2010. - Vols. 149-172 'The corona discharge'.

[13] E Kuffel W S Zaengl High Voltage Engineering [Book Section] // High Voltage Engineering. - [s.l.] : 311-322, Ionization and decay process 1984.

[14] M Abdel-Salam H Anis, A El-Morshedy, R Radwan High Voltage Engineering [Book Section] // High Voltage Engineering. - [s.l.] : Marcel Dekker, 2010. - Vols. 81-103 'Ionization and deionization processes in gases'.

[15] E Kuffel W S Zaengal High Voltage Engineering [Book Section] // High Voltage Engineering. - [s.l.] : 346-361, 'The streamer or 'Kanal' breakdown of a spark' 1984.

[16] M Abdel-Salam H Anis, A El-Morshedy, R Radwan High Voltage Engineering [Book Section] // High Voltage Engineering. - [s.l.] : Marcel Dekeer, 2010. - Vols. 115-139 'Electrical breakdown of gases'.

[17] Cairns B 'Triggered operation of a corona stabilised switch in air'. - MSc thesis, Glasgow : University of Strathclyde, 2014.

[18] E Kuffel W S Zaengal High Voltage Engineering [Book Section] // High Voltage Engineering. - [s.l.] : 364-366, 'Breakdown in non-uniform fields' 1984.

[19] J. M. Meek, J. D. Craggs - ‘Electrical breakdown of gases’ - Chichester, New York : Wiley series in plasma physics, 1978. - Vol. chapter 7.

[20] E Kuffel W S Kaengl High Voltage Engineering [Book Section] // High Voltage Engineering. - [s.l.] : 371-382, 'Partial breakdown, corona discharges' 1984.

[21] S J Macgregor F A Tuema, S M Turnbull, O Farish 'The operation of repetitive high-pressure spark gap switches' : *J Phys, D: Appl Phys, 1993. - Vol. 26*

[22] P A Lawless K J Maclean, L E Sparks and G H Ramsey - 'Negative corona in wire-plate electrostatic precipitators, part I: Characteristics of individual tuft-corona discharges' [Journal]. - [s.l.] : Journal of Electrostatics, 1986. - Vol. 18 p 199 - 217.

[23] P A Lawless K J Maclean, L E Sparks, G H Ramsey 'Negative corona in wire-plate electrostatic precipitators, part II: calculation of electrical characteristics of contaminated discharge electrodes' [Journal]. - [s.l.] : Journal of Electrostatics, 1986. - Vol. 18. p 219 - 231.

[24] L. Benussi, S. Bianco, M. Ferrini, L. Passamonti, D. Pierluigi, D. Piccolo, A. Russo, G. Saviano, "A study of HFO-1234ze (1,3,3,3-Tetrafluoropropene) as an eco-friendly replacement in RPC detectors," arXiv:1505.01648 [physics.ins-det] INFN-REPORT-INFN-14-14-LNF.

[25] F. A. Tuema, S. J. Macgregor, J. A. Harrower, J. M. Koutsoubis, O. Farish, “Corona-stabilisation for high repetition rate plasma closing switches” *1999 Eleventh International Symposium on High Voltage Engineering*, London, 1999, pp. 280-284 vol.3.

[26] J. R. Beveridge, S. J. Macgregor, M. J. Given, I. V. Timoshkin and J. M. Lehr, “A corona-stabilised plasma closing switch” *IEEE Transactions on Dielectrics and Electrical Insulation*, vol. 16, no. 4, pp. 948-955, August 2009.

[27] S. J. MacGregor, S. M. Turnbull, F. A. Tuema and O. Farish, "The application of corona stabilised breakdown to repetitive switching," *'96 IEE Colloquium on Pulsed Power*, London, UK, 1996, pp. 21/1-21/3.

[28] S. J. Macgregor, G. A. Woolsey, D. B. Ogle and O. Farish, "The Influence of Electrode-Fluorine Reactions on Corona and Glow Discharges in SF6," in *IEEE Transactions on Plasma Science*, vol. 14, no. 4, pp. 538-543, Aug. 1986.

[29] S. J. MacGregor, S. M. Turnbull and F. A. Tuema, "A corona stabilised, high PRF closing switch," *IEEE Conference Record - Abstracts. 1996 IEEE International Conference on Plasma Science*, Boston, MA, USA, 1996, pp. 258-.

[30] S. J. MacGregor, S. M. Turnbull, F. A. Tuema and O. Farish, "Factors affecting and methods of improving the pulse repetition frequency of pulse-charged and DC-charged high-pressure gas switches," in *IEEE Transactions on Plasma Science*, vol. 25, no. 2, pp. 110-117, April 1997.

[31] P Gao B Zeng, J Cheng, J Su, R Li, L Zhao "Experimental Investigation on the Breakdown Voltage Jitter of Corona-Stabilized Switch at Low Repetition Rate," in *IEEE Transactions on Plasma Science*, vol. 45, no. 8, pp. 2351-2357, Aug. 2017.

[32] Plasmawise, Marseille, France. ‘Corona Discharge’ http://plasmasynergie.com/technology/plasma-discharges/ - visited 18/7/2018

[33] J. A. Harrower, F. A. Tuema, S. J. Macgregor, “Critical volume effects on corona stabilised repetitive breakdown” *Pulsed Power '99 (Digest No. 1999/030), IEE Symposium*, 1999, pp. 30/1-30/4.

[34] I. V. Timoshkin, S. J. Macgregor, M. J. Given, J. R. Beveridge, J. M .Lehr, “Dynamic characteristics of corona discharges in point-plane electrode topologies influenced by space charge” *2008 IEEE International Power Modulators and High-Voltage Conference*, Las Vegas, NE, 2008, pp. 495-498

[35] M. J. Given, M. P. Wilson, I. V. Timoshkin, S. J. MacGregor, T. Wang and J. M. Lehr, "The triggered behaviour of a controlled corona stabilised cascade switch," *2011 IEEE Pulsed Power Conference*, Chicago, IL, 2011, pp. 1015-1020.

[36] Chachereau, A & Rabie, M & M Franck, C. (2016). “Electron swarm parameters of the hydrofluoroolefine HFO1234ze”. Plasma Sources Science and Technology. 25. 045005. 10.1088/0963-0252/25/4/045005.

[37] change United nations framework convention on climate UNFCCC [Online]. - UN, 2014. - 28 July 2017. - http://unfccc.int/ghg_data/items/3825.php.

[38] Kilpinen & Zevenhoven - Greenhouse gases, ozone-depleting gases – June, 2001.

[39] Poulsen T S 'Ozone-depleting substances and the greenhouse gases HFC's, PFC's and SF6' - [s.l.] : Dansih consumption and emissions, 2006.

[40] Maiss, M & Brenninkmeijer, Carl. (2018). Atmospheric SF6: Trends, sources and prospects. Environmental Science & Technology, v.32, 3077-3086 (1998).

[41] Koch D 'SF6 properties and use in MV and HV switchgear' [Online] // SF6 properties and use in MV and HV switchgear. - 14 09 2017. - www2.schneider-electric.com/documents/technical-publications/en/shared/electrical-engineering/breaking-techniques-switchgear/general-knowledge/ect188.pdf.

[42] M P Wilson I V Timoshkin, S J Macgregor, M J Given, J M Lehr 'Characterisation of a triggered corona-stabilised switch in dry air' [Journal] // Proceedings of the 18th international conference on gas discharges and their applications, Grieswald,

Germany. - Grieswald, Germany : Proceeding of the 18th int conference on gas discharges and their applications, 2010. - pp. 474 - 477.

[43] Honeywell Flammability Assessment. - Heverlee : Honeywell 2008

[44] Honeywell Safety data sheet Solstice ze refrigerant [Report]. - [s.l.] : Honeywell, 2016.

[45] Christophorou L. G. - Research and findings on alternatives to pure sf6 - Gaithersburg MD : National institute of standards and technology.

[46] Honeywell Solstice ze - The low carbon. high efficient cooling system solution for a leading retailer. - Heverlee : Honeywell, 2016.

[47] Honeywell Solstice ze refrigerant (HFO-1234ze) [Report]. - Heverlee : Honeywell, 2014.

[48] International Harp Safety data sheet solstice 1234ze [Report]. - Rhondda Cynon Taff : Harp International, 2006.

[49] M. J. Given, I. V. Timoshkin, M. P. Wilson and S. J. MacGregor, "A novel design for a multistage corona stabilised closing switch," *2010 IEEE International Power Modulator and High Voltage Conference*, Atlanta, GA, 2010, pp. 556-559.

[50] S Kondo K Takizawa, K Tokuhashi 'Effects of temperature and humidity on the flammability limits of several 2L refrigerants' [Journal]. - Ibraki, Japan : *Journal of fluorine chemistry, Elsevier, 2012. - Vol. 144.*

[51] T Ma Q Wang, M Larranaga 'Correlations for estimating flammability limits of pure fuels and fuel-inert mixtures' [Journal]. - Oklahoma : Fire safety journal, Elsevier, 2013. - Vol. 56.

[52] S Kondo K Takizawa, K Tokuhashi 'Flammability limits of binary mixtures of ammonia with HFO-1234yf, HFO-1234ze, HFC-134a and HFC-125'. - Ibaraki, Japan : *Journal of fluorine chemistry, Elsevier, 2013. - Vol. 149.*

[53] Beroual, Abderrahmane & Haddad, A. (2017). Recent Advances in the Quest for a New Insulation Gas with a Low Impact on the Environment to Replace Sulphur Hexafluoride (SF6) Gas in High-Voltage Power Network Applications. Energies. *Energies* 10, no. 8: 1216

[54] McHutchon A 'Electromagnetism Laws and Equations' [Book Section] // Electromagnetism Laws and Equations. - [s.l.] : Michaelmas, 2013.

[55] J. M. Koutsoubis and S. J. MacGregor, "Lifetime effects in triggered corona stabilised (TCS) switches," *Pulsed Power '99 (Digest No. 1999/030), IEE Symposium*, 1999, pp. 29/1-29/6

[56] J. M. Koutsoubis and S. J. MacGregor, "Effect of gas type on high repetition rate performance of a triggered, corona stabilised switch," in *IEEE Transactions on Dielectrics and Electrical Insulation*, vol. 10, no. 2, pp. 245-255, April 2003.

[57] A. Larsson, D. Yap, and Y. W. Lim, “Time Jitter Study of a Corona-Stabilized Closing Switch” in *IEEE Transactions on Plasma Science*, vol. 40, no. 10, pp. 2646-2652, Oct. 2012

[58] M. G. Hogg I. V. Timoshkin, M. J Given, M. P. Wilson, S. J. MacGregor, T. Wang, R. A. Fouracre "Impulse breakdown of water with different conductivities," in *IEEE Transactions on Dielectrics and Electrical Insulation*, vol. 19, no. 5, pp. 1559-1568, October 2012.

[59] E Kuffel W S Kaengl High Voltage Engineering [Book Section] // High Voltage Engineering. - [s.l.] : 383-391, 'Surge breakdown voltage - time lag' 1984.

[60] M J Given M. P Wilson, I V Timoshkin, S J Macgregor, T Wang, M A Sinclair, K J Thomas, J M Lehr "Modifications to the von Laue statistical distribution of the times to breakdown at a polymer-oil interface," in *IEEE Transactions on Dielectrics and Electrical Insulation*, vol. 24, no. 4, pp. 2115-2122, 2017

[61] M. P. Wilson M. J. Given, I. V. Timoshkin, S. J. Macgregor, T. Wang, M. A. Sinclair, K. J. Thomas and J. M. Lehr "The statistical and formative times for breakdown at a polymer-oil interface," *2012 IEEE International Power Modulator and High Voltage Conference (IPMHVC)*, San Diego, CA, 2012, pp. 43-46.

[62] N.A. Downie, "Industrial gases" *Filling procedure for mixtures Maran and co Guildford, UK, 2002. p145*

[63] R. Young, G. James, B. Boston, "Compressible turbulent mixing" *University at Stony Brook, New York, USA July 1995. p129.*

[64] M P Wilson W Boekhoven, I V Timoshkin, M J Given, S J Macgregor, T Wang, J M Lehr "Performance of a corona-stabilised switch activated by fast-rising trigger pulses," *2012 IEEE International Power Modulator and High Voltage Conference (IPMHVC)*, San Diego, CA, 2012, pp. 136-139.

[65] Alisoy, H & Yesil, Ali & Koseoglu, Murat & Unal, Ibrahim. (2011). "An approach for unipolar corona discharge in N2/O2 gas mixture by considering townsend conditions". Journal of Electrostatics - J ELECTROSTAT. 69. 284-290.

[66] L. G. Christophorou and L. A. Pinnaduwage, "Basic physics of gaseous dielectrics" in *IEEE Transactions on Electrical Insulation*, vol. 25, no. 1, pp. 55-74, Feb 1990.

[67] A. Larsson, D. Yap, and J. Au, "Operating Conditions and Switching Delay Time of a Corona-Stabilized Switch During Repetitive Operation" in *IEEE Transactions on Plasma Science*, vol. 41, no. 10, pp. 2605-2608, Oct. 2013.

[68] J. M. Koutsoubis, S. J. MacGregor. S. M. Turnbull, "Triggered switch performance in SF6, air and SF6/air mixture," in *IEEE Transactions on Plasma Science*, vol. 27, no. 1, pp. 272-281, Feb 1999.

[69] P. Koukos, “Impulse electrical breakdown and time lags in SF6,” M.Phil. thesis, University of Strathclyde, Glasgow, U.K., 1988.

[70] P. Koukos, S. J. MacGregor, O. Farish, and N. Spyrou, “Electrical breakdown in SF6 under negative impulse voltage,” presented at the *6th Int. Symp. High Voltage Eng.*, New Orleans, LA, 1988, Paper 49.08.

[71] S. J. MacGregor, “Electrical breakdown in SF6 and SF6/air mixtures,” Ph.D. dissertation, Univ. Strathclyde, Glasgow, U.K., 1986.

[72] ThoughtCo, 'Table of electrical resistivity and conductivity' https://www.thoughtco.com/table-of-electrical-resistivity-conductivity-608499 Visited 18/7/2018.

[73] Y. Chen, J. Dickens, J. Mankowski and M. Kristiansen, "Optimization of a low jitter, 50 kV, 100 Hz triggered spark gap with high pressure gas mixtures," in *IEEE Transactions on Dielectrics and Electrical Insulation*, vol. 16, no. 4, pp. 971-978, August 2009.

[74] N. G. Trinh, "Partial discharge XIX: discharge in air part I: physical mechanisms," in *IEEE Electrical Insulation Magazine*, vol. 11, no. 2, pp. 23-29, March/April 1995.

[75] N.A. Kaptzov, Elektricheskie Yavleniya v Gazakh I Vakuume, Moscow, OGIZ, 1947.

[76] M. von Laue, "Bemerkung zu K. Zubers messung der verzögerungszeiten bei der funkenentladung", Ann. der Physik, Vol.381,pp. 261-265,1925.

[77] O. Farish and D. J. Tedford, "Temporal development of spark breakdown in nitrogen and air," in *Proceedings of the Institution of Electrical Engineers*, vol. 114, no. 2, pp. 277-283, February 1967.

[78] S. J. MacGregor, F. A. Tuema, S. M. Turnbull and O. Farish, "The influence of polarity on trigatron switching performance," in *IEEE Transactions on Plasma Science*, vol. 25, no. 2, pp. 118-123, April 1997.

[79] T. H. Martin, “Pulse charged gas breakdown,” in Proc. 5th IEEE Pulsed Power Conf., Arlington, VA, 1985, p. 74

[80] F. E. Peterkin and P. F. Williams, “Triggering of trigatron spark gaps,” in Proc. 7th IEEE Pulsed Power Conf., Monterey, CA, 1989, pp. 559–562

LIST OF PUBLICATIONS AND PRESENTATIONS

Throughout the course of this study, work has been presented at international conferences and symposiums. This has resulted in the publication of one conference paper and one journal paper as well as one oral and one poster presentation. The details of each individual presentation and publication are shown below in chronological order.

1. R. W. Macpherson[1], M. P. Wilson, S. J. MacGregor, I. V. Timoshkin, M. J. Given, T. Wang 'Characterisation of a corona-stabilised switch in alternative gas mixtures' PPC 2017 Poster presentation, June 20th, 2017, Brighton, UK.

2. R. W. Macpherson, M. P. Wilson, S. J. MacGregor, I. V. Timoshkin, M. J. Given and T. Wang, "Characterisation of a corona-stabilised switch in alternative gas mixtures," *2017 IEEE 21st International Conference on Pulsed Power (PPC)*, Brighton, 2017, pp. 1-5. doi: 10.1109/PPC.2017.8291235

3. R. W. Macpherson, M. P. Wilson, S. J. MacGregor, I. V. Timoshkin, M. J. Given, T. Wang "Characterisation and Statistical Analysis of Breakdown Data for a Corona-Stabilised Switch in Environmentally-Friendly Gas Mixtures" Oral presentation, UHVnet, January 15th, 2018, Winchester, UK. – Achieved 2nd place in best oral presentation at UHVnet 2018.

4. R. W. Macpherson, M. P. Wilson, S. J. MacGregor, I. V. Timoshkin, M. J. Given and T. Wang, "Characterization and Statistical Analysis of Breakdown Data for a Corona-Stabilized Switch in Environmentally Friendly Gas Mixtures," in *IEEE Transactions on Plasma Science*, vol. 46, no. 10, pp. 3557-3565, Oct. 2018. doi: 10.1109/TPS.2018.2844954

APPENDIX A: TABLES AND FIGURES OF COMPLETED WORK

In this section each of the graphs which were generated when using von laue analysis for each individual mixture at their respective pressure was recorded. The same process was conducted for figure a.1 – a.48 as in figure 85 and 86 to determine the formative and statistical times for each of the mixtures. In von Laue analysis, it is common to see a normal and exponential distribution within the work conducted showing two different time to breakdown processes. However, for some of the tests for example figure a.10, only one time to breakdown process is evident therefore, this rules out any evidence of other processes. In some von Laue analysis (figure a.21) this shows only one point with the von Laue graph. The reason for this is as the accuracy of the time delay test was 200ns, this particular test had time to breakdown within this time accuracy so therefore only 1 delay time was seen for all 25 shots which can be shown in figure 79, therefore the statistical time can be ruled out.

Von Laue graphs in atmospheric air

0 bar analysis

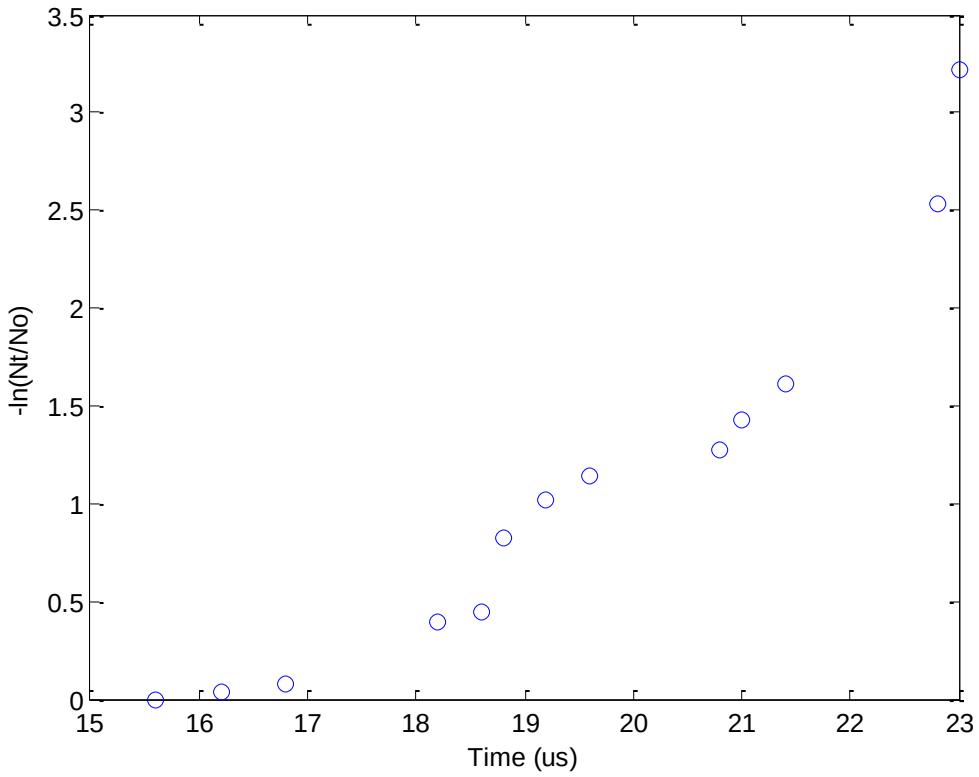

Figure a.1 - Air 5-3 Positive polarity von laue analysis for 0 bar gauge

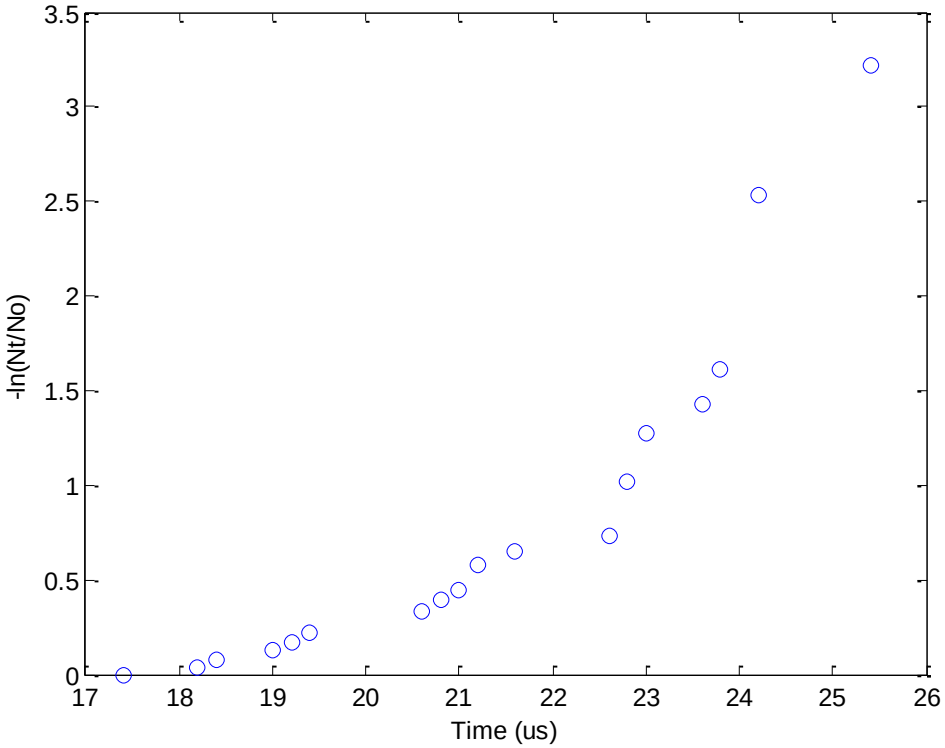

Figure a.2 - Air 5-4 Positive polarity von laue analysis for 0 bar gauge

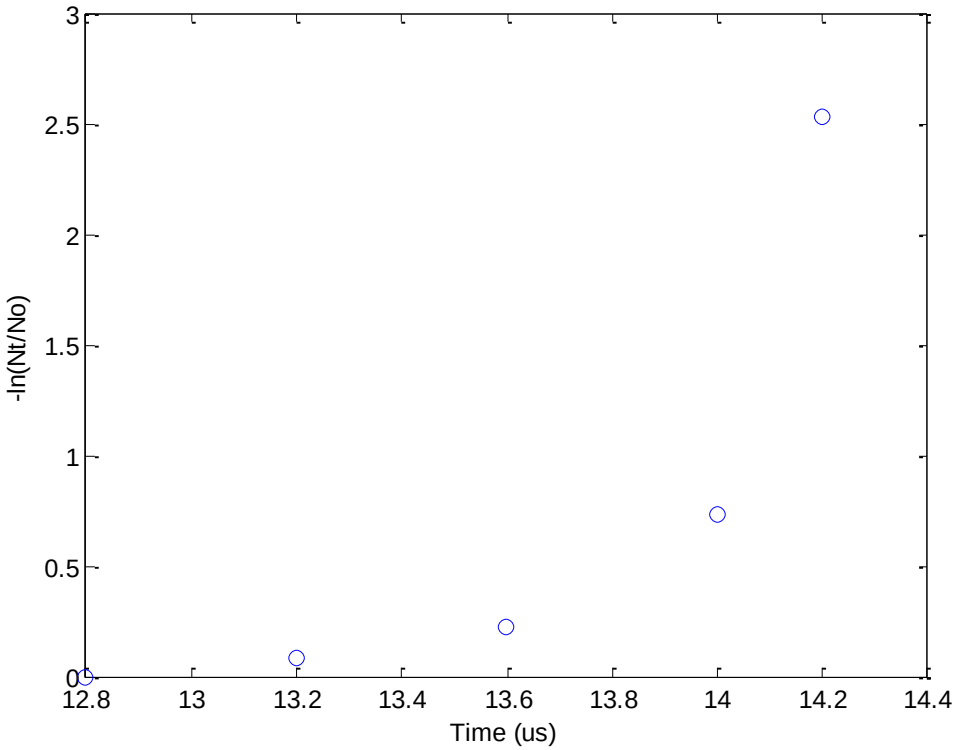

Figure a.3 - Air 5-3 Negative polarity von laue analysis for 0 bar gauge

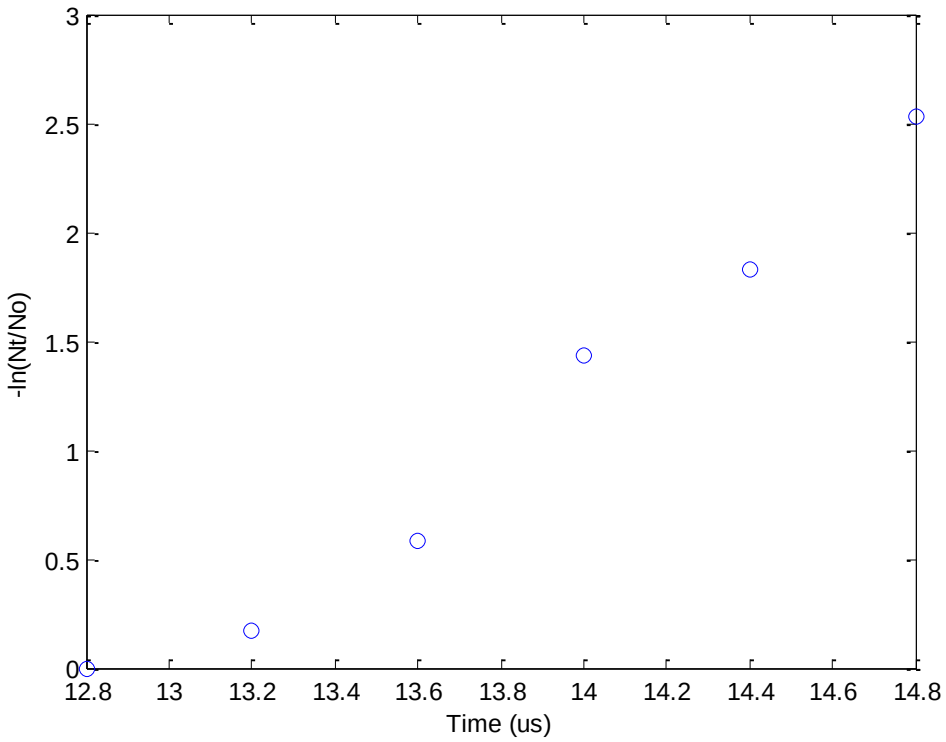

Figure a.4 - Air 5-4 Negative polarity von laue analysis for 0 bar gauge

1 bar analysis

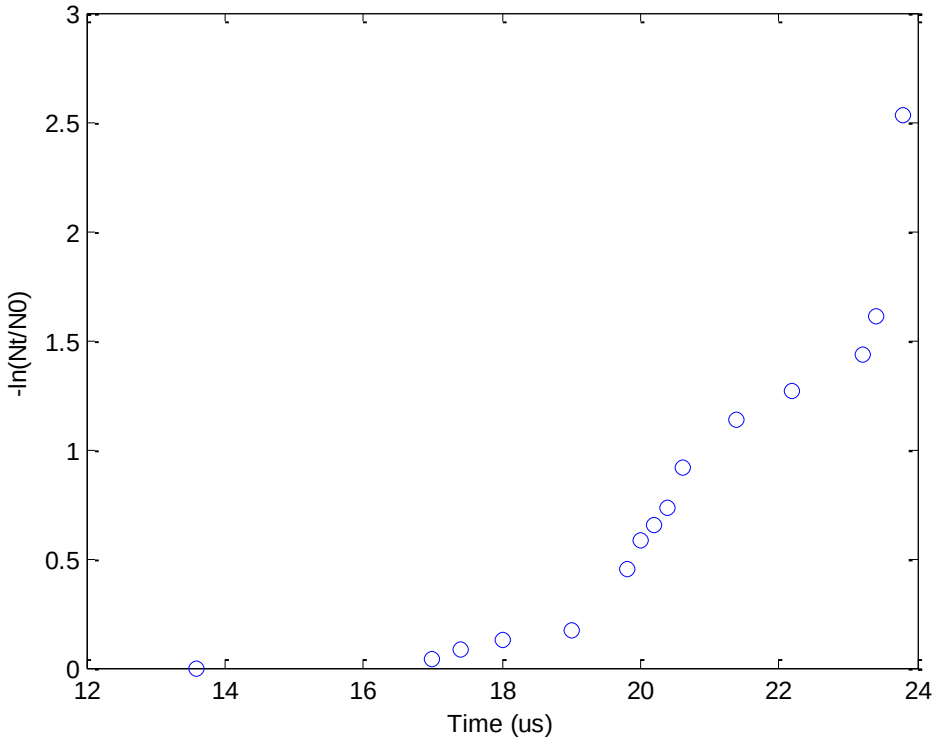

Figure a.5 - Air 5-3 Positive polarity von laue analysis for 1 bar gauge

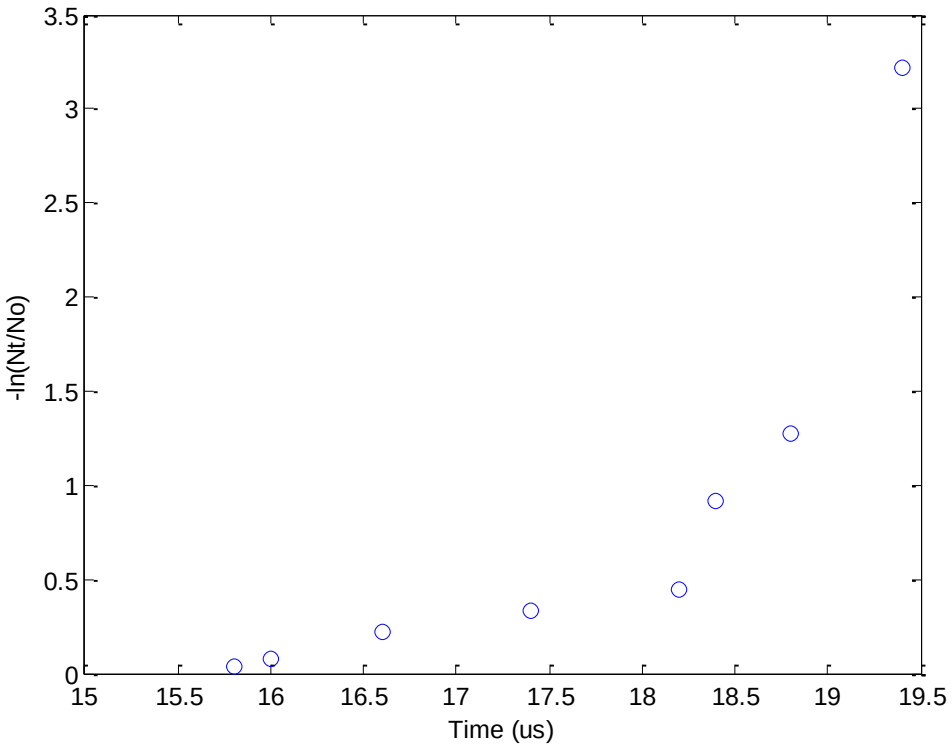

Figure a.6 -Air 5-4 Positive polarity von laue analysis for 1 bar gauge

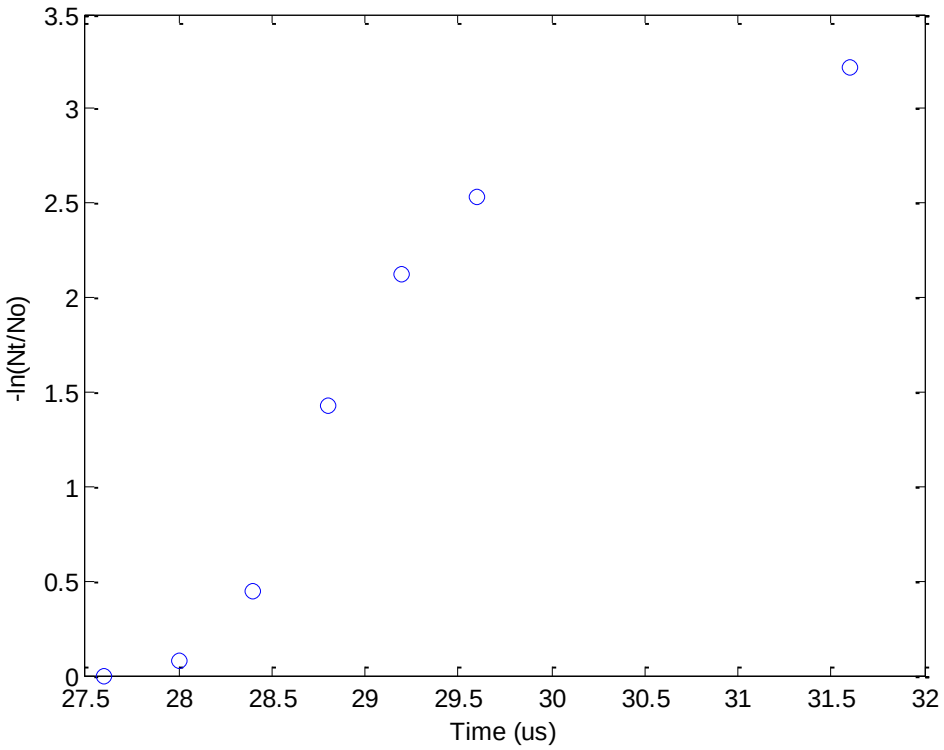

Figure a.7 - Air 5-3 Negative polarity von laue analysis for 1 bar gauge

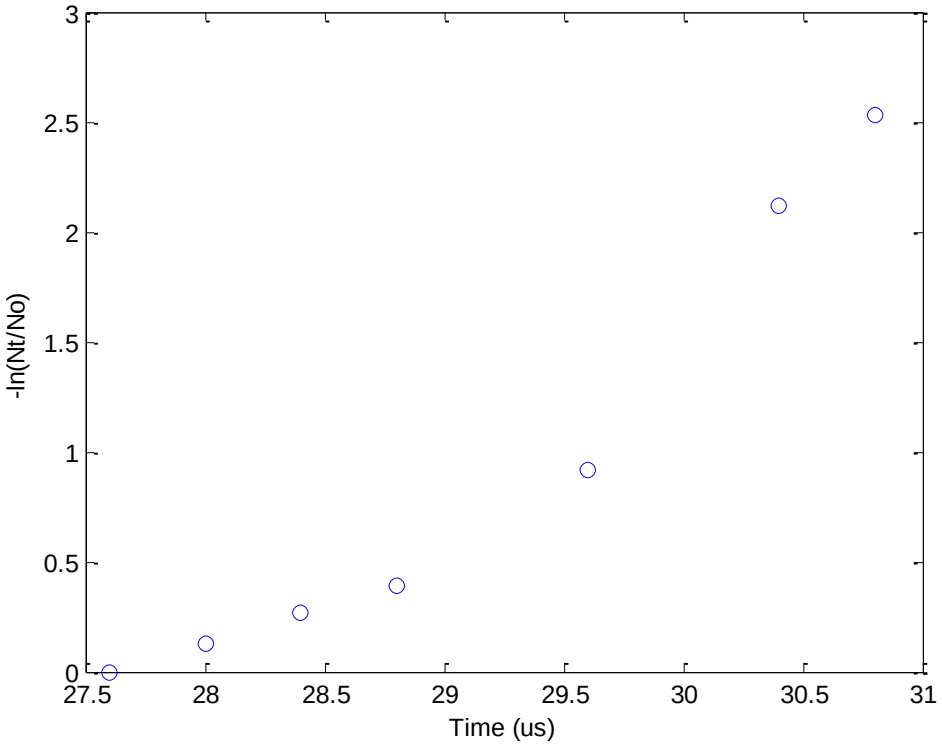

Figure a.8 - Air 5-4 Negative polarity von laue analysis for 1 bar gauge

2 bar analysis

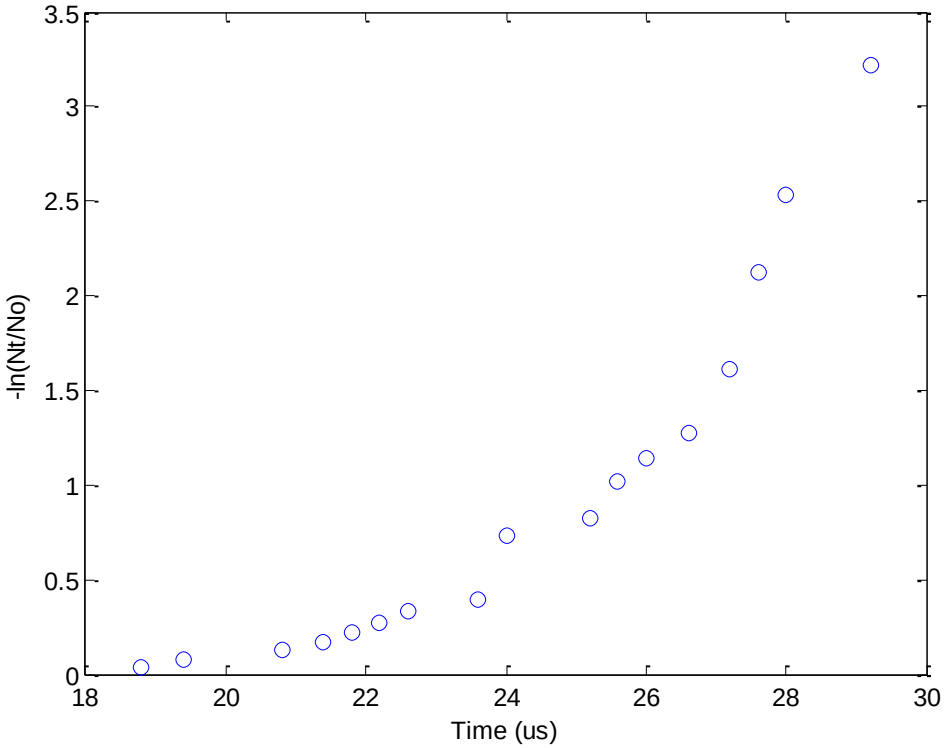

Figure a.9 - Air 5-3 Positive polarity von laue analysis for 2 bar gauge

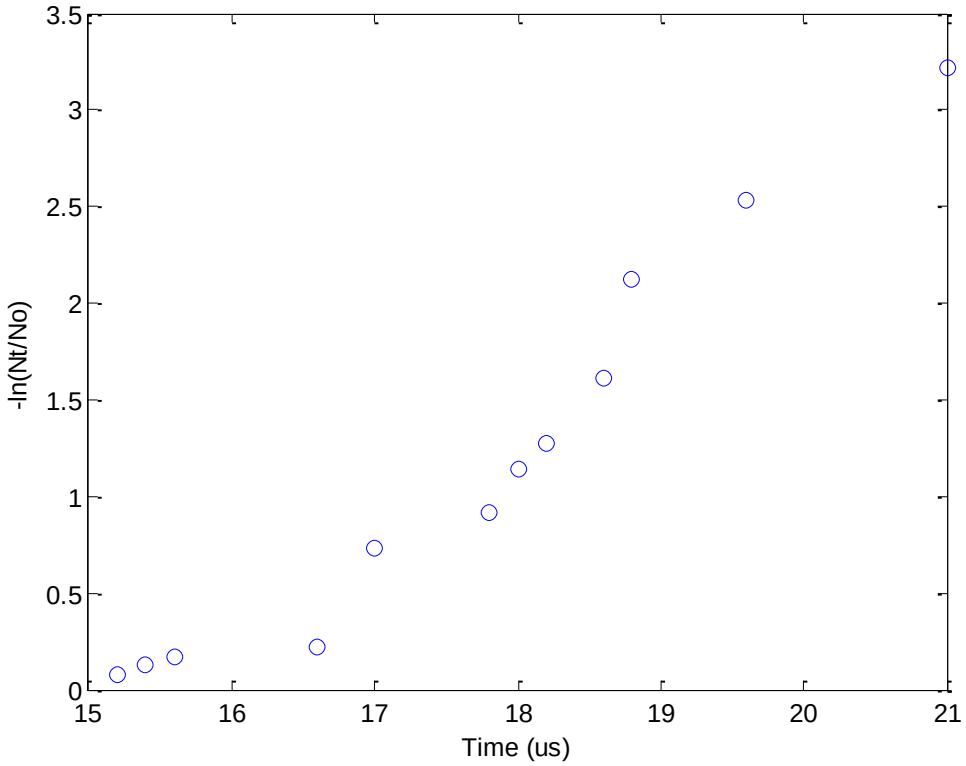

Figure a.10 - Air 5-4 Positive polarity von laue analysis for 2 bar gauge

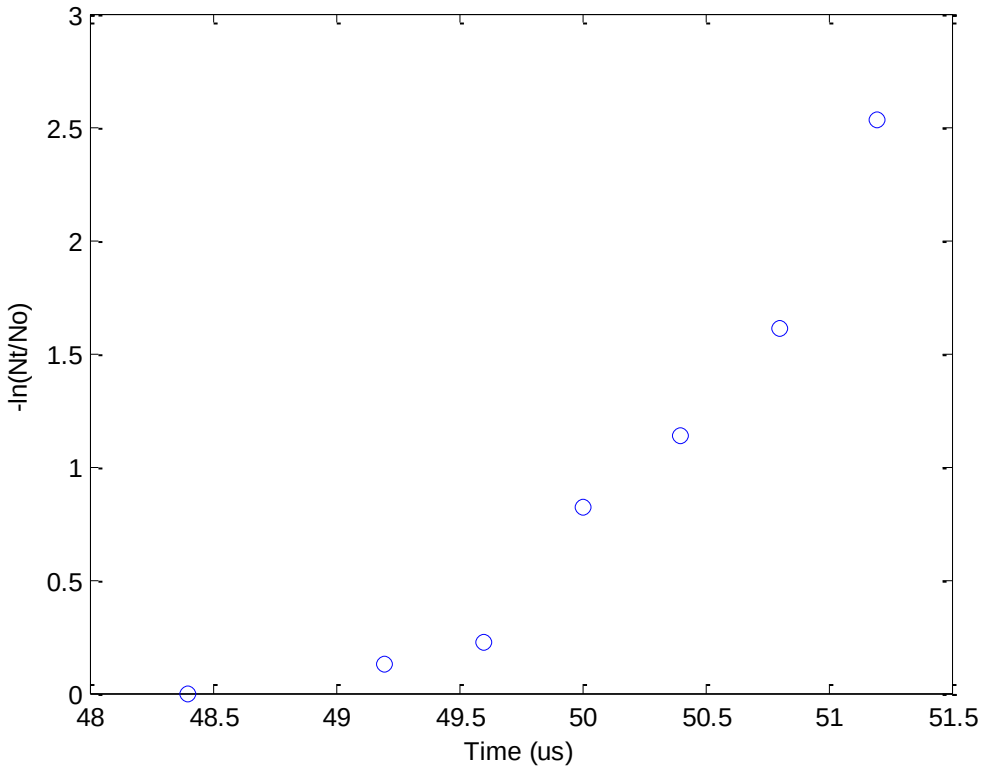

Figure a.11 - Air 5-3 Negative polarity von laue analysis for 2 bar gauge

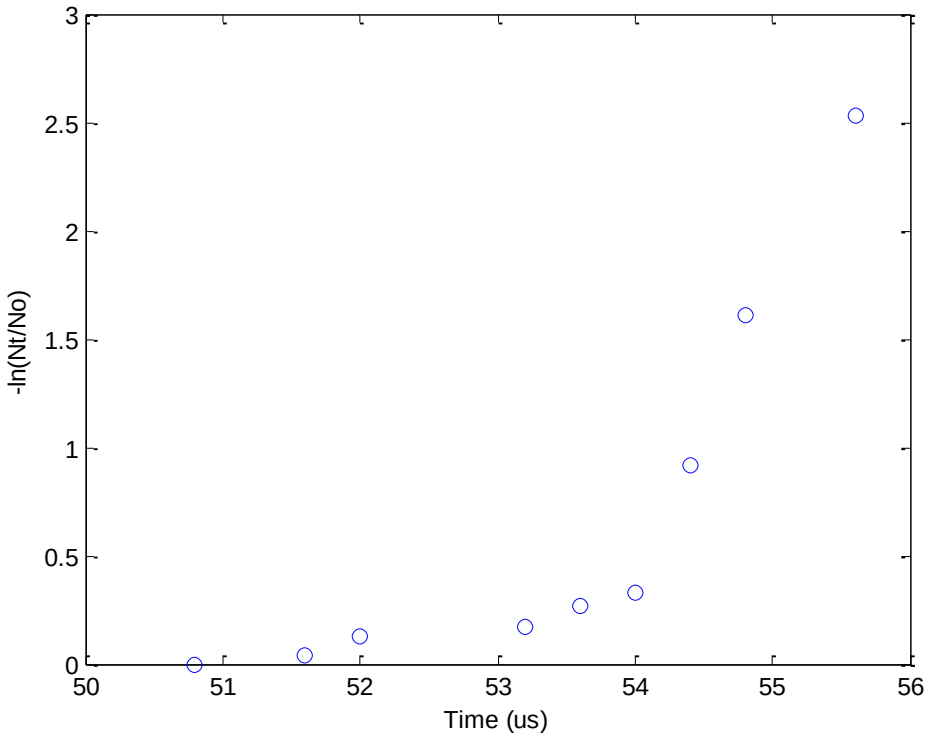

Figure a.12 - Air 5-4 Negative polarity von laue analysis for 2 bar gauge

3 bar analysis

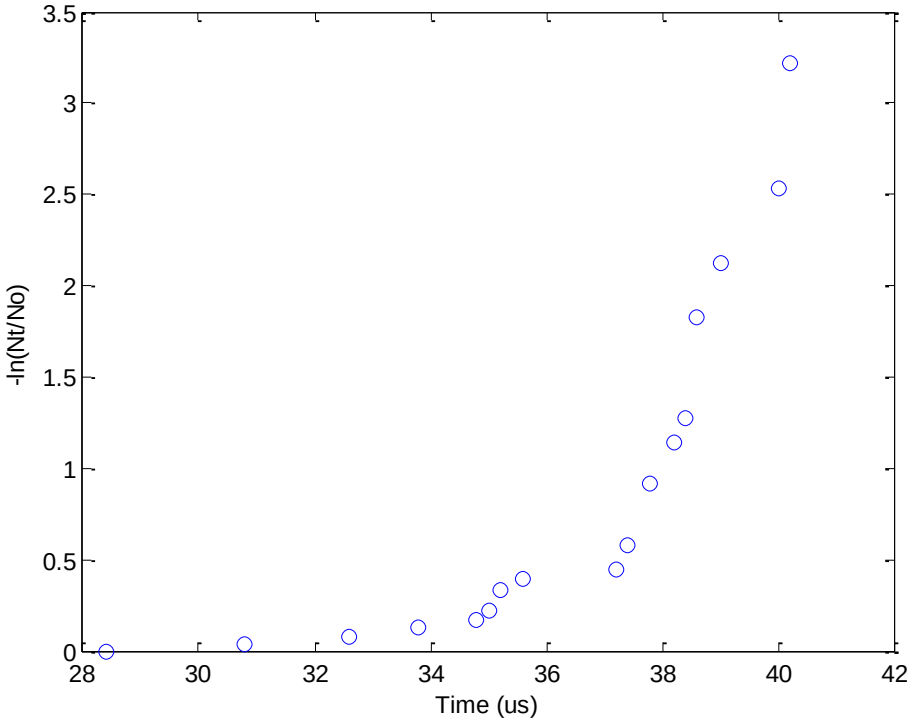

Figure a.13 - Air 5-3 Positive polarity von laue analysis for 3 bar gauge

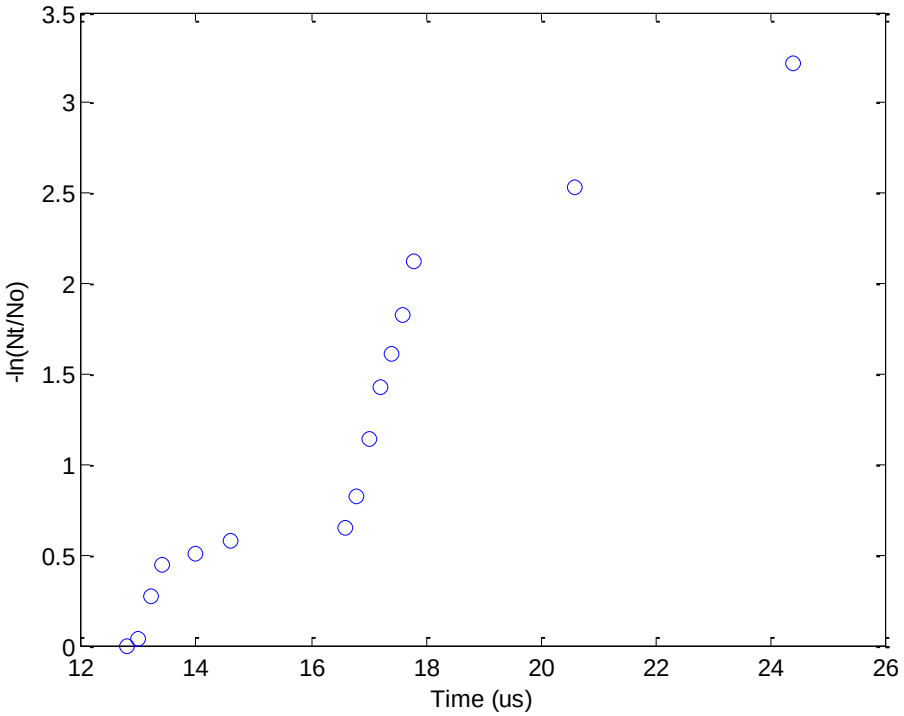

Figure a.14 - Air 5-4 Positive polarity von laue analysis for 3 bar gauge

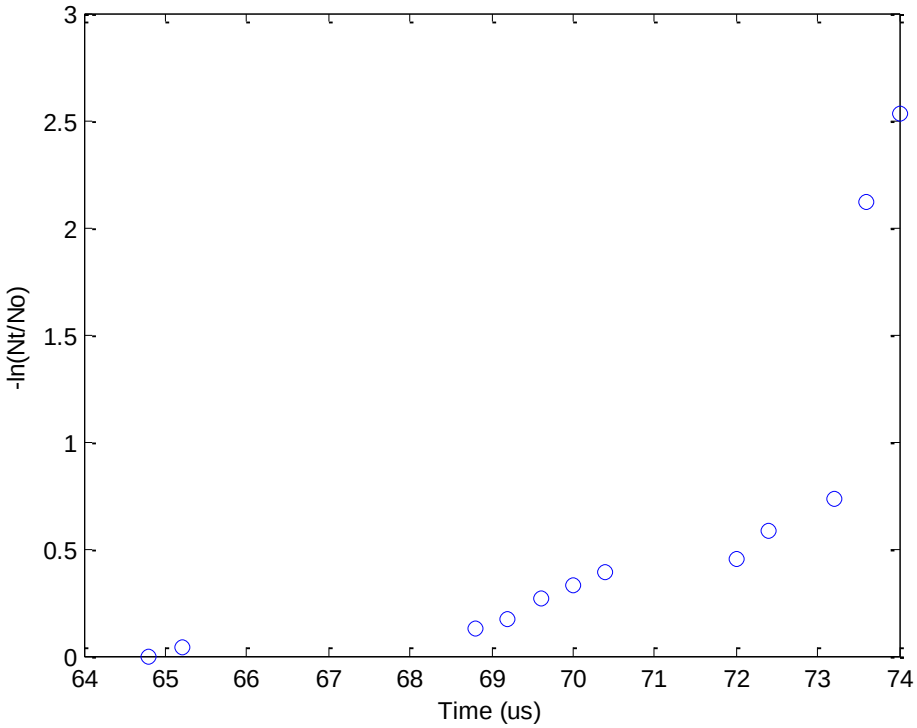

Figure a.15 - Air 5-3 Negative polarity von laue analysis for 3 bar gauge

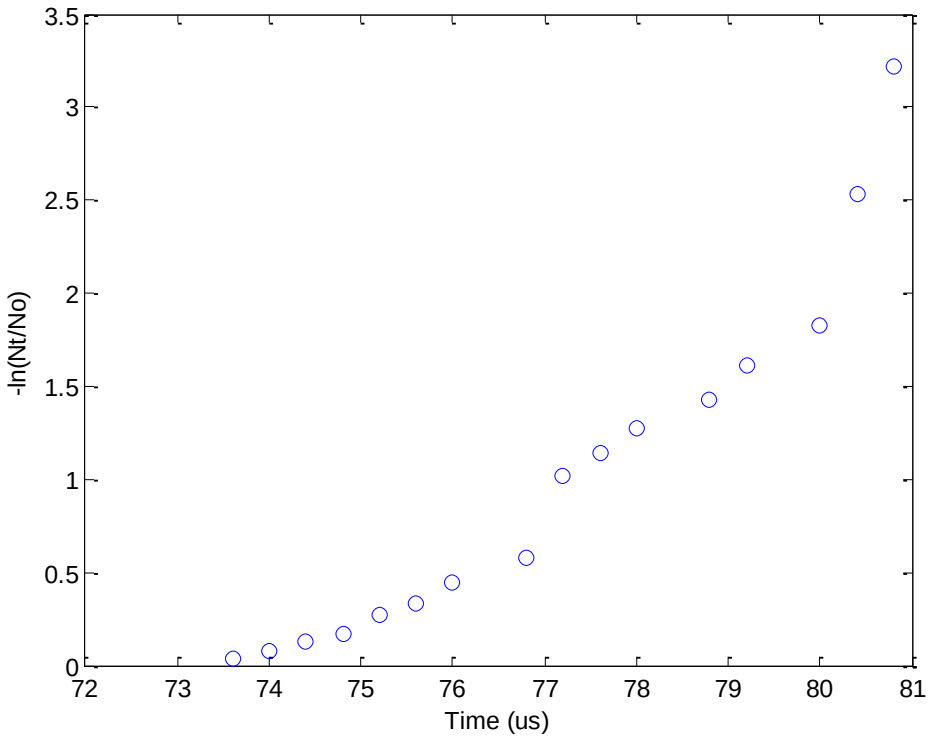

Figure a.16 - Air 5-4 Negative polarity von laue analysis for 3 bar gauge

Von Laue graphs in HFO-1234ze mixtures

0 bar analysis

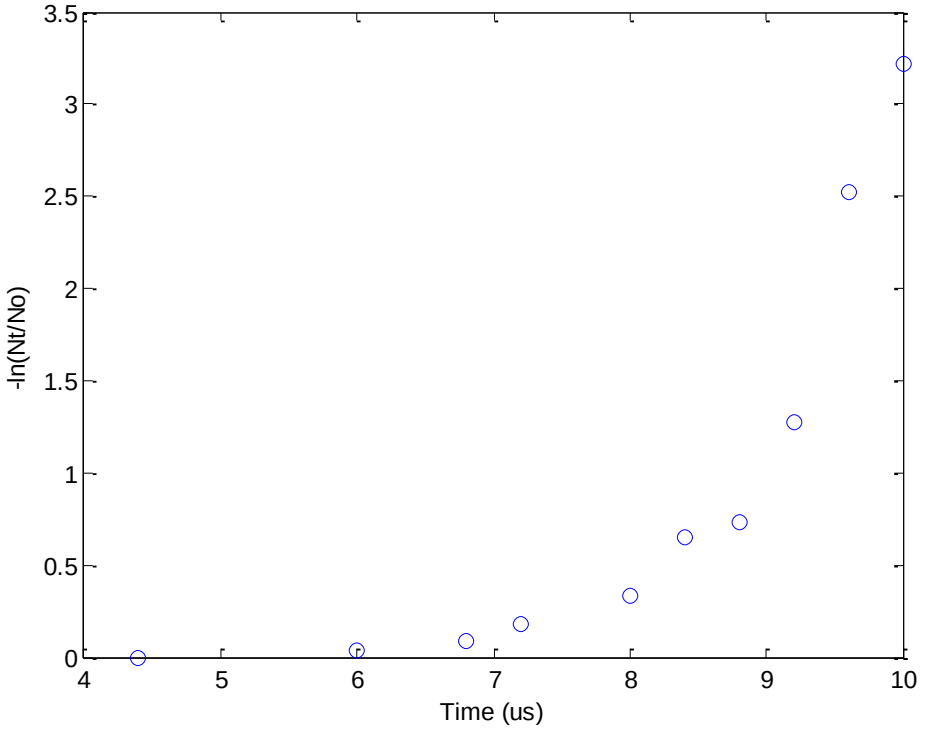

Figure a.17 - Positive polarity 100% N2 von laue analysis for 0 bar gauge

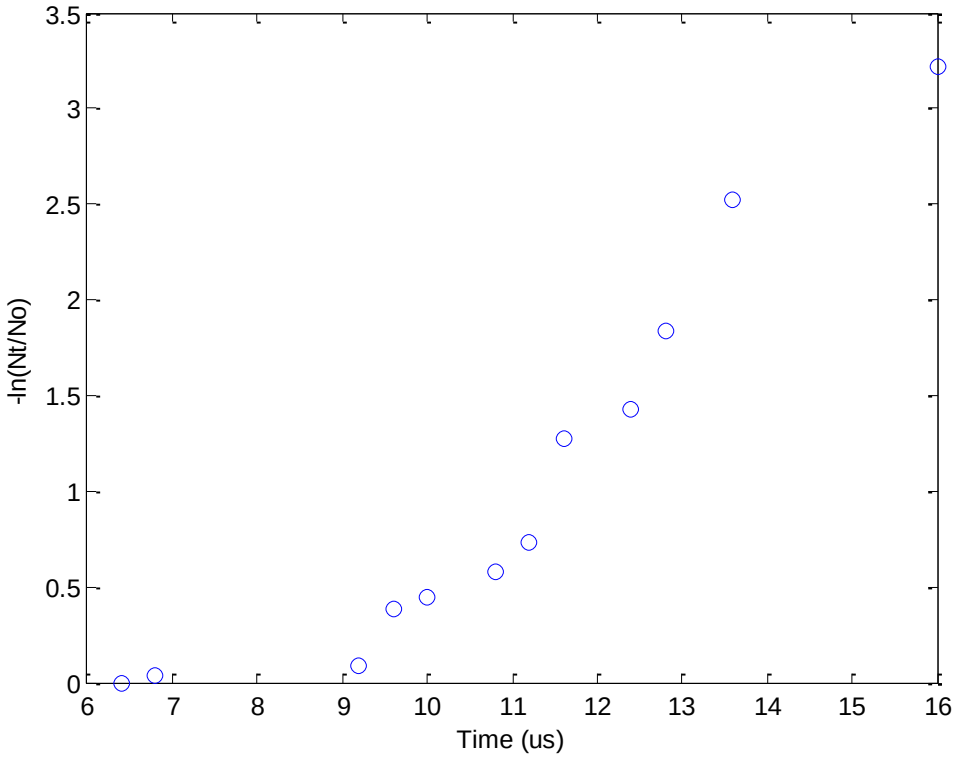

Figure a.18 - Positive polarity 95% N2 5% HFO-1234ze von laue analysis for 0 bar gauge

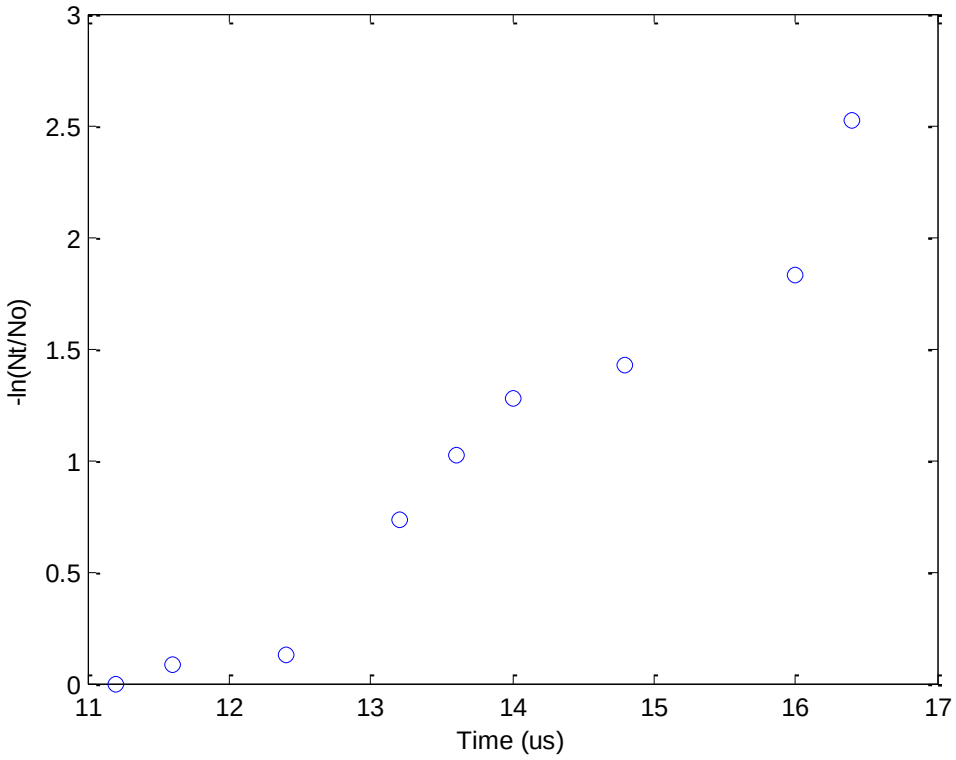

Figure a.19 - Positive polarity 90% N2 10% HFO-1234ze von laue analysis for 0 bar gauge

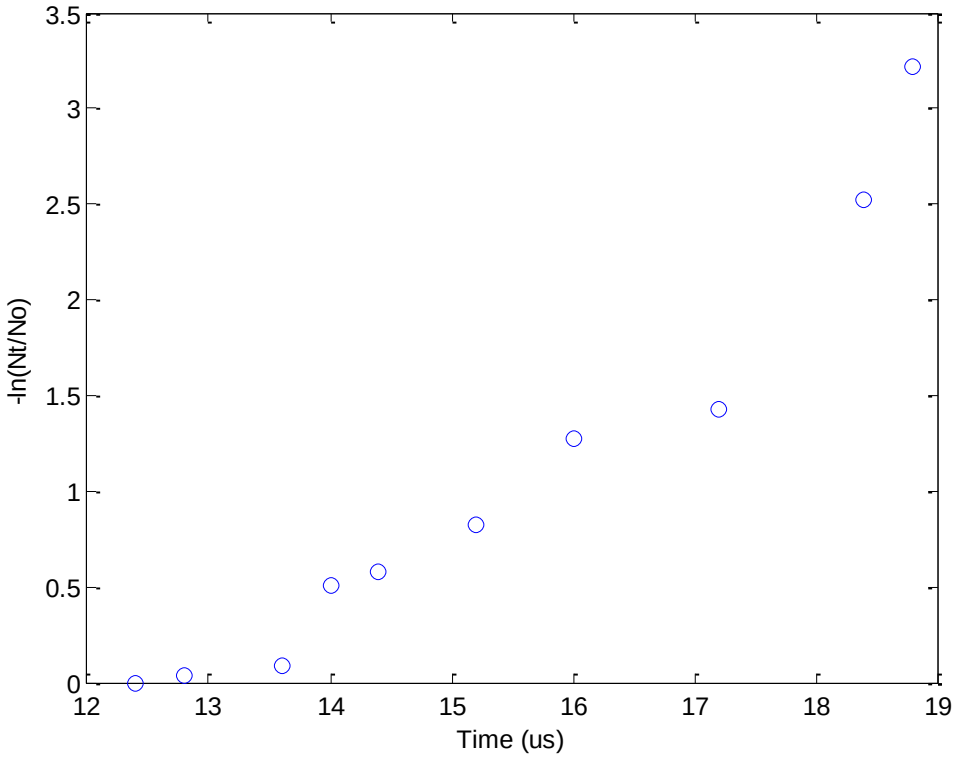

Figure a.20 - Positive polarity 80% N2 20% HFO-1234ze von laue analysis for 0 bar gauge

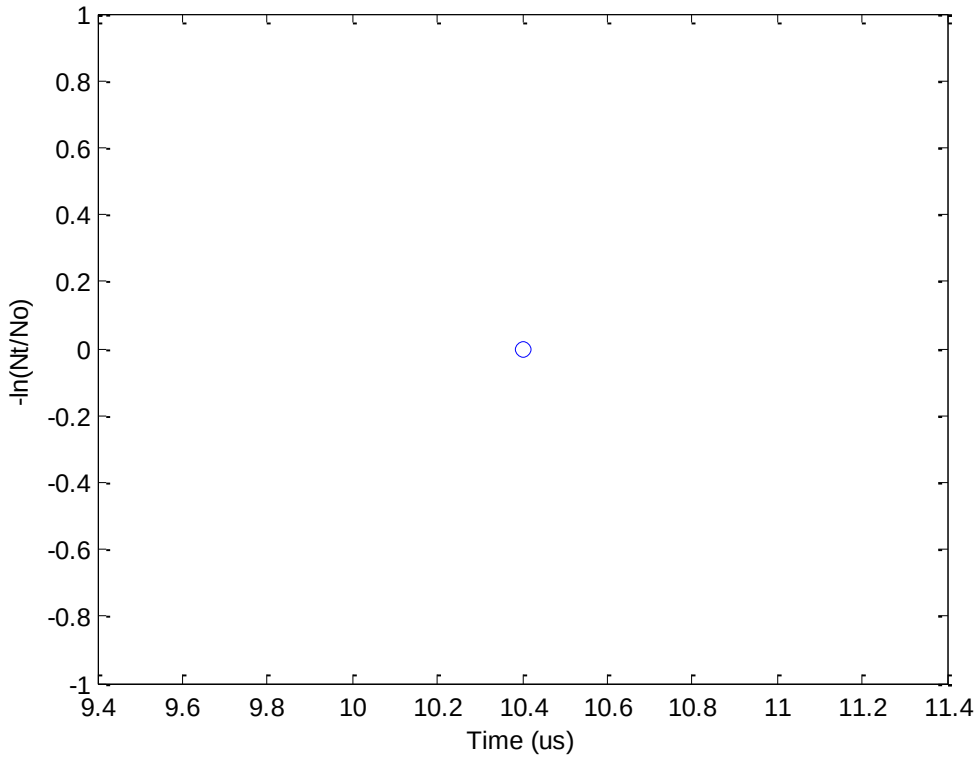

Figure a.21 - Negative polarity 100% N2 von laue analysis for 0 bar gauge

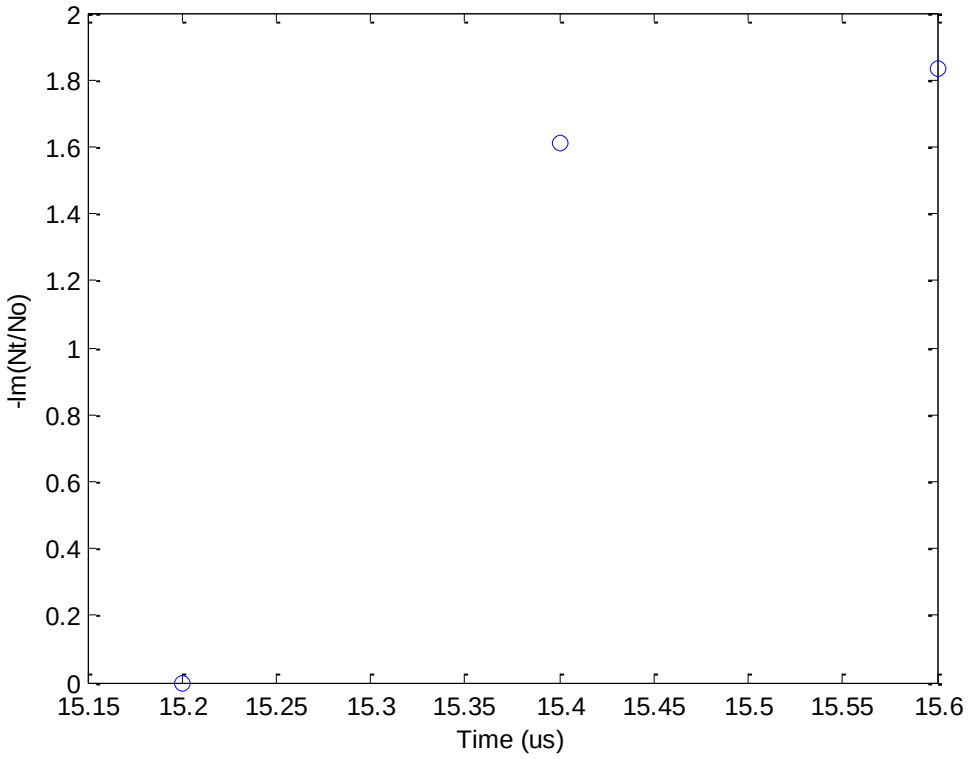

Figure a.22 - Negative polarity 95% N2 5% HFO-1234ze von laue analysis for 0 bar gauge

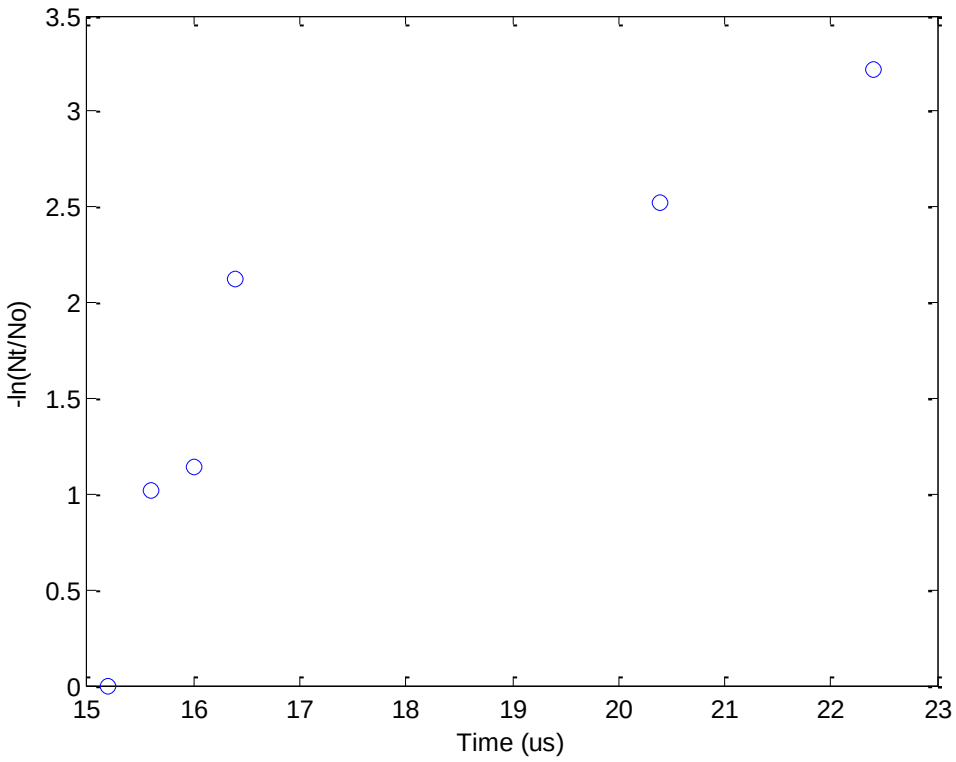

Figure a.23 - Negative polarity 90% N2 10% HFO-1234ze von laue analysis for 0 bar gauge

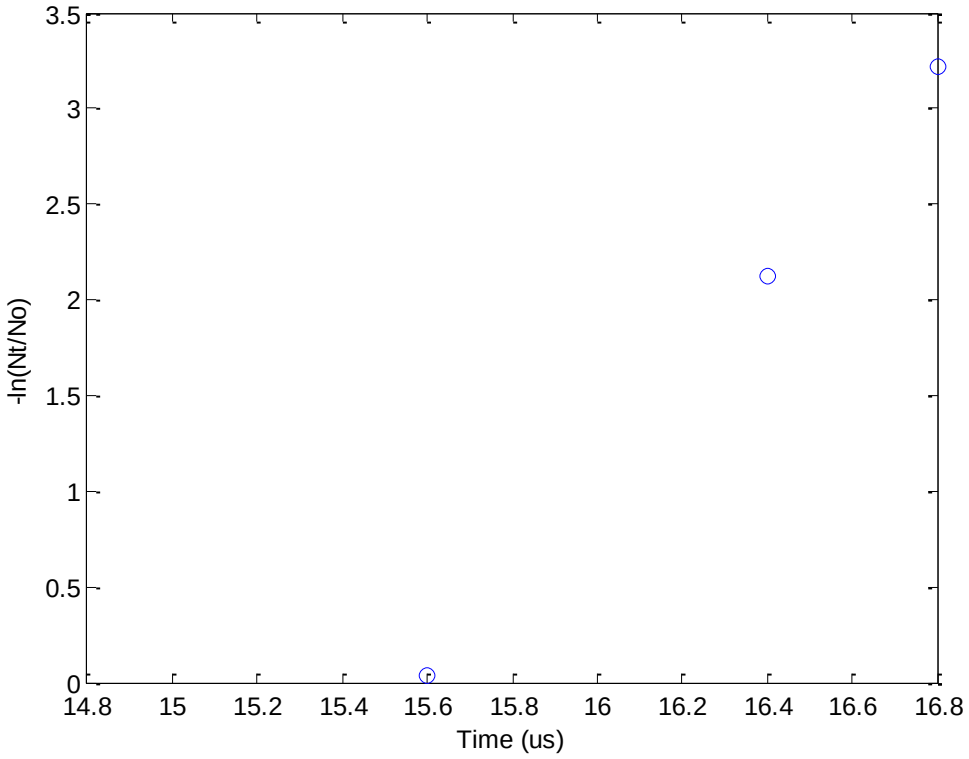

Figure a.24 - Negative polarity 80% N2 20% HFO-1234ze von laue analysis for 0 bar gauge

1 bar analysis

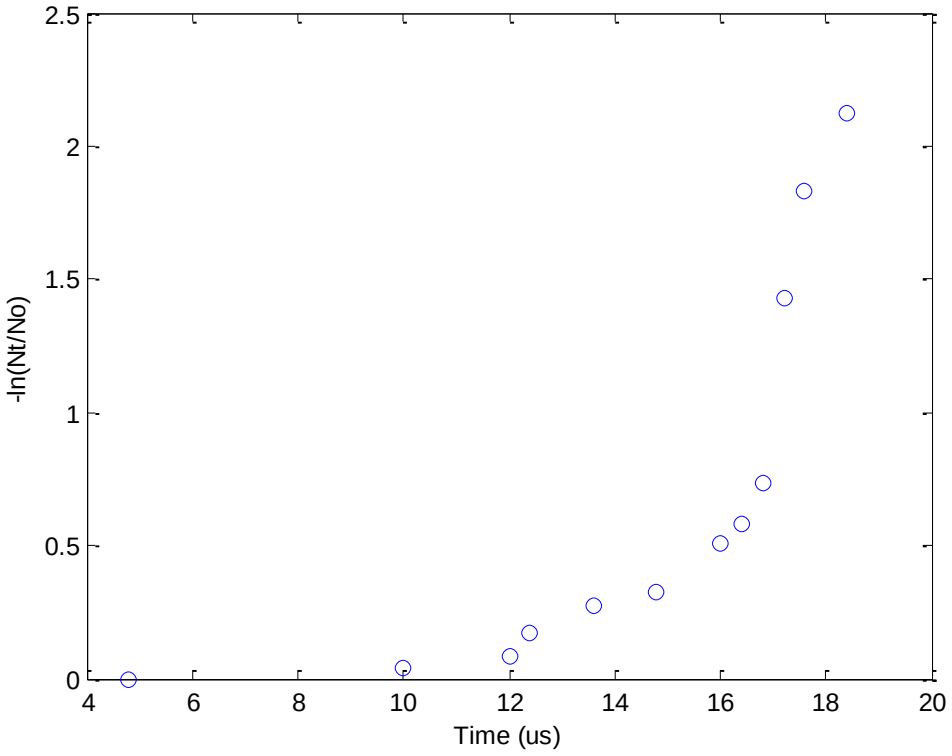

Figure a.25 - Positive Polarity 100% N2 von laue analysis for 1 bar gauge

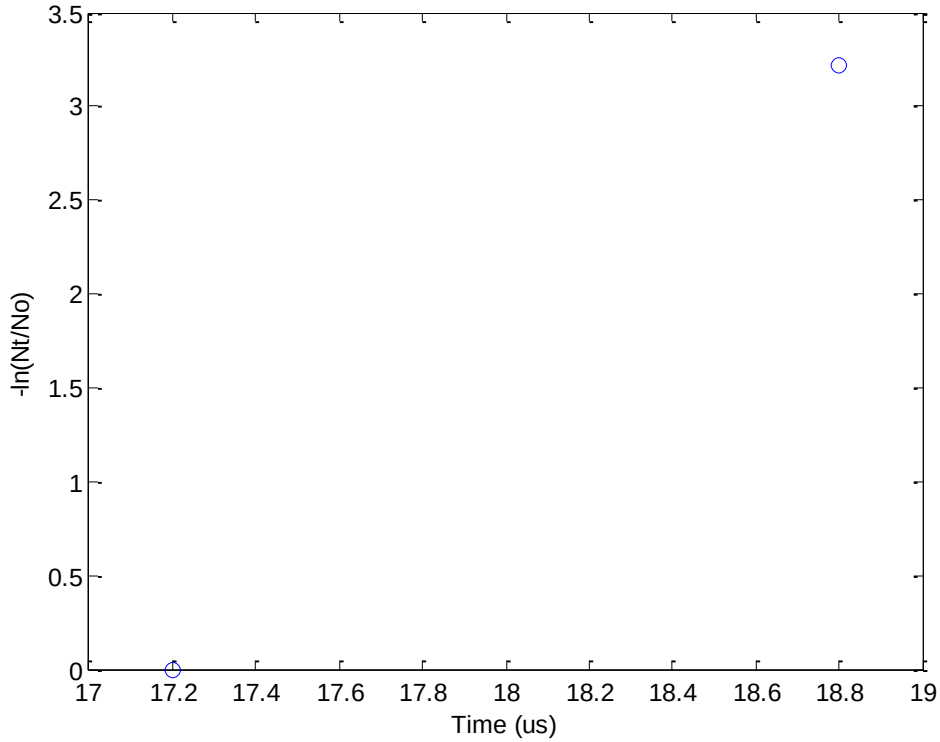

Figure a.26 - Positive polarity 95% N2 5% HFO-1234ze von laue analysis for 1 bar gauge

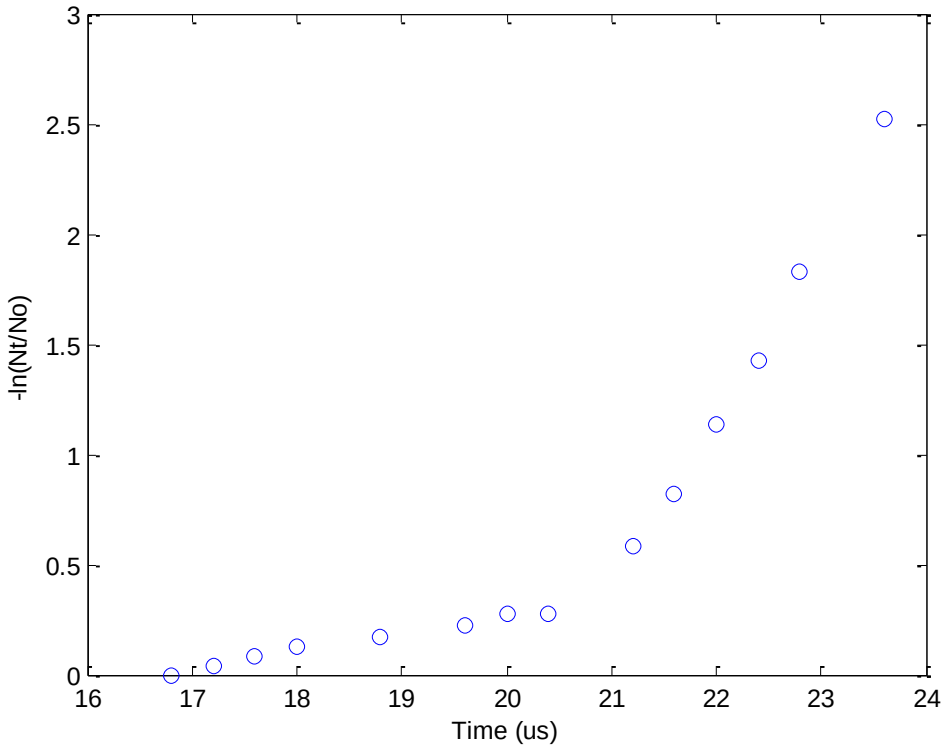

Figure a.27 - Positive polarity 90% N2 10% HFO-1234ze von laue analysis for 1 bar gauge

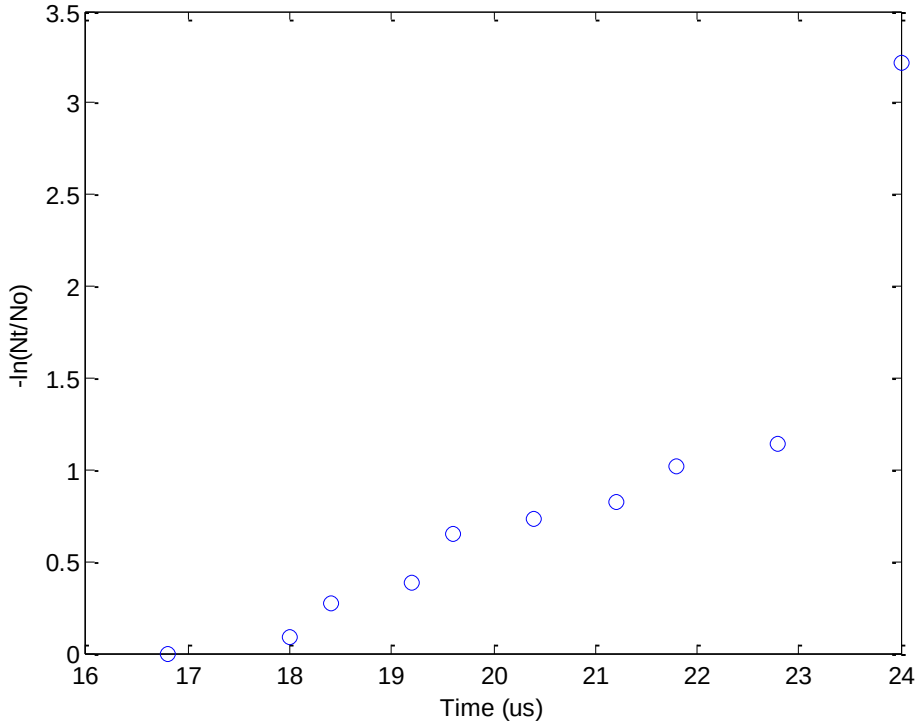

Figure a.28 - Positive polarity 80% N2 20% HFO-1234ze von laue analysis for 1 bar gauge

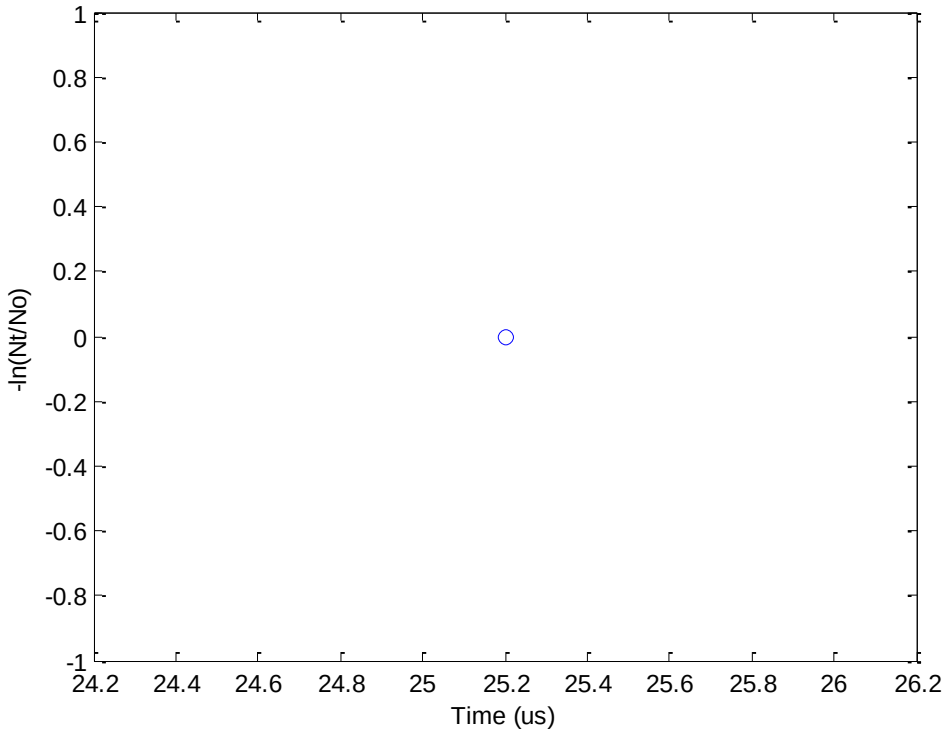

Figure a.29 - Negative Polarity 100% N2 von laue analysis for 1 bar gauge

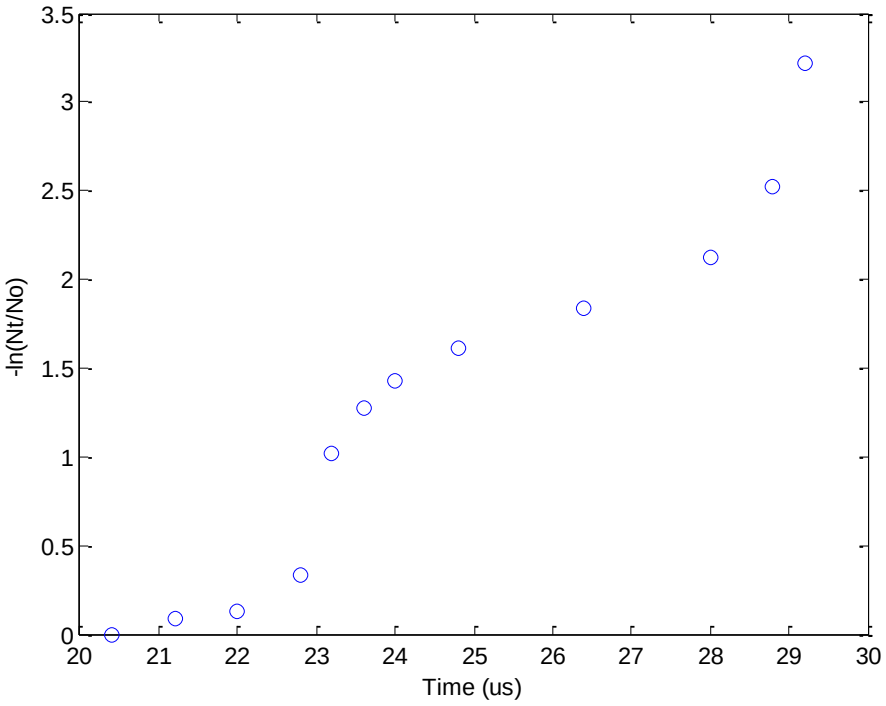

Figure a.30 - Negative polarity 95% N2 5% HFO-12324ze von laue analysis for 1 bar gauge

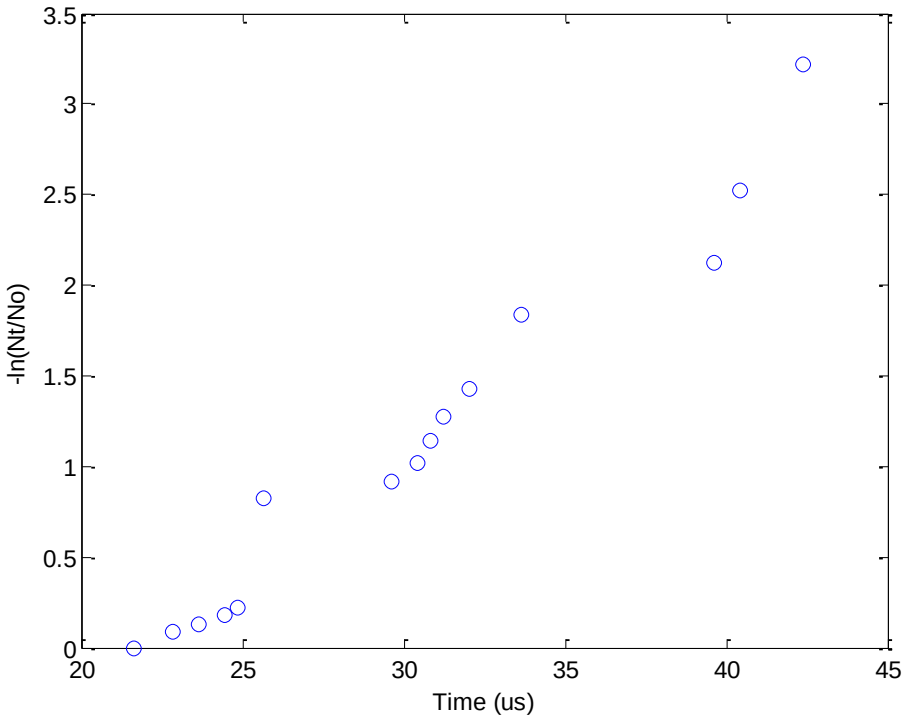

Figure a.31 - Negative polarity 90% N2 10% HFO-1234ze von laue analysis for 1 bar gauge

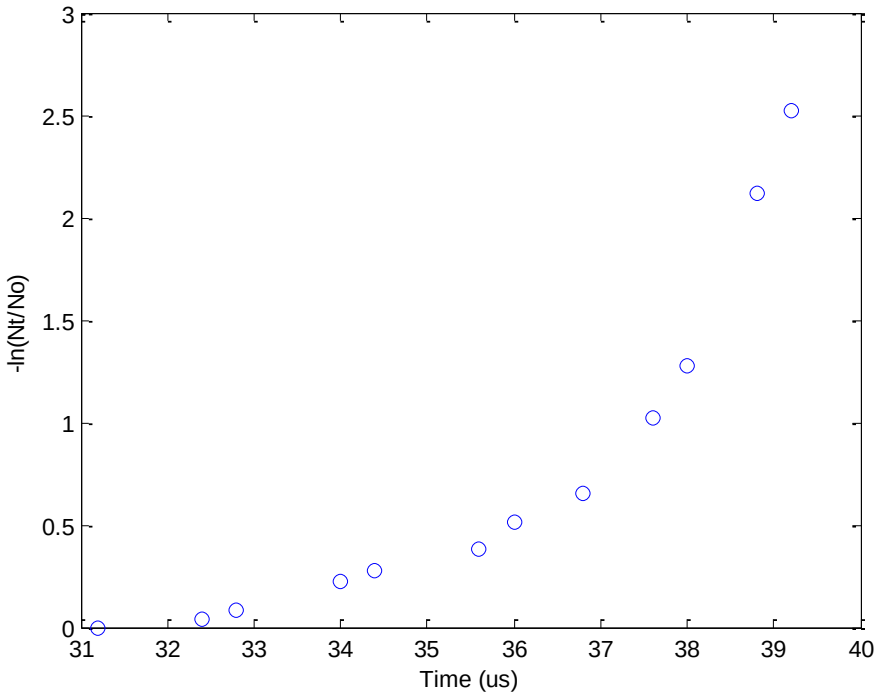

Figure a.32 - Negative polarity 80% N2 20% HFO-1234ze von laue analysis for 1 bar gauge

2 bar analysis

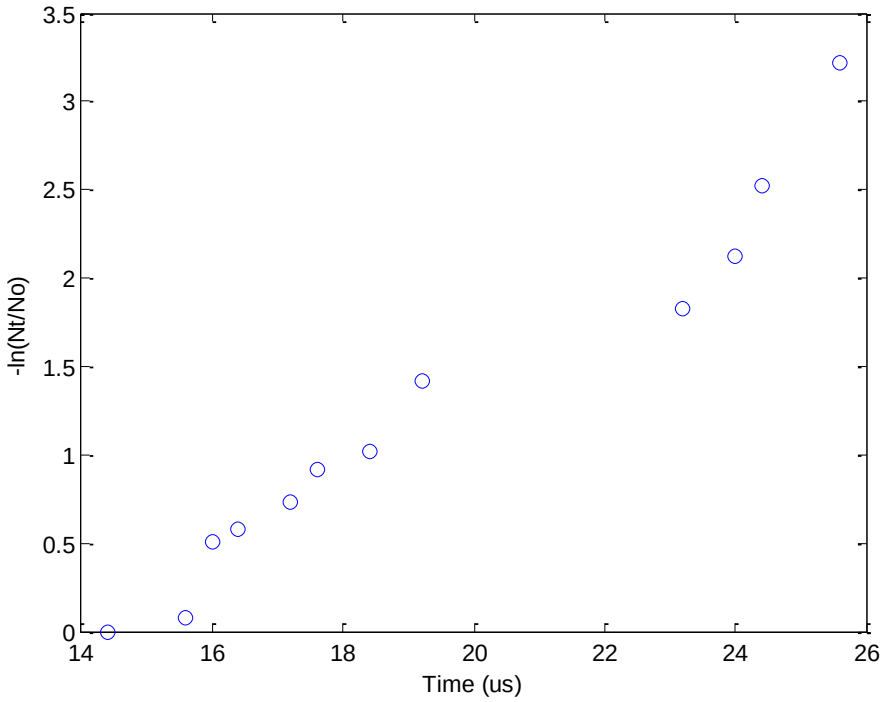

Figure a.33 - Positive polarity 100% N_2 von laue analysis for 2 bar gauge

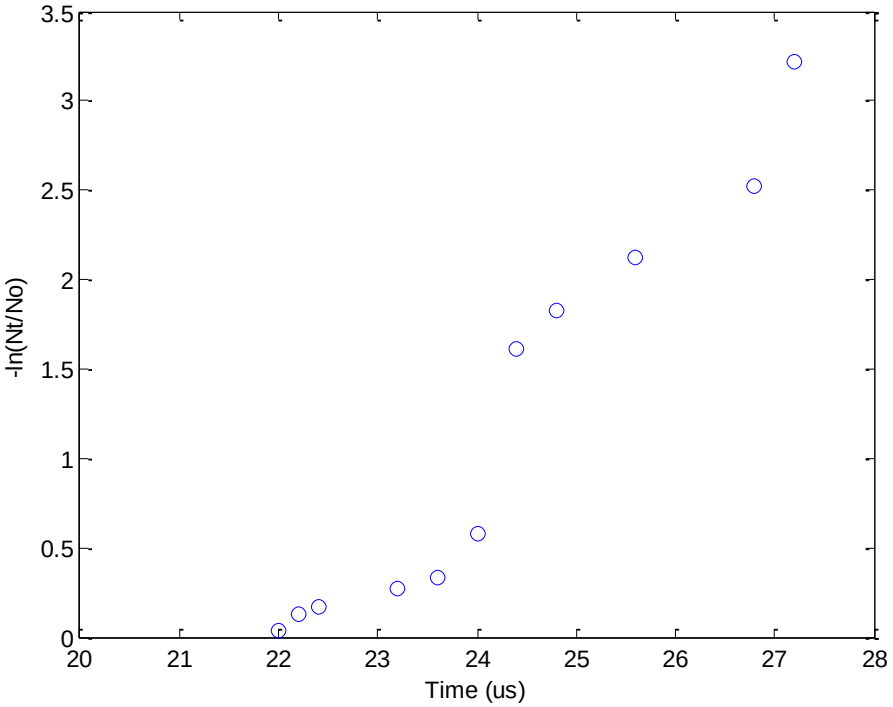

Figure a.34 -Positive polarity 95% N2 5% HFO-1234ze von laue analysis for 2 bar gauge

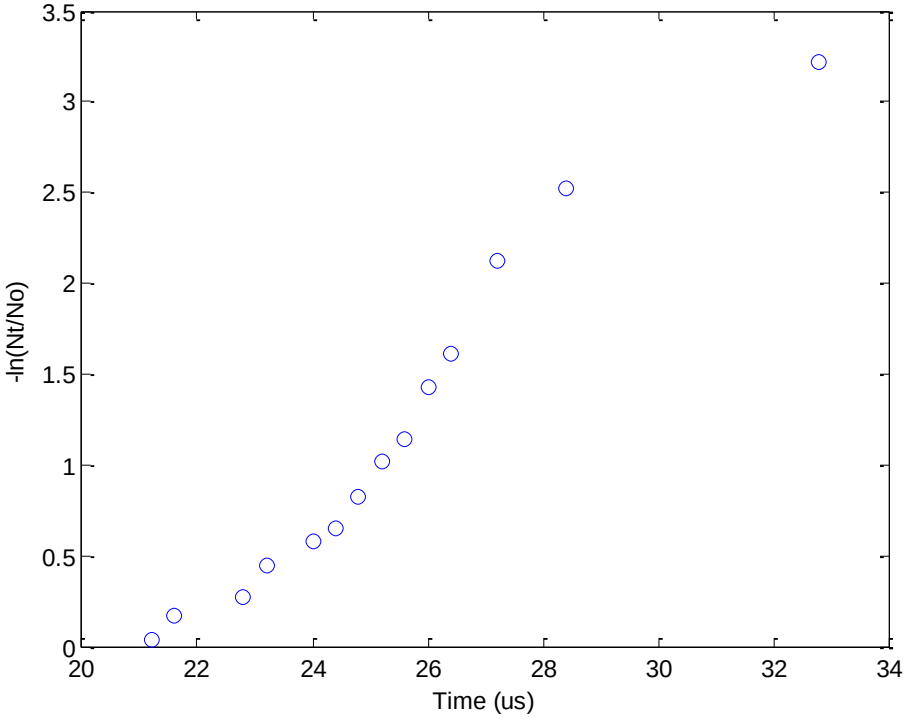

Figure a.35 - Positive polarity 90% N2 10% HFO-1234ze von laue analysis for 2 bar gauge

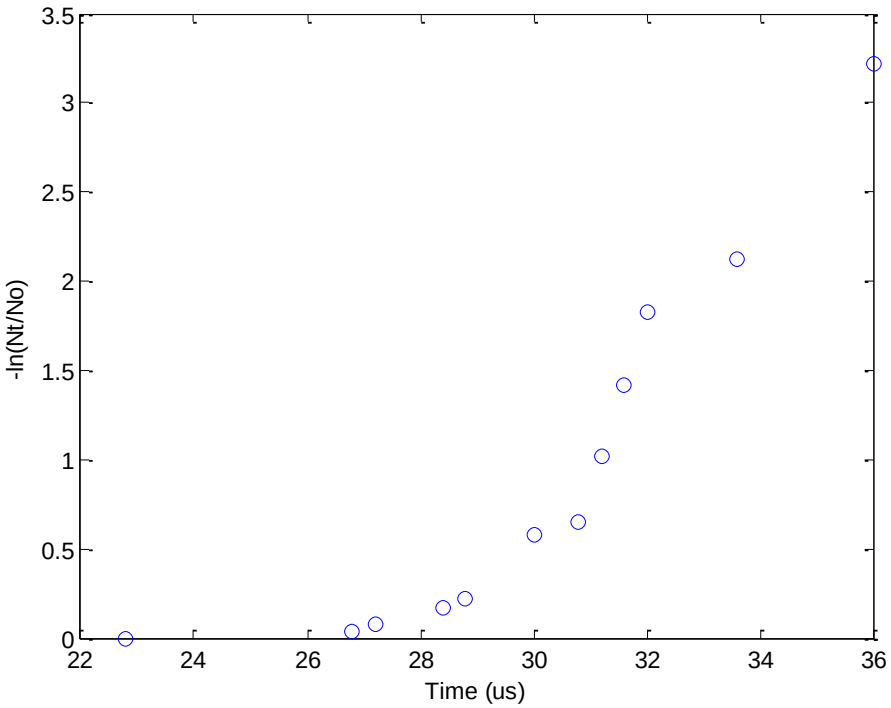

Figure a.36 - Positive polarity 80% N2 20% HFO-1234ze von laue analysis for 2 bar gauge

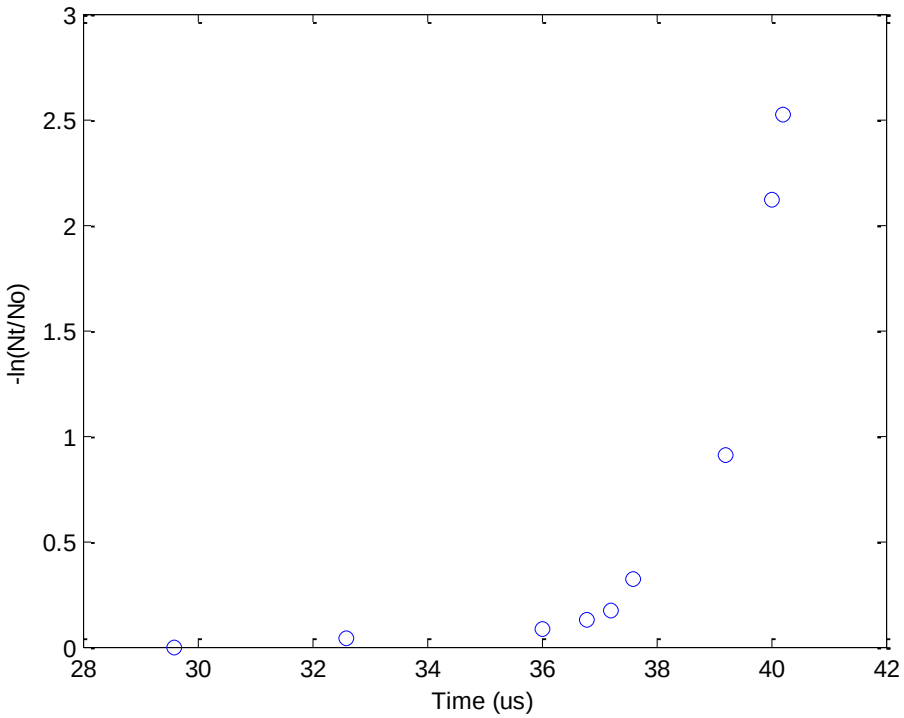

Figure a.37 - Negative polarity 100% N2 von laue analysis for 2 bar gauge

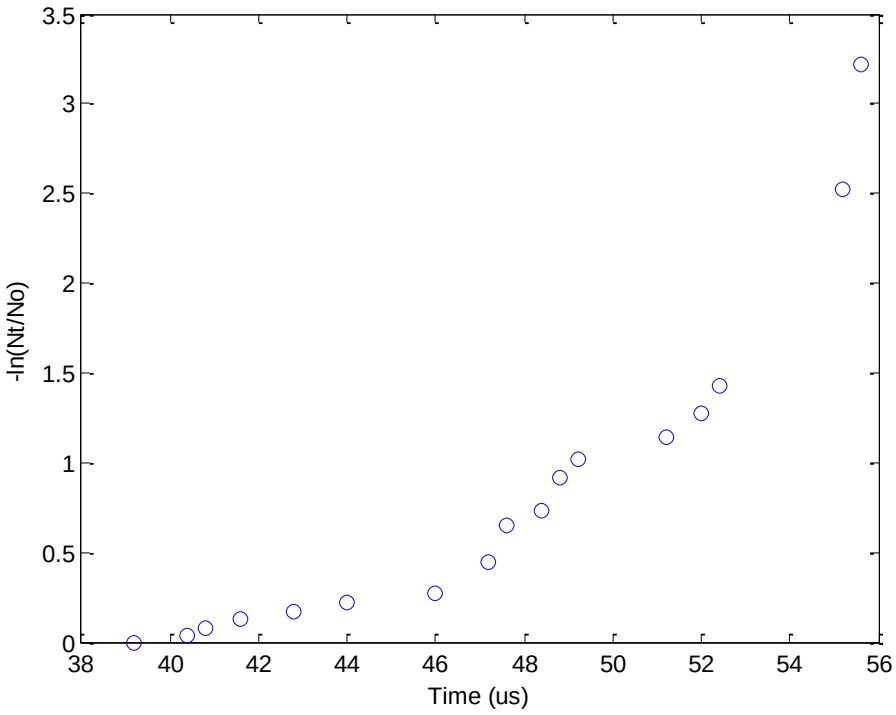

Figure a.38 - Negative polarity 95% N2 5% HFO-1234ze von laue analysis for 2 bar gauge

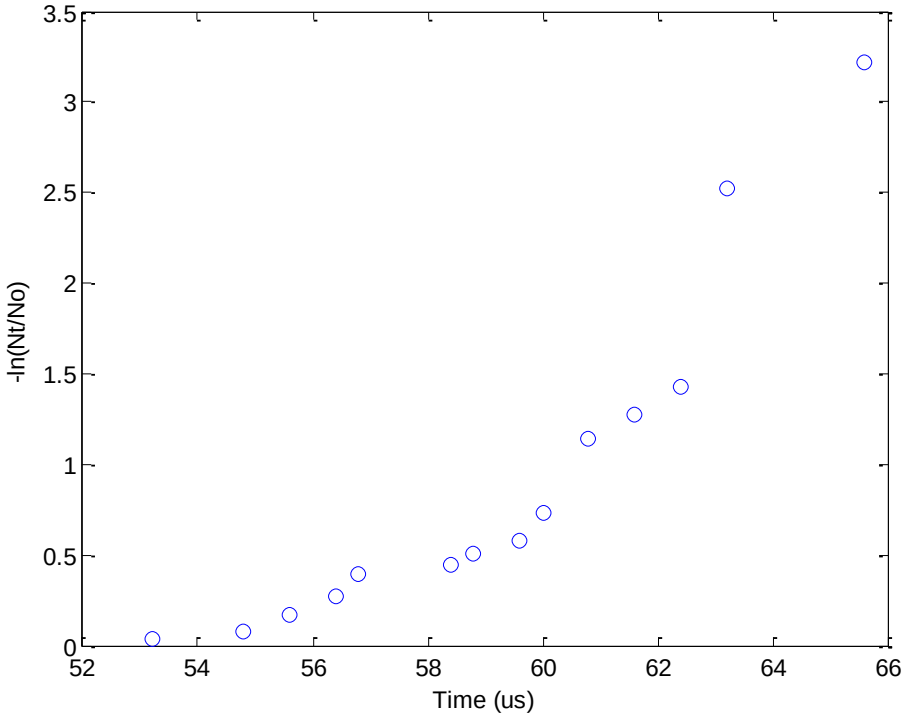

Figure a.39 - Negative polarity 90% N2 10% HFO-1234ze von laue analysis for 2 bar gauge

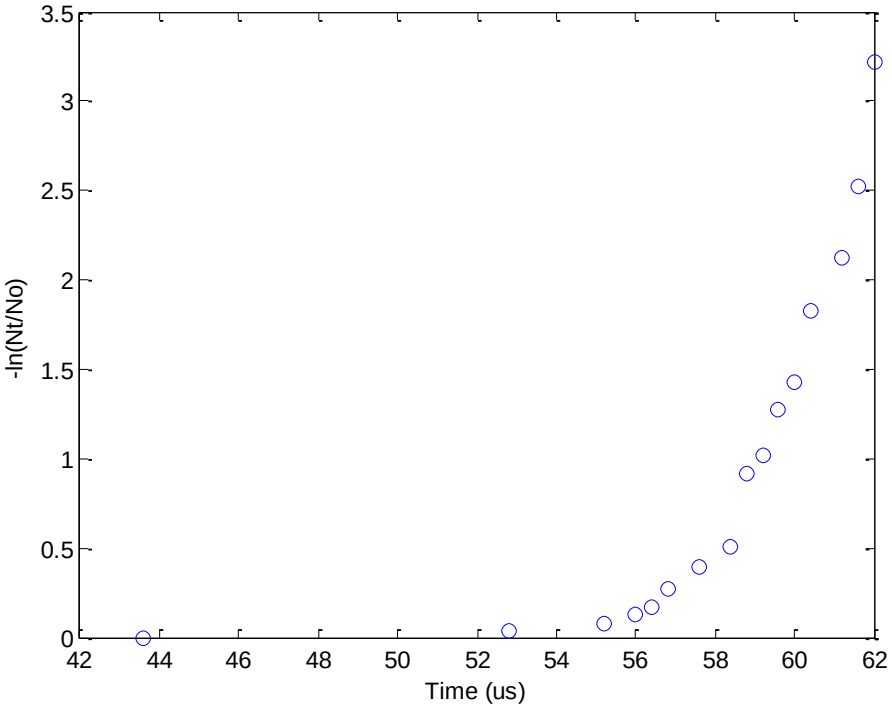

Figure a.40 - Negative polarity 80% N2 20% HFO-1234ze von laue analysis for 2 bar gauge

3 bar analysis

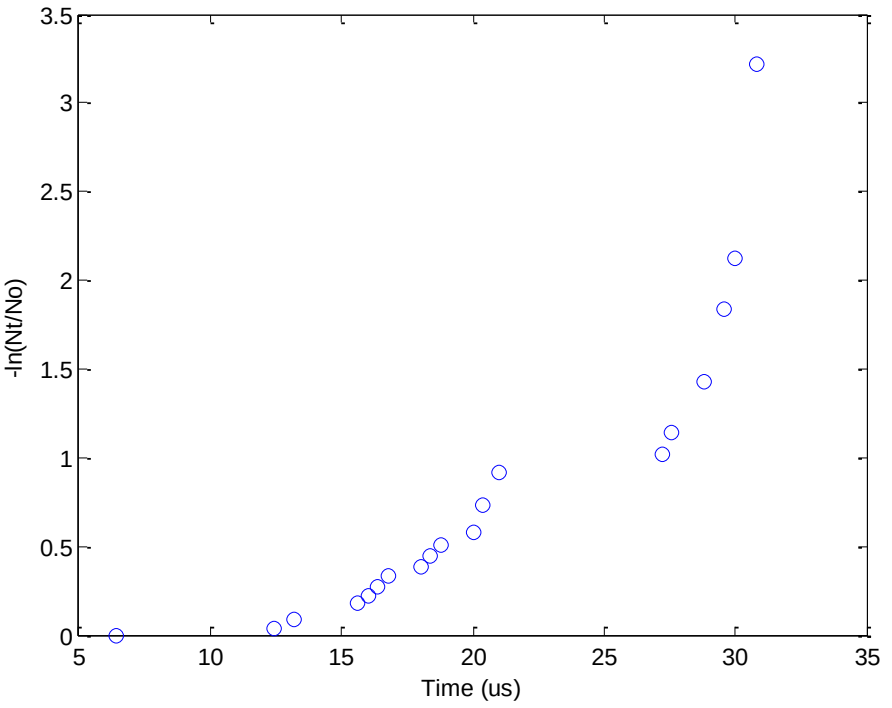

Figure a.41 - Positive polarity 100% N2 von laue analysis for 3 bar gauge

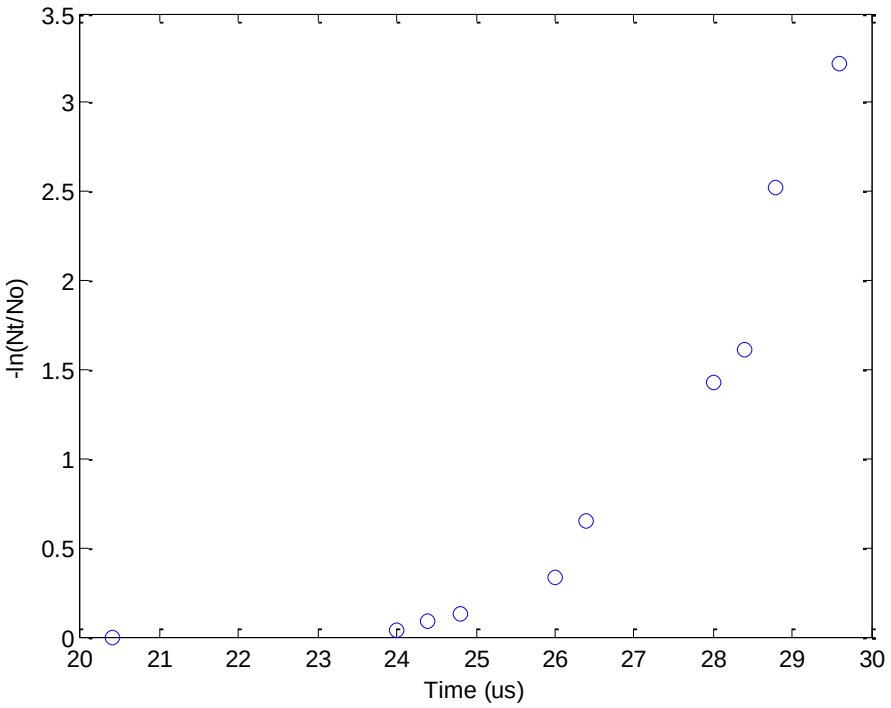

Figure a.42 - Positive polarity 95% N2 5% HFO-1234ze von laue analysis for 3 bar gauge

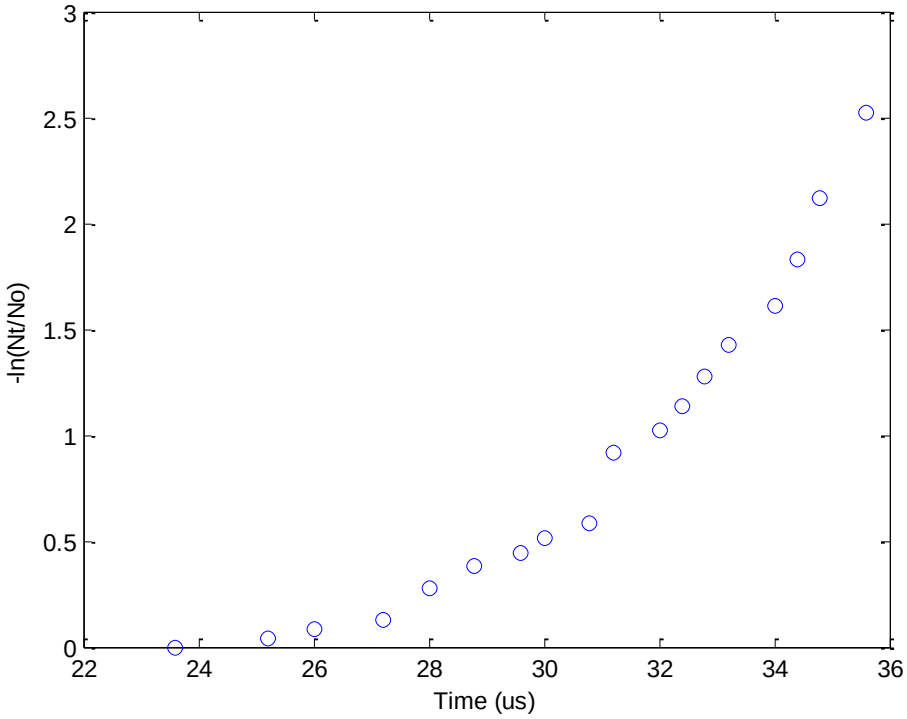

Figure a.43 - Positive polarity 90% N2 10% HFO-1234ze von laue analysis for 3 bar gauge

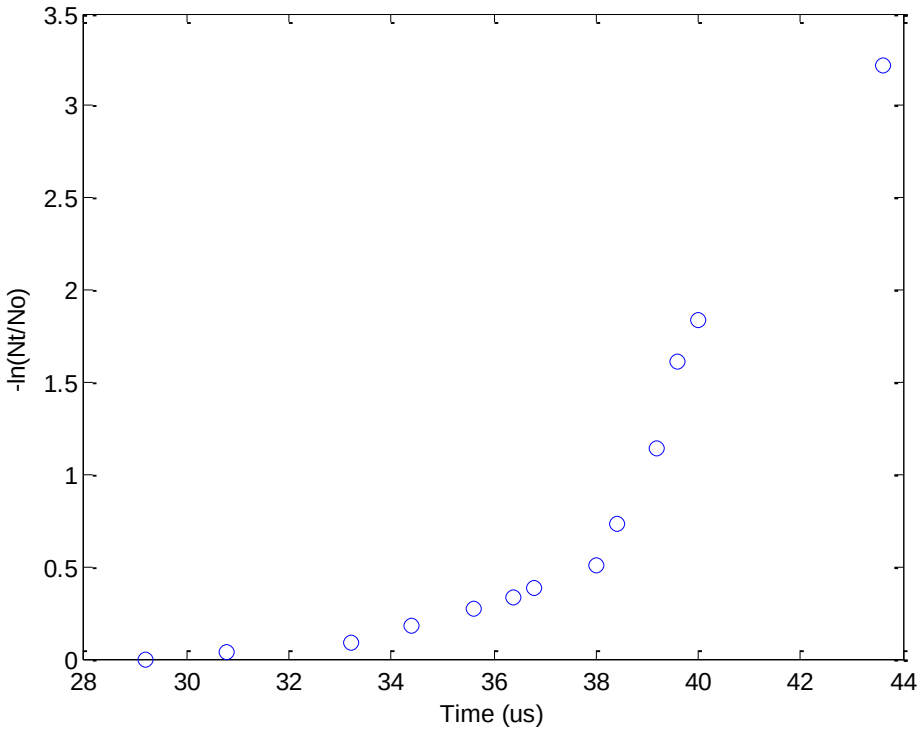

Figure a.44 - Positive polarity 80% N2 20% HFO-1234ze von laue analysis for 3 bar gauge

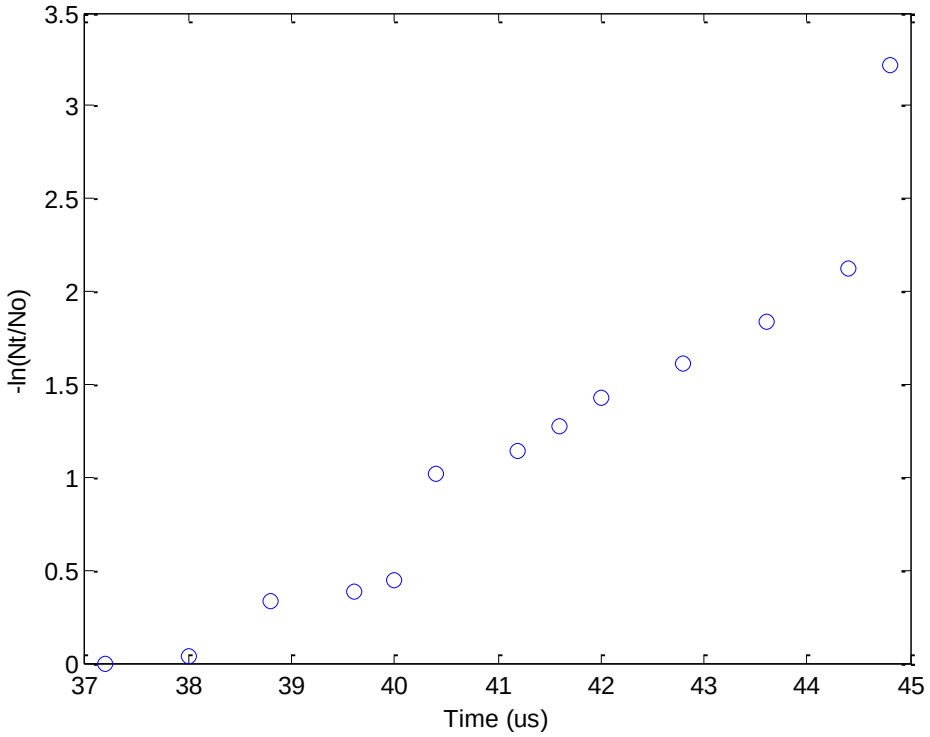

Figure a.45 - Negative polarity 100% N2 von laue analysis for 3 bar gauge

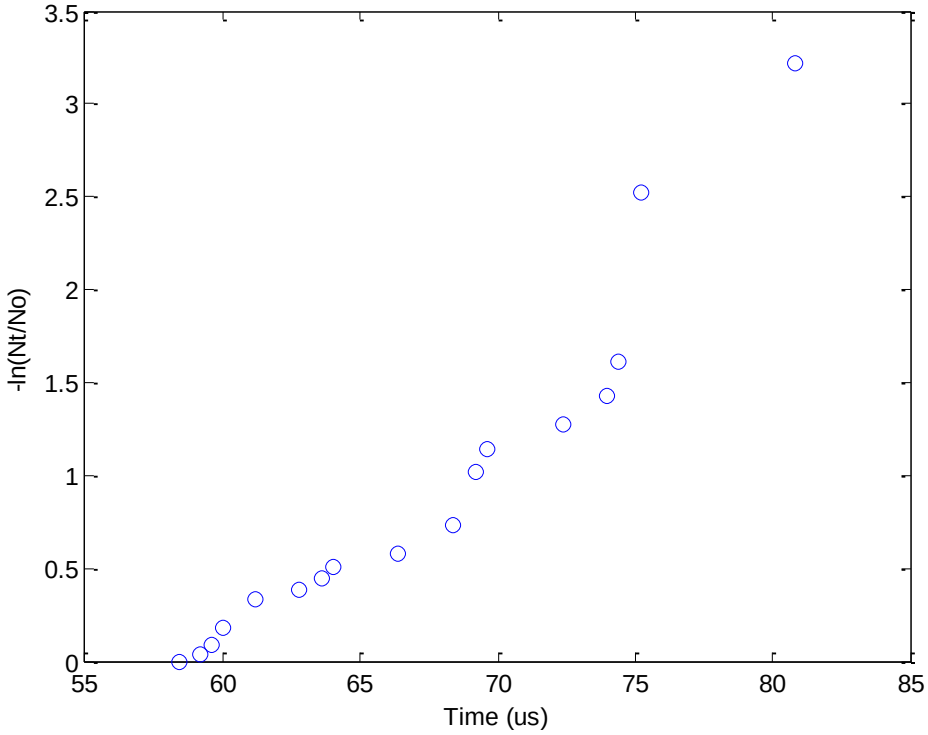

Figure a.46 -Negative polarity 95% N2 5% HFO-1234ze von laue analysis for 3 bar gauge

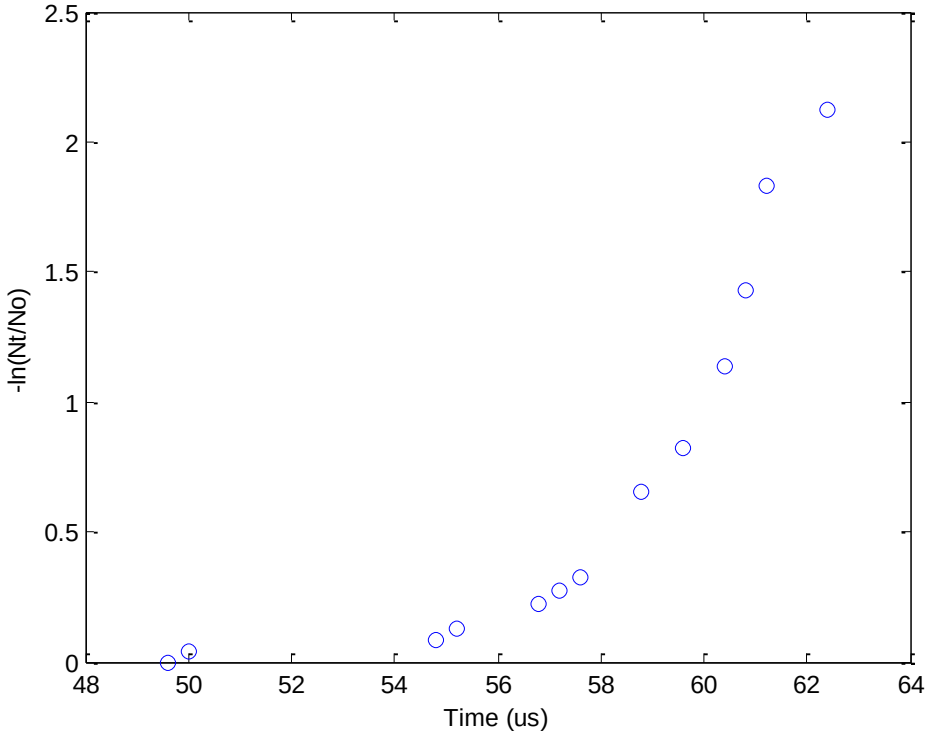

Figure a.47 -Negative polarity 90% N2 10% HFO-1234ze von laue analysis for 3 bar gauge

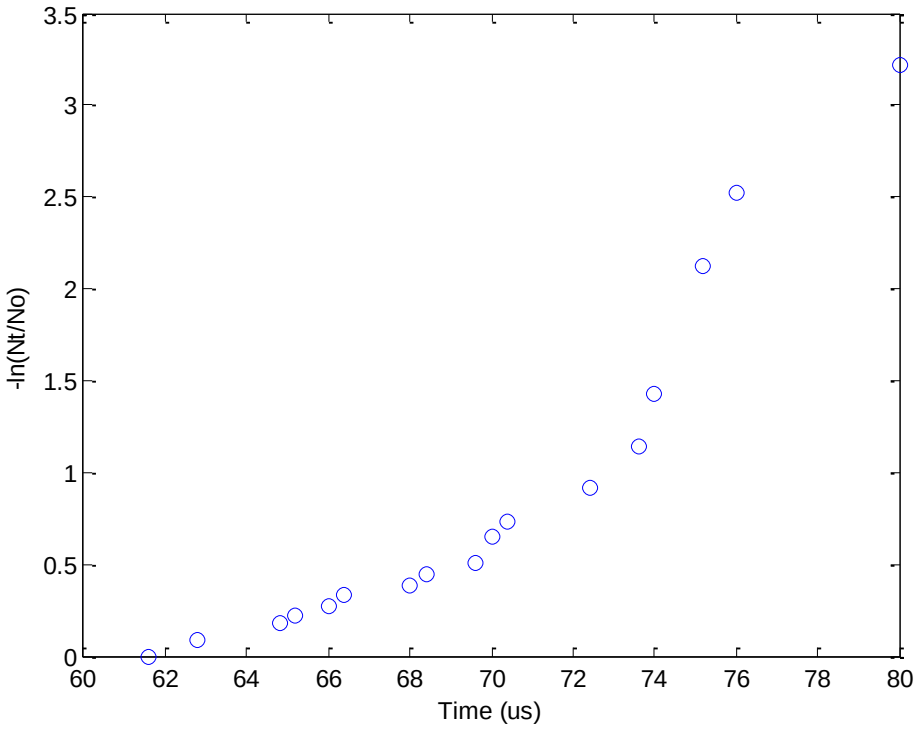

Figure a.48 - Negative polarity 80% N2 20% HFO-1234ze von laue analysis for 3 bar gauge